Department of Engineering Science



Adaptive Optics for Microscopy and Photonic Engineering

A thesis submitted for the Degree of Doctor of Philosophy
at the University of Oxford

Richard Simmonds
Lincoln College

Trinity Term 2012

Richard Simmonds
Lincoln College

Submitted for the Degree of *Doctor of Philosophy*
Trinity Term 2012

Adaptive Optics for Microscopy and Photonic Engineering

Aberrations affect the operation of optical systems, particularly those designed to work at the diffraction limit. These systems include high-resolution microscopes, widely used for imaging in biology and other areas. Similar problems are encountered in photonic engineering, specifically in laser fabrication systems used for the manufacture of fine structures. The work presented in this thesis covers various aspects of adaptive optics developed for applications in microscopes and laser fabrication.

By mathematically modelling a range of idealised fluorescent structures, the effect of different aberrations on their intensity in various microscopes is presented. The effect of random aberrations on the contrast of these different structures is then calculated and the results displayed on idealised images. Images from a two-photon microscope demonstrate the predicted results. The contrast of two structures is compared when imaged first by a conventional microscope and then by the two-photon or confocal sectioning microscopes. The different specimen structures were seen to be affected to varying extents by each aberration mode.

In order to correct for aberrations in microscopy and other photonic applications, adaptive elements such as deformable mirrors are incorporated into the optical setups. An important step is to train the deformable mirror so that it produces appropriate mode shapes to apply a phase to optical wavefronts. One such mirror is modelled using the membrane equation to predict the surface shape when an actuator is applied. Each of these influence functions is combined to produce a set of orthogonal mirror modes, which are used to experimentally produce a set of empirical modes in a two-photon microscope. An alternative method of training a deformable mirror from a spatial light modulator is employed. The focal spot of an optical system is imaged to provide a feedback metric for the mirror to replicate the phase pattern on the spatial light modulator.

A two-photon microscope with adaptive optics is demonstrated by imaging the brains of *Drosophila* deep within the bulk, correcting for both system and specimen induced aberrations using the deformable mirror with empirical mirror modes applied. A harmonic generation microscope is also used to image both biological and non-biological specimens whilst performing aberration correction with a deformable mirror. Adaptive optical methods are also applied to a laser fabrication system, by constructing a dual adaptive optics setup to correct for aberrations induced when fabricating deep in the bulk of a substrate. The efficiency and fidelity of fabrication in diamond substrate is shown to be significantly increased as a result of the dual aberration correction.

An outstanding problem in microscopy is the effect of spatially variant aberrations. Using measurements from the adaptive microscopes, the extent to which they are present in a range of specimens is quantified. One potential technique to be used to correct for these aberrations is multi-conjugate adaptive optics. Different configurations of a multi-conjugate adaptive optics system are modelled and the improvement on the Strehl ratio of aberrated images quantified for both simulated images and real data. The application of this technique in experimental microscopes is considered.

Acknowledgements

I would like to take this opportunity to thank some of the people who have helped me through the process of completing this thesis. Primarily to Dr. Martin Booth, I am extremely grateful for the enthusiasm, support and patient advice he has offered from the first day which has continued, unwavering, ever since. I am also indebted to Patrick Salter, for all the help, guidance and enlightening discussions. For so much time-saving assistance I would like to thank Azmeen Rahman, Dr. Ed Botcherby, Dr. Alexander Jesacher, Dr. Simon Tuohy and Dr. Brian Patton. I am also hugely thankful for all the efforts made behind the scenes by Prof. Tony Wilson. Without the friendship of the research group, my time spent would have been much less interesting. For this I would like to thank Dr. Alex Corbett, Dr. Anisha Kubasik-Thayil, Dr. Chris Smith, Biru Wang, Dr. Dan Burke and all members past and present of the Holder Coffee Club.

Many thanks also to everyone who has provided me with specimens to subject to my imaging skills: Dr. Toby Braun, Dr. Robert Thomson, Dr. Shankar Srinivas, Dr. Patrick Salter, Dr. Jason Smith, Phil Dolan and Dr. David Owald.

I am expressly grateful for the financial support and assistance offered by the Engineering and Physical Sciences Research Council and Lincoln College which has been fundamental in allowing me to continue my studies.

Thanks also to my family for the continued support and guidance. To my friends, thanks for providing me with some fantastic experiences, wide-ranging discussions and entertaining photo opportunities. Finally, Id like to say a huge thank-you to Trish, for putting up with me and giving me the impetus to leave my comfort zone. The last four years would have been much less enjoyable without you.

Contents

1 Introduction and background **6**
- 1.1 Optical microscopes . . . 6
- 1.2 Direct laser writing . . . 10
- 1.3 Aberrations and adaptive optics . . . 11
- 1.4 Structure of thesis . . . 13

2 Theory of focussing and imaging **16**
- 2.1 Focussing and image formation . . . 16
  - 2.1.1 Diffraction theory . . . 17
  - 2.1.2 Diffraction by a lens . . . 18
  - 2.1.3 The point spread function . . . 21
  - 2.1.4 The optical transfer function . . . 26
- 2.2 Image formation in optical microscopes . . . 27
  - 2.2.1 Conventional fluorescence microscope . . . 28
  - 2.2.2 Confocal microscope . . . 29
  - 2.2.3 Two-photon microscope . . . 30
  - 2.2.4 Harmonic generation microscope . . . 32
- 2.3 Imaging in the presence of aberrations . . . 32

3 Effects of aberrations and specimen structure in fluorescence microscopy **37**
- 3.1 Introduction . . . 37
- 3.2 Aberrations and the pupil function . . . 39
- 3.3 Image formation in fluorescence microscopes . . . 40
- 3.4 Image formation in the conventional fluorescence microscope . . . 43
- 3.5 Image formation in the confocal and two-photon fluorescence microscopes 45
- 3.6 Confocal and two-photon fluorescence microscope contrast calculations . 51
- 3.7 Contrast effects in aberrated microscope images . . . 52
- 3.8 Conclusions . . . 55

4 Deformable mirror training **58**
- 4.1 Introduction . . . 59
- 4.2 Theoretical mirror modes . . . 61
  - 4.2.1 Mirror modelling . . . 62
- 4.3 Empirical mirror modes . . . 64
  - 4.3.1 Empirical mirror modes for a two-photon microscope . . . 67
- 4.4 Training DM by nulling SLM applied phase . . . 72
  - 4.4.1 Method . . . 73
  - 4.4.2 Training results . . . 76
  - 4.4.3 Limitations . . . 80

4.5 Conclusions 81

5 Aberration corrected imaging in multiphoton microscopy 84
5.1 Introduction 84
5.2 Two-photon fluorescence microscopy 85
5.2.1 *Drosophila* brains 86
5.3 Second and third harmonic generation microscopy 91
5.3.1 Mouse embryos 92
5.3.2 Polymer samples 94
5.3.3 Waveguides 94
5.3.4 Fabrication in diamond 103
5.4 Conclusions 104

6 Laser processing of diamond 106
6.1 Introduction 106
6.2 Experimental set-up 108
6.3 Aberration correction routine 109
6.4 Aberration corrected point fabrication 112
6.5 Pulse front and phase front effects 115
6.6 Fabrication of extended structures 118
6.7 Aberration corrected diamond imaging 120
6.7.1 Determining signal emission mechanism 121
6.7.2 Harmonic generation diamond images 123
6.8 Conclusions 125

7 Spatially variant aberration correction 127
7.1 Introduction 127
7.2 Measuring spatially variant aberrations 129
7.2.1 Calculating spatially variant aberrations 129
7.2.2 Spatially variant aberration maps 134
7.3 Modelling multi-conjugate correction 141
7.3.1 One-dimensional aberration correction 143
7.3.2 Two-dimensional aberration correction 148
7.3.3 Simulation of correction for a real specimen 150
7.4 Conclusions 155

8 Conclusions and summary 157

A Mathematical functions 160

B Zernike polynomials 162

C Aberration correction routine 165

D Design of multi-conjugate system 168

Bibliography 170

Publications arising from this research 176

Chapter 1

Introduction and background

Optical microscopes are capable of imaging structures at the scale of the diffraction limit of the objective lens. Similarly, laser fabrication systems have the potential to fabricate structures at the diffraction limit of the final optical element. Many microscopes and laser fabrication systems are almost identical in their structure: both consist of a laser, optical components, scanners, high NA lenses and a specimen or substrate. As such, the diffraction-limited focal spot employed by both to image or fabricate is detrimentally affected by system- and specimen- or substrate-induced aberrations. The work that follows investigates how adaptive optics can be used to help recover the diffraction-limited focal spots by compensating for these aberrations.

Since the structure of both optical microscopes and laser fabrication systems are similar, much of the modelling and techniques presented are common to both applications. The effects of aberrations in such optical systems are modelled and quantified and methods for utilising adaptive optics to help compensate and correct for them are presented. The use of adaptive optics is also demonstrated, both in optical microscopes and a laser fabrication system in order to correct for any aberrations present.

1.1 Optical microscopes

In this section, an overview of the methods of optical microscopy is presented, covering conventional, confocal, two-photon and harmonic generation microscopes. In the con-

ventional microscope, a light source uniformly illuminates the sample. Light transmitted by the sample is then captured by a lens and focussed into a 2D image in the observation plane. Since the whole specimen is imaged simultaneously, the conventional microscope is an example of a parallel processing system [Wilson and Sheppard, 1984]. This is a demanding scenario for the optical components, indeed, this method leads to only a single plane of the specimen being in focus at any one time in the observation plane. However, de-focussed light is also present in the observation plane and contributes to the image, resulting in a blurred image and reducing the image quality. If the plane in focus could be imaged individually, without the interference from other out-of-focus planes, then the image quality could be greatly improved.

The confocal microscope takes advantage of optical sectioning in order to exclude the out-of-focus light from the image [Wilson and Sheppard, 1984, Wilson, 1990, Pawley, 1995]. In this microscope, the image is obtained sequentially. The image intensity of a point in the sample is obtained by focussing a laser into a diffraction limited spot in a specimen and collecting the light subsequently emitted from that point, as shown in Fg. 1.1. To ensure that it is predominately the light from the desired plane that is collected, a pinhole is placed before the detector, as shown, to prevent most of the de-focussed light from entering the detector and contributing to the image. The entire image is built, point by point, by scanning the spot throughout the specimen and computationally constructing the image.

Fg. 1.2 shows a comparison of the images obtainable from conventional and confocal microscopes. By imaging a tilted microcircuit, Fg. 1.2(a) shows that only a single plane is focussed by a conventional microscope, but with the out-of-focus side regions included in the image. Fg. 1.2(b) shows that only the in-focus plane is imaged by a confocal microscope and Fg. 1.2(c) is the superposition of many of these individual planes. By comparison, it is clear from Fg. 1.2(a) and Fg. 1.2(c) that the confocal microscope has superior contrast than the conventional microscope.

Both the conventional and confocal microscope can operate in fluorescence mode. This often requires the sample to be fluorescently labelled prior to the imaging process.

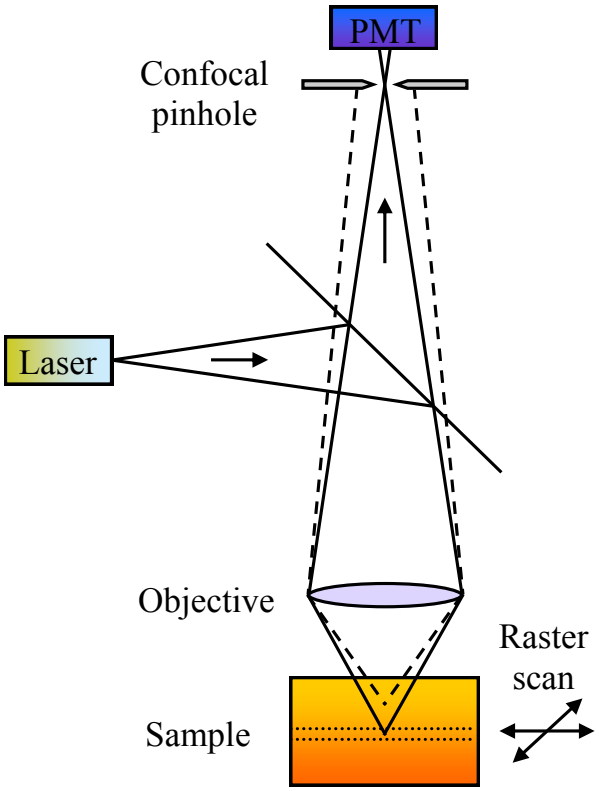


Figure 1.1: *A diagram of a confocal microscope. Laser illumination is focussed into the sample, which is scanned to illuminate the region of interest point by point. Light from the desired optical section is reflected, passing through a pinhole and detected by the PMT. Out of focus light from other layers of the specimen is also reflected but prevented from being included in the image by the pinhole.*

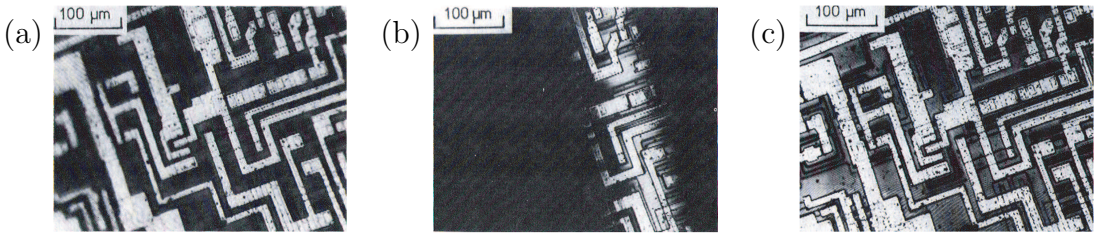


Figure 1.2: *Images of a tilted microcircuit comparing the conventional and confocal microscopes, where (a) is from a conventional microscope, (b) is a confocal image of the same specimen and (c) is the superposition of the confocal images, showing the improvement of images from a confocal microscope compared to conventional images. Taken from [Wilson, 1990]*

Fluorescence molecules in the sample are raised to an elevated energy state by the illumination light at a rate proportional to the illumination intensity. As these molecules return to the ground state, they release a fluorescence photon and it is this photon which contributes to the image. Typically the fluorescence wavelength is distinct to the illumination wavelength, so the two can be separated through use of a wavelength filter.

An extension from the single-photon fluorescence mode is the two-photon fluorescence

microscope [Denk et al., 1990, So et al., 2000]. In this setup, just as in the confocal setup, a diffraction-limited spot is scanned throughout the sample to build the image point by point. However, two-photon fluorescence requires the simultaneous absorption of two photons to excite the fluorescence molecules. In the confocal fluorescence setup, fluorescence molecules are excited throughout the beam path in the sample but out-of-focus fluorescence is blocked by the pinhole, giving the optical sectioning property. One property of two-photon microscopy is that the fluorescence is excited at a rate proportional to the illumination intensity squared and as such significant fluorescence is only excited in the focal spot. So, unlike the confocal microscope, a pinhole is not required for a two-photon fluorescence microscope to exhibit optical sectioning.

Another advantage of two-photon over confocal microscopy is the fact that the fluorescence molecules are only excited when in the focal spot. After multiple excitations, fluorescence molecules may lose the ability to fluoresce; this is known as photo-bleaching. This is a much greater concern in the confocal setup, since molecules are unnecessarily excited outside the focal plane, with the resulting fluorescence light blocked by the pinhole. An additional advantage is that in biological specimens, the scattering is generally lower at longer wavelengths and the two-photon microscope usually uses longer wavelengths than the confocal microscope for illumination. Consequently this allows deeper imaging of a sample.

A relatively new microscopy technique that is gaining prominence is that of harmonic generation microscopy [Barad et al., 1997, Yelin and Silberberg, 1999]. Unlike the previous examples, this does not rely on the distribution of fluorescence to generate an image, but the intrinsic optical properties of the specimen. Like the two-photon technique, harmonic generation microscopy is a non-linear process. It involves the spontaneous conversion of two or three photons to second or third harmonic photons respectively. A consequence of this non-linearity is that, again like the two-photon method, the harmonic generation microscope exhibits (3D) optical sectioning. This allows the generation of well focussed 2D images from a 3D structure, as shown in Fg. 1.3. Fg. 1.3(a) shows a slice through a *C. elegans* specimen taken using a third harmonic generation (THG)

microscope, with Fg. 1.3(b) showing an enlarged section. These images were taken at approximately $20\mu m$ from the upper surface of the *C. elegans* structure, showing that, even at this depth, the optical sectioning properties allow images to be taken without any out-of-plane signal to blur the images.

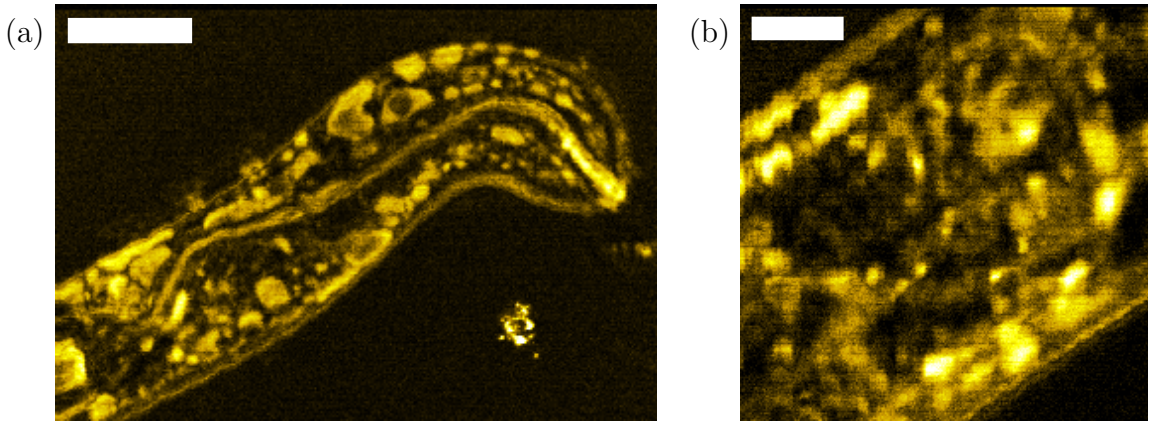


Figure 1.3: *xy images taken using the THG microscope of a C. elegans specimen. Scale bars are* $20\mu m$ *(a) and* $5\mu m$ *(b).*

1.2 Direct laser writing

Direct laser writing (DLW) is gaining popularity for laser microfabrication of materials [Davis et al., 1996]. This method, when used in conjunction with microscope-like optics, is capable of fabricating micron-scale structures on or within a transparent substrate. This has particular benefits in photonic engineering, where applications such as embedded waveguides, photonic crystals and microfluidics can be implemented with such a method of fabrication [Kim et al., 2005, Wong et al., 2006, Mauclair et al., 2008]. A variety of different materials can be used as the substrate, including polymers, glasses, and some less conventional materials including diamond. The process typically employs a high power, short-pulsed laser, focussed into a substrate, as shown in Fg. 1.4. Since the substrate is transparent, there is no linear absorption at optical wavelengths. However, by using a high power laser the electric field at the focus may become large enough for multiphoton absorption. Thus an energetic plasma may be generated in the focal volume. The effect of this is that the material structure of the substrate can be per-

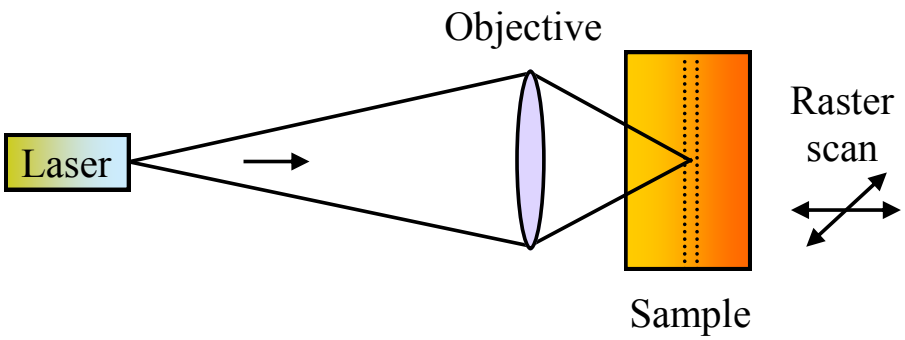


Figure 1.4: *A diagram of a laser fabrication system. Laser illumination is focussed into the sample, which is scanned to illuminate the region of interest. The basic structure is identical to that of the optical microscopes presented previously.*

manently altered. In order to achieve an electric field intensity high enough to perform such non-linear processes and fabricate within the bulk of a substrate, it is necessary to use a pulsed laser. Since the achievable instantaneous intensity is greater with shorter pulses, the pulse length must generally be in the femtosecond, rather than picosecond, nanosecond or continuous wave region. If pulses are longer than this, then there is a danger that there may be some surface damage due to linear absorption. By using a laser with pulse lengths in the femtosecond region, the pulse duration is shorter than typical thermal diffusion timescales. Therefore the entire focal energy may be delivered to the focal volume and any structural modification confined to that region.

To enable 3D fabrication, the focus is scanned relative to the substrate using either beam scanning with mirrors or substrate scanning using a translation stage. By scanning a beam through specific substrates, whilst maintaining a consistent focal intensity, this method has been shown to increase the local refractive index of the substrate and so produce an optical waveguide. Fg. 1.5 shows an example of one such laser-written waveguide.

1.3 Aberrations and adaptive optics

Throughout the previous description of microscopes and laser fabrication systems, it has been assumed that the focal spot was diffraction-limited. An aberration is the departure of a wavefront from its ideal or desired form. When aberrations are present,

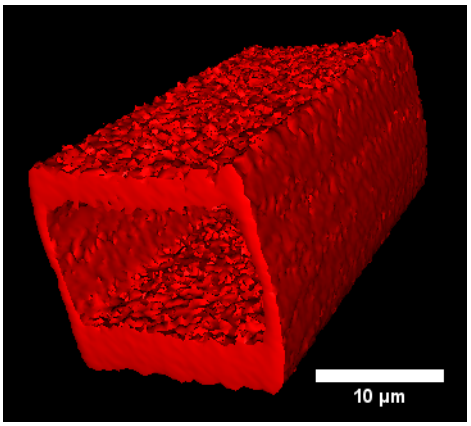


Figure 1.5: *Rendering of a 3D stack of xy THG images of a square single-mode waveguide. Waveguide courtesy of Robert Thomson, Heriot Watt University.*

they in turn cause the focal spot to depart from its ideal diffraction-limited form. These aberrations can be introduced in various ways: by improper setup of the optical system, from refractive index mismatches or from the specimen itself. As the focal spot departs from its diffraction-limited form, it increases in size and reduces its peak intensity. This in turn reduces the intensity and the resolution of the image, introducing a blurring effect.

Adaptive optics can be used to remove the effect of aberrations [Tyson, 1991]. This was first used in astronomy [Hardy, 1998] where aberrations are introduced by atmospheric interference, the effect of which is most easily noticeable by the presence of star twinkle. This technique has since been adapted for use in microscopy [Booth, 2006], where it is used to restore a diffraction limited focal spot and minimise the negative consequences of aberrations.

Aberration correction is achieved by placing an adaptive element into the optical system. Aberrations can be modelled as phase variations in the wavefront; the adaptive element adds a phase to the wavefront to correct for aberrations present in the system. If an aberration is introduced by the system components, then the adaptive element can be set such that it cancels out the unwanted wavefront phase. This will often be a fixed correction that does not change over time. However, if the aberration is introduced by the specimen this will typically be unknown and dependent upon the position within the specimen that is imaged. Hence, a correction process must be run every time the focal

region of the specimen changes. If the specimen of interest is a biological specimen which may be constantly changing (particularly for in-vivo imaging), the correction process will need to be repeated for every image taken even if the sample is not moved.

In order to correct for aberrations, first the type of aberration present must be determined (i.e. what undesired phase is present in the aberrated wavefront). The traditional method for doing this is to use a wavefront sensor to measure the phase of the wavefront. This information can then be used to control an adaptive element to add an equal and opposite phase to the wavefront to cancel the aberration. This is known as a direct method of aberration measurement. Another method of aberration correction is indirect measurement. The indirect process takes a set of images, each with a different aberration applied, then by assigning a quality metric to each image the optimum correction required can be determined [Booth, 2006, Facomprez et al., 2012].

Common correction elements used for adaptive optics are deformable mirrors (DMs) and spatial light modulators (SLMs). The DM consists of a small mirror (typically approximately 1cm by 1cm), built with an electrostatically actuated membrane with a reflective coating. Behind the mirror is an electrode array. By applying a potential between the membrane and the electrode, the shape of the mirror can be controlled. The SLM is a small liquid crystal device, also approximately 1cm by 1cm. As the SLM pixel array is individually addressed, the precise shape is easier to control than that of a DM. However, unlike the DM membrane, the phase applied by an SLM is typically limited to a range of 0 to 2π radians, so can only create phase-wrapped discontinuous phase patterns. Precise positioning of the DM or SLM in an optical setup allows the addition of phases to a wavefront, enabling the cancelling or introduction of aberrations.

1.4 Structure of thesis

The theory behind image formation and how it is applied to conventional, confocal and two-photon microscopes is covered first. These microscopes are extremely useful as they can provide 3D images of thick specimens. However, the 3D nature of the specimen also introduces aberrations as the microscope focusses deeper, resulting in a deterioration

in image quality as the depth of focus increases. The problem is exacerbated as the depth of image increases, since the light must pass through more of the specimen itself. The imaging theory in Chapter 2 is then extended to include image formation with aberrations and the use of adaptive optics to compensate for the aberrations.

These aberrations exhibit the well known effects: loss of image intensity; loss of image resolution; and image blurring. Additionally, the intensity of the different structures present are affected in different ways. It has been noticed that the smaller, point-like objects in a specimen have a much larger reduction in intensity than larger, volume-like objects [Débarre et al., 2008, 2009]. These effects are all shown in Fg. 1.6.

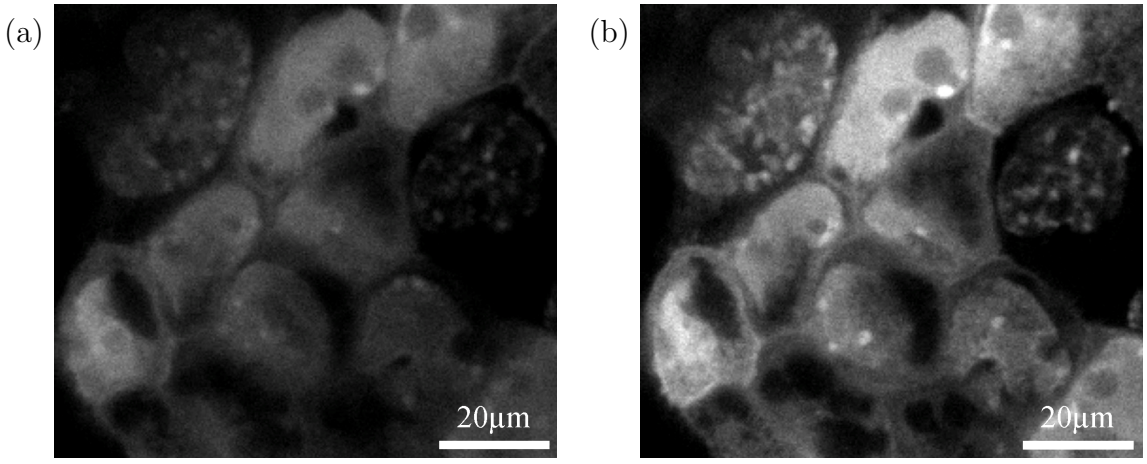


Figure 1.6: *Figure comparing an image taken without aberration correction and an image taken with aberration correction. Image obtained by Débarre et al. [2009]*

In Fg. 1.6 we can see that the intensity in the corrected image is much greater than that of the image without aberration correction. However, upon closer inspection it is also evident that the smaller structures are worst affected, almost disappearing from the image without aberration correction. It is this phenomenon that we will investigate in Chapter 3. Although we can qualitatively state the effect, there is no quantitative information available on this phenomenon. More important than the individual intensity of a structure is the image contrast between the different structures. It is possible that an image with a strong background signal may be assumed to be aberration free, however, it is now clear that the presence of aberrations may remove the fine detail without removing significantly the background signal. It is therefore important to quantify the effect of aberrations on the individual specimen structures and their image contrast.

In order to correct for system or image induced aberrations, adaptive optic elements are employed. To correct for the phase aberrations in optical microscopes, the element that is typically used is a deformable mirror. However, the precise shape of the DM is difficult to control. It is this problem that is addressed in Chapter 4. Once the adaptive optics is fully operational, the problems with imaging mentioned above can be addressed. The aberration correction was utilised in a two-photon and a harmonic generation microscope, the results of which are presented in Chapter 5.

Whilst adaptive optics have been gaining prominence in microscopy, they may also be utilised in other optical systems where aberrations are detrimental. Chapter 6 discusses the use of adaptive optics in a laser fabrication system. In this scenario, any refractive index mismatch between the immersion medium and the substrate induce aberrations to the focal spot, reducing the efficiency and fidelity of fabrication. The optical fabrication of diamond is chosen as a specific demonstration, as this is one scenario where aberrations can cause a significant problem due to the high refractive index mismatch between the diamond substrate and any immersion medium chosen. The demonstration also utilises a dual adaptive optics setup, harnessing the optical power of two adaptive elements in series to correct for the significant aberration problem highlighted in the fabrication system.

To this point, all aberration correction considered has been for a constant aberration across the field of view. However, it is not surprising to consider that any phase aberration present, particularly those induced by the specimen, is not likely to be constant across the specimen. Therefore, the potential for adaptive optics to be able to correct for spatially varying aberrations, and the extent to which they would be able to perform this, is considered in Chapter 7.

Chapter 2

Theory of focussing and imaging

This chapter describes the theory behind focussing and optical image formation in order to develop models for the operation of microscopes and laser fabrication systems. First the underlying theory is reviewed, beginning with the Huygens-Fresnel principle and using Fresnel diffraction theory to describe focussing by a lens. The point spread function and its role in image formation and the optical transfer function are then introduced, which are used to describe the operation of conventional, confocal, two-photon and harmonic generation microscopes.

Imperfections in the imaging system, commonly known as aberrations, are described. Focussing and image formation in the presence of aberrations are discussed, including a definition and mathematical description of aberrations. This is relevant to both microscopy and optical fabrication. Finally, adaptive optics is described and its use for aberration correction in both optical microscopy and fabrication.

2.1 Focussing and image formation

In order to understand the operation of microscopes, or indeed any optical system, first the basis of light propagation must be understood. Diffraction theory is then developed in order to understand the effect of a lens in an optical system. This is used in the construction of the point spread function and the optical transfer function, both commonly used to describe imaging systems.

2.1.1 Diffraction theory

To understand optical image formation, we first consider how the propagation of light fields is affected by the process of diffraction. The Huygens-Fresnel principle [Goodman, 2005] states that: each point on a wavefront can be considered as a point source, emitting a spherical secondary wave; the light field at any point beyond the aperture is given by the sum of these secondary wavefronts; the field in the aperture, shown by Fg. 2.1, is the same as it would be if the obstruction were not present.

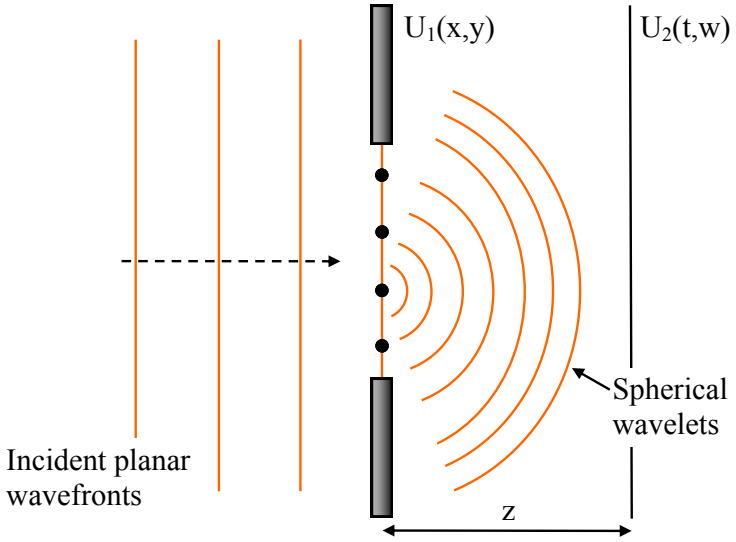


Figure 2.1: *Incident planar wavefronts can be modelled as point sources emitting spherical wavelets. The sum of these wavelets gives the light field at any point*

A spherical wavelet is described mathematically as $\frac{\exp[-jkr]}{r}$, where j is the imaginary unit, $k = 2\pi/\lambda$ is the wave number of the light and r is the distance from the point source. As we know the field $U_1(x, y)$ in the aperture plane, we can calculate the light field $U_2(t, w)$ as the sum of contributions from all the spherical wavelets:

$$U_2(t,w) = \iint_{-\infty}^{\infty} U_1(x,y)\frac{\exp[-jkr]}{r}\mathrm{d}x\mathrm{d}y \tag{2.1}$$

The dimension r can be related to the Cartesian coordinates as follows:

$$r = \sqrt{z^2 + (t-x)^2 + (w-y)^2} \tag{2.2}$$

If we assume $z \gg (t-x)^2 + (w-y)^2$, we can use the binomial expansion approximation $\sqrt{1+x} \approx 1 + \frac{x}{2}$ to represent r as:

$$r \approx z + \frac{1}{2z}\{(t-x)^2 + (w-y)^2\} \tag{2.3}$$

Eq. 2.3 can be substituted into Eq. 2.1 to find:

$$\begin{aligned} U_2(t,w) &= \frac{\exp[-jkz]}{z} \iint_{-\infty}^{\infty} U_1(x,y) \\ &\quad \exp\left[-\frac{jk}{2z}\{(t-x)^2 + (w-y)^2\}\right] \mathrm{d}x\mathrm{d}y \end{aligned} \tag{2.4}$$

This is known as the Fresnel diffraction formula [Gu, 1999]. This allows us to calculate the propagation of optical fields, where the approximation given in Eq. 2.3 holds, from any plane (x, y) to a secondary plane (t, w).

2.1.2 Diffraction by a lens

In this section we see how incident light may be focussed by a lens. Using the Fresnel diffraction formula as a starting point, we combine this with the transmission function of a lens to describe the light field after the lens. This can be used to model both the light field and intensity in and around the focal plane of the lens.

Geometric optics predicts that when a uniform plane wave is incident on a thin lens, as shown in Fg. 2.2, the light will be focussed down to a point in the focal plane of the lens (a lens is defined as a thin lens if a ray entering at coordinates (x, y) on one face exits at approximately the same coordinates on the opposite face). However, as we shall see the light distribution is not a point, described by a Dirac delta function, $\delta(t, w)$, as predicted by geometric optics, but has a finite width.

When a beam of light passes through a thin lens, a phase delay proportional to the thickness of the lens is introduced to the beam. Due to the varying thickness of the lens a planar wavefront is transformed, as shown in Fg. 2.2 for a thin lens with spherical surfaces, to a spherical cap. The lens is also finite in size, so a pupil function is used to

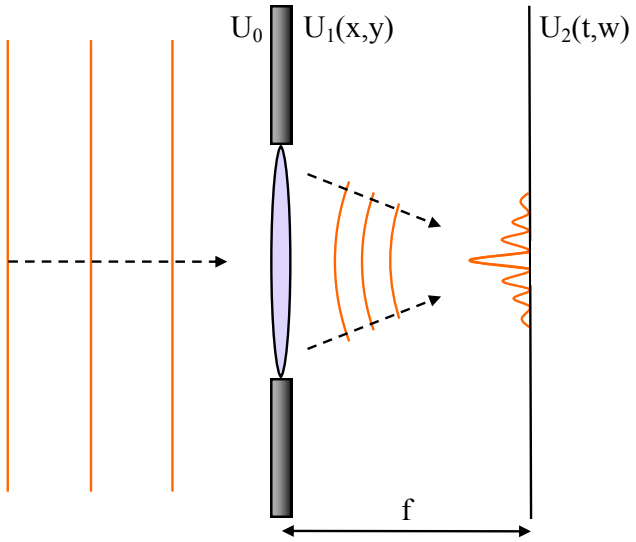


Figure 2.2: *A plane wave incident on a thin lens, focussed onto the focal plane producing a finite distribution*

describe the limits:

$$P(x,y) = \begin{cases} 1, & \text{inside lens aperture} \\ 0, & \text{otherwise} \end{cases} \tag{2.5}$$

A pupil function can be used to describe any aperture stop in a system and is not restricted to the plane of the lens. The transmission function of the lens, which includes the quadratic exponent approximating the transformation of planar wavefronts to spherical wavefronts, can therefore be expressed as $t(x,y)$:

$$t(x,y) = P(x,y)\exp\left[\frac{jk}{2f}(x^2+y^2)\right] \tag{2.6}$$

where f is the focal length of the lens. This uses the quadratic approximation to describe spherical wavefronts, so this only holds in the paraxial case. This would not be correct for a lens with a large focussing angle (i.e. a high NA lens). Eq. 2.6 permits us to describe the optical field immediately after the lens:

$$U_1(x,y) = U_0 P(x,y)\exp\left[\frac{jk}{2f}(x^2+y^2)\right] \tag{2.7}$$

where U_0 is a constant describing the light field immediately before the lens and $U_1(x,y)$

describes the light field immediately after the lens (see Fg. 2.2). We typically set $U_0 = 1$ without loss of generality. The field an arbitrary distance z after the lens can now be derived by substituting Eq. 2.7 into the Fresnel diffraction formula, Eq. 2.4:

$$\begin{aligned} U_2(t,w,z) &= \frac{\exp[-jkz]}{z} \iint_{-\infty}^{\infty} P(x,y) \exp\left[\frac{jk}{2f}(x^2+y^2)\right] \\ &\quad \exp\left[-\frac{jk}{2z}\{(t-x)^2+(w-y)^2\}\right] \mathrm{d}x\mathrm{d}y \end{aligned} \tag{2.8}$$

Since we are interested in the values when z is close to the focus we can set $z = f + \Delta z$ in Eq. 2.8 and consider the regions where $\Delta z \ll f$:

$$\begin{aligned} U_2(t,w,\Delta z) &= \frac{\exp[-jkz]}{z} \exp\left[-\frac{jk}{2f}(t^2+w^2)\right] \iint_{-\infty}^{\infty} P(x,y) \\ &\quad \exp\left[\frac{jk\Delta z}{2f^2}\{(t-x)^2+(w-y)^2\}\right] \exp\left[\frac{jk}{f}(tx+wy)\right] \mathrm{d}x\mathrm{d}y \end{aligned} \tag{2.9}$$

For the case of a circular lens (of radius a), we can convert this representation to use polar coordinates. We can also greatly simplify using the following parameters [Born and Wolf, 1983]:

$$\begin{aligned} \rho &= \frac{r_{xy}}{a} && && \text{normalized radial co-ordinate} \\ N &= \frac{\pi a^2}{\lambda z} && && \text{Fresnel number} \\ u &= \frac{2\pi}{\lambda}\left(\frac{a}{f}\right)^2 \Delta z &= k\Delta z(\sin\alpha)^2 && \text{axial optical co-ordinate} \\ v &= \frac{2\pi}{\lambda}\frac{a}{f} r_{tw} &= k r_{tw} \sin\alpha && \text{radial optical co-ordinate} \end{aligned} \tag{2.10}$$

where $r_{xy} = \sqrt{x^2+y^2}$, $r_{tw} = \sqrt{t^2+w^2}$ and α is the maximum angle of convergence of the light rays after passing through the lens, i.e. $\sin\alpha = a/f$. The pupil function (Eq. 2.5) now becomes:

$$P(\rho) = \begin{cases} 1, & \rho \le 1 \\ 0, & \text{otherwise} \end{cases} \tag{2.11}$$

and so Eq. 2.8 now becomes:

$$U_2(u,v) = 2jN \exp\left[-jkf\right] \exp\left[-\frac{jku}{2N}\right] \exp\left[-\frac{jkv^2}{4N}\right] \int_0^1 \exp\left[-\frac{ju\rho^2}{2}\right] J_0(v\rho)\rho \mathrm{d}\rho \quad (2.12)$$

where J_0 is a Bessel function of the first kind of order zero (see Eq. A.1). The expression in Eq. 2.12 describes the amplitude of the optical field. The intensity distribution is given by the modulus squared of the amplitude distribution, $U_2(u,v)$. By using the identity Eq. A.2, we can find the intensity distributions in the focal plane (i.e. the focal spot) as:

$$I(v,0) = \left(\frac{2J_1(v)}{v}\right)^2 \quad (2.13)$$

where we have normalised the expression so that the on-axis intensity is unity. This function is plotted in Fg. 2.3(a). The first zero if this intensity distribution is at $v = 1.22\pi$, which corresponds to $r_{tw} = \dfrac{0.61\lambda}{\sin\alpha}$. The variation in intensity along the optical axis can be found as:

$$I(0,u) = \left(\frac{\sin\left(u/4\right)}{u/4}\right)^2 \quad (2.14)$$

This function has a first zero at $u = 4\pi$, so $\Delta z = 2\lambda(\sin\alpha)^2$ (where Δz is the distance from the focal plane). Eq. 2.13 and Eq. 2.14 describe one dimensional sections through the focal spot. Fg. 2.3 gives two dimensional slices through the focal spot at the planes where $u = 0$ (Fg. 2.3(a), the 1D section of this is expressed by Eq. 2.13) and along the optic axis (Fg. 2.3(b)). The 1D analytic expression of this is given for $v = 0$ by Eq. 2.14.

Eq. 2.12 allows us to calculate the diffraction pattern in the focus of a lens. This forms the basis for derivation of the image formation process.

2.1.3 The point spread function

To understand image formation by a lens we must consider how the field in the an object plane is transformed by the lens, as shown in Fg. 2.4. The complex field immediately behind the object is described by $U_0(\xi,\eta)$ and the plane (ξ,η) is often termed the object plane or the pupil plane (not to be confused with the pupil function, as given by Eq. 2.11).

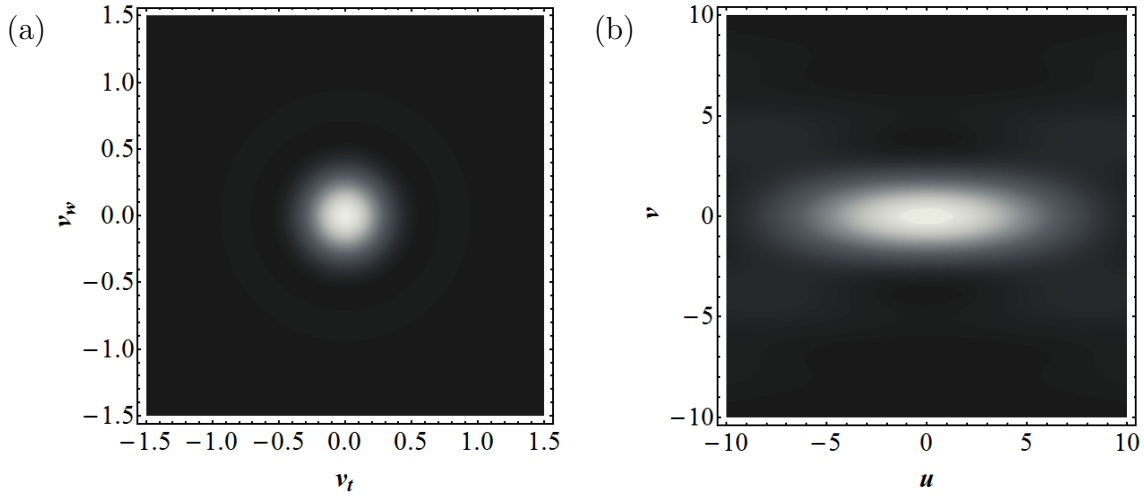


Figure 2.3: *Density plots showing the intensity distribution formed by a lens in its focal plane (a) and along the optical axis, u, and around the focal plane (b) when plane light waves are incident upon it*

Using this general setup we can then find an expression for the light field in the plane a distance z_2 behind the lens, labelled $U_2(t, w)$, where (t, w) is known as the image plane. We want to find the conditions where U_2 provides a mathematically identical (or identical but magnified) image of U_0. This can be used to construct the expression for the image of a complete two dimensional object.

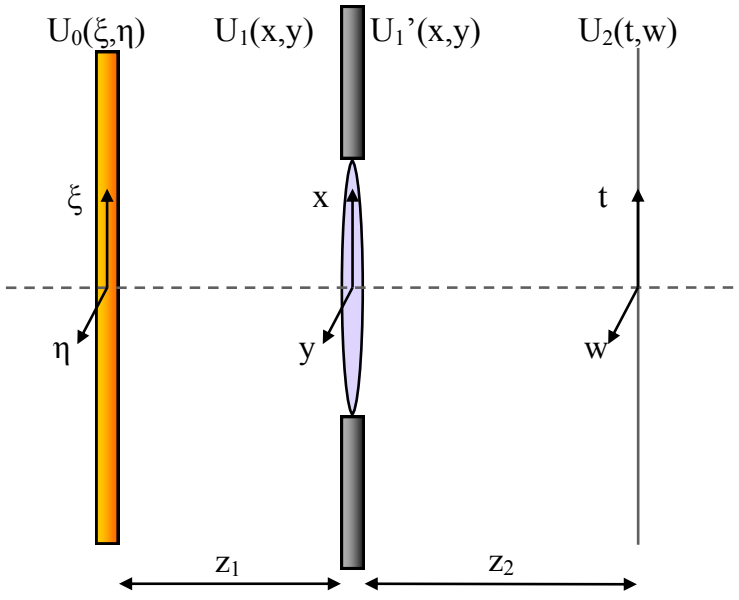


Figure 2.4: *The coordinate system for analysing the imaging of a single lens.*

Let us define the field $U_2(t, w)$ in terms of the field in the object plane, $U_0(\xi, \eta)$, as:

$$U_2(t, w) = \iint_{-\infty}^{\infty} h(t, w; \xi, \eta) U_0(\xi, \eta) \mathrm{d}\xi \mathrm{d}\eta \tag{2.15}$$

where $h(t, w; \xi, \eta)$ is the field amplitude produced at coordinates (t, w) by a (unit amplitude) point source located at (ξ, η). The function h describes the properties of the imaging system.

Following the derivation used by Goodman [Goodman, 2005], by applying the Fresnel diffraction formula (Eq. 2.4) and the lens law [Born and Wolf, 1983] it is possible to write the field amplitude as the spatially invariant function:

$$\begin{aligned} h(t, w; \xi, \eta) &= \iint_{-\infty}^{\infty} P(x, y) \exp\left[\frac{jk}{z_2}\{(t - M\xi)x + (w - M\eta)y\}\right] \mathrm{d}x\mathrm{d}y \\ &= h(t - M\xi, w - M\eta) \end{aligned} \tag{2.16}$$

where $M = -\dfrac{z_2}{z_1}$ is the system magnification. If the delta function is placed in the object plane on-axis so that $(\xi, \eta) = (0, 0)$ and the normalisations $t' = \dfrac{\lambda t}{z_2}$ and $w' = \dfrac{\lambda w}{z_2}$ are used, Eq. 2.16 can be written:

$$h(t', w') = \iint_{-\infty}^{\infty} P(x, y) \exp\left[2\pi j(t'x + w'y)\right] \mathrm{d}x\mathrm{d}y \tag{2.17}$$

Clearly h is the inverse 2D Fourier transform (see Eq. A.8) of the lens pupil function, P. h is known as the point spread function, or PSF. If we convert Eq. 2.17 to polar coordinates for a circular lens, using $x' = 2\pi x$, $y' = 2\pi y$, $x' = \rho\cos\theta$, $y' = \rho\sin\theta$, $t' = v\cos\phi$ and $w' = v\sin\phi$, we find:

$$h(v) = \frac{1}{2\pi} \int_0^{2\pi} \int_0^1 P(\rho) \exp\left[jv\rho\cos\left(\theta - \phi\right)\right] \rho \mathrm{d}\rho \mathrm{d}\theta \tag{2.18}$$

Using Eq. A.1, Eq. 2.18 simplifies to:

$$h(v) = \int_0^1 J_0(v\rho)\rho \mathrm{d}\rho \tag{2.19}$$

Using Eq. A.2, Eq. 2.19 simplifies to:

$$h(v) = \frac{J_1(v)}{v} \tag{2.20}$$

This is known as the amplitude PSF, and links back to Eq. 2.13, showing that the PSF is equivalent to the distribution found in the focus when a plane wave is incident on a lens.

Coherent and incoherent imaging

At this stage, it is necessary to distinguish between the two forms of image formation. Eq. 2.17 describes the amplitude response in the image plane, $U_2(t, w)$, generated by each point in the object plane, $U_0(\xi, \eta)$. However, the image intensity in the image plane is dependent on the nature of the light illuminating the object. If the phase of the illumination light varies in unison, this is known as spatially coherent illumination (referred to as coherent). Conversely, if the illumination field phase at all points in the object vary in an uncorrelated fashion, the illumination is termed as spatially incoherent (referred to as incoherent).

When the object illumination is coherent, so the response in the image plane from each point in the object is also coherent. Therefore the amplitude responses must be added to give the total amplitude response, which must be squared to give the total image intensity. When the object illumination is incoherent, so the responses in the image plane also vary in an uncorrelated manner. As such, the power or intensity of incoherently imaged objects must be added to give the total intensity response [Goodman, 2005].

The image intensity for coherent imaging can be written as the sum of the amplitude responses squared:

$$I_2(t, w) = \left| \iint_{-\infty}^{\infty} U_0(\xi, \eta) h(t - M\xi, w - M\eta) \mathrm{d}\xi \mathrm{d}\eta \right|^2 \tag{2.21}$$

The image intensity for incoherent imaging can be written as the sum of the squared

amplitude responses:

$$I_2(t,w) = \iint_{-\infty}^{\infty} |U_0(\xi,\eta)|^2 |h(t - M\xi, w - M\eta)|^2 \mathrm{d}\xi\mathrm{d}\eta \tag{2.22}$$

Fluorescence imaging

In microscopy, fluorescence is used to mark objects or structures of interest in a sample of interest. For linear fluorescence techniques, the process of generation of fluorescence is such that the fluorescence intensity is proportional to the intensity of the illumination, i.e. it is one example of an incoherent imaging technique. As such, the image intensity is the sum of the intensities of the generated fluorescence, as defined in Eq. 2.22. This may also be represented by a convolution integral [Wilson and Sheppard, 1984]:

$$I_2(t,w) = \iint_{-\infty}^{\infty} |U_0(\xi,\eta)|^2 \epsilon(\xi,\eta) |h(t - M\xi, w - M\eta)|^2 \mathrm{d}\xi\mathrm{d}\eta \tag{2.23}$$

where $\epsilon(\xi,\eta)$ is the distribution of fluorophores throughout the object. Therefore we can define the distribution of generated fluorescence as $f(\xi,\eta)$:

$$f(\xi,\eta) = |U_0(\xi,\eta)|^2 \epsilon(\xi,\eta) \tag{2.24}$$

We now define the intensity point spread function, IPSF, as the square of the modulus of the PSF:

$$h_i(t,w) = |h(t,w)|^2 \tag{2.25}$$

Using Eq. 2.24 and Eq. 2.25, the convolution in Eq. 2.23 can now be expressed as:

$$I_2(t,w) = \iint_{-\infty}^{\infty} f(\xi,\eta) h_i(t - M\xi, w - M\eta) \mathrm{d}\xi\mathrm{d}\eta \tag{2.26}$$

We now have a concise relationship for the image intensity as a function of the object distribution and the lens PSF for incoherent fluorescence imaging.

2.1.4 The optical transfer function

The transfer function method gives a complementary understanding of image formation in an optical system. The structure of an object can be considered in terms of its spatial frequencies, but, as we will see, the lens (and hence the transfer function) acts as a spatial low pass filter. Therefore, the detail will be limited by the properties of the lens. We can use the Fourier transform introduced above as an outcome of Eq. 2.17 to analyse the properties of the optical system.

We use Eq. 2.26 as our starting point. By applying the Fourier convolution theorem (as defined in Eq. A.5), we can rewrite Eq. 2.26 as:

$$I_2(t,w) = \iint_{-\infty}^{\infty} F(m,n)C(m,n)\exp\left[2\pi j(mt+nw)\right]\mathrm{d}m\mathrm{d}n \tag{2.27}$$

where $F(m,n)$ and $C(m,n)$ are the Fourier transforms (as defined by Eq. A.7) of $f(\xi,\eta)$ and $h_i(\xi,\eta)$ respectively. $C(m,n)$ is known as the optical transfer function (OTF) and describes how efficiently the various spatial frequencies are transmitted through an optical system. It should be noted that there is an equivalent function for coherent imaging (the coherent transfer function) but it is not discussed here. By substituting Eq. 2.17 into Eq. 2.25 and applying the Fourier transform, we can write the OTF (with a change of variables) as:

$$C(m,n) = \iint_{-\infty}^{\infty} P(x+\frac{\lambda z_x m}{2}, y+\frac{\lambda z_y n}{2})P^*(x-\frac{\lambda z_x m}{2}, y-\frac{\lambda z_y n}{2})\mathrm{d}x\mathrm{d}y \tag{2.28}$$

where P is the 2D pupil function, P^* is its complex conjugate, $z_x = \dfrac{2}{\lambda m}(x'-x)$ and $z_y = \dfrac{2}{\lambda n}(y'-y)$. This equation has a very simple geometric interpretation; the area of overlap of two displaced pupil functions, shown in Fg. 2.5.

If we let $C(m,n) \rightarrow C(\delta)$, where $\delta = \sqrt{m^2+n^2}$, we can find the mathematical expression for the OTF, $C(\delta)$, which is given by [Goodman, 2005]:

$$C(\delta) = \frac{2}{\pi}\left[\arccos\left(\frac{\delta}{2}\right) - \left(\frac{|\delta|}{2}\right)\sqrt{1-\left(\frac{\delta}{2}\right)^2}\right] \tag{2.29}$$

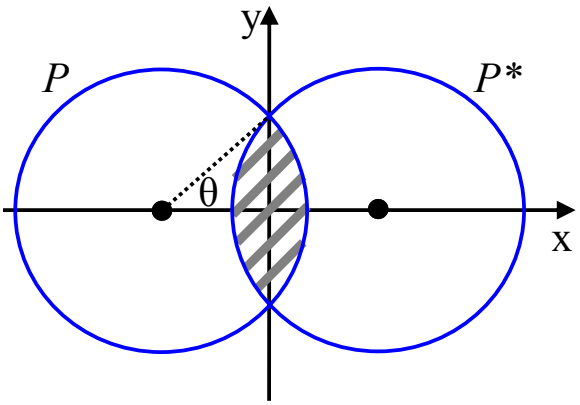


Figure 2.5: *The geometrical autocorrelation of two pupil functions*

This gives the distribution shown in Fg. 2.6(b). The optical transfer function for a (two-dimensional) circular pupil is shown in Fg. 2.6. The smooth frequency roll-off of this OTF indicates that in incoherent imaging the aperture acts as a low pass filter resulting in the attenuation of high spatial frequencies (and corresponding softening of sharp edges) in the image.

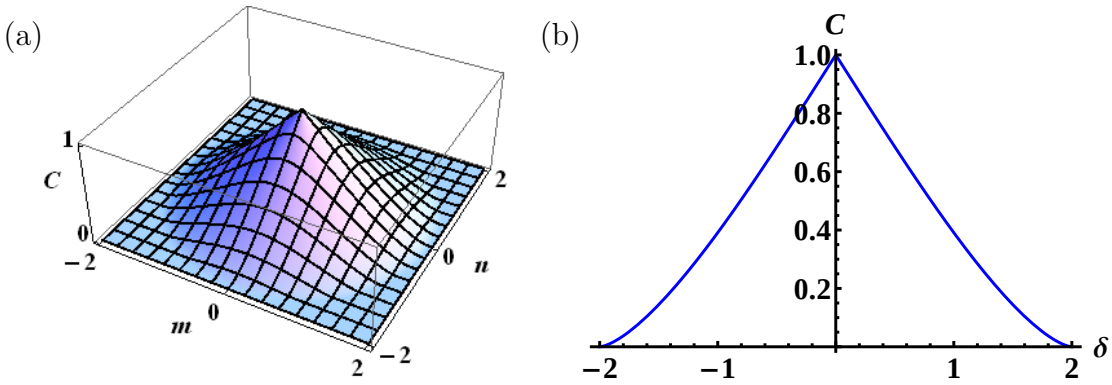


Figure 2.6: *The optical transfer function of a diffraction limited system with a circular pupil of radius* 1 *(a) and a section of the first result, where* $\delta = \sqrt{m^2 + n^2}$ *(b).*

2.2 Image formation in optical microscopes

This section covers the imaging theory of four types of microscope: the conventional, confocal and two-photon fluorescence microscopes, and the harmonic generation microscope. Using the theory introduced previously, we derive expressions that describe the imaging process in each of these microscopes.

2.2.1 Conventional fluorescence microscope

The basic layout of a conventional fluorescence microscope is shown in Fg. 2.7. A light source illuminates a wide area of the sample. This illumination excites fluorescent molecules in the sample, raising them to a higher energy state upon absorption of a single photon. These molecules subsequently decay back to the ground state, emitting a typically longer wavelength photon. A lens collects the fluorescence light and forms a 2D image in the observation plane.

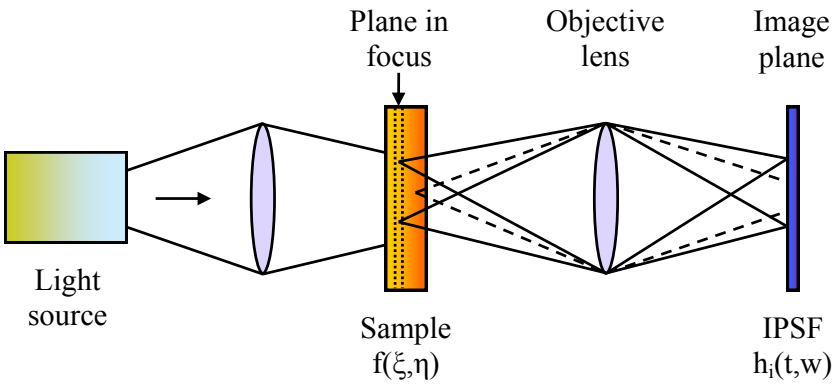


Figure 2.7: *A diagram of a conventional microscope, showing how out of focus light (dashed lines) also appears on the observation plane.*

From Eq. 2.26 we can say that in a conventional fluorescence microscope, the image is the convolution of the fluorescence distribution f with the IPSF h_i:

$$I(t,w) = h_i(t,w) * f(t,w) \tag{2.30}$$

Although only a single plane of the sample is in focus in the observation plane, all illuminated planes in the sample contribute to the image but these are not focussed (see dashed line in Fg. 2.7). This results in the out-of-focus images being superimposed upon the focussed image, leading to an image that is blurred and suffers from a decrease in contrast.

The conventional microscope provides high resolution images of 2D specimens but is not best suited to the imaging of 3D objects due to the out-of-focus blur. As we shall see, the confocal microscope helps overcome this limitation.

2.2.2 Confocal microscope

The operation of a confocal microscope is described in Section 1.1. It is possible to redraw the confocal microscope in an optically equivalent manner to that shown in Fg. 1.1 to make the mathematical modelling easier to understand. Fg. 2.8 shows the layout of a confocal microscope with the illumination and detection paths separated.

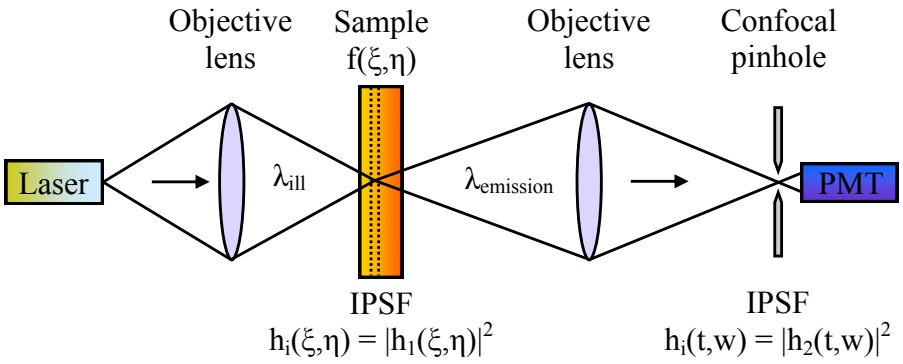


Figure 2.8: *The basic layout of a confocal microscope, showing the key features.*

Using the layout shown in Fg. 2.8 as a basis, it is possible to construct an expression for the image intensity in a confocal microscope. The two objective lenses shown are, in a real microscope, the same physical lens, so have the same IPSF, h_i. However, due to the Stokes shift of the fluorescence emission the wavelength of the light passing through them is different, therefore the PSFs are written $|h_1|^2$ and $|h_2|^2$, as shown.

The laser source creates a focal spot in the sample, exciting fluorescent molecules at a rate proportional to the intensity ($\propto |h_1(\xi,\eta)|^2$). As each of these molecules fluoresce they act as another point source and so create an image equivalent to the IPSF in the (t,w) plane, $\propto |h_2(\xi - Mt, \eta - Mw)|^2$. Therefore, the image intensity in the pinhole plane (t,w) can be expressed (setting $M = 1$ for convenience) as:

$$I(t,w) = \iint_{-\infty}^{\infty} |h_1(\xi,\eta)|^2 \, f(\xi - x_s, \eta - y_s) \, |h_2(\xi + t, \eta + w)|^2 \, \mathrm{d}\xi \mathrm{d}\eta \qquad (2.31)$$

where (x_s, y_s) is the scan position. By placing a pinhole at $(t,w) = (0,0)$, the image intensity is the sum of the intensity contributions from each fluorescing point in the

sample:

$$I(0,0) = \iint_{-\infty}^{\infty} |h_1(\xi,\eta)|^2 \, f(\xi - x_s, \eta - y_s) \, |h_2(\xi,\eta)|^2 \, \mathrm{d}\xi \mathrm{d}\eta \tag{2.32}$$

Therefore, the image intensity is a convolution of the product of $|h_1|^2$ and $|h_2|^2$ with f and can be written as a function of the scan position:

$$I(x_s, y_s) = |h_1(\xi,\eta)|^2 |h_2(\xi,\eta)|^2 * f(\xi - x_s, \eta - y_s) \tag{2.33}$$

Although this derivation has used only 2D coordinates, a similar expression is valid for 3D specimens and PSFs. In general, $\lambda_{illumination} < \lambda_{emission}$ for fluorescent markers due to the Stokes' shift. Hence $h_1 \neq h_2$ but is scaled by the change in wavelength. However, many fluorophores exhibit a small Stokes' shift so we can make the approximation $\lambda_{illumination} \approx \lambda_{emission}$ and can therefore reasonably use the approximation $h_1 \approx h_2$ such that $|h_1|^2 \approx |h_2|^2$ and so the confocal fluorescence image intensity is given by the 3D convolution:

$$I(x_s, y_s, z_s) = \iiint_{-\infty}^{\infty} h_{eff}(\xi,\eta,\zeta) f(\xi - x_s, \eta - y_s, \zeta - z_s) \mathrm{d}\xi \mathrm{d}\eta \mathrm{d}\zeta \tag{2.34}$$

where $h_{eff}(\xi,\eta,\zeta) = |h_1(\xi,\eta,\zeta)|^4$ is the effective IPSF of a confocal microscope.

2.2.3 Two-photon microscope

Fg. 2.9 shows the basic layout and operation of the two-photon microscope. A more detailed discussion of its operation is given in Section 1.1. The imaging of the two-photon microscope is very similar to the confocal microscope, but with a few key differences. Instead of requiring just one photon to excite the fluorescent molecule, two-photon fluorescence requires the simultaneous absorption of two photons to give the necessary excitation energy. A single photon is then emitted at approximately half the excitation wavelength.

We can use a similar derivation as for the confocal microscope. As the fluorescence

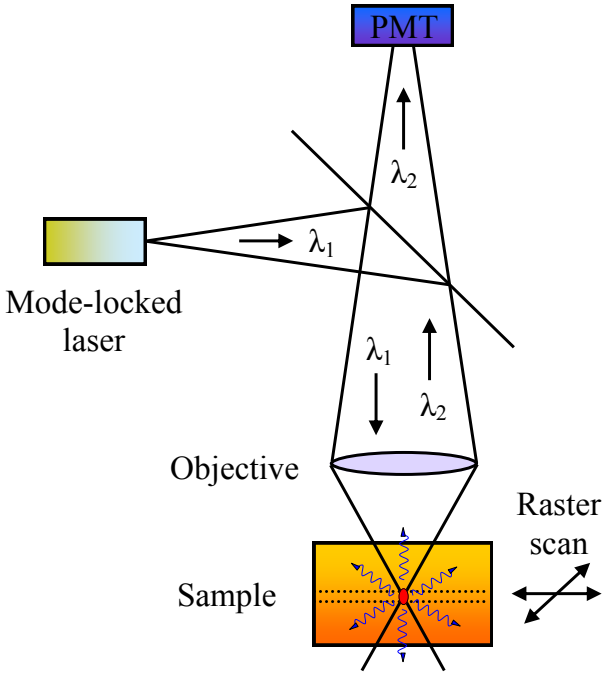


Figure 2.9: *A diagram of a two-photon microscope, showing how only light from the focus is included in the image.*

excitation is proportional to the square of the intensity, Eq. 2.33 becomes:

$$I(t,w,u) = |h_1(t,w,u)|^4 \, |h_2(t,w,u)|^2 * f(t,w,u) \tag{2.35}$$

Since the two-photon fluorescent process already exhibits optical sectioning, the confocal pinhole is no longer required and can be removed such that $h_2 = 1$, and so:

$$I(t,w,u) = |h_1(t,w,u)|^4 * f(t,w,u) \tag{2.36}$$

Clearly this is the same expression as Eq. 2.34. Therefore, if we assume that the excitation wavelengths are the same in both the confocal and two-photon microscopes (and the single photon emission is at the same wavelength as the excitation), the same mathematical modelling can be applied for both the confocal and two-photon cases.

2.2.4 Harmonic generation microscope

By utilising the optical properties of a material, the harmonic generation microscope is able to create three-dimensional images without any additional fluorescent markers. The polarisation density of a material describes the response to an applied electric field. It has been shown theoretically that by applying an electric field to a region with non-linear susceptibility, a second or third harmonic (SHG or THG) signal can be generated [Kleinman, 1962, Barad et al., 1997, Cheng and Xie, 2002, Thayil et al., 2010]. Typically this non-linear susceptibility also coincides with regions of non-uniform refractive index. In order to generate significant SHG and THG signal, a short pulsed laser is tightly focussed within the specimen. This is necessary as, like two-photon microscopy, harmonic generation microscopy is non-linear. Two or three photons (at wavelength λ), for SHG or THG respectively, are spontaneously converted into harmonic photons due to the non-linear optical properties of the material. It is this non-linearity that gives the harmonic generation microscope its three dimensional resolution. From this point, any SHG (at $\lambda/2$) and THG (at $\lambda/3$) signal is collected and recorded by PMTs. For the purpose of illustration, the layout of harmonic generation microscopes is considered to be identical to that of the two-photon microscope, shown in Fg. 2.9.

It is non-trivial (and beyond the scope of this thesis) to mathematically describe the harmonic imaging process in the same convolution form as written previously for the conventional, confocal and two-photon microscopes. However, the harmonic generation microscope is still affected by aberrations in the same manner as other microscopes, resulting in a drop in image intensity and resolution. Although mathematical modelling is more complex, a similar practical process is used to correct for the aberrations.

2.3 Imaging in the presence of aberrations

So far we have only considered the diffraction limited case when modelling the imaging system. However, in most practical situations aberrations will be present. Aberrations are the deviation of a wavefront from its ideal form [Welford, 1986]. For example,

in a collimated beam the ideal wavefront is planar, or in a focussed beam it takes the form of a spherical cap. Aberrations can be caused by various different factors, including the imperfect design or set up of the optical system, such as misalignment or focussing errors [Mahajan, 2001]. In microscopes, aberrations may also be introduced by the specimen which is typically inhomogeneous and has variations in refractive index throughout [Schwertner et al., 2004a].

Aberrations can be described by the difference in path length between the ideal wavefront position and its actual position. This gives a phase error, $\phi(x, y)$, which can be written:

$$\phi(x, y) = kW(x, y) \tag{2.37}$$

where k is the wave number and $W(x, y)$ is the path length error, as shown in Fg. 2.10 for both a planar wavefront (e.g. when considering a collimated laser source, Fg. 2.10(a)) and a spherical wavefront (e.g. when considering a wavefront after a focussing lens, Fg. 2.10(b)).

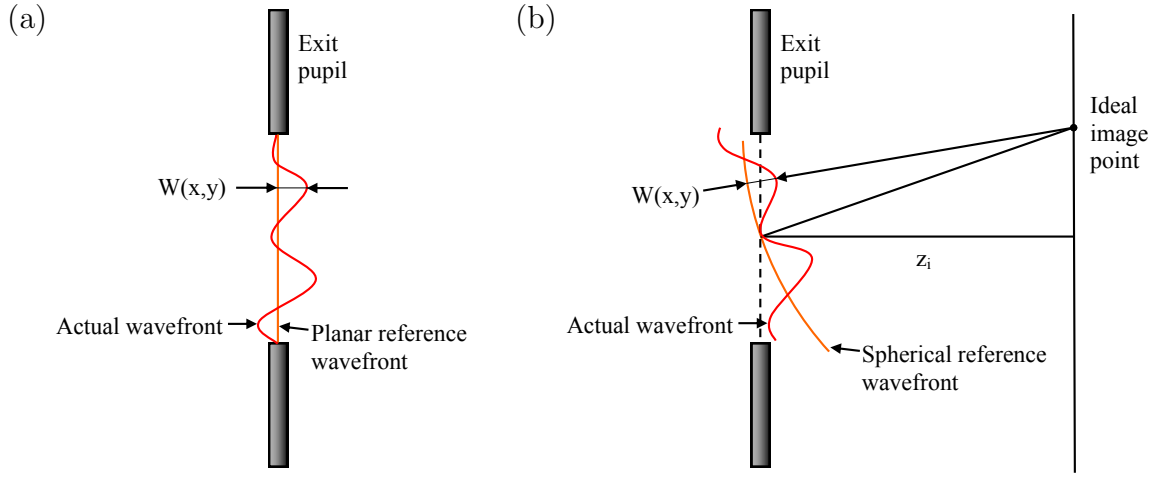


Figure 2.10: *Geometry used to define the aberration. The path length deviation from an ideal planar wavefront (a) and a focussing spherical wavefront (b) is shown.*

Given that aberrations are the error of a wavefront from its ideal form, it is clear, when considering the diffraction theory described previously, that they will alter the form of the point spread function when focussed by a lens. Typically this will result in the enlargement, reduction in intensity and distortion of the focal spot. Mathematically, the focal spot PSF is given by Eq. 2.17, which is the inverse Fourier transform of the

pupil function. By including in the definition of the pupil function a term for aberrations, we can compute the effect that they will have on the PSF. We can consider the complex amplitude transmittance $\mathbf{P}(x, y)$ as the generalised pupil function, given by:

$$\mathbf{P}(x, y) = P(x, y) \exp[j\phi(x, y)] \tag{2.38}$$

where $P(x, y)$ is the amplitude pupil function (Eq. 2.5) and $\exp[j\phi(x, y)]$ represents the phase error. Therefore, the aberration is completely described as a phase error.

Considering incoherent imaging we must look at the OTF. When aberrations are present, Eq. 2.38 can be substituted into Eq. 2.28 to give an overlap integral:

$$\begin{aligned} C_1(m, n) &= \iint_{-\infty}^{\infty} P(x + x', y + y') \exp\left[j\phi\left(x + x', y + y'\right)\right] \\ &\quad P^*(x - x', y - y') \exp\left[-j\phi\left(x - x', y - y'\right)\right] \mathrm{d}x\mathrm{d}y \end{aligned} \tag{2.39}$$

where $x' = \dfrac{\lambda z_i m}{2}$ and $y' = \dfrac{\lambda z_i n}{2}$. This directly relates wavefront aberrations to the OTF. Fg. 2.11 shows the two-dimensional OTF with astigmatism present and a slice through the OTF at $n = 0$, showing the effect of aberrations. This shows that (for $n = 0$) the efficiency of transmission of all spatial frequencies, except for those when $|m|$ approaches 0 or 2, is reduced compared to the unaberrated case. Fg. 2.11(a) shows that if a slice was taken at another point, e.g. when $m = n$, then the slice would look very different to Fg. 2.11(b), so care must be taken when considering 1D sections through 2D OTFs.

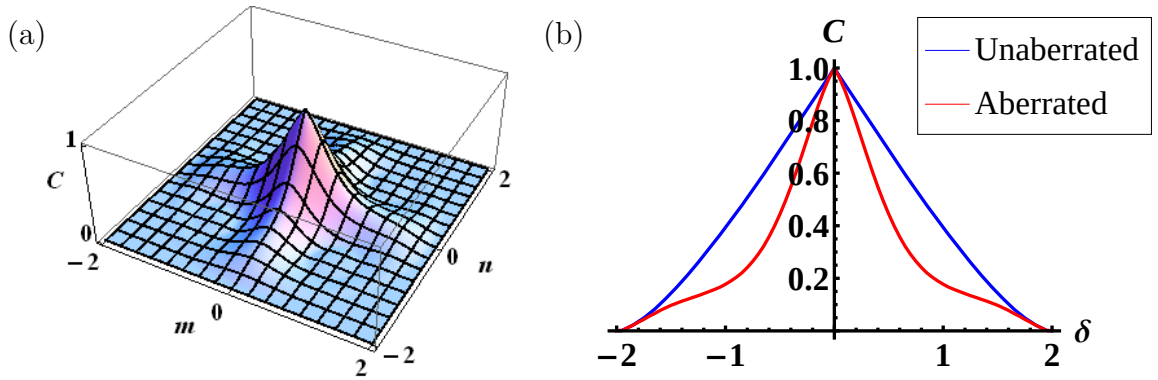


Figure 2.11: *The optical transfer function of a system with astigmatism aberration with a circular pupil of radius 1 (a) and a slice at $n = 0$ (b).*

The Zernike polynomials

In the above analysis, wavefront aberrations are represented by the phase aberration function $\phi(x, y)$. It is useful to decompose this aberration into a series of component aberration modes. Zernike polynomials, orthogonal functions defined within the unit circle [Zernike, 1934], are typically used for this purpose [Tango, 1977]. For the full definition of the Zernike polynomials, see Appendix B

From this point on we have used Noll's definition of the Zernike polynomials, where the mean of $Z_i(r, \theta)$ over the unit circle is zero, provided $i \neq 1$ (when $i = 1$ the mean value is 1), and the root-mean-square value over the unit circle is 1. The polynomials form a complete function basis, so mathematically, an infinite Zernike series can represent any phase aberration desired. In practice, many realistic aberrations can be adequately represented by a finite series of a small number of Zernike modes.

Aberrations causing displacements

As shown by Fg. 2.11, aberration terms affect the OTF and, equivalently, they also degrade the focal spot by distortion and reduction of intensity. However, this is not the case for the first four Zernike modes: piston (Z_1), tip (Z_2), tilt (Z_3) and defocus (Z_4). Piston adds a constant phase to the pupil function, so is generally disregarded as we are considering aberrations as a phase-only phenomenon. Tip and tilt add a linearly varying phase to the pupil. This does not result in any distortion of the focal spot, but shifts the PSF from its original position to another position in the focal plane. Defocus also does not distort the PSF, but displaces it but along the optic axis. Since there is no change in the focal spot, the effect of these modes in a microscope is that tip and tilt physically alter the region of the specimen that is being imaged. By adding a small amount of tip or tilt whilst imaging (in the xy plane), it would appear that the imaged region has moved to the side slightly. As defocus displaces the PSF axially, the (xy) plane that is being imaged would change.

Using the defocus term, it is possible to further generalise the aberration description and include the third dimension. The focussing phase aberration will be proportional to

the radius squared (the relationship is $\phi(r,\theta,z) = \frac{ur^2}{2}$, where u is defined in Eq. 2.10). Zernike polynomials and the focussing error can therefore be used in the generalised pupil function to describe the phase variation. Converted to cylindrical coordinates and applying Eq. 2.5 to Eq. 2.38, we can create a new generalised pupil function, describing phases that represent displacements and distortions of the focal spot:

$$\mathbf{P}(r,\theta,u) = \begin{cases} \exp\left[j\left(\sum a_i Z_i(r,\theta) + \frac{ur^2}{2}\right)\right] & r \leq 1 \\ 0 & r > 1 \end{cases} \tag{2.40}$$

where a_i describes the amplitude of each Zernike polynomial $Z_i(r,\theta)$.

Chapter 3

Effects of aberrations and specimen structure in fluorescence microscopy

Specimen-induced aberrations cause a reduction in signal levels and resolution in fluorescence microscopy. Aberrations also affect the image contrast achieved by these microscopes. In this chapter the effects of aberrations on the fluorescence signals acquired from different specimen structures, namely point-like, linear, planar and volume structures, are modelled when imaged by conventional, confocal and two-photon microscopes. From this the image contrast obtained when observing combinations of such structures is derived. The effect of aberrations on the visibility of fine features is shown to depend upon the specimen morphology and it is found that the contrast is less significantly affected in microscopes exhibiting optical sectioning. For example, it is shown that point objects become indistinguishable from background fluorescence in the presence of aberrations, particularly when imaged in a conventional fluorescence microscope. This demonstrates the significant advantage of using confocal or two-photon microscopes over conventional instruments when aberrations are present.

3.1 Introduction

It is widely acknowledged that specimen-induced aberrations detrimentally affect the quality of the image which can be achieved by high-resolution optical microscopes [Gib-

son and Lanni, 1992, Hell et al., 1993, Booth et al., 1998]. These aberrations limit the ability of microscopes to image deep within thick specimens [Diaspro et al., 2002], although recent developments in adaptive optics for aberration correction have led to improvements [Booth, 2006, Girkin et al., 2009, Ji et al., 2010]. The effects of aberrations on microscope images include reduction in resolution, blurring and detected signal intensity. An important but less well-known consequence of specimen induced aberrations is that they affect different specimen features in different ways [Débarre et al., 2009]. It is important to appreciate these differences since they have implications on the visibility and contrast with which specimen structures appear in the final image.

The imaging of idealised specimen structures (point, line, plane and volume objects) in conventional, confocal and two-photon fluorescence microscopes is numerically modelled. The effects of aberrations on the peak image intensity for each of these structures is examined and it is shown that the sensitivity to aberrations is highest for lower dimensional objects. The effects of aberrations on image contrast are also considered when different structures are present in the same specimen, for example when a point-like object is embedded in a fluorescent volume. As aberrations affect the peak image intensity for each specimen structure differently, a differential effect on the image contrast for combinations of structures is shown. This leads to the possibility that small objects may be in effect invisible, whilst an appreciable background fluorescence is detected.

This phenomenon could have important consequences in the interpretation of images in biological microscopy, where it may not be obvious that the apparent absence of small features is due to aberrations. Furthermore, when considering sensorless aberration correction routines, the metric used to correct for aberrations is dependent on properties of the image [Débarre et al., 2007]. Ideally, this should be independent of specimen structure. However, the results presented here show that the image properties are dependent on the combination of aberration modes and specimen structure. Therefore, understanding these phenomena could be important when designing a sensorless adaptive optics routine.

3.2 Aberrations and the pupil function

For this analysis, it is assumed that the aberrations are phase-only in nature and can be represented by phase variations introduced into the pupil of the objective lens. This assumption is generally applicable to microscopy; an amplitude aberration would indicate that the illumination is being blocked, reflected or absorbed, whilst a biological specimen would typically scatter light. The consequence of amplitude aberrations is typically considered to be less than that of phase aberrations, so is not considered here. For convenience, we assume that this pupil has a normalised radius of one. Since the Zernike polynomials are defined using radial coordinates (see Eq. B.2), the complex pupil function defined in Eq. 2.38 is rewritten and thus given by:

$$\mathbf{P}(r,\theta) = \begin{cases} \exp\left[j\phi(r,\theta)\right], & r \leq 1 \\ 0, & \text{otherwise} \end{cases} \tag{3.1}$$

where $\phi(r,\theta)$ is the phase aberration and j is the imaginary unit. We model the phase aberration as a series of Zernike polynomials, defined in Eq. B.2 and Tab. B.1, which are represented by the functions $Z_i(r,\theta)$:

$$\phi(r,\theta) = \sum_i a_i Z_i(r,\theta) \quad , \tag{3.2}$$

where a_i represents the amplitude coefficient of each mode, measured in radians. Not included are the low order polynomials piston, tip, tilt and defocus in the analysis as they do not contribute to a change in the image quality (although tip, tilt and defocus do cause image distortion [Schwertner et al., 2007], see also Section 2.3).

In the analysis that follows, the effects on image quality of single Zernike modes and of random combinations of multiple Zernike modes was considered. In the case of single modes, the phase aberration was defined as $\phi(r,\theta) = a_i Z_i(r,\theta)$. The effects are illustrated using the six Zernike modes 5 to 10, encompassing the lowest order astigmatism, coma, and trefoil modes. Whilst results from other modes could have been presented, the trends shown for the first six Zernike modes are found to be common to all other Zernike modes

and hence for brevity results only for the first six are presented in detail. However, higher order modes, such as spherical, are included in the analysis of random aberrations. For these further calculations, random combinations of a set of N Zernike modes was used, for which the phase was defined as:

$$\phi(r,\theta) = A\sum_{i=1}^{N} a_i Z_i(r,\theta) \tag{3.3}$$

where A is the aberration amplitude. To generate the random aberration, the modal coefficients a_i were assigned a random value between -1 and 1. The coefficients were then renormalised so that the total mean square value $\sum_i a_i^2$ was 1. Since the rms value of Z_i is 1 (as defined in Appendix B), this ensured that the rms amplitude of the phase defined by Eq. 3.3 was equal to A.

For calculations involving volume structures it was necessary to calculate the field in out-of-focus planes. For this purpose, an additional quadratic phase component is included in the pupil function, as defined in Eq. 2.40 and rewritten as:

$$\mathbf{P}(r,\theta) = \exp\left[j\phi(r,\theta) + j\frac{ur^2}{2}\right] \tag{3.4}$$

where u is the normalised axial coordinate which is related to the real coordinate z, as defined by Eq. 2.10.

3.3 Image formation in fluorescence microscopes

For all incoherent fluorescence microscopes, Eq. 2.26 states that the image intensity can be described by the convolution of the intensity point spread function (IPSF) of the imaging lens evaluated at the fluorescence wavelength, h_i, with the fluorescence distribution, f [Wilson and Sheppard, 1984]:

$$I = h_i * f \tag{3.5}$$

where $*$ denotes the convolution operation (see Eq. A.3). In the case of the conventional, non-scanning fluorescence microscope, the IPSF h_i is rewritten H_{conv}. H_{conv} is mathematically equivalent to the modulus squared of the amplitude point-spread function (PSF) h, as defined by Eq. 2.30, and can be written:

$$H_{conv} = |h|^2 , \tag{3.6}$$

whilst for the confocal microscope, the effective IPSF h_i is rewritten as H_{conf}. H_{conf} is given by the product of the IPSF of the objective lens which excites the fluorescence and that of the objective which focusses the fluorescence onto the confocal pinhole. If we ignore the Stokes shift between the excitation and the fluorescence and assume that the illumination and detection objectives are the same, then the effective IPSF is given by [Wilson and Sheppard, 1984]:

$$H_{conf} = |h|^4 , \tag{3.7}$$

as stated in Eq. 2.34. Using the scalar approximation to diffraction theory, the field in the focus of the objective lens can be expressed as the Fourier transform of the pupil function. Hence, the amplitude PSF h presented in Eq. 2.18 is rewritten for a system that no longer exhibits radial symmetry and given in two dimensions by:

$$h(t,w) = \int_{\theta=0}^{2\pi} \int_{r=0}^{1} \mathbf{P}(r,\theta) \exp\left[j(tr\cos\theta + wr\sin\theta)\right] r\mathrm{d}r\mathrm{d}\theta \ , \tag{3.8}$$

where $(t,w) = (\frac{2\pi t^{\dagger} NA}{\lambda}, \frac{2\pi w^{\dagger} NA}{\lambda})$, $t^{\dagger}$ and $w^{\dagger}$ are the real Cartesian coordinates in the image plane and NA is the numerical aperture of the objective lens. Since $\mathbf{P}(r,\theta)$ incorporates aberrations (see Eq. 3.1), Eq. 3.8 may be used to calculate the aberrated amplitude PSF. In Eq. 3.8 and from this point on we have omitted premultiplying constants to the integrals, since the constants have no effect on the normalised results that are presented.

The two-photon excitation efficiency is proportional to the square of the intensity of the excitation light and so, as stated by Eq. 2.36, can be described by the IPSF in

Eq. 3.7 when evaluated at the excitation wavelength. This is the same expression as that used to describe the confocal microscope, so the effects of aberrations on both types of microscope can be modelled by the same equations.

The image formation process described by Eq. 3.5 can equivalently be written in terms of the product of the optical transfer function (OTF), C, and the Fourier transform of the fluorescence distribution, F (see Eq. 2.27) [Wilson and Sheppard, 1984], written here in two dimensions:

$$I(t,w) = \iint C(m,n)F(m,n)\exp\left[2\pi j(tm+wn)\right]\mathrm{d}m\mathrm{d}n \tag{3.9}$$

where C is the Fourier transform of h_i, F is the Fourier transform of f and (m,n) are the normalised spatial frequencies in the Fourier domain. In the case of the conventional, non-scanning fluorescence microscope, C can be defined as Eq. 2.28, which can be more simply written as:

$$C_{conv}(m,n) = \mathbf{P}(m,n) * \mathbf{P}^*(m,n) \tag{3.10}$$

where $\mathbf{P}$ is the complex pupil function defined by Eq. 3.1 and * represents the complex conjugate. For the confocal or two-photon microscopes, C can be defined as [Wilson and Sheppard, 1984]:

$$C_{conf}(m,n) = C_{conv}(m,n) * C_{conv}(m,n) \tag{3.11}$$

For clarity of explanation, the expressions that follow are written in terms of continuous integrals and continuous Fourier transforms. In practice, the calculations were performed using sampled functions and discrete Fourier transform algorithms.

3.4 Image formation in the conventional fluorescence microscope

In this section, we describe the effects of aberrations on the imaging properties of conventional non-scanning fluorescence microscopes for different specimen structures. In these microscopes, the two-dimensional image intensity is described by Eq. 3.5, which can be rewritten as:

$$I(t,w) = \iint_{-\infty}^{\infty} H_{conv}(t',w') f(t-t', w-w') \mathrm{d}t' \mathrm{d}w' \tag{3.12}$$

Eq. 3.9 can also be written for the conventional fluorescence microscope as:

$$I(t,w) = \iint_{-\infty}^{\infty} C_{conv}(m,n) F(m,n) \exp\left[2\pi j(tm+wn)\right] \mathrm{d}m\mathrm{d}n \tag{3.13}$$

We note that $C_{conv}(m,n)$ is non-zero only for $\sqrt{m^2+n^2} < 2$. The formulation of either Eq. 3.12 or Eq. 3.13 can be used to determine the image intensity and the choice depends upon convenience for numerical calculation.

We first model the effects of aberration on the imaging of a point object, for which $f(t,w) = \delta(t)\delta(w)$, where $\delta(.)$ is the Dirac delta function. The on-axis intensity is calculated using Eqs. 3.6, 3.8 and 3.12 as:

$$I(0,0) = H_{conv}(0,0) = \left| \int_{r=0}^{1} \int_{\theta=0}^{2\pi} P(r,\theta) r \mathrm{d}r \mathrm{d}\theta \right|^2 \tag{3.14}$$

The second specimen structure that we consider is a line of infinite length oriented along the t-axis. This is described by the specimen function $f(t,w) = \delta(w)$ or alternatively by its Fourier transform $F(m,n) = \delta(m)$. The image of this linear object can be expressed using Eq. 3.13 as:

$$I(t,w) = I(0,w) = \int_{-2}^{2} C_{conv}(0,n) \exp\left[2\pi j w n\right] \mathrm{d}n \tag{3.15}$$

So the on-axis intensity can be derived as:

$$I(0,0) = \int_{-2}^{2} C_{conv}(0,n)\mathrm{d}n \tag{3.16}$$

where the limits of integration correspond to the finite non-zero extent of the OTF $C_{conv}(m,n)$. This calculation is performed in the frequency domain, due to the finite support of the integrand.

For a planar object, the specimen function $f(t,w) = 1$, so we find that the on-axis image intensity is given by:

$$I(0,0) = \iint H_{conv}(t,w)\mathrm{d}t\mathrm{d}w \tag{3.17}$$

in the spatial domain. More conveniently, this can be written as the on-axis image intensity $(t, w = 0)$ in the Fourier domain as:

$$I(0,0) = C_{conv}(0,0) = \iint |P(r,\theta)|^2 \, r\mathrm{d}r\mathrm{d}\theta = const. \tag{3.18}$$

Since the pupil function varies only in phase and not amplitude, $|P| = 1$. Eq. 3.18 therefore holds for all aberrations and defocus, hence the same constant result is also found for the signal from a uniform volume object. This insensitivity to defocus confirms the well known phenomenon that the conventional microscope does not exhibit optical sectioning in the manner that the confocal and two-photon microscopes do.

Fg. 3.1 shows the variation of the on-axis image intensity of the images of point and line specimens, where the specimens lie in the focal plane and individual Zernike aberration modes are present. For each structure, the on-axis intensity is normalised to the value found for zero aberration. In all cases, the on-axis intensity reduces as aberration amplitude increases. Differences are seen in the relative change in signal level from point and line structures for the different modes. Comparing the graphs for modes 5 and 6 (astigmatism modes that differ only by a 45 degree rotation), it can be seen that the change in on-axis intensity is identical for the point object, but differs between

the two modes for the line object. This is due to the different relative orientation of the object and the aberration mode, which corresponds to the orientation of the distorted focal spot. Similar effects are seen for mode pairs 7 and 8 (coma) and 9 and 10 (trefoil), which also differ only by rotations.

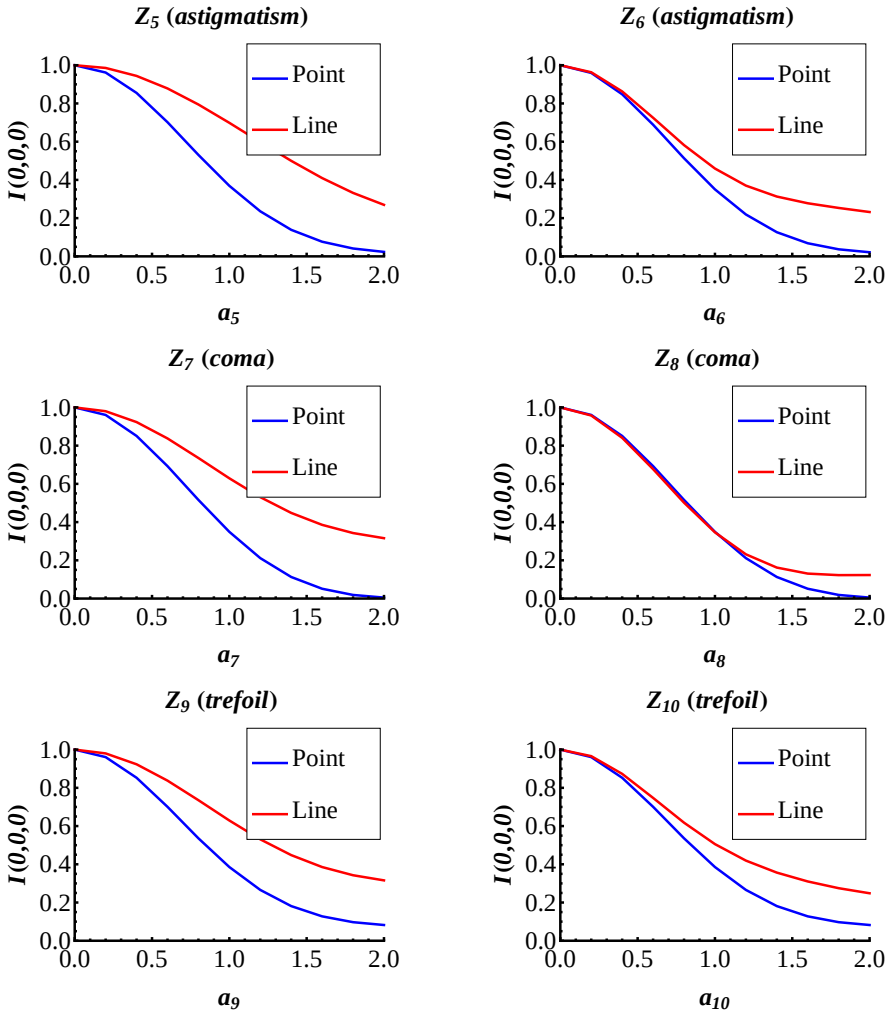


Figure 3.1: *The on-axis image intensity variation, I(0,0), of point and line structures as a function of single Zernike mode aberration amplitude, a_i, in a conventional fluorescence microscope.*

3.5 Image formation in the confocal and two-photon fluorescence microscopes

In this section we investigate the effects of aberrations on the imaging of different specimen structures in confocal and two-photon fluorescence microscopes. As with the con-

ventional microscope, the imaging properties of these microscopes can also be described in either the spatial or Fourier domain as shown by Eq. 3.5 and Eq. 3.9 respectively.

Expressing Eq. 3.5 in three dimensions for the confocal case gives us the 3D convolution Eq. 2.34. Normally the detector is placed in the $u = 0$ plane (i.e. $z_s = 0$ from Eq. 2.34), so Eq. 2.34 can be written as the integral along u of a 2D convolution in t and w:

$$I(t, w, 0) = \iiint_{-\infty}^{\infty} H_{conf}(t', w', u) f(t - t', w - w', u) \mathrm{d}t' \mathrm{d}w' \mathrm{d}u \tag{3.19}$$

Equivalently, we can rewrite Eq. 3.9 using 3D coordinates as:

$$I(t, w, 0) = \iiint_{-\infty}^{\infty} C_{conf}(m, n; u) F(m, n; u) \exp\left[2\pi j(tm + wn)\right] \mathrm{d}m \mathrm{d}n \mathrm{d}u \tag{3.20}$$

where the notation $(m, n; u)$ describes m and n in the frequency domain and u in the spatial domain. Therefore $F(m, n; u)$ is the 2D Fourier transform of $f(t, w, u)$, transforming (t, w) into (m, n) and not performing any transform in the u direction. We note that $C_{conf}(m, n; u)$ is the 2D OTF of a confocal microscope taking defocus into account and is non-zero only for $\sqrt{m^2 + n^2} < 4$.

Point, line, plane and volume objects can be described in either the spatial or Fourier domains as shown in Table 3.1. These definitions are used with Eqs. 3.19 or 3.20 to give expressions for image intensity for the different specimen structures. We first consider

	$f(t, w, u)$	$F(m, n; u)$
Point	$\delta(t)\delta(w)\delta(u)$	$\delta(u)$
Line along t-axis	$\delta(w)\delta(u)$	$\delta(m)\delta(u)$
Plane	$\delta(u)$	$\delta(m)\delta(n)\delta(u)$
Volume	1	$\delta(m)\delta(n)$

Table 3.1: *The mathematical description of the 3D specimen structures modelled*

the image of a point object positioned at the origin. For small aberration amplitudes, the maximum intensity of this image is on the optical axis. This on-axis image intensity is given by:

$$I(0, 0, 0) = H_{conf}(0, 0, 0) = \left| \int_{r=0}^{1} \int_{\theta=0}^{2\pi} P(r, \theta) r \mathrm{d}r \mathrm{d}\theta \right|^4 \tag{3.21}$$

For the line object, the substitution of $f(t, w, u) = \delta(w)\delta(u)$ into Eq. 3.19 yields:

$$I(0, 0, 0) = \int_{-\infty}^{\infty} H_{conf}(t, 0, 0)\mathrm{d}t \tag{3.22}$$

For the planar object, we use Eq. 3.20 with Eq. 3.11 and $F(m, n; u) = \delta(m)\delta(n)\delta(u)$ to give the on-axis intensity:

$$I(0, 0, 0) = C_{conf}(0, 0; 0) \tag{3.23}$$

Eq. 3.23 describes the image signal from a planar object when the plane is located in the focal plane ($u = 0$). When located at an arbitrary position, u, the signal is given by $C_{conf}(0, 0; u)$. For a volume object we can write the on-axis image intensity as:

$$I(0, 0, 0) = \int_{u} C_{conf}(0, 0; u)\mathrm{d}u = \iiint_{mnu} \left|C_{conv}(m, n; u)\right|^2 \mathrm{d}m\mathrm{d}n\mathrm{d}u \tag{3.24}$$

Using the expressions derived above, the effects of aberrations on the on-axis image intensity for the different specimen structures in confocal and two-photon microscopes was calculated. The on-axis intensity for the four specimen structures was modelled in the presence of individual Zernike modes for point, line and plane specimens lying in the focal plane. In each case, the aberrated on-axis intensity was normalised to the unaberrated equivalent for the same specimen structure. The results for modes 5 to 10 are shown in Fg. 3.2.

For all modes and for all structures, as the aberration amplitude increases, the on-axis intensity decreases. As a general trend, it can be seen that the normalised on-axis intensity of the point object is most sensitive to aberrations, followed by the line, plane and volume structures. This confirms the empirical results of [Débarre et al., 2009], which showed that the image intensity of a fluorescent bulk should be less sensitive to aberrations than a fluorescent point. As was observed in the results for the conventional microscope, differences can be seen between similar modes (e.g. the coma modes 7 and 8) due to the relative orientation of the linear structure and the aberration mode.

With practical specimens, the induced aberrations generally consist of combinations of aberration modes [Schwertner et al., 2004a]. The effects of multiple aberration modes

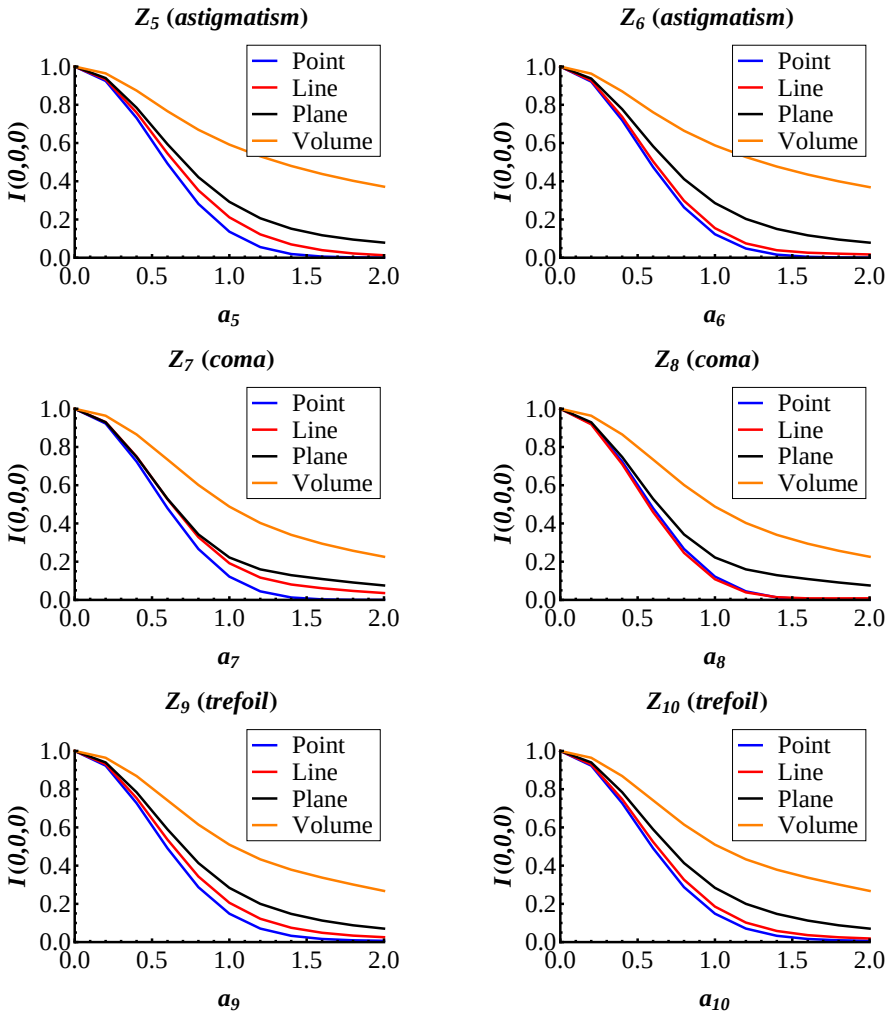


Figure 3.2: *The on-axis image intensity, $I(0,0,0)$, for point, line, plane and volume structures as a function of a single Zernike mode aberration amplitude, a_i in a confocal or two-photon fluorescence microscope.*

on confocal/two-photon imaging of the four structures were also modelled. A set of 100 aberrations consisting of random combinations of Zernike modes 5 to 30, were derived according to Eq. 3.3 for a chosen amplitude A. The corresponding on-axis image intensities were calculated for each specimen structure. The mean, 10th and 90th percentiles of the resulting distribution of intensities are plotted in Fg. 3.3. For ease of comparison, the mean values of these distributions are also shown together in Fg. 3.4. The same general trend is seen that the peak intensity from point objects is affected most strongly by aberrations, with linear, planar and volume objects being less affected.

The marked difference between the on-axis intensity detected from the volume object in comparison to the other structures can be explained geometrically. As aberrations are

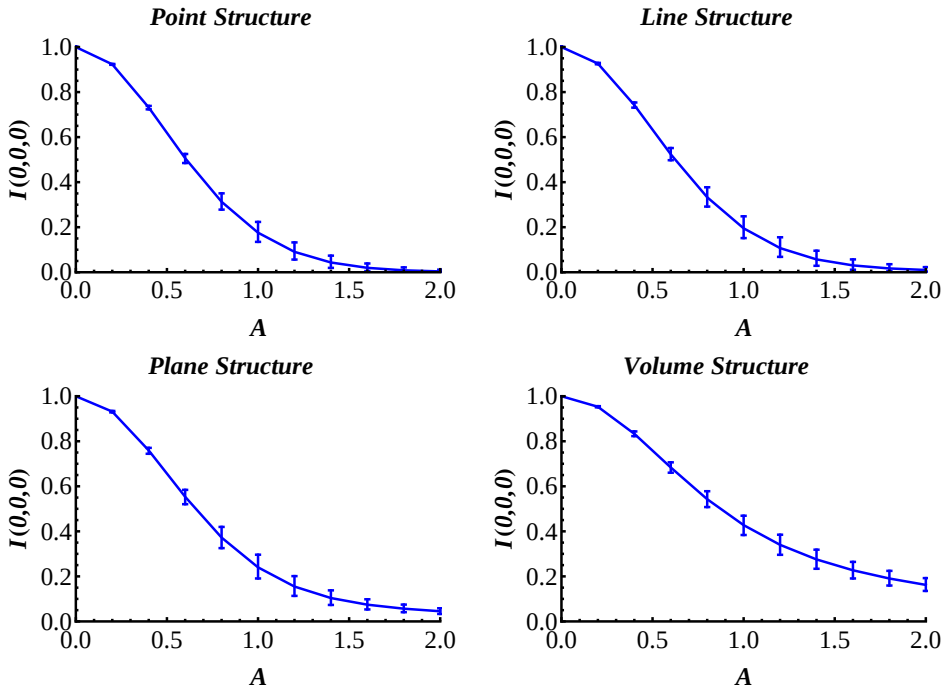


Figure 3.3: *The mean on-axis image intensity variation, $I(0,0,0)$, with aberration amplitude, A, for a point, line, plane and volume structure when imaged in a confocal or two-photon microscope with random combinations of Zernike mode aberrations (modes 5 to 30 were used). The bars mark the 10th and 90th percentiles of the statistical distribution.*

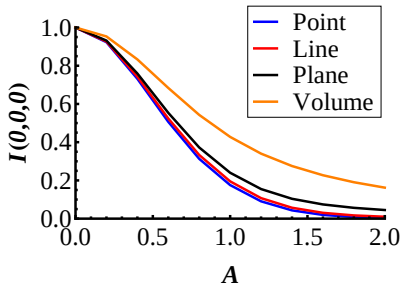


Figure 3.4: *The mean normalised on-axis intensity variation, $I(0,0,0)$ as a function of aberration amplitude, A, for a point (blue), line (red), plane (black) and volume object (orange) when imaged in a confocal or two-photon microscope.*

introduced and the effective point-spread function (PSF) increases in size, a significant proportion of the effective PSF will be removed from the region where the point, line and plane objects lie. This in turn reduces the amount of fluorescence detected via the detection PSF and hence leads to a decrease in on-axis image intensity. However, for the volume specimen the distorted focus is predominantly within the fluorescent material, so the on-axis image intensity does not decrease as significantly when compared to the other finer structures.

Comparing Fg. 3.2 with Fg. 3.3, the widths of the volume intensty responses are noticeably different; the on-axis image intensity variation for the volume structure with a random combination of aberrations applied (Fg. 3.3) has a narrower full-width-half-maximum than that for the same structure when individual modes are applied (Fg. 3.2). Fg. 3.5 compares the on-axis image intensity for individual Zernike modes 5 to 30 (Fg. 3.5(a)) with the mean on-axis image intensity for 100 random combinations of these same modes for a volume structure (Fg. 3.5(b)).

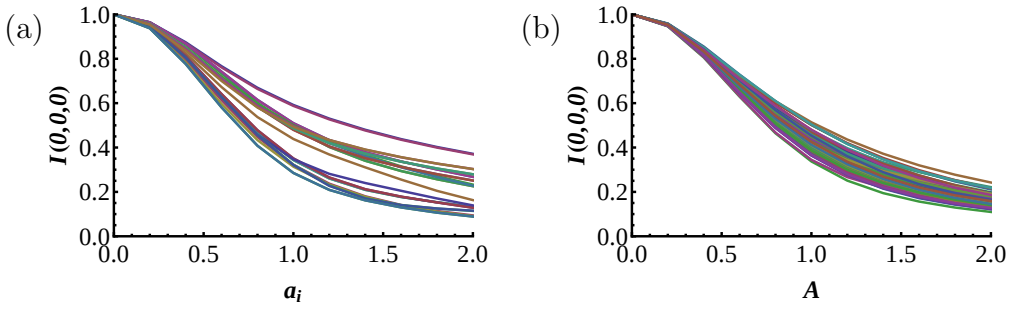


Figure 3.5: *The mean on-axis image intensity variation, $I(0,0,0)$ with aberration amplitude a_i/A for individual Zernike modes (a) and with a random combination of modes (b), both for a volume structure when imaged in a confocal or two-photon microscope. (a) shows the response to individual Zernike mode aberrations 5 to 30. (b) shows the response to 100 random combination of modes 5 to 30.*

At low aberration amplitudes (i.e. between amplitudes of 0 and 0.2) the intensity response of a volume object due to aberration by individual Zernike modes (as shown in Fg. 3.5(a)) follows the $1 - \alpha_i a_i^2$ approximation, where α_i is a constant. At low aberration amplitudes, the intensity response of random combinations of modes (as shown in Fg. 3.5(b)) follows the $1 - \beta A^2$ approximation, where β is a constant but is dependent on the combination of aberration modes.

By comparing the two graphs in Fg. 3.5, the on-axis intensity responses of a volume object to random aberrations are shown to be similar to the responses to individual Zernike modes. The small selection of Zernike modes used in Fg. 3.2 was such that all of the volume curves were wider than the volume curve for random aberrations in Fg. 3.3. However, by looking at the distributions for the first 30 Zernike modes and a selection of random aberrations in Fg. 3.5, the responses are shown to be comparable.

3.6 Confocal and two-photon fluorescence microscope contrast calculations

The differential effect of aberrations on the imaging of different specimen structures means that aberrations reduce both the overall image intensity and the relative visibility of objects. Consider, for example, the image of a small fluorescent object superimposed upon a uniform background fluorescence signal. As aberrations become larger the signal from the small object will decrease more rapidly than the signal from the background and, eventually, the small object will become indistinguishable from the background. In order to quantify this effect, we examine the image contrast when one object is superimposed on another. For example, the image intensity of a fluorescent point object (I_{point}) on a fluorescent plane (I_{plane}) is given by

$$\text{Image Intensity} = I_{plane} + I_{point} = I_{plane}\left[1 + \frac{I_{point}}{I_{plane}}\right] \tag{3.25}$$

and so it follows that the contrast of the image of a fluorescent point object embedded in a fluorescent plane is defined as:

$$\text{Image Contrast} = \frac{I_{point}(0,0,0)}{I_{plane}(0,0,0)} \tag{3.26}$$

Following this definition, the contrast is unity when there is no aberration present and decreases in value as aberration amplitudes increase. Fg. 3.6 shows the contrasts obtained for different combinations of specimen structures and the variation with aberration amplitude. The plots were obtained by calculating the contrast for 100 different random combinations of Zernike mode aberrations (using modes 5 to 30) and plotting the mean, 10th and 90th percentiles of resulting distribution.

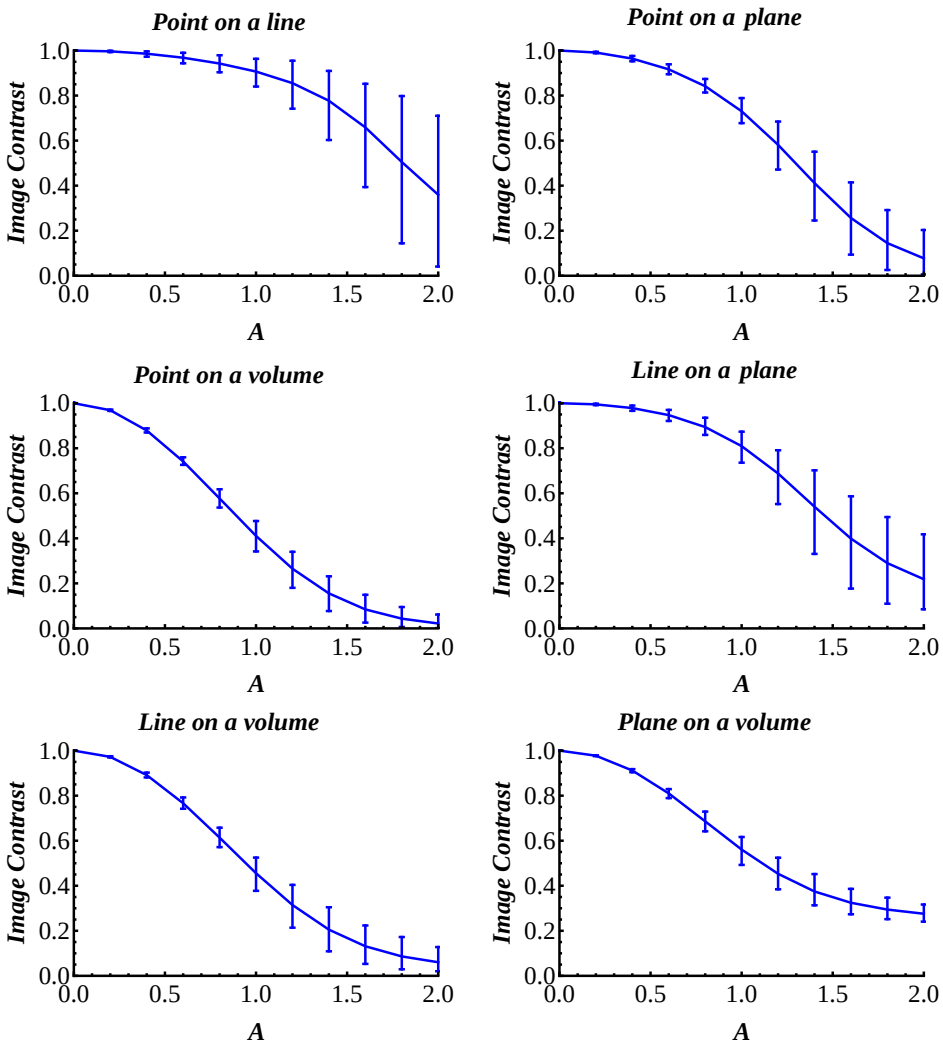


Figure 3.6: *The variation of confocal or two-photon image contrast as a function of aberration amplitude, A, for combinations of specimen structures. The mean, 10th and 90th percentiles of the distribution are shown.*

3.7 Contrast effects in aberrated microscope images

The results show that the contrast of the point object embedded in a volume object is most strongly affected by aberrations. The general trend observed is that the contrast sensitivity depends upon the relative size (or dimension) of the two specimen structures. For example, for structures embedded in a volume, the sensitivity to aberrations is worst for a point object, followed by the line object then the planar object. Since specimen induced aberrations tend to increase with focal depth, this explains why small objects seem to disappear in a fluorescent (volume-like) background as an image is taken deeper into a sample (see e.g. [Débarre et al., 2008]).

We have further simulated the imaging of a combination of idealised specimens, including points, lines and volume objects, in the presence of aberrations. These images are shown in Fig. 3.7. Fig. 3.7(a) shows simulated images of a two-dimensional specimen

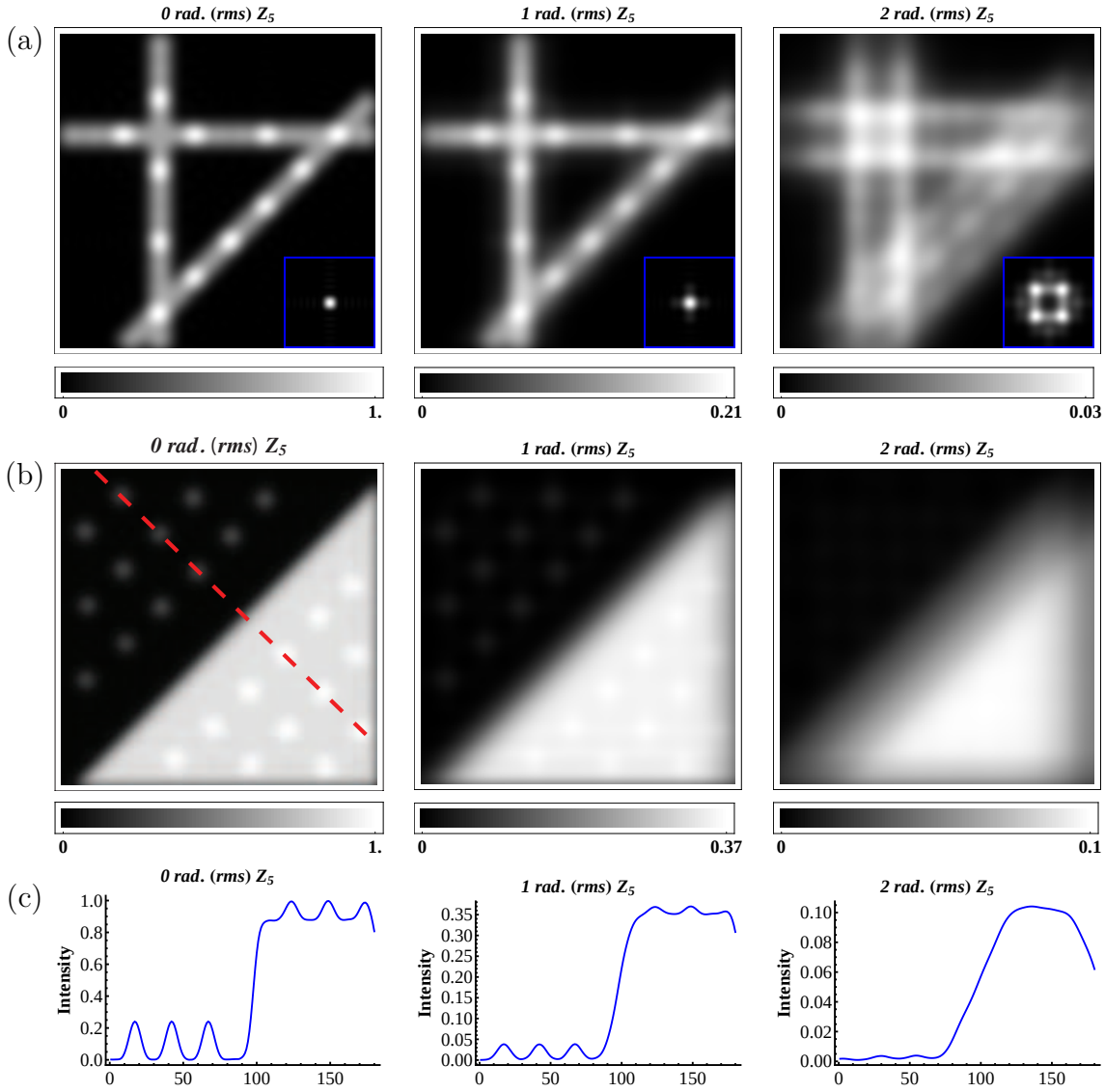


Figure 3.7: *Images modelling the effect of aberrations, in this case astigmatism (Zernike mode 5), on different structures in a confocal or two photon microscope (a and b), and the cross-sectional on-axis intensity graphs (c), taken from the dashed line in (b). Inset in (a) is the corresponding point-spread function at the same scale as the images. All images in (a) and (b) have been renormalised, as shown by the respective scales.*

structure, placed in the focal plane, in which point objects are superimposed upon linear structures. The aberration applied was 0 rad (rms) (left), 1 rad (rms) (centre) and 2 rad (rms) (right) of Zernike mode 5 (astigmatism). Whilst the points and lines become less distinct as the aberration increases, the background fluorescence remains clearly visible.

Fg. 3.7(b) shows simulated imaging of a 3D specimen in which an array of point objects (each with a normalised intensity of 1) lies in the focal plane together with an infinite fluorescent triangular volume object (with a normalised intensity of 0.5), which extends above and below the focal plane in the bottom right-hand corner of the specimen. For simplicity, the object structure was assumed not to extend outside of the displayed region which has led to the intensity drop-off seen at the edges of Fg. 3.7(b). Fg. 3.7(c) is the cross-sectional on-axis intensity of the images shown in Fg. 3.7(b) along the dashed line, showing clearly the reduction in contrast of the fluorescent points on the background fluorescence as the aberration increases. The difference in relative intensities of the fluorescent points when imaged on no fluorescent background and within an infinite fluorescent volume is not significant; rather it is a result of the initial relative intensity difference. The points not within the fluorescent volume had an unaberrated intensity of 1, whilst those within the fluorescent volume had an unaberrated intensity of 0.5 relative to the fluorescent background. Significantly, it is the reduction in visibility of the point-like structures when superimposed on the fluorescent volume-like background that is clear from Fg. 3.7(c), as the relative on-axis intensity drops from approx. 0.1 in the unaberrated case, to approx. 0.03 with 1 rad. (rms) of Zernike mode 5 present and approx. 0.005 with 2 rad. (rms) of Zernike mode 5 present. This follows the predictions made for the contrast reduction of a point in a volume for random aberrations (see Fg. 3.6).

In addition to the simulations in Fg. 3.7 above, Fg. 3.8 shows two images taken using a two-photon microscope of a fixed *Drosophila* brain. Fg. 3.8(a) shows an xy slice approximately $50\mu m$ from the surface without significant aberration (this was achieved through the use of adaptive optics to correct for the aberrations). Thin, line-like structures are visible, passing between point- and larger volume-like structures, all visible against the (volume-like) background fluorescence. Fg. 3.8(b) shows the same xy slice but in the presence of aberrations (induced by the layers of brain of varying refractive index through which the excitation beam passes). As predicted by Fg. 3.6, the contrast between the smaller, point- and line-like structures and the volume-like background sig-

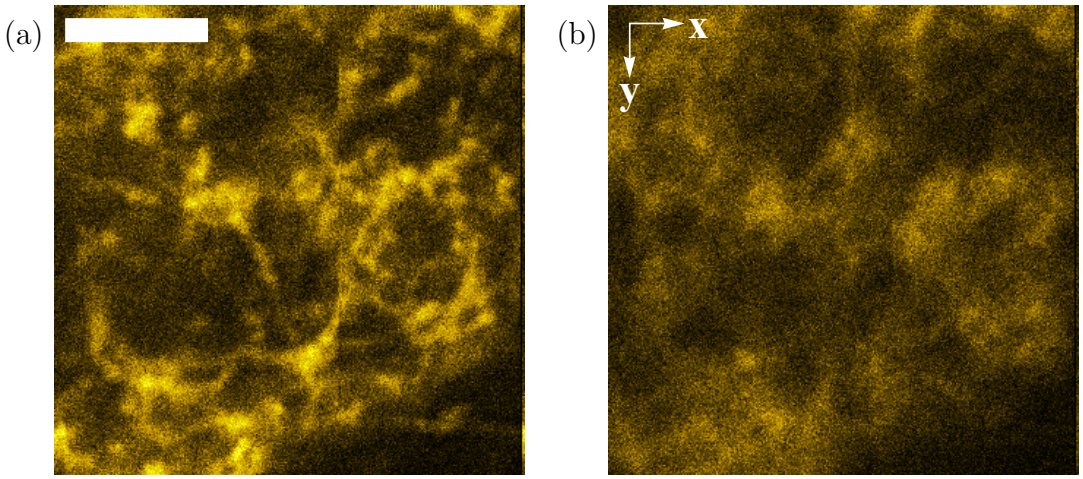


Figure 3.8: *xy images from two-photon microscope of fixed Drosophila (commonly know as the 'fruit fly') brain at approximately* $50\mu m$ *from the surface. Images shown without significant aberration (a) and with aberrations (b). Scale bar is* $5\mu m$.

nal within the *Drosophila* brain are worst affected. There is still a visible fluorescent background, but the small point- and line-like structures have lost their contrast with the background fluorescence and are effectively invisible. Only the largest volume-like structures are distinguishable from the background. This goes to confirm that the modelling and predictions made mathematically hold for a real optical imaging system.

3.8 Conclusions

We have shown the variations in effects that aberrations have on conventional, confocal and two-photon fluorescence images for different specimen structures and in particular point-like, linear, planar and volume structures. Whilst it is well known that aberrations reduce the on-axis intensity of microscope images, we have shown here that they affect the images of different specimen structures to varying extents. The calculations show that the larger the structure is dimensionally, the less sensitive the corresponding on-axis image intensity is to the presence of aberrations. Point-like structures are worst affected, giving the lowest relative on-axis intensity in the presence of aberrations, whilst volume-like structures are the least affected, giving the highest relative on-axis intensity.

The contrast between different structures was also shown to be affected by aberrations and the differing contrast causes some fine detail of images to effectively disappear

without significant reduction of the background intensity. An important consequence of this phenomenon concerns the effect of aberrations on the visibility of small structures in the presence of larger structures. Such situations frequently occur in biological imaging where fine, low-dimensional features are embedded in a larger, higher-dimensional structure. An example of this would be point-like objects situated within a background volume fluorescence. As the aberration amplitude increases, as might happen for example when focussing deep within a specimen, the volume-like background will retain much more of its brightness than the smaller point-like structures. Eventually, the point-like structures would become effectively invisible as their brightness becomes insignificant compared to the background. This would occur even though an appreciable background would still be visible in the images. This matches experimental observations of the reduction in contrast of small objects in a thick fluorescent specimen [Débarre et al., 2009]. This behaviour is particularly important to consider when developing a sensorless aberration correction routine. In the case where image brightness is used as the correction metric, it may be possible to correct for aberrations such that the background fluorescence is increased, so satisfying the correction metric, but the contrast of e.g. point-like structures with the background is not increased. In this case, it may be necessary to include another factor such as image sharpness in the correction metric, since this would be improved by an increase in the contrast of different structures.

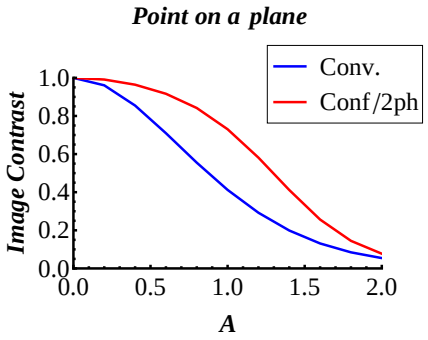


Figure 3.9: *The variation of image contrast in conventional (Conv.) and confocal or two-photon (Conf/2ph) microscopes as a function of aberration amplitude, A, for point specimen structures superimposed on plane specimen structures in the focal plane when aberrated by a random selection of Zernike modes.*

The comparison of the conventional microscope with the confocal or two-photon

microscope is emphasised in Fg. 3.9, where the image contrast of a fluorescent point superimposed on a fluorescent plane (both situated in the focal plane) is plotted for a conventional and confocal or two-photon microscope. The image contrast is more significantly affected in the case of the conventional microscope than the confocal or two-photon for all modes presented and particularly so at lower aberration amplitudes. This clearly demonstrates the significant advantage of using confocal microscopes over conventional instruments when aberrations are present.

Chapter 4

Deformable mirror training

Deformable mirrors are essential components of adaptive optical systems, whether to correct for aberrations in microscopy [Zhu et al., 1999a] or other areas of photonic engineering such as micron-scale laser fabrication systems, where the effect of aberrations on these systems is increasingly detrimental with more complex fabrication requirements [Huot et al., 2007, Thomson et al., 2008]. The shape of a deformable mirror (DM) is controlled by the application of forces to the reflective surface by an array of actuators. In practice, it is desirable not to drive the individual actuators directly, but instead address the actuators collectively, as a set of modes. When controlling the shape of the DM to correct for aberrations, using a well-chosen set of mirror modes can greatly enhance the efficiency of the correction. In this chapter, a variety of methods are shown to determine mode shapes for DMs. Firstly, by using the membrane equation to model the DM surface, theoretical mode shapes are calculated that are specific to the particular DM being modelled. Using these mirror modes as a basis, system-specific mirror modes are calculated using images taken from the microscope itself. This avoids the use of an additional wavefront sensor or interferometric setups, as are typically used to calibrate a DM [Bor, 1989, Zhu et al., 1999b, Booth et al., 2005].

4.1 Introduction

In chapter 3 we have seen how aberrations can negatively affect the quality of an optical focus or an image in a microscope, whilst in chapter 2, it was outlined how adaptive optics can be used to correct for the aberrations and help restore the optical performance. Therefore, it is desirable to introduce an adaptive element such as a DM into many microscopes and other optical systems. However, the control of a DM to correct for aberrations is a non-trivial task. For example, a typical aberration correction routine in an adaptive microscope system involves taking an initial image, measuring the aberration present (either through direct [Booth, 2003] or indirect [Murray et al., 2005] methods) then adjusting the DM to compensate for the aberrations present.

The shape of the surface of a DM can often be described as the superposition of the influence function of each actuator. If we make the assumption that the DM is controlled by linear actuator control signals, it is possible to describe the phase on a DM, $\Phi(\mathbf{r})$, as the linear sum of the mirror actuator influence functions:

$$\Phi(\mathbf{r}) = \sum_{\mathbf{i=1}}^{\mathbf{N}} \mathbf{c_i}\phi_{\mathbf{i}}(\mathbf{r}) \tag{4.1}$$

where N is the number of actuators, c_i is the control signal, $\phi_i(\mathbf{r})$ is the influence function for the ith actuator and $\mathbf{r}$ is the position vector of the ith actuator in the pupil plane. Furthermore, it is possible to describe this same mirror phase $\Phi(\mathbf{r})$ as the sum of a set of orthogonal modes:

$$\Phi(\mathbf{r}) = \sum_{i=1}^{M} a_i X_i(\mathbf{r}) \tag{4.2}$$

where M is the total number of modes and a_i is the mode coefficient for the ith mode, X_i. From Eq. 4.1 and Eq. 4.2, we can define a transformation matrix relating the influence function control signals (c_i) to the aberration mode amplitude coefficient (a_i):

$$\mathbf{c} = \mathbf{Ba} \tag{4.3}$$

where $\mathbf{B}$ is the $N \times M$ transformation matrix and $\mathbf{c}$ and $\mathbf{a}$ have elements c_i and a_i

respectively. Since the deformation modes X_i are derived from the influence functions ϕ_i, the number of modes must equal the number of actuators, i.e. $N = M$ [Thayil and Booth, 2011].

When using a direct aberration measurement, e.g. a wavefront sensor, the aberrations are often reconstructed in terms of Zernike modes. The corresponding Zernike modes will then be applied to the DM. However, due to the finite number of actuators present, the deformations that are possible with the DM are limited by the shapes of the influence functions. It follows that the Zernike polynomials cannot be reproduced perfectly by a DM. Therefore, it is highly likely that in performing any correction using these modes, additional aberrations will be introduced during the correction routine, so affecting the effectiveness of any correction routine. When performing aberration correction using an indirect method of aberration measurement, the aberration measured is exactly that produced by the mirror and there is no additional source of aberrations to be introduced by the system. If the modes produced are not orthogonal (which would be the case when the modes produced are not those desired e.g. when reproducing Zernike polynomials on a DM), then when each additional mode is corrected, previously corrected modes will lose their optimised shape due to mode crosstalk. This will again result in the necessity of additional rounds of aberration correction, or even the possibility of failure to converge. This reduction in both the speed and efficiency of the aberration correction is not ideal, but on their own may be acceptable. However, the potential of failure to correct for aberrations certainly is not. Therefore, efficient aberration correction is desired, for which a well-chosen set of basis modes is a necessity.

When using a DM with a continuous, deformable, membrane surface, the physical structure results in crosstalk between actuators, since the influence function for each actuator affects an area not restricted to the region directly over that actuator, but one spread across the entire mirror. This is not a problem for segmented DMs where each actuator is independent of the adjacent actuator. A second problem that affects all designs of DMs is the crosstalk between the modes used to control the DM shape in the way that they affect for example image quality. Because of this (and the desire

for efficient aberration correction routines) it is preferable to train a DM to produce orthogonal modes. Various different methods have been employed in the training and control of deformable mirrors [Zhu et al., 1999a, Booth et al., 2005, Stewart et al., 2007].

Two methods of DM training are presented here. The first is a method used to create empirical, orthogonal, system-specific mirror modes that will be optimal in correcting image-based aberrations. These modes would be useful when correcting for aberrations when imaging (but not restricted to) biological specimens. The second is for a scenario where the aberration phase to be corrected is known and the DM can be trained to reproduce this shape. For example, this may be for correcting depth-dependent aberrations in a material with uniform refractive index.

The first method is achieved by modelling a set of orthogonal, mirror-specific modes from the influence functions of the mirror. From an appropriate image set, the displacement introduced by each mirror mode is calculated and used to create true displacement modes. From the information gathered it is possible to produce a displacement-free orthogonal set of system-specific mirror modes to be used for optimised correction procedures. In the second scenario, where the aberration is known, the DM is trained by correcting for the phase of the known aberration. By imaging the focal spot whilst under the influence of the aberration, the shape of the DM required to correct for this phase can be determined.

4.2 Theoretical mirror modes

The target of the following section is to produce a set of orthogonal modes that can be reproduced by the DM used for aberration correction. To do this, firstly an approximate mechanical model is used to represent the DM. From this, the mirror influence functions ($\phi_i(\mathbf{r})$, as defined in Eq. 4.1) are derived as a basis set of modes from which an orthogonal set of modes ($X_i(\mathbf{r})$, as defined in Eq. 4.2) can be derived. The definition of "orthogonal" may depend on the adaptive optics system used, but here the same definition of orthogonality is used as that used to derive the Zernike polynomials.

4.2.1 Mirror modelling

The method first used in [Paterson et al., 2000] demonstrated one technique for modelling a membrane mirror, specifically the OKO DM, and produced a set of orthogonal modes using the mirror influence functions. This was also demonstrated by [Wang and Booth, 2009] and [Thayil and Booth, 2011] for the Multi-DM from Boston Micromachines and MIRAO 52-e from Imagine Optic respectively. Each of the OKO, Multi-DM and MIRAO mirrors exhibited distinct orthogonal modes (despite using the same modelling technique) as the DMs all have different properties (i.e. number of actuators, layout and size). Therefore the influence functions, and, consequently, the mirror modes produced are also unique to each DM. This method is once more presented here, this time applied to the Hi-Speed DM69-15 from ALPAO to create a new and unique set of orthogonal modes from its influence functions.

The influence functions of the ALPAO Hi-Speed DM69-15 DM were modelled by using the membrane equation (Eq. 4.4) to calculate the shape of the membrane when a voltage is applied to each actuator of the DM [Grosso and Yellin, 1977]. The membrane equation is defined below:

$$\nabla^2 z = -kV^2 \tag{4.4}$$

where ∇ is the gradient operator, z is the membrane displacement, k is a constant and V is the voltage applied to an actuator. Eq. 4.4 is only a good approximation for the membrane mirrors, as the deformable membrane does exhibit some stiffness and also because the underlying actuator structure restricts a full range of motion. However, for smaller deformations of the DM this model does offer a very good first approximation. Fg. 4.1 shows the influence functions modelled for each actuator of the mirror:

Fg. 4.1 shows the effect of each actuator on the mirror membrane, i.e. when zero voltage is applied to every other actuator. The resulting influence functions looked similar to that expected for this type of DM, suggesting that the modelling, whilst unlikely to reproduce exactly the mirror influence functions, is able to produce shapes that model reasonably well the deformations of the DM. Orthogonalisation of the influence functions using singular value decomposition allowed the deformation modes to be obtained.

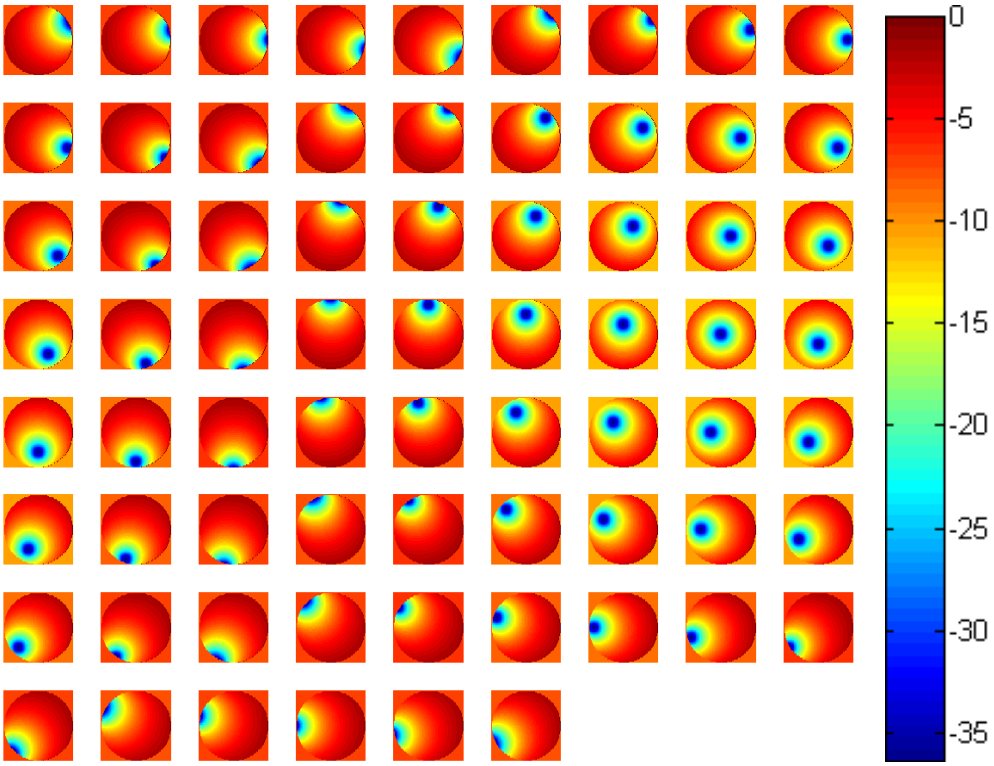


Figure 4.1: *Modelled influence functions for each actuator of the ALPAO Hi-Speed DM69-15 deformable mirror. The resulting distortion is shown with an arbitrary scale.*

These eigenmodes are the new mirror-specific basis modes, from which the control matrix **B** (see Eq. 4.3) can be defined.

The normalised eigenmodes for the ALPAO DM are shown in Fg. 4.2. In comparing these to the Zernike polynomials (see e.g. Fig. B.1), it is possible to see many similarities. Across the top row, the modes bear a very strong resemblance to Zernike modes tip, tilt, defocus, astigmatism one and two, trefoil one and two and coma one and two. This is very useful for the correction of aberrated microscopes, since it is common to describe aberrations using these Zernike modes and the fact that the mirror is able to produce very similar modes makes it much easier to draw parallels with the Zernike mode set.

These eigenmodes represent a new set of mirror modes (represented by X_i, see Fg. 4.2) that are both orthogonal and closely reproducible by the ALPAO DM. These modes can be used to shape the DM.

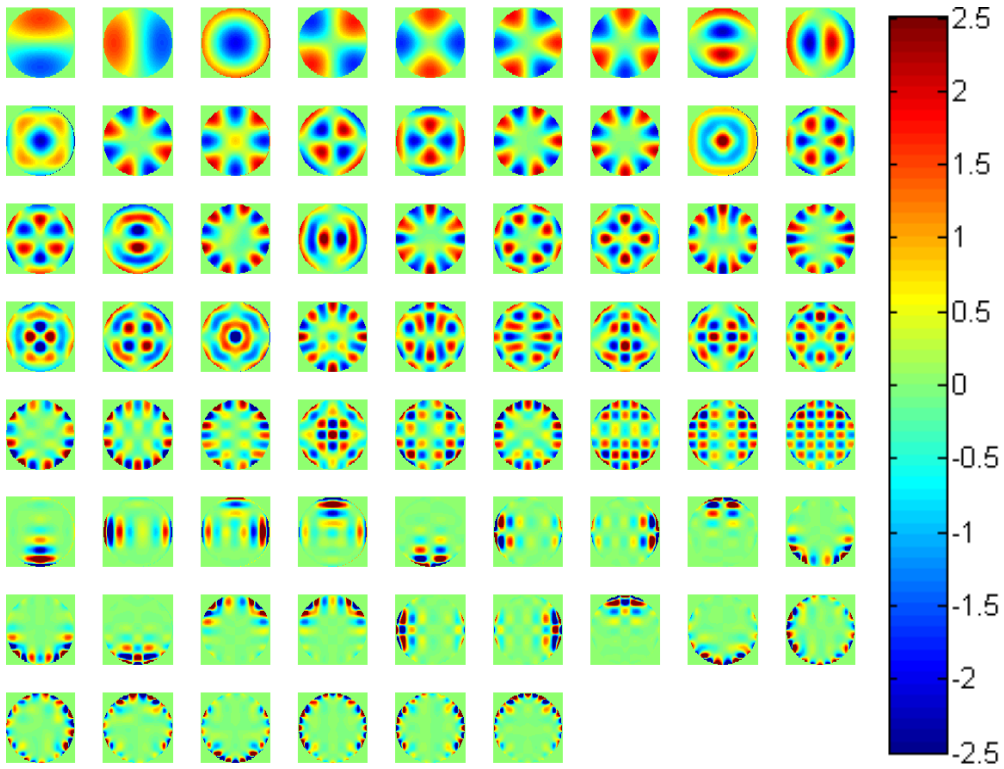


Figure 4.2: *Normalised eigenmodes X_i for the ALPAO Hi-Speed DM69-15 deformable mirror, from eigenmode 1. This is generally referred to as mirror mode 2, in equivalence with the well-known single-indice Zernike mode set.*

4.3 Empirical mirror modes

Having calculated the theoretical modes for the ALPAO Hi-Speed DM69-15 DM, the mirror was built into a two-photon optical microscope setup. By imaging the surface of the DM onto the back aperture of the objective lens, any deformation applied to the DM would result in a phase being applied to the illumination wavefronts in the pupil plane. It is possible to use the microscope in this way to perform aberration correction for specimens using a set of mirror modes such as the Zernike polynomials or the theoretically derived modes derived in Section 4.2 above. However, practically this is not ideal. A significant source of aberration in microscopes is system-induced aberration, namely from the alignment of the setup. If the mirror is perfectly centred and imaged onto the pupil of the objective lens, then the ideal set of modes to use for aberration correction would be, for this DM, the theoretical modes, since they would be perfectly orthogonal and introduce no phase to the pupil other than that which they were intentionally applying and correcting for. However, when building a custom

microscope, both the lateral and axial positioning of any optical element is a non-trivial task, therefore it is only reasonable to expect some error. Furthermore, it is extremely difficult to perfectly image the active area of the DM to the back aperture of the objective lens, since off-the-shelf lenses, with a limited range of focal lengths, are typically used to build such a microscope. To reduce (and potentially eliminate) this error, the calibration procedure outlined in [Thayil and Booth, 2011] (which was applied to the Imagine Optic MIRAO 52-e DM in a harmonic generation microscope) was utilised and modified for the ALPAO Hi-Speed DM69-15 DM and two-photon microscope used here.

In an optical system that requires 3D precision, whether for imaging or fabrication, it is important that the adaptive optics do not introduce focal shifts. Any set of modes used should therefore not contain any components that create these shifts. These shifts would be introduced by displacement modes, tip, tilt and defocus. In a low NA system the defocus can be modelled approximately as a quadratic phase, though this does not hold for high NA systems. By imaging a specimen using a set of basis mirror modes, the displacement modes (tip, tilt and defocus) can be empirically derived. Using these, it is possible to remove any displacement components from the other basis modes and create a displacement-free set of orthogonal mirror modes, specific to the microscope in which they were derived. A control specimen was imaged in the presence of each of the basis modes X_i in turn to determine the presence of displacement present in each of these modes. For this demonstration, the mirror modes chosen were the theoretical modes X_i shown in Fg. 4.2, but any set could be used including Zernike polynomials or even the mirror influence functions shown in Fg. 4.1.

The DM calibration procedure is shown in Fg. 4.3. The method developed in [Thayil and Booth, 2011] used a three-dimensional image stack, $I_0(x, y, z)$, and cross-correlated this with a second stack, $I_1(x, y, z)$, which was acquired with amplitude a of mode X_i applied, to determine the x, y and z displacements. A correlation is defined in one dimension in Eq. A.4, and is rewritten in three dimensions as:

$$I_0(x, y, z) \otimes I_1(x, y, z) = \int I_0(x + x', y + y', z + z') I_1(x', y', z') \mathrm{d}x' \mathrm{d}y' \mathrm{d}z' \tag{4.5}$$

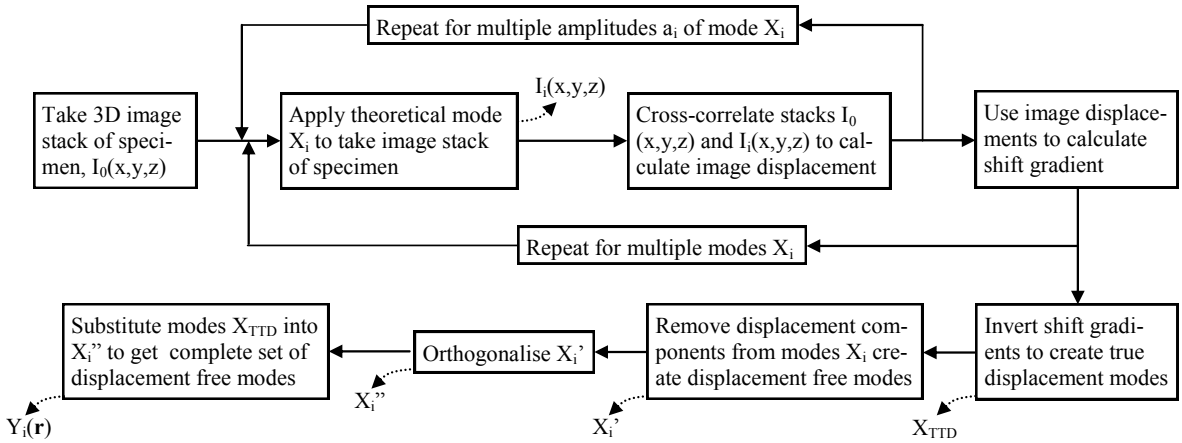


Figure 4.3: *A flowchart displaying the process of creating empirical, system-specific mirror modes* ($Y_i(\mathbf{r})$) *from a starting set of basis modes* ($X_i(\mathbf{r})$).

However, it is possible to perform a similar process that requires a greatly reduced volume of data. In order to determine the three-dimensional mirror mode-induced displacement of a specimen, if a specimen with a regular structure is chosen (such as a single bead), all that is required are two two-dimensional slices: one slice in the xy plane (which can provide the x and y image shifts) and a second in the xz or yz plane (which can provide the z shift). Mathematically, these images can be reduced further to three line scans along each of the axes, but for practical, noise-reduction purposes it was found to be a more robust measurement if the scans had a finite width, so two two-dimensional slices were used. In Fg. 4.3, these two slices are still referred to as $I_i(x, y, z)$ for generality.

Having taken the unaberrated image slices $I_0(x, y, z)$, a unit amplitude of one mirror mode was applied to the DM and the slices $I_1(x, y, z)$ imaged. $I_0(x, y, z)$ and $I_1(x, y, z)$ were then cross-correlated to calculate the image displacement introduced by the DM mode. Using the same mirror mode, further slices were taken and the image displacement calculated using the cross-correlation of images. Having taken measurements for multiple amplitudes of the mode, the shift gradient introduced by this mirror mode was determined. This process was then repeated for a set of the lower order mirror modes (see Fg. 4.4). From the set of shift gradients, modes exhibiting purely x, y and z displacements were calculated (labelled X_{TTD} in Fg. 4.3). Using the shift gradients once more, the displacement components were removed from the mirror modes, producing a set of displacement-free modes, X_i'. These modes were then orthogonalised to ensure no

crosstalk between modes, and the displacement modes X_{TTD} were finally combined to create a complete set of modes including the pure tip, tilt and defocus modes, labelled $Y_i(\mathbf{r})$ in Fg. 4.3. The non-displacement modes in the set $Y_i(\mathbf{r})$ will now affect only the image quality without any additional image displacement. This is ideal when performing aberration correction in a microscope, to ensure there are no additional image shifts when measuring the correction metric. This new set of modes can now be used with the DM to correct for pupil phase aberration with the confidence that no mode other than the designated displacement modes will introduce any image displacement.

4.3.1 Empirical mirror modes for a two-photon microscope

In order to apply the above procedure to the two-photon microscope with the ALPAO DM built in, a suitable specimen was required for the image based displacement measurements. A suitable bead size would be much larger than the focal spot diameter, but much smaller than the maximum field size. For this, Eq. 2.13 can be utilised, which has a full-width-half-maximum (FWHM) at $\nu = 1.616$. Using the definition for ν given by Eq. 2.10 and the definitions $NA = n \sin \alpha$ and $n = 1.33$ (for water immersion objectives, or $= 1.5$ for oil immersion objectives), we can state that:

$$\text{Focal spot diameter} \approx \frac{\lambda}{2NA} \tag{4.6}$$

and so for the two-photon microscope we can write:

$$\text{2-photon focal spot diameter} \approx \frac{850nm}{2 \times 1.33} \approx 0.32\mu m \tag{4.7}$$

Therefore beads of approximately 10μm diameter were used since they would be easily resolved.

Images were taken and cross-correlated to give the image shifts for a subset of the basis modes (X_i). Fg. 4.4 contains plots which show how the image shift varied along each axis for each basis mirror mode tested. Using Fg. 4.5 as a reference, it is possible to distinguish the significant causes of displacement. The shift along the x-axis (Fg. 4.4(a))

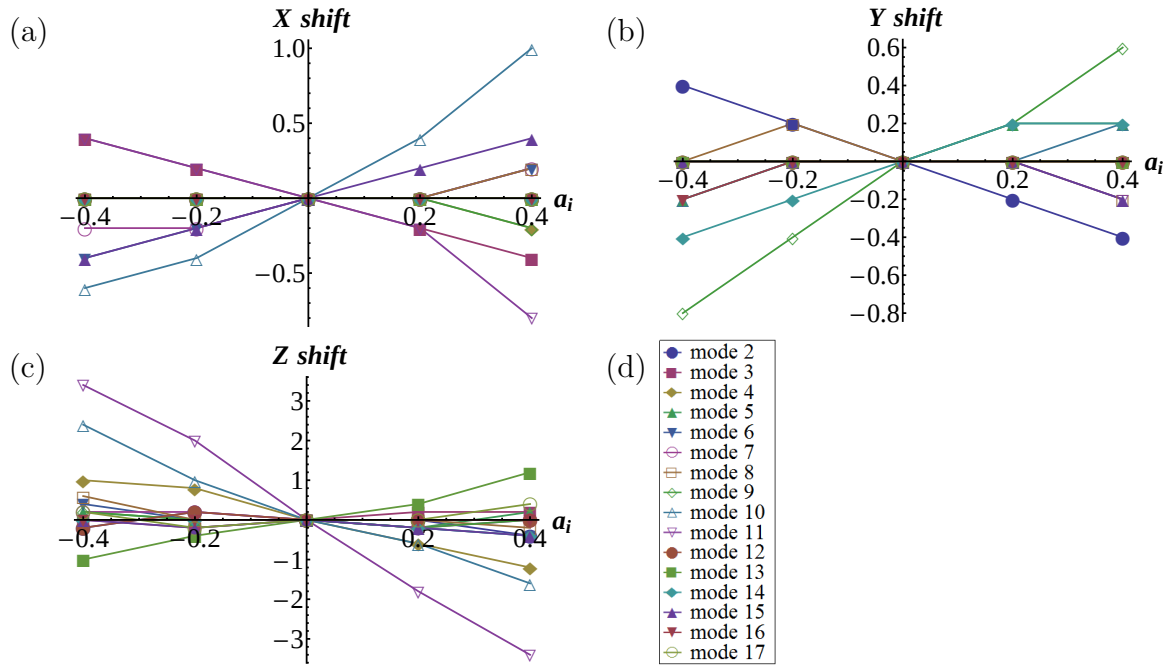


Figure 4.4: *The plots of image shift magnitude against aberration mode amplitude for each mirror mode, X_i. Shown are the plots for the shifts along each the x-axis (a), y-axis (b) and z-axis (c). (d) shows which line represents the results for which mirror mode X_i.*

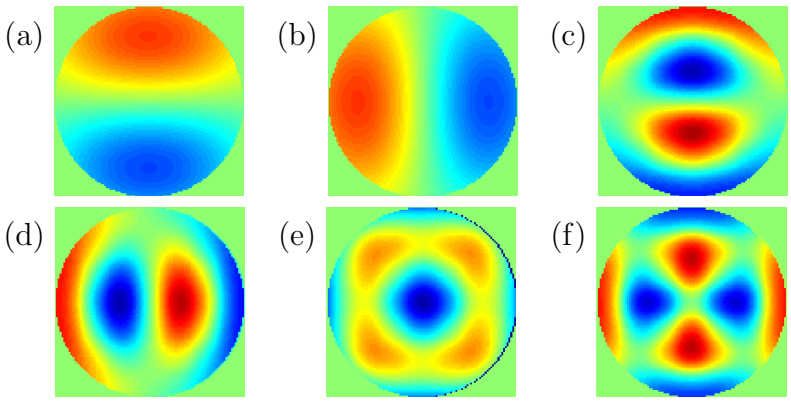


Figure 4.5: *Enlarged images of the significant modes from the basis set (the complete set is shown in Fg. 4.2). Modes shown are 2 (a), 3 (b), 9 (c), 10 (d), 11 (e) and 15 (f).*

is dominated by modes 3 and 10 (Fg. 4.5(b) and Fg. 4.5(d)), with modes 11 and 15 (Fg. 4.5(e) and Fg. 4.5(f)) also appearing significant. Mode 3 is a tilt-like mode and 10 is coma with the same directional symmetry, so it is understandable that these may introduce x-shift, particularly, in the case of the coma, if the image of the DM overfills the objective pupil and so is clipped by the objective back aperture, limiting the extent of the DM's active area. Modes 11 and 15 also share the same symmetry but have additional symmetry along the perpendicular axis, so these should not be significant,

unless the DM is not imaged centrally in the objective pupil. Equivalently, the y-axis shift (Fg. 4.4(b)) is dominated by modes 2 and 9 (Fg. 4.5(a) and Fg. 4.5(c)), which are identical to 3 and 10 but rotated by 90 degrees, matching the displacement direction. The magnitude of the modes contributing to y shift is smaller than those contributing to x shift, so it seems that, if the mirror is not centrally imaged onto the objective pupil, that the main offset is in the x direction. The axial shift (z shift, Fg. 4.4(c)) is dominated by mode 11 which, whilst it does not have perfect rotational symmetry, is the mode most similar to the spherical aberration, which would be expected to feature in any axial image displacement with the defocus mode dominating. However, if the image of the DM is clipped by the objective aperture (as postulated previously), then the spherical aberration would exhibit a component similar to defocus and so would then dominate.

From these shift plots, it is possible to find the total displacement along each of the Cartesian axes and so produce the system specific displacement modes. The normalised empirical displacement modes are shown in Fg. 4.6. The fact that they are all off-centre

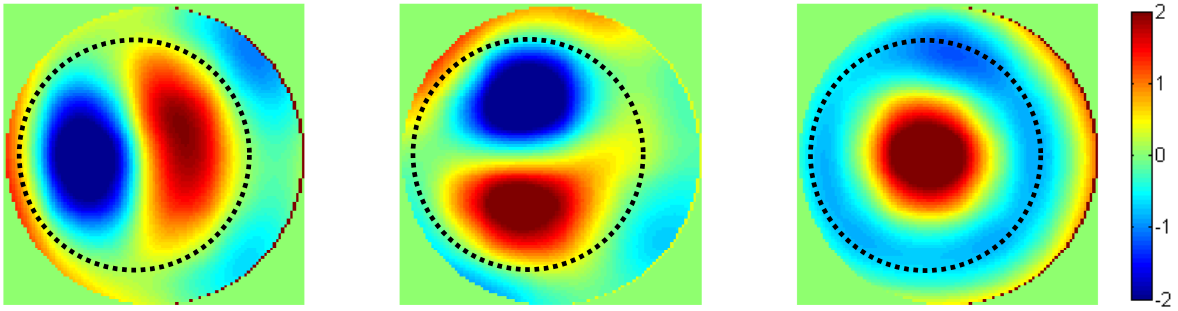


Figure 4.6: *The empirically calculated mirror modes for the tip (left), tilt (middle) and defocus (right) modes for the ALPAO Hi-Speed DM69-15 deformable mirror in a two-photon microscope setup. The black dashed line shows the predicted actual illumination region of the mirror. Note that these plots are approximations to the shape of the DM based upon the assumed mechanical model, so are only a rough guide to the true shape of the DM.*

to the left suggests that the mirror was not centrally imaged, as was suggested by the results in Fg. 4.4(a). The defocus mode seems to resemble a spherical aberration, rather than the expected defocus. If this is to be believed it would suggest that the mirror image is also clipped by the objective aperture (as implied by the results in Fg. 4.4(c)), which would limit the active region and so make it look more like the known defocus

shape, as illustrated in Fg. 4.6. This is an inherent benefit of the method, since small alignment errors are compensated for. Having determined the empirical displacement modes (shown in Fg. 4.6), they were then subtracted from the basis modes shown in Fg. 4.2 to leave the system-specific displacement-free aberration modes, shown in Fg. 4.7.

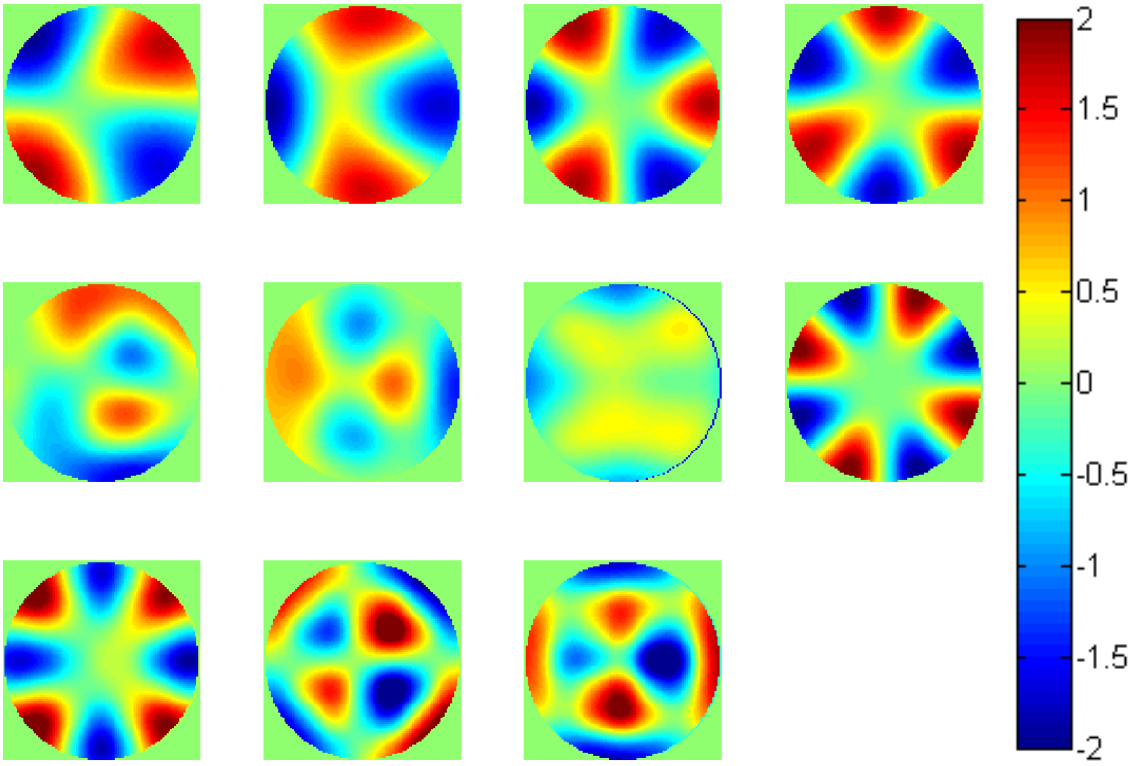


Figure 4.7: *The first 11 empirically determined aberration modes for the two-photon microscope with the ALPAO Hi-Speed DM69-15 deformable mirror.*

The aberration modes empirically determined, shown in Fg. 4.7, remain generally very similar to the basis modes from which they are derived. The fact that the mirror appears to be positioned slightly off-centre has led to some distortion in the direction of the offset in the first four and last four of the modes. The two coma-like modes and the spherical-like mode have been significantly affected however; the coma-like modes have retained very little of their original shape and the spherical-like mode has been largely flattened. This can be accounted for if the previous postulations are true, that the image of the mirror overfills the pupil of the objective, and so the outer region is cut off. However, whilst they may appear to bear little resemblance to the modes that are being replicated, when using these modes to correct for aberrations in a specimen they do show efficient aberration correction, as demonstrated below.

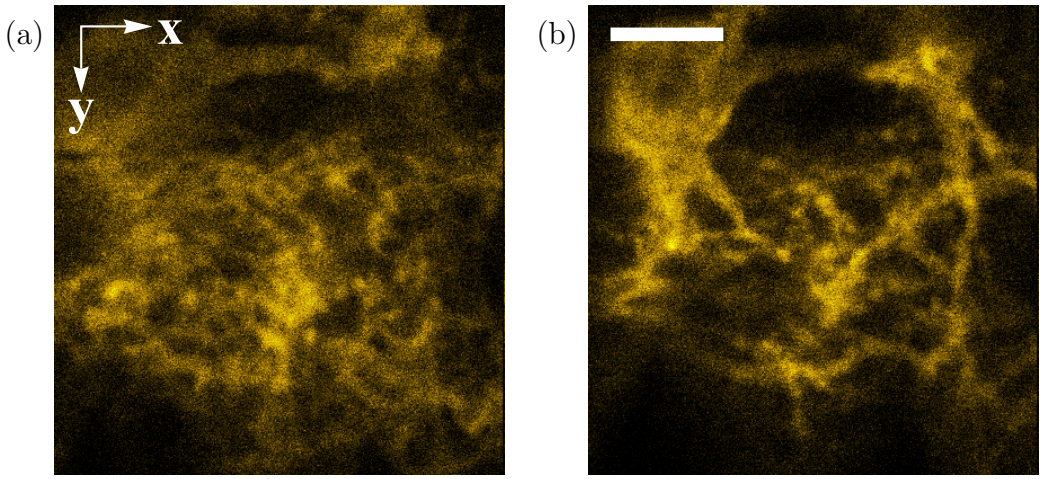


Figure 4.8: *xy images from two-photon microscope of fixed Drosophila (commonly known as the 'fruit fly') brain at approximately* $50\mu m$ *from the surface. Images shown without aberration correction (a) and with aberration correction (b), after a single correction routine using empirically derived mirror modes shown in Fg. 4.7. Scale bars* $10\mu m$.

Fg. 4.8 shows images demonstrating the aberration correction using the two-photon microscope with the ALPAO DM, with the correction routine using the empirically derived modes discussed previously. The correction routine is described in detail in Appendix C. Fg. 4.8(a) shows an image of a region within the *Drosophila* ('fruit fly') brain at approximately 50μm from the surface. Due to the depth of the imaged region, it is heavily aberrated since the illumination must pass through a thick layer of tissue before it is focussed. By performing a single aberration correction routine, the average brightness of the image can be significantly improved, as demonstrated in Fg. 4.8(b). This shows the same region of the *Drosophila* brain as Fg. 4.8(a). The average signal intensity from the image employing aberration correction is greatly enhanced, with the cellular structure having a much greater contrast with the background and further structures have become visible. Due to the depth of imaging, it is likely that a significant aberration present is spherical aberration. From Fg. 4.7 it seemed that the spherical-like mode had been cancelled out. However, given the improvement demonstrated in Fg. 4.8 and the depth of the image, it suggests that this mode is still contributing to some extent, possibly even significantly.

4.4 Training DM by nulling SLM applied phase

The modes calculated empirically in Section 4.3 are ideal for performing adaptive aberration correction of unknown aberrations. However, there are scenarios where the predictive correction of known aberrations is preferable. One example of this is in an optical fabrication system where structures are created within a substrate whose refractive index is known (see Fg. 4.9). By using the numerical aperture (NA) of the objective lens and the refractive index of both the substrate and the immersion medium, the depth-dependent aberrations (which are typically the most significant of the aberrations present) can be calculated [Booth et al., 1998]. In the previous method, the exact form of the modes produced by the DM was not known, although their relative orthogonality properties were defined. As the form was not known it is not possible to use this method to produce a desired phase function.

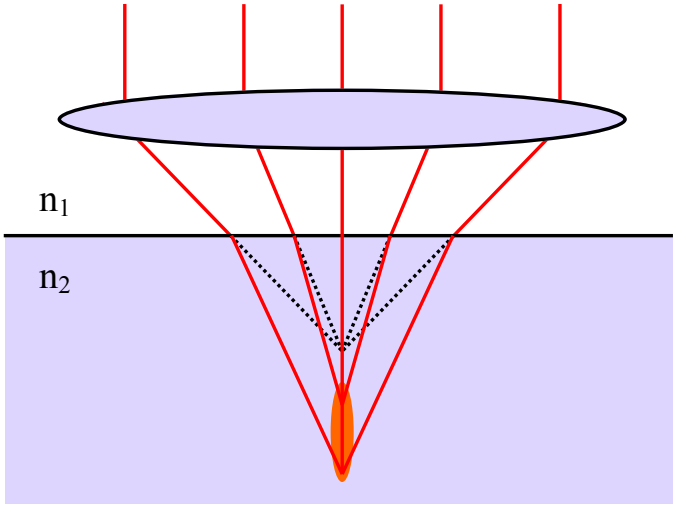


Figure 4.9: *A diagram to illustrate the problem of a refractive index mismatch. When a laser is focussed into a substrate, if the immersion medium, n_1, has a different refractive index than the substrate, n_2, then refraction will occur at the boundary. In the diagram, $n_1 < n_2$. The result of this is an aberrated focal spot, as shown.*

Adaptive optics integrated into laser fabrication systems have been demonstrated [Jesacher et al., 2010]. In the case where a spatial light modulator (SLM) is used as the adaptive element, having calculated the depth-dependent aberration the phase correction mask can be displayed onto the SLM. One advantage an SLM has over a DM is that it can have multiple phase masks combined such that the effects of both are applied

simultaneously. However, the more complex the phase mask is on the SLM, the more the optical efficiency is reduced and so the correction is subsequently degraded [Jesacher and Booth, 2010]. One option to improve this is to use a DM to correct for the main (e.g. depth-dependent) aberration then use an SLM to correct any additional aberration and/or display additional phase masks, so reducing the complexity of the required phase mask. Unlike the previous empirical method, the phase correction applied by the mirror must be known, so the mirror training must result in a known phase.

4.4.1 Method

An SLM can be used to apply the necessary phase from which to train the DM. By optically imaging an SLM onto the surface of a DM, it is possible to then train the DM by applying the opposite phase to that introduced by the SLM in order to minimise the residual phase. The optical setup schematic used to do this is shown in Fg.4.10.

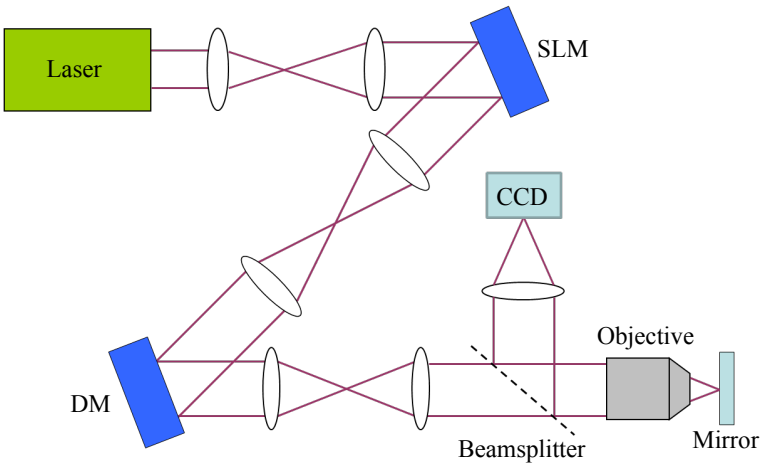


Figure 4.10: *Schematic of the DM training layout. The SLM and DM were both imaged onto the pupil plane on the objective lens. The objective focus was imaged onto a CCD camera.*

As shown in Fg.4.10, the laser was expanded to fill the SLM, which was imaged using a $4f$ system onto the DM. The DM was imaged with a second $4f$ system onto the pupil plane of the objective lens. By placing a mirror at the focus of the objective lens, the focal spot was reflected and, through use of a beamsplitter, imaged onto a CCD camera. It is necessary to pass the beam through the objective lens in order to define the aperture of the system. When a non-zero phase mask is applied to the SLM, the focal spot will be

aberrated and this is imaged by the CCD camera. By applying the equal and opposite phase to the DM, the focal spot is returned to its original, unaberrated state. In order to determine the mirror shape necessary to provide the required correction phase, whilst imaging the focal spot each mirror mode X_i (as calculated in Section 4.2) was scanned across a small amplitude range. This altered the shape and peak intensity of the focus. The peak focal intensity was measured for each mode amplitude and a Gaussian curve fitted to the results, from which the mirror mode amplitude at which the focal spot intensity was maximised was recorded. Fg. 4.11 shows an example of one such plot.

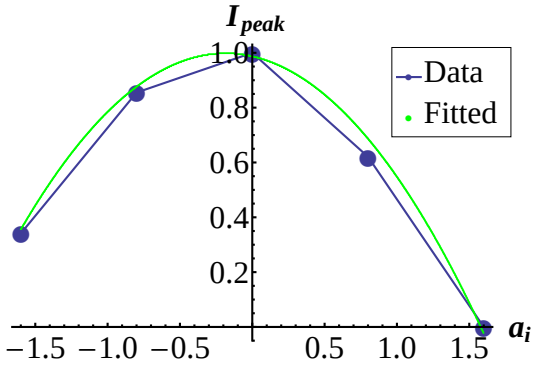


Figure 4.11: *A plot showing the measurements of normalised peak focal spot intensity, I_{peak}, against the mode amplitude, a_i (mode 4 shown here). A Gaussian curve is fitted to the data points and the centre value (μ) determined. Here $\mu = -0.03$.*

Having measuring the amplitude of one mirror mode for which the focal spot peak intensity was maximised (as demonstrated in Fg. 4.11), this mode amplitude was applied to the mirror. The process was then repeated for other mirror modes to return the focal spot to an unaberrated shape and so produce a mirror shape that exhibits the equal and opposite phase to that applied to the SLM. For this method to be efficient, it relies on the mirror modes being orthogonal and not demonstrating any crosstalk between modes. However, when performing this mirror training routine, significant and detrimental crosstalk was observed between modes X_4 and X_{13} (defocus-like and spherical-like; see Fg. 4.2). This is not altogether surprising; the central region of both exhibit a very similar shape, so if there is any slight apodisation of the beam, the two modes would look very similar. The crosstalk was quantified by measuring the peak focal spot intensity under the influence of varying amplitudes of the two modes. These

measurements are shown in Fg. 4.12(a).

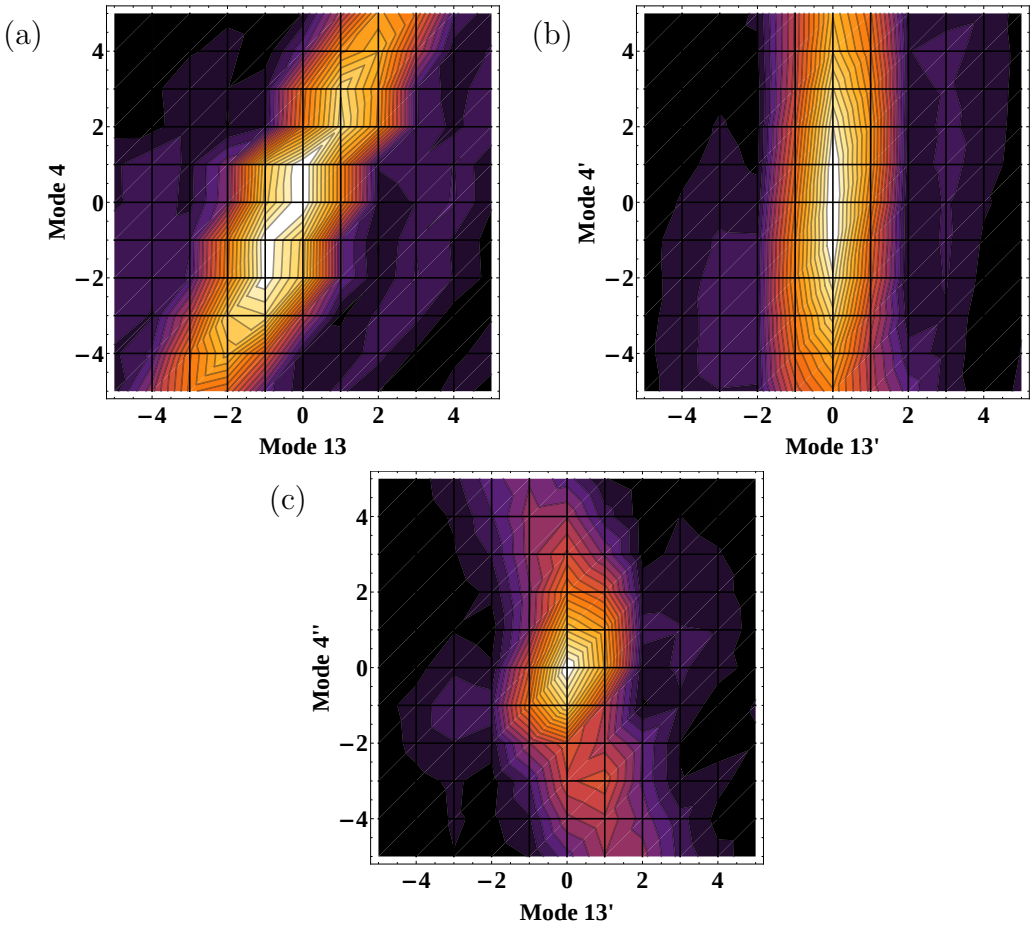


Figure 4.12: *Contour plots showing the measurements of the crosstalk between mirror modes 4 and 13 (defocus-like and spherical-like) with the original DM control matrix (a), after rotating the two modes (b) and after compressing mode 4' (c). The grid on each plot marks the points at which readings were taken.*

By plotting the contour plot (Fg. 4.12(a)), the level of crosstalk between mirror modes X_4 and X_{13} was quantified. The rows of the DM control matrix relating to these modes were rotated (using the standard rotation matrix) to remove the mode interdependence. The contour plot measured using the rotated DM control matrix (Fg. 4.12(b)) shows that there is no longer any crosstalk between the two modes. From Fg. 4.12(b), it is clear that the $X_{4'}$ aberration amplitude is much less sensitive to aberrations than that of $X_{13'}$; small adjustments in the amplitude of $X_{13'}$ from zero aberration gave a significant decrease in peak focal spot intensity, whilst a similar small adjustment in the amplitude of $X_{4'}$ did not give a similar decrease in peak focal spot intensity. Again, if there is any slight apodisation of the beam or clipping of the DM aperture, the two modes would look very

similar but with X_{13} having a much sharper gradient than X_4. This might explain why the response to $X_{13'}$ is more sensitive than $X_{4'}$. Since the DM training method requires the calculation of the mode amplitude at the peak focal spot intensity, a mode sensitive to small changes in the aberration amplitude around the peak is desired. Therefore, the DM control matrix was again adjusted to 'compress' the plot along $X_{4'}$ by scaling the corresponding values in the control matrix. The crosstalk contour plot resulting from the new, rotated and compressed DM control matrix is shown in Fg. 4.12(c). This shows that the sensitivity of $X_{4'}$ has been increased to similar levels to $X_{13'}$ and that, by using this control matrix for the DM, the training routine no longer suffers from significant crosstalk between the two modes.

4.4.2 Training results

To produce a mirror shape for depth-dependent aberration correction, the phase mask required for the SLM for aberration correction at a specific depth in a material of a known refractive index (dependent also on the immersion medium and the objective's numerical aperture) was calculated. Having focussed the focal spot onto the CCD, the phase mask for the depth-dependent aberration was applied to the SLM. Each mirror mode X_i was then corrected in turn, as illustrated in Fg. 4.11. Having performed the correction for this depth aberration, a phase mask for a second, greater depth was passed to the SLM and, using the correction parameters from the first aberration depth as a starting DM reference shape, the focal spot was corrected for the second depth by measuring the mode amplitudes that produced the maximum focal spot peak intensity. This was repeated for aberration depths from -40μm to $+40\mu$m, with a 5μm spacing. The results of the significant mirror modes from mode 2 (X_2) to mode 15 (X_{15}) are shown in Fg. 4.13.

Fg. 4.13 shows the mirror mode optimisation values for a range of depth aberrations. The amplitude of each of the lower order modes that was found to maximise the focal spot intensity is plotted. Each of these mode amplitude plots exhibited an approximately linear relationship with depth. Therefore, by fitting a linear function to these results,

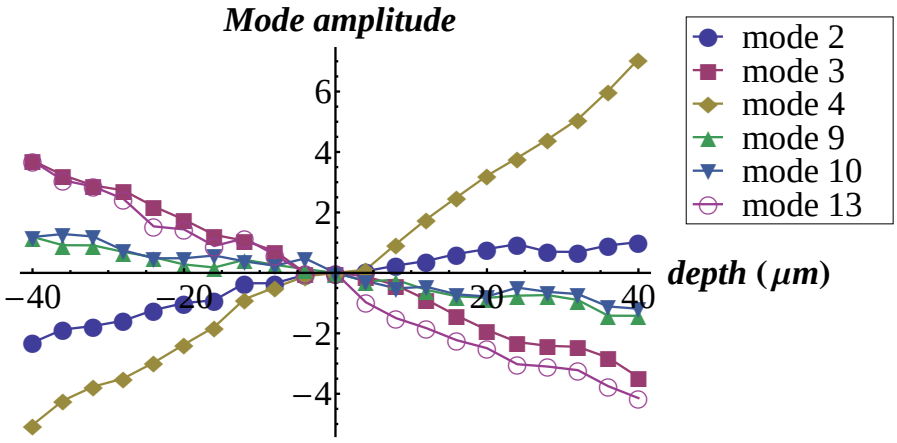


Figure 4.13: *The measured mirror mode amplitudes (a_i) found to best correct the observed focal spot for aberrations at a range of nominal depths.*

it was possible to predict the combination of mode amplitudes required for aberration correction at depths between the sampled values and beyond the measured range. From this information it was possible to create a control matrix for the DM with a single input, depth, that returns the combination of mode amplitudes required to correct for the calculated depth-dependent aberration. This new DM control matrix, **D**, can be defined as:

$$\mathbf{D} = \mathbf{B} \wedge \mathbf{G} \tag{4.8}$$

where **B** is the original control matrix (as defined in Eq. 4.3), $\wedge$ is the matrix-vector product and **G** is the vector of linear gradients, as calculated from Fg. 4.13. The new control matrix, **D**, describes the DM actuator settings at unit depth (so is a control matrix with just one mode). This can then be multiplied by the desired depth, giving the necessary actuator settings to correct for that depth. This is now not constrained to the depths tested for (as shown in Fg. 4.13) but the results can be extrapolated for any depth. This control matrix is specific to the system where the objective NA, immersion medium and substrate refractive index are known, and should also help correct for any system misalignment since the optical path used for mirror training is the same path used when fabricating structures.

Using the new, depth-dependent aberration correcting DM control matrix **D**, the

MIRAO DM could be adjusted to correct for depth-dependent aberrations. Fg. 4.14 shows the mirror shapes produced when using **D** and correcting for the aberrations caused by the refractive index mismatch from an oil ($n = 1.52$) immersion objective lens ($NA = 1.4$) focussing into a diamond substrate ($n = 2.4$) at depths of 0μm (i.e. correcting for system aberrations; Fg. 4.14(a)) and 20μm (Fg. 4.14(b)).

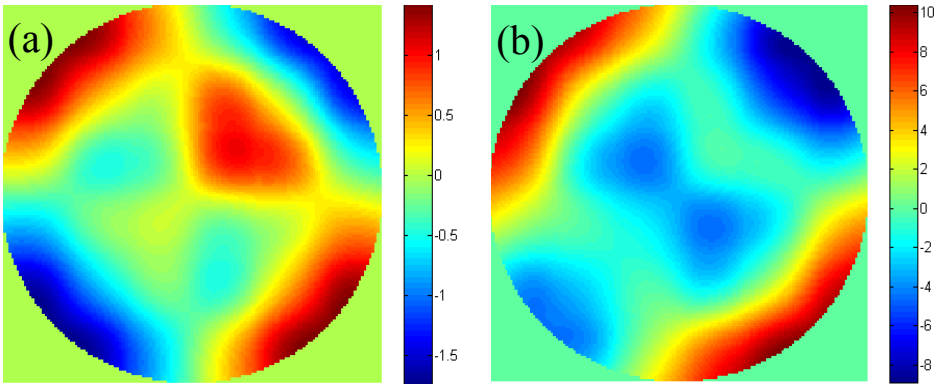


Figure 4.14: *Approximate mirror shapes determined for depth-dependent aberration correction, correcting for aberrations in diamond when using an oil-immersion objective with* $NA = 1.4$ *at nominal focussing depths of* 0μm *(a) and* 20μm *(b). The scale represents the amplitude* a_i *of the mirror modes* X_i *used to produce the new mirror shapes.*

The mirror shape in Fg. 4.14(a) shows that, in correcting for the aberrations present in the system, there was a significant amount of astigmatism present combined with some second-order astigmatism and potentially some coma. This alone should significantly improve the efficiency of the fabrication. When correcting for refractive index-induced, depth-dependent aberrations, the expected shape was a combination of mainly defocus and the spherical aberration modes. It was not clear that these were the modes being reproduced in Fg. 4.14(b), however, as it was noted in Section 4.3 it may not be easy to determine the level of mirror training success from the shape alone, it is necessary to see how it performs.

The primary purpose for this specific method of DM training was to enable controlled fabrication of graphitic structures within the bulk of diamond substrates (see Chapter 6). When focussing an amplified pulsed Ti:S laser, if the illumination intensity is great enough at the focus, the diamond structure can be permanently altered into a graphite-like phase. Since the fidelity of the focal spot is directly dependent on the aberration correction, the threshold pulse energy required for fabrication can be used as a measure

to determine the quality of aberration correction.

To measure the performance of the mirror training, the threshold pulse energy required for fabrication of graphitic structures in bulk diamond was measured at a variety of depths. This was performed for three cases: where there was no aberration correction applied; where the SLM alone was used for correction (with the mirror flat); and where the DM alone was used for correction (with no phase mask on the SLM). Fg. 4.15 shows the results of these measurements. Fg. 4.15(a) shows structures fabricated using no aberration correction (top) and when using the DM for aberration correction (bottom) viewed along the optic axis. The graphitised region for the structures created without aberration correction exhibit approximately circular symmetry around the optic axis. This was expected, since the aberrations should be most significant in stretching the focal spot in the axial (z) direction. The structures fabricated using the DM for aberration correction have lost this symmetry. Since the actuator layout of the MIRAO 52-e DM was in a square array, the structure may be expected to exhibit some slightly square-looking features. However, the shape is neither square nor circular, but an irregular shape. This suggests that the astigmatic mirror shapes shown in Fg. 4.14 are not reproducing the SLM phase mask from which they were trained. Quantitative information is displayed in Fg. 4.15(b).

Fg. 4.15(b) compares the pulse threshold energy for each of the three aberration correction scenarios tested. When there is no aberration correction applied the significance of the refractive index mismatch becomes clear. Since the focal spot becomes increasingly aberrated at greater depths, the maximum intensity at the focus is reduced resulting in the pulse threshold energy increasing in an approximately linear fashion with depth. Using the SLM to correct for these aberrations, the results suggest that it is able to correct for them by maintaining the fidelity of the focal spot and so keeping the pulse threshold energy approximately constant over the range of fabrication depths tested. Using the DM to correct for the aberrations at a low depth of fabrication (i.e. $< 100\mu$m) reduces the pulse threshold fabrication energy by approximately a half compared to the uncorrected system, but this threshold energy is approximately double that

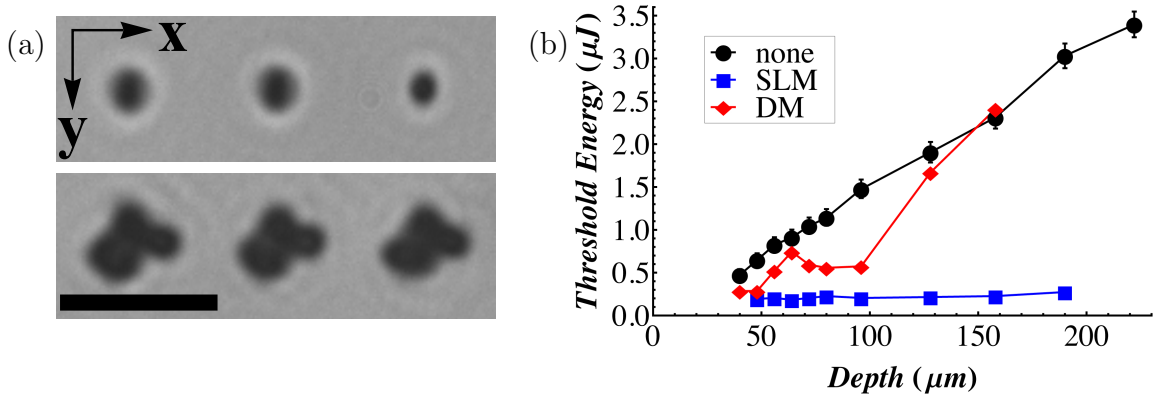


Figure 4.15: *Images showing the lateral extent of point fabrications in diamond at a depth of* $80\mu m$ *(a), made using no aberration correction with a threshold energy of* $1.14\mu J$ *(top) and using the mirror for aberration correction with a threshold energy of* $0.55\mu J$ *(bottom). Laser propagation direction is along the z-axis (i.e. into the image). Scale bar is* $5\mu m$*. Graph comparing the threshold fabrication pulse energy over a range of fabrication depths when using no aberration correction, SLM only aberration correction and DM only aberration correction (b).*

when using the SLM to correct for the aberrations. Although the mirror has introduced lateral aberration to the focal spot in comparison to the uncorrected case (see Fg. 4.14(a)), it has still had some success in performing aberration correction within a diamond substrate. This suggests that the axial extent of the fabrication, when compared with the uncorrected case, has been reduced, so increasing the intensity of the focal spot and reducing the pulse threshold energy.

4.4.3 Limitations

The DM was trained over a limited depth range ($\pm 40\mu$m nominal depth, shown in Fg. 4.13). Therefore, when correcting for any depths not in this range, the measured results must be extrapolated to determine the correct actuator values. As such, any small error in the training regime will be amplified the further from this regime the depth to be corrected for is.

As the DM was trained from the phase shape on the SLM, unless the DM reproduced the phase shape very accurately then the threshold energy will always be greater when using the DM for correction compared to when fabricating using the SLM for aberration correction. But the threshold energies shown in Fg. 4.15(b) suggest that the training

method was not very accurate. As the depth of fabrication passes 100μm (well outside the training regime), the pulse threshold energy increases to levels of the uncorrected fabrication and, if this trend is to continue, they would surpass the uncorrected threshold levels, i.e. at these depths the DM adds further aberration to the focal spot and worsens the fabrication efficiency. This behaviour is most likely due to the quality of the training routine, since any errors in each mirror mode gradient measured at the lower depths will magnify the error in the required mode value at greater depths. This seems especially likely as, for speed and convenience, the range over which the mirror was trained was up to $\pm$64μm (or $\pm$40μm nominal depth). As the mirror has performed aberration correction with some degree of success at the depths over which it was trained, this theory would seem to hold.

An additional source of error that may also affect the mirror shape when correcting for aberrations at greater depths is the precision at which the mirror is able to reproduce the desired shape. As the DM actuators move closer to the limit of their travel, it is likely that they are not able to respond in such a precise manner since they are potentially driving a membrane between each actuator to very different levels, and so additional stresses from the deformation of the membrane surface introduce a further source of error to the mirror shape.

4.5 Conclusions

This chapter has introduced two methods for training DMs, both using mirror modes derived specifically for the DM used. The derived mirror modes are required for the training methods described, but they are also useful in their own right. Rather than controlling a DM using another mode set that the DM may not be able to naturally produce (due to the number of actuators present and their layout), aberration correction routines are more efficient when using a mode set that is optimised for the DM used. However, these modes are mathematically orthogonal but, because they are used in an imperfectly aligned system with non-uniform illumination, they lose their orthogonality and as such are not ideal for aberration correction in microscopy.

The first method describes the empirical creation of novel system-specific mirror modes for both the ALPAO Hi-Speed DM69-15 DM and a two-photon microscope. These modes remove any displacement introduced by the mirror modes optimised and create true displacement modes for the setup. This process compensates for any misalignments and imperfect imaging of the DM onto the objective back aperture in the microscope setup. The resulting orthogonal mode set is efficient when used in indirect aberration correction routines and preferable to using the original mirror-specific modes. However, when the aberration is known, e.g. when performing direct aberration measurement, the modes are not useful since the phase applied is not known without further measurement.

The second method describes an iterative process of training a DM from a second adaptive element, specifically a SLM. This is used to train the DM to correct for depth-dependent aberration in an optical fabrication setup. The resulting mirror control can be used to correct for the aberrations introduced when focussing into a material with a known refractive index mismatch to the immersion medium. It is, however, limited to the specific situation for which it is trained, although clearly the training could be repeated for depth correction in other materials, or indeed for alternative modes, e.g. Zernike polynomials. The results presented show that this training method was only effective to a limited extent at lower values of depth correction within the region trained. The extrapolation to depths beyond the region trained was not successful. The likely reason is that only one xy plane of the focus was imaged when performing the correction, meaning that if the focus moved axially at all during the procedure then it would not be well imaged onto the CCD. Because of this limitation, a lot of information is lost by not imaging in three dimensions. The process involves applying a phase mask to the SLM to simulate aberrations, and in doing so stretch the focus axially. This should theoretically be compensated for in the DM training process, however, the metric used means that the DM only corrects for the aberrations in the xy plane, not axially (where the focus is worst affected). There is likely some correction of out of focus planes, but there is no way of knowing using the process described. Further work is now being performed on this technique to take images at multiple planes of the PSF and in doing so retrieve

the true phase applied by the DM [Débarre et al., 2011]. The results have so far shown this method to be extremely accurate at determining the phase applied by the DM. When compared with the technique presented here, further work would need to be done to introduce the necessary feedback from the phase retrieval to DM control, but this method looks to be a good future progression for improved DM correction.

Another possible improvement to the process described above would be to utilise the plasma generated at the focus in the substrate itself [Jesacher et al., 2010], to correct for the aberrations in a real fabrication situation rather than simulating the depth-dependent aberration on an SLM. The focal spot used for the mirror training has been defined as the reflection of the laser when focussed onto a mirror in the specimen plane. However, it has been demonstrated that light intensity from a plasma produced at the focus of an objective when fabricating in a substrate can be used as the metric from which aberration correction can be performed [Jesacher et al., 2010]. To do this, the mirror shown at the objective focus in Fg. 4.10 is removed and a substrate put in its place (the SLM is also no longer required so can too be removed). When focussing into the substrate, if the focal intensity is great enough (but before fabrication occurs) a plasma may be created. The light from this plasma can be focussed back onto the CCD, just as the reflected focal spot was previously, to perform the mirror correction as before. This technique would have the advantage that any error introduced by the SLM (e.g. misalignment, light-loss at phase wraps) would be removed. However, the limitation of only imaging one xy plane of the focal spot (or now the plasma) still applies. Furthermore, light levels from the plasma would be lower in diamond (as this setup was designed to correct for) than in the glass substrates demonstrated previously, so any measurements would suffer from increased noise levels. Therefore, it is unlikely that this change would result in a significant improvement in the training results and a more involved experimental redesign would be necessary.

Chapter 5

Aberration corrected imaging in multiphoton microscopy

5.1 Introduction

In previous chapters, the effects of aberrations in microscopy have been discussed and some methods to perform aberration correction have been explained. In this chapter, the adaptive optics methods are applied to aberration-corrected multiphoton microscopy for various applications. The effect of aberration correction is often striking. In some cases, the resolution and contrast of images is clearly improved. In other cases, the effects of aberrations are so severe that images are essentially unobtainable without aberration correction. It is only through the use of adaptive optics to correct for the aberrations that any practical imaging is possible.

The microscopes used are the two-photon microscope and the harmonic generation microscope (see Section 1.1 for microscope descriptions), which is able to detect signal from both the second and third harmonics. Images of biological specimens and other structures (e.g. waveguides) are shown.

5.2 Two-photon fluorescence microscopy

In this section, images taken with the two-photon microscope are shown. A schematic of the microscope layout is displayed in Fg. 5.1. The illumination source in the two-photon

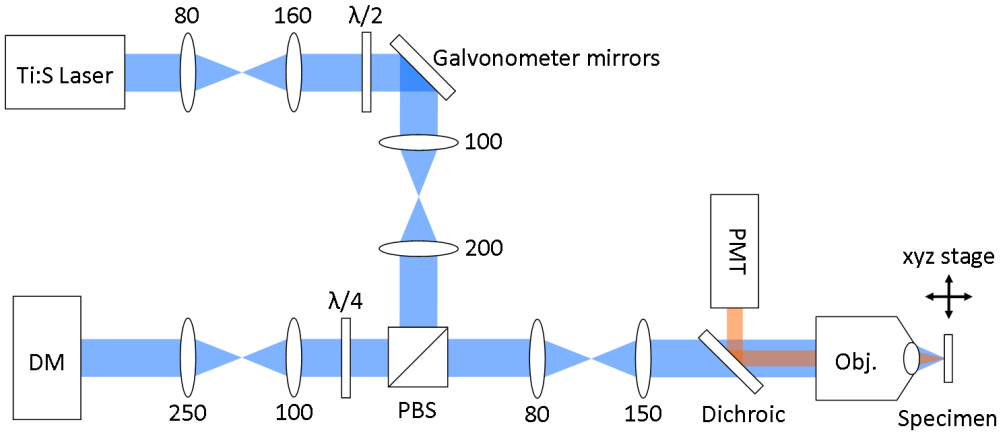


Figure 5.1: *Layout of the two-photon microscope. Ti:S, titanium-sapphire laser. $\lambda/2$, half-wave plate. $\lambda/4$, quarter-wave plate. PBS, polarising beam-splitter. DM, deformable mirror. Obj., objective lens. PMT, photo-multiplier tube.*

microscope was a pulsed titanium-sapphire (Ti:S) laser with a centre wavelength of 850nm and a pulse width of 100fs. The beam was expanded onto a pair of galvanometer mirrors, which provided lateral (x and y) scanning. The beam was again expanded before being passed through a polarising beam-splitter (PBS). The half-wave plate ($\lambda/2$) prior to the galvanometer mirrors was aligned such that all of the illumination light was directed towards the deformable mirror (DM) rather than being passed through the PBS. The beam was then expanded onto the DM, an ALPAO Hi-Speed DM69-15, such that the galvanometer mirrors were imaged onto the DM. The use of a quarter-wave plate ($\lambda/4$) converted the linearly polarised light into circularly polarised light as it passed towards the DM. As the light passed back through $\lambda/4$, it was converted back to linearly polarised light but with a polarisation perpendicular to the original illumination, so allowing it to pass through the PBS towards the objective. The beam was expanded to fill the back aperture of the objective (Zeiss Plan Apochromat, oil immersion, 63× magnification, $NA = 1.4$, or Zeiss C-Apochromat, water immersion, 63× magnification, $NA = 1.2$) such that the DM (and galvanometer mirrors) were imaged onto the objective pupil plane. The excitation was then focussed onto a specimen. Two-photon excited

fluorescence emission (at wavelengths of approximately 425nm) was collected by the objective lens and into a photo-multiplier tube (PMT) via a dichroic mirror.

Aberration correction was performed through indirect aberration measurement. Indirect measurement, where no wavefront sensor is used, can be easier to use in an adaptive optical system than direct measurement as the adaptive element is the only additional component required [Booth, 2007]. The complete process is described in Appendix C. The quality metric used was total image intensity, from which a prediction of the aberration amplitude required to correct for one aberration mode was calculated [Jesacher et al., 2009]. This process was repeated for each of the low order aberration modes. The system-specific mirror modes, determined in Section 4.3, were used for the DM modes.

5.2.1 *Drosophila* brains

Images of *Drosophila* (commonly know as the fruit fly) brain were taken using the two-photon microscope with aberration correction. These specimens are challenging to image since the particular region of interest is often many tens of microns below the surface (e.g. 10μm - 200μm) of the brain. The entire brains are typically $<$ 1mm in diameter, so it is very difficult to dissect and for any imaging the excitation beam must pass through many layers of tissue before reaching a focus. As the refractive index of the brain tissue is different to that of the oil or water immersion media and has an inhomogeneous optical structure, any resulting images are heavily aberrated. These images exhibit low spatial resolution, fluorescence brightness and image contrast. Therefore, aberration corrected microscopy is essential for the imaging of *Drosophila* brains. These images are shown in Fg. 5.2 to 5.6; further examples can be seen in Fg. 4.8.

Fg. 5.2(a) and (b) show images of a large section of a layer within the *Drosophila* brain, at a depth of $\approx 50\mu$m from the surface. Fg. 5.2(a) presents an image taken with no specimen aberration correction applied, i.e. system aberrations have been corrected for but not specimen-induced aberrations. This is an image equivalent to that from a well aligned two-photon microscope without any aberration correction. Fg. 5.2(b) is an image of the same region, but after having performed the aberration correction

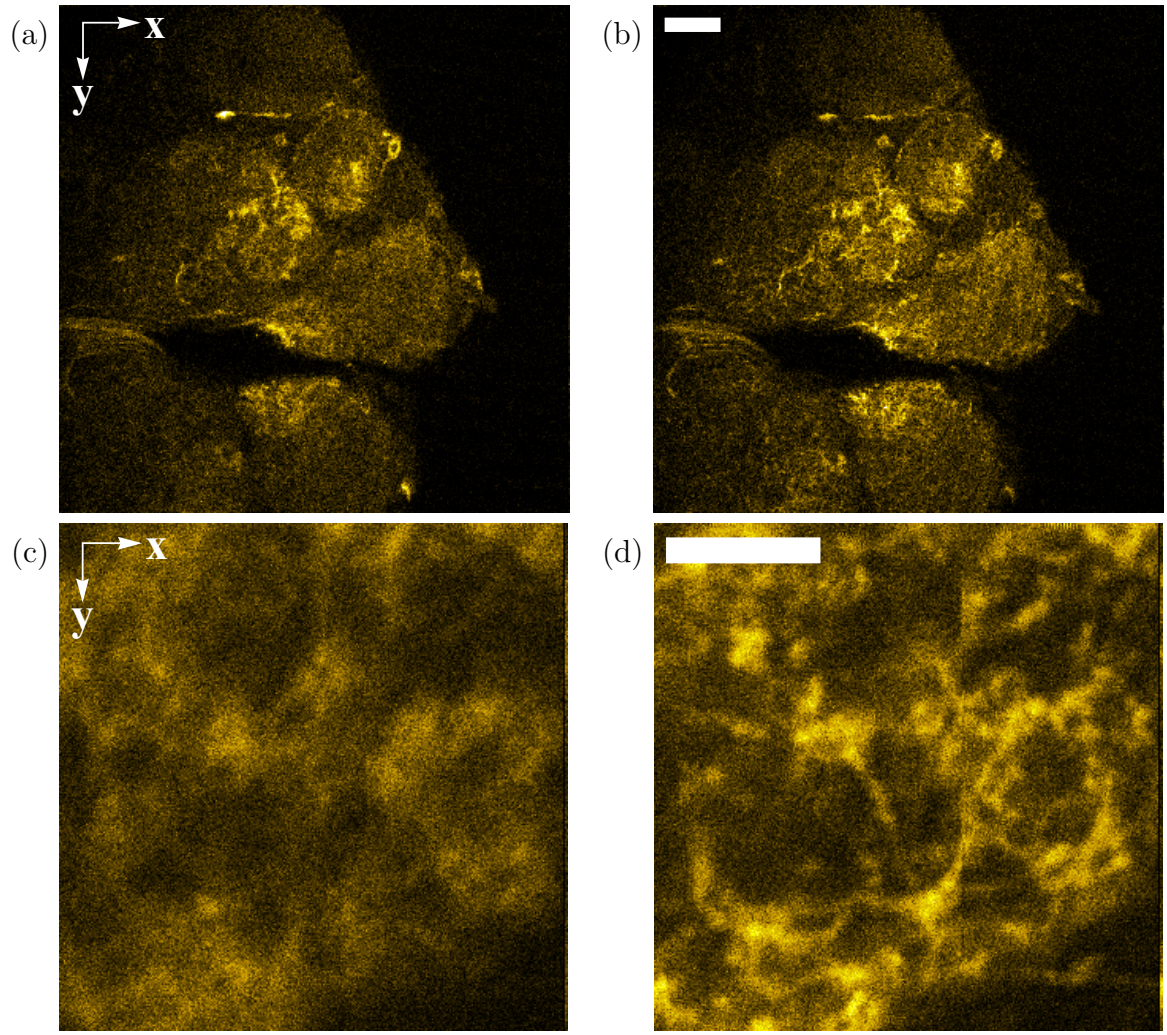


Figure 5.2: *Images from the adaptive two-photon microscope, using the oil immersion objective lens, of fixed Drosophila brain at approximately* $50\mu m$ *from the surface. The fluorophore used was GFP. Images shown using a linear colour scale without aberration correction, (a) and (c), and with aberration correction, (b) and (d), using empirically derived mirror modes shown in Fg. 4.7. Scale bar for (a) and (b) is* $20\mu m$*, scale bar for (c) and (d) is* $5\mu m$*.*

routine, correcting for the low order mirror modes (see Chapter. 4). The metric used for correction was the total image intensity. An increase in intensity is noticeable, and an increase in image detail is visible. This method of aberration measurement and correction relies upon averages taken across the image field. It is clear from Fg. 5.2(b) that the correction of the low order aberrations common across the field of view can provide useful image improvement. It is likely for large fields that aberrations vary across the image (see Chapter. 7). If this is the case, one would expect to obtain more significant improvement by correcting aberrations over a smaller region, as there is less

aberration variation so the correction will be better for more of the image. Fg. 5.2(c) shows one such small region without specimen aberration correction, whilst Fg. 5.2(d) shows the same region imaged after aberrations have been corrected by first performing a correction routine on just this region of the *Drosophila* brain. Not only has the total image intensity visibly increased after aberration correction (as would be expected, since this was the correction metric used), but structures that were not visible without the use of adaptive optics are now evident. The increase in image intensity gives an increased signal-to-noise ratio (SNR), since the fluorescing structures return a stronger signal for a given exposure time and illumination power. This in turn reduces the photo-bleaching of specimens as the illumination power used for the imaging can be reduced. By correcting for the axial elongation of the focal spot, 3D sectioning is also improved, which is the main blurring effect exhibited in Fg. 5.2(c). The improved imaging of fine structures deep within a specimen will enable biologists to study the brain structures situated further from the surface in vivo, i.e. without requiring further prior sample preparation.

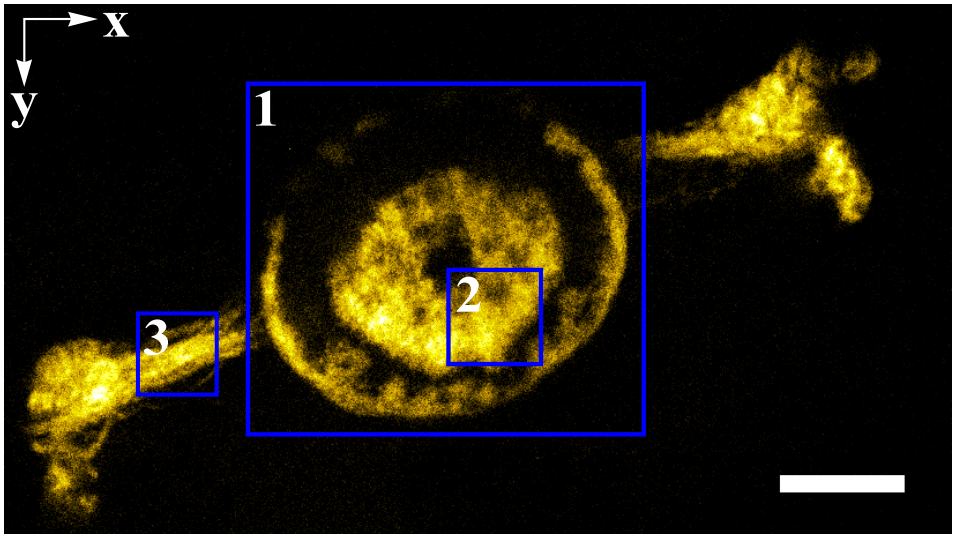


Figure 5.3: *Images from two-photon microscope, using the water immersion objective lens, of the central complex of Drosophila brain at approximately* 100μm *from the surface. The fluorophore used was GFP. Enlarged images of the highlighted regions are shown below as follows: 1. See Fg. 5.4. 2. See Fg. 5.5. 3. See Fg. 5.6. Scale bar is* 20μm.

Fg. 5.3 shows an aberration-corrected two-photon microscope image of the central cortex and linking neurites of a *Drosophila* brain. Three regions are highlighted, for which enlarged images were also taken, shown below.

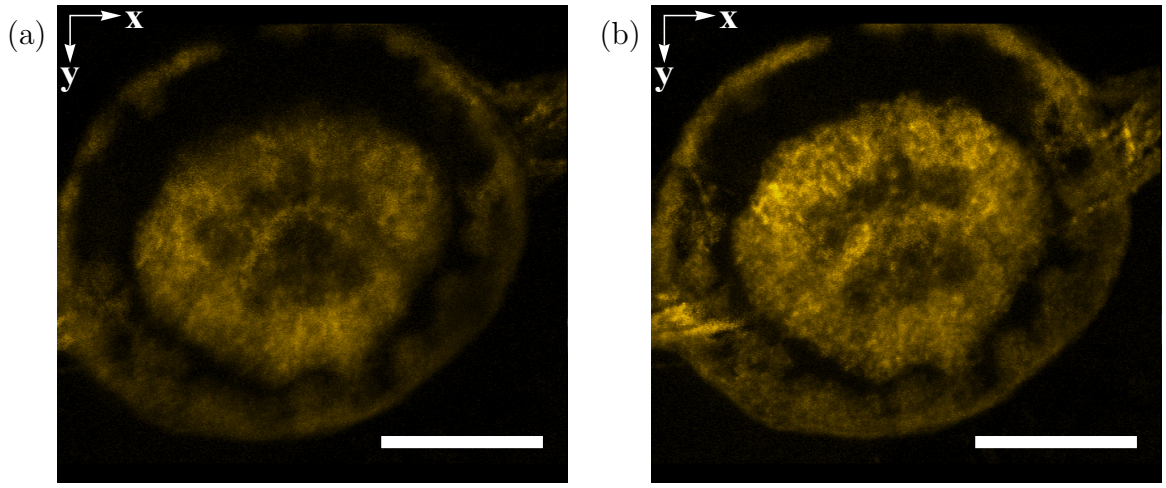


Figure 5.4: *Images from two-photon microscope of the central complex of Drosophila brain at approximately* $100\mu m$ *from the surface. Enlarged from region 1 in Fg. 5.3. Images shown are without any aberration correction (a) and with aberration correction (b). Scale bar is* $20\mu m$.

Fg. 5.4 shows a cross-section of the central complex. From Fg. 5.4(a), taken without the use of aberration correction, the general structure can be seen. However, by performing aberration correction, using the image brightness as a metric, not only is the brightness of the image increased but also the detail that is shown is improved. Structure within the central circular shape is more visible now (shown in further detail in Fg. 5.5), as are the neurite strands on either side of the central complex (shown in further detail in Fg. 5.6). The image sharpness has also been improved, which is visible by comparing the outer edge of the central complex when imaged with (Fg. 5.4(b)) and without (Fg. 5.4(a)) aberration correction.

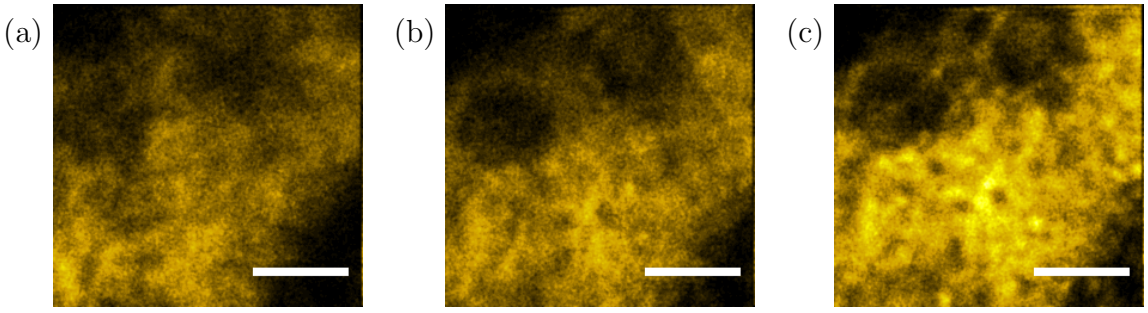


Figure 5.5: *xy images from two-photon microscope of the central complex of Drosophila brain at approximately* $100\mu m$ *from the surface. Enlarged from region 2 in Fg. 5.3. Shown are images with no correction (a), depth correction (i.e. correction of mirror modes with circular symmetry) (b) and aberration correction of mirror modes* X_5 *to* X_{13} *(c). Scale bars are* $4\mu m$.

Fg. 5.5 shows region 2 of Fg. 5.3 without any aberration correction (Fg. 5.5(a)), with depth correction (i.e. correcting for the circularly symmetric modes, Fg. 5.5(b)) and with complete aberration correction (i.e. correcting for all the lower order mirror modes, Fg. 5.5(c)). There is clearly an improvement in the imaging as the adaptive optics are utilised. Whilst there is a good image brightness without any aberration correction, the structures are very blurred and the image sharpness is poor. By introducing depth correction, there is not a significant increase in the brightness but more structures are visible. This is particularly noticeable in the top left where the circular gap is clearer in the corrected image. This is because the corrected focal spot is well confined along the optic axis, so the fluorescence contributing to the image is from a narrower focal region and there is much less fluorescence excited from other xy planes. Finally, by correcting for all the lower order mirror modes (modes X_5 to X_{13} were corrected), not only does the sharpness of structures remain (e.g. the top left region), but further structures emerge from the bulk fluorescence. This is a good example of the problems modelled in Chapter 3.

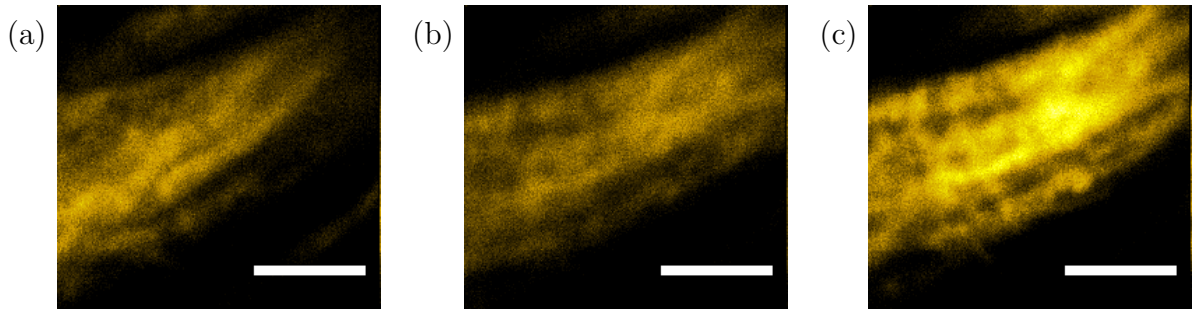


Figure 5.6: *xy images from two-photon microscope of the central complex of Drosophila brain at approximately* $100\mu m$ *from the surface, enlarged from region 3 in Fg. 5.3. Shown are images with no correction (a), depth correction (i.e. correction of mirror modes with circular symmetry) (b) and aberration correction of mirror modes* X_5 *to* X_{13} *(c). Scale bars are* $4\mu m$*.*

Fg. 5.6 shows the neurite highlighted in region 3 of Fg. 5.3. As with Fg. 5.5, shown are images taken without any aberration correction (Fg. 5.6(a)), with depth correction only (Fg. 5.6(b)) and with low-order mirror mode aberration correction (Fg. 5.6(c)). The trend of imaging improvements is, naturally, similar. Without any aberration correction, the broad structure is visible; indeed, some of the neuron strands are partially

distinguishable. There are regions that have too little fluorescence intensity to be seen, which become visible in Fg. 5.6(b). The most likely cause of this is some inadvertent defocus of the image. However, the mirror modes used, as discussed in Section 4.3, should not have any defocus component present. Perhaps this is evidence that, on this occasion, the new modes were not perfectly created. Alternatively, there may be been some slight axial movement of the specimen, perhaps due to the pressure of the objective lens on the specimen cover slip. The depth aberration correction increases the fluorescence intensity across the structure, particularly at the right-hand end (although this may be in part due to some refocussing, as mentioned above). But, interestingly, because the aberration correction metric used was total image intensity, whilst the total intensity is increased, some of the sharpness has been lost and the neuron strands are harder to distinguish at points than in the uncorrected image. However, by performing a full aberration correction routine for mirror modes X_5 to X_{13}, both the brightness of the neurite along its length and the sharpness of the neuron strands are improved. This demonstrates that, in some examples, the aberration correction metric may lead to improvement of some regions of the image at the expense of other regions, and emphasises the importance of defining an appropriate metric to use for aberration correction.

5.3 Second and third harmonic generation microscopy

A schematic of the adaptive second and third harmonic generation microscope (SHG and THG) is shown in Fg. 5.7 [Jesacher et al., 2009]. A pulsed chromium-forsterite laser with a centre wavelength of 1235nm and pulse frequency of $75MHz$ is expanded onto a pair of scanning galvanometer mirrors. These are imaged onto the active region of the DM, an Imagine Optic MIRAO 52-e which applies a phase to the illumination wavefronts. The DM was then imaged onto the back aperture of the objective lens (Obj. 1: Olympus UAPO 40XW3/340, water immersion, 40× magnification, $NA = 1.15$). The back aperture was deliberately under-filled such that rather than the usual "top-hat" beam profile entering the objective, the beam profile was Gaussian in order to increase the illumination power incident on the specimen. Second and third harmonic signals were

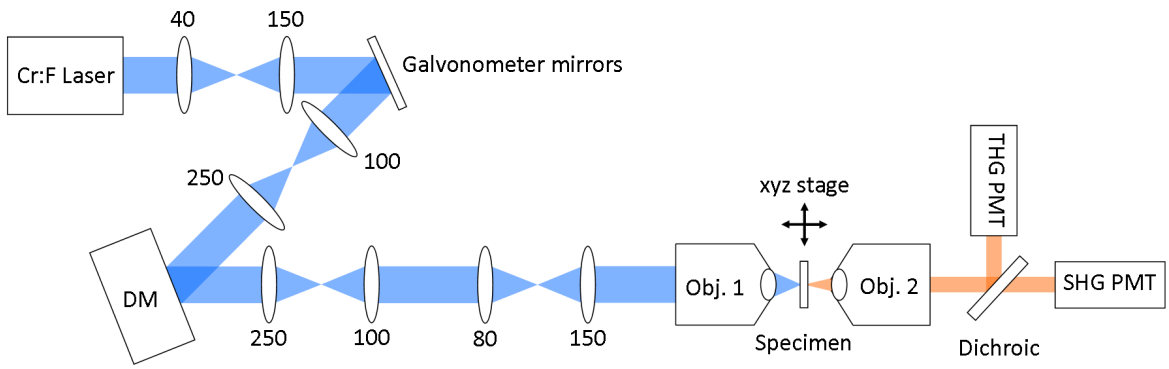


Figure 5.7: *Schematic of the second- and third-harmonic microscope. Cr:F, chromium forsterite laser. DM, deformable mirror. Obj., objective lens. SHG, second-harmonic generation. THG, third-harmonic generation. PMT, photo-multiplier tube. Focal lengths are in mm.*

then collected by a second objective (Obj. 2: Olympus U-ACC Aplanat Achromat, oil condenser, $NA = 1.4$), before a dichroic mirror separated the two wavelengths (≈ 617nm and ≈ 412nm respectively) to be recorded by two PMTs.

The method for aberration correction was the same to that of the two-photon microscope, using image intensity as the correction metric. Empirical mirror modes were derived for the MIRAO 52-e DM for optimised correction, so were different to the mirror modes used with the ALPAO Hi-Speed DM69-15 in the two-photon microscope.

5.3.1 Mouse embryos

It has previously been demonstrated that harmonic generation microscopy, when combined with adaptive optics, can be used in the imaging of mouse embryos to reveal micron-scale features tens of microns below the surface of the structure [Jesacher et al., 2009]. As with other biological specimens (e.g. *Drosophila* brains), these specimens present a challenge when imaging as they have a refractive index that is both different to the immersion medium and spatially variant. Imaging below the surface, particularly at a depth of many tens of microns, presents an optically challenging environment.

Fg. 5.8 shows an xy image of a mouse embryo, taken using the THG microscope with adaptive optics for aberration correction. Fg. 5.8(a) shows that, having corrected for aberrations, the bright lipid droplets [Watanabe et al., 2010] are visible but it still appears that large regions of the image are without signal. However, by adjusting the

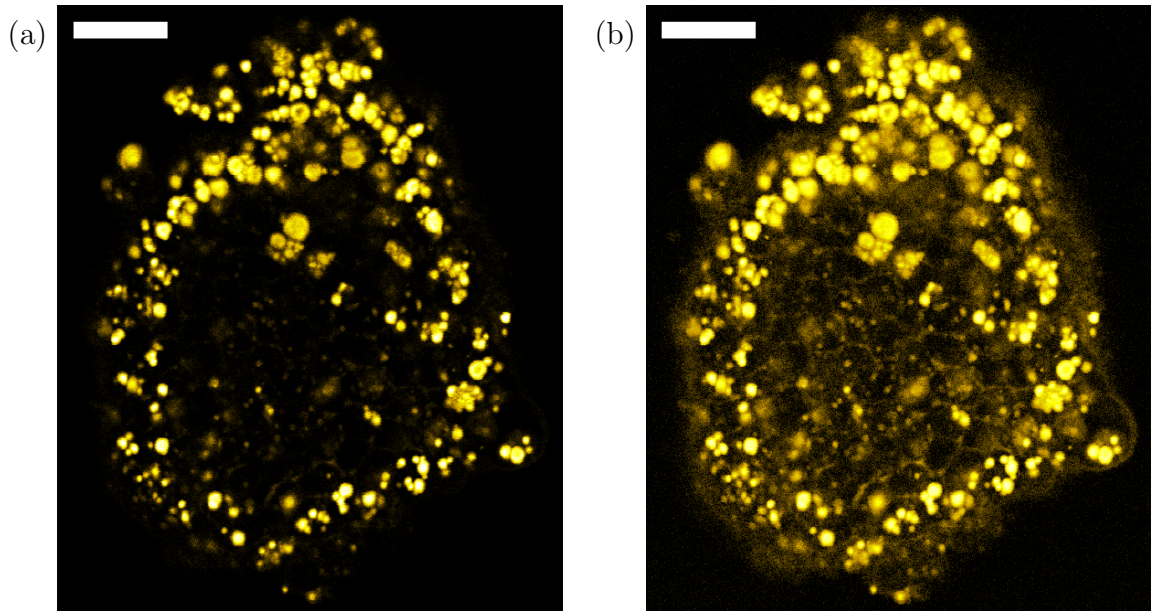


Figure 5.8: *xy images taken using the THG microscope of mouse embryo specimen. The original image is shown in (a) and by adjusting the gamma, detail is revealed (b). Scale bars are* $20\mu m$.

gamma levels of the image (with no additional optical adjustment, see Fg. 5.8(b)), details are visible that were not before, e.g. in the centre of the image where cell membranes can now be determined. This demonstrates that care must be taken with images in the post-processing, as useful information may be recorded that is lost due to the method by which the signal levels are displayed. This is a worthy point of note, particularly when using adaptive optics to correct for aberrations, since in this case details can be recovered that may previously have been lost due to aberrations. However, these details may not be visible since the structures visible in the presence of aberrations will also be increased in intensity, so because of the colour scale they may continue to obscure the image detail.

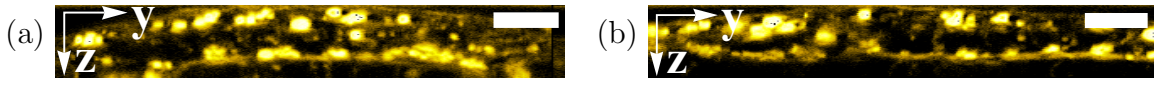


Figure 5.9: *xz (a) and yz (b) images taken using the THG microscope of mouse embryo specimen, with aberration correction utilised for both. Scale bars represent* $10\mu m$.

Fg. 5.9 shows axial slices of the mouse embryo. This demonstrates that, with the use of aberration correction, micron-scale structures can be imaged at 10μm below the surface of the embryo.

5.3.2 Polymer samples

A novel use for the harmonic generation microscope is shown in Fg. 5.10. THG images of specimens consisting of different blends of polymer (polyester melamine). Different structures are revealed in each by the THG signal, showing differences in the distinct blends.

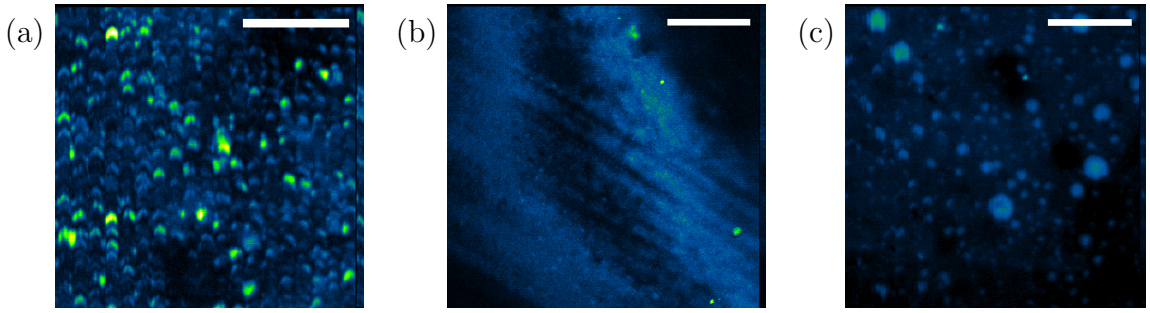


Figure 5.10: *xy images of three blends of polyester melamine specimens taken using the THG microscope, with aberration correction utilised for all three. Scale bars are* $10\mu m$ *for (a) and (c), and* $20\mu m$ *for (b). Polymer samples courtesy of Alexander Jesacher, Innsbruck Medical University.*

5.3.3 Waveguides

By focussing an ultrashort pulsed laser source into a bulk transparent material (e.g. glass), through careful control of pulse energy it is possible to alter the structure of the material in a volume confined to the focal region [Huot et al., 2007]. In doing so, this may subtly alter the localised refractive index and by moving the focal spot through the bulk material so create an optical waveguide structure [Davis et al., 1996, Gattass and Mazur, 2008, Mauclair et al., 2008, Valle et al., 2009, Salter et al., 2012]. By writing multiple waveguides into a bulk material, complex photonic circuits can be created, including Bragg gratings, interferometers and power splitters [Valle et al., 2009]. In order to view the fabricated devices, it is common to use widefield or phase-contrast microscopes. Whilst these are powerful techniques in their own right, they only provide a 2D representation of the (3D) structure. Microscopes with 3D sectioning include the confocal and two-photon microscopes, however, due to the subtle refractive index change (often < 0.1) and lack of fluorophores, these two techniques are not suitable. However,

the second- and third-harmonic generation microscopes (SHG and THG) offer both 3D sectioning and the ability to detect structures that exhibit a $\chi^{(2)}$ or $\chi^{(3)}$ variation (which, in practice, usually coincides with interfaces of differing refractive index), such as these. This makes the SHG and THG microscopes extremely powerful tools in the imaging of these waveguides.

A variety of waveguides were imaged using the THG microscope with adaptive optics. Unlike the biological specimens shown previously, without the use of adaptive optics the signal obtained from the waveguides is very low, and as such this makes obtaining images very difficult. Since the waveguides are fabricated at depths of 120μm or greater, the aberrations affecting the illumination cone, particularly the spherical aberration, are such that the focal spot fidelity is significantly reduced. As the harmonic signal is created by a third-order process, these aberrations have a strongly detrimental effect on the signal level and so the adaptive optics is a necessity in this instance. As the method typically used to correct for aberrations is to optimise the image intensity, some initial signal is required to carry out the optimisation process. For practical purposes, it was therefore common to fabricate a large guide structure or a damaged region close to the waveguides on which to perform initial aberration correction, as the signal from the waveguides of interest was typically too low to detect without any aberration correction. For this reason, none of the figures below include any images without aberration correction applied, as no significant signal was obtained.

Single mode guides

Single mode waveguides fabricated at a depth of 150μm were imaged in the THG microscope. These guides (and also the multimode guides and photonic lantern shown below), supplied by Robert Thomson, Heriot Watt University, were fabricated using ultrafast laser inscription in glass [Thomson et al., 2011]. These waveguides were created by translating a focus (possibly aberrated) through the glass substrate to produce a tall, thin region of modified refractive index in the glass. By repeating this process with the focus adjacent to the previous position, a waveguide with a square cross-section can be

fabricated. An image of one such waveguide is shown in Fg. 5.11(a). Fg. 5.11(a) was

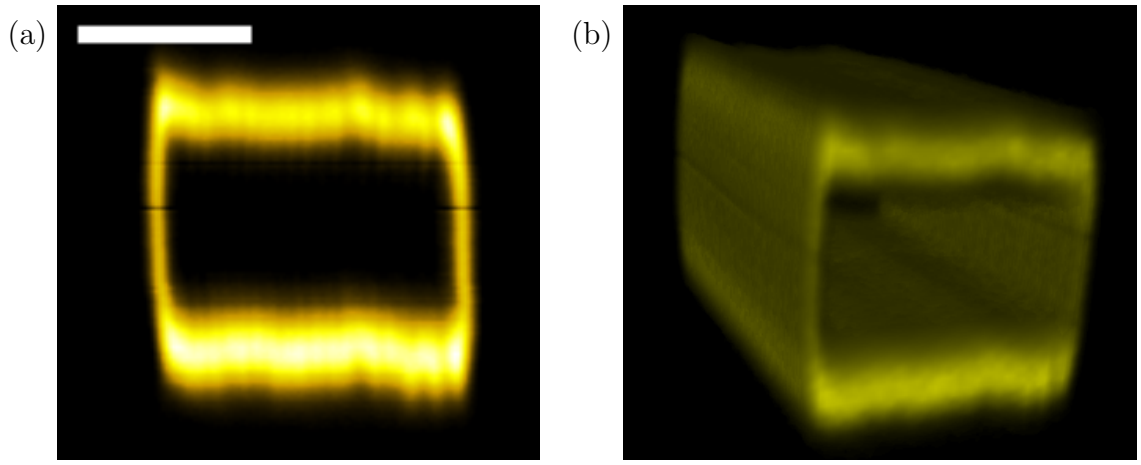


Figure 5.11: *xz section of a single mode waveguide, taken from a 3D stack of xy images (a). 3D image of the guide, created by taking an image stack and rendering (b). Scale bar is* $5\mu m$.

created by taking an image stack of a section of one such single mode guide and summing the images along the axis of the guide. The approximately square shape guide is clearly visible. Since the third harmonic microscope imaging process distinguishes interfaces of differing $\chi^{(3)}$, this suggests that the $\chi^{(3)}$ (and probably refractive index) in the centre of the waveguide is homogeneous. Less clear, but still visible, is some undulation along the top and bottom edges of the guide. The undulations across the top and bottom are caused by small variations in the axial positioning of the focal spot. This variation is $< 1\mu$m but it is possible to resolve this using the THG microscope. The image stack is rendered as a three-dimensional image in Fg. 5.11(b).

These images illustrate the benefit of using the THG microscope to image laser written waveguide structures. The gathered image stacks offer 3D sectioning with 3D micron-scale resolution and can be obtained in situ. If the THG microscope has the addition of an aberration-correcting element, as demonstrated here, then the structures can be imaged at a great depth below the surface (up to 150μm depth shown in Fg. 5.11, but much greater depths may be possible) whilst maintaining the 3D resolution. The THG also offers a non-destructive analysis, a combination of properties that no other method offers at present.

Multi-mode guides

Using the same technique as above, larger multi-mode guides can be created by fabricating single mode waveguides adjacent to each other, so building the multimode guide in a blockwise fashion. An image of one such multimode guide, fabricated at 150μm below the surface, is shown in Fg. 5.12. As with the single mode waveguide, the regions

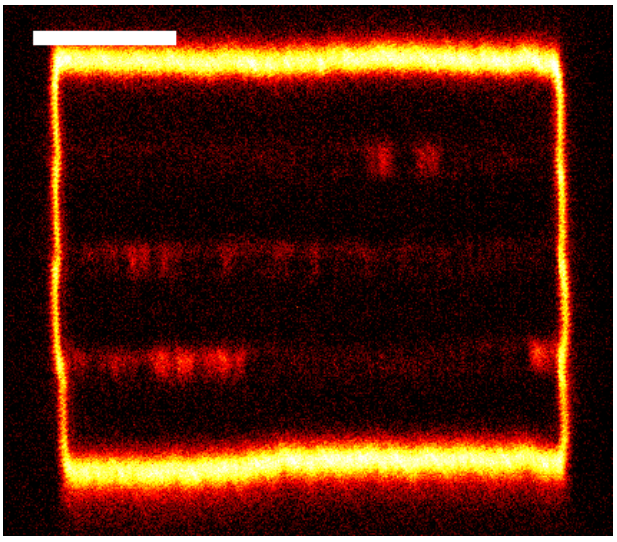


Figure 5.12: *xz image of a multimode waveguide, made by constructing single mode guides adjacent to each other. The joins of these single mode guides are visible within the larger guide. Scale bar is* 10μm.

of transition between differing values of $\chi^{(3)}$ are clearly visible. Unlike the single mode images, it is now also possible to detect third-harmonic signal from within the bulk of the multimode waveguide. These multimode guides were constructed from a 4×4 array of the single mode waveguides, therefore, from the positioning of the signal within the multimode guides, it is reasonable to state that this signal is from the interfaces between the adjacent single mode guides. This signal suggests that either there was a small gap in the fabrication or a small region of overlap between the single mode guides, resulting in a slight inhomogeneity within the multimode waveguide. On the left and right sides of the multimode waveguide it is also possible to distinguish the very slight difference in extents to which the four layers of single mode guides were fabricated.

Photonic lantern

A further application to the construction of the multimode waveguides is to create a photonic lantern, i.e. a waveguide where multiple single mode waveguides converge and join to form a single multimode guide. Such a guide was created [Thomson et al., 2011]. xz slices of this guide are shown in Fg. 5.13, the centre depth of which is 150μm below the substrate surface. Fg. 5.13 shows the effect that depth dependent aberrations have

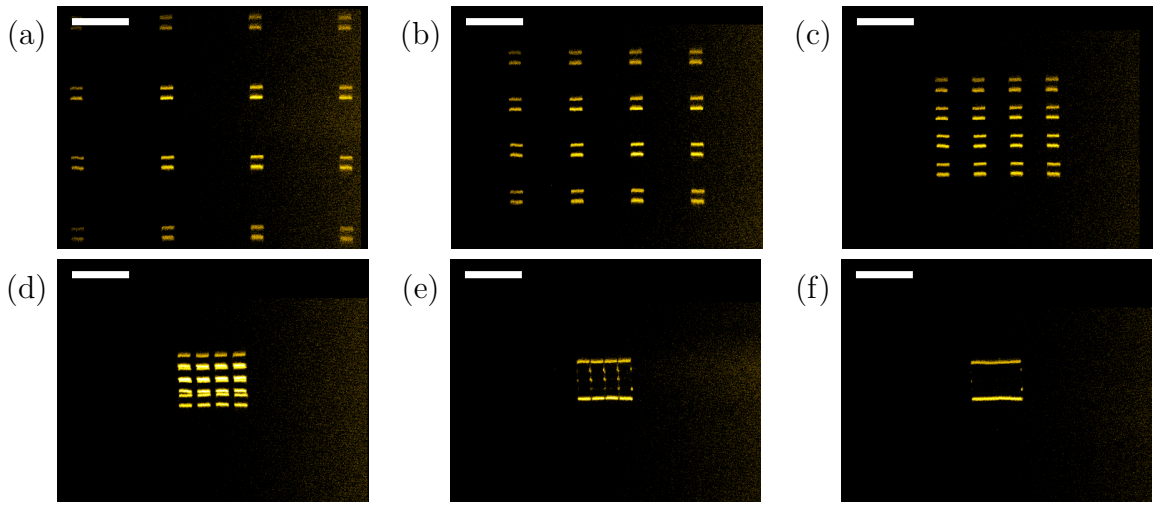


Figure 5.13: *xz slices of a photonic lantern waveguide, made by constructing an array of single mode guides that merge into each other. Scale bar is* 40μm.

on the imaging process. The aberration correction was optimised for the central depth of the lantern, which, in the slices, gives a brighter signal than the regions above and below. This is particularly striking in Fg. 5.13(a) where there is the greatest spread of depths: the middle two rows of single mode guides have a much brighter signal than the top and bottom rows. As the top and bottom rows are affected by residual depth dependent aberration not corrected for by the DM, when imaging these structures the illumination focal spot will be aberrated to a greater extent than when imaging the central structures, resulting in a reduced third-harmonic signal. This effect is also noticeable in Fg. 5.13(d), where there is a smooth increase in structure image intensity from the upper guides to the central guides, then a decrease in image intensity down to the lower guides.

By taking thirty slices along the length of the photonic lantern (six of which are shown in Fg. 5.13), the complete 3D structure could be visualised. The rendering is shown in Fg. 5.14. The images from the image stack were interpolated, using a standard

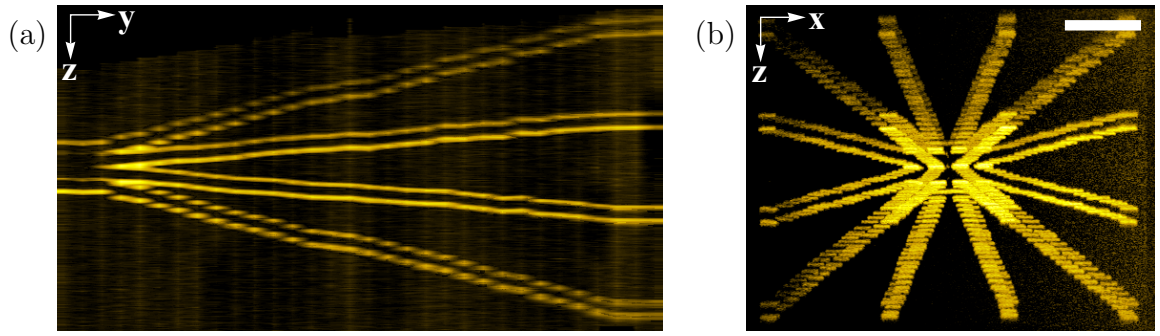


Figure 5.14: *yz (a) and xz (b) projections of a photonic lantern waveguide, made by constructing an array of single mode guides that merge into each other. The y and z dimensions of (a) do not have an equal scale; the dimensions of the overall image are* $3200\mu m$ *in the y direction and* $170\mu m$ *in the z direction. The images were interpolated in (a). Scale bar is* $40\mu m$.

function of the *ImageJ* imaging software, in Fg. 5.14(a) to give a complete rendering of the photonic lantern. Fg. 5.14(a) shows a projection from the side of the lantern stack and Fg. 5.14(b) shows a projection looking along the main axis of the lantern stack, from the single mode end (where there is a 4×4 array of single mode waveguides) towards the multimode end (where there is one large, multimode waveguide).

Bragg guides

By modulating the illumination power reaching the objective lens whilst fabricating a waveguide, it is possible to fabricate Bragg grating waveguides [Salter et al., 2012]. Two such examples of these are imaged below. Fg. 5.16 shows the structure fabricated by modulation of the laser output power to modulate the fabrication. Fg. 5.15 shows the structure created having used a spatial light modulator (SLM) to modulate the illumination power. The SLM is utilised by imaging it onto the pupil plane of the objective lens. The illumination is diffracted into the first order by a hologram placed onto the SLM and the zero order blocked. By controlling the proportion of the illumination entering the diffracted first order, so the illumination power used for fabrication can be modulated.

Fg. 5.15 shows the xy and xz images of the Bragg guide, with the grating controlled by fabrication with an SLM to control illumination power. The imaged structures exhibit a waveguide diameter of $\approx 5\mu$m and a Bragg period of $\approx 2\mu$m. This demonstrates the

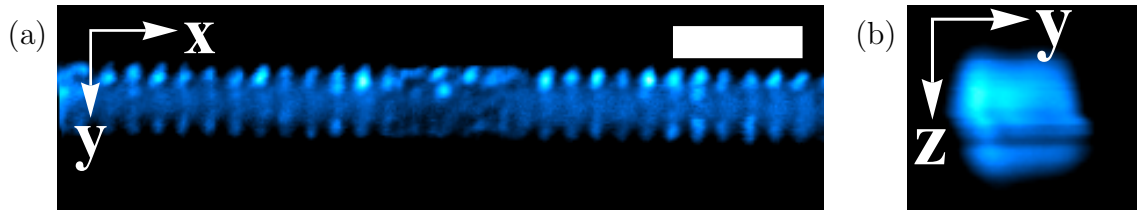


Figure 5.15: *xy (a) and yz (b) THG image of a Bragg waveguide with a circular cross-section. Bragg periodicity is* $\approx 2\mu m$*. Scale bar is* $5\mu m$*. Guides courtesy of Patrick Salter, University of Oxford.*

ability of the aberration correction to resolve structures of $\approx 1\mu$m in size.

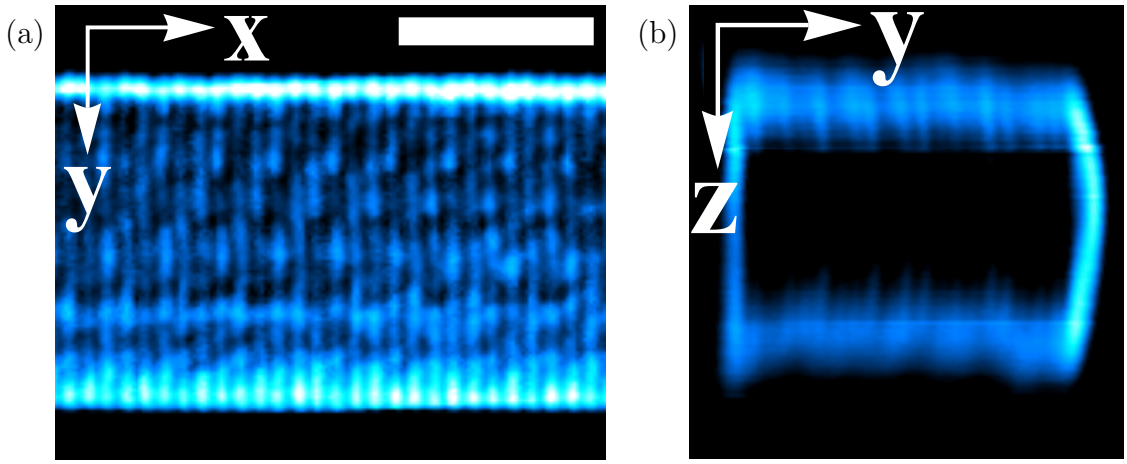


Figure 5.16: *xy (a) and yz (b) THG image of square section Bragg waveguide. Bragg periodicity is* $\approx 0.5\mu m$*. Scale bar is* $5\mu m$*. Guides courtesy of Robert Thomson.*

Fg. 5.16 shows the xy and xz images of the Bragg guide, exhibiting a square waveguide with width of approximately 8μm and a Bragg period of approximately 0.5μm. This demonstrates the ability of the aberration corrected microscope to resolve structures of sub-micron dimensions (as predicted by Eq. 7.3). As the measured period of the modulation in the images was 0.5μm we can be sure that the images show the Bragg grating and not another imaging artefact since the intended modulation period was ≈ 520nm. This reinforces the necessity for adaptive optics when optically imaging such structures, as the grating would not have been visible had adaptive optics not been used.

Curved waveguides

All waveguides imaged previously in this chapter have both been straight and exhibited a uniform cross-section. However, the use of adaptive optics offers further possibilities

when it comes to fabrication, as, by adjusting the focal spot shape, the cross-sectional shape of a waveguide can be controlled and adjusted. By displaying a hologram on an SLM, imaged onto the pupil plane of an objective lens (as shown in Fg. 6.1), waveguides were fabricated that exhibited a controlled cross-section [Salter et al., 2012]. This method was used to fabricate aberration-corrected curved waveguides with an approximately circularly-symmetric cross-section, deep in the bulk of the substrate, by placing a slit on the hologram and maintaining the slit orientation perpendicular to the waveguide direction. A circular guide was created to demonstrate this, which was imaged using the THG microscope. Without the use of the DM built into the THG microscope, it was not possible to image the waveguides as the aberrations were too severely detrimental to the fidelity of the focal spot. The images obtained by correcting for the aberrations are shown in Fg. 5.17.

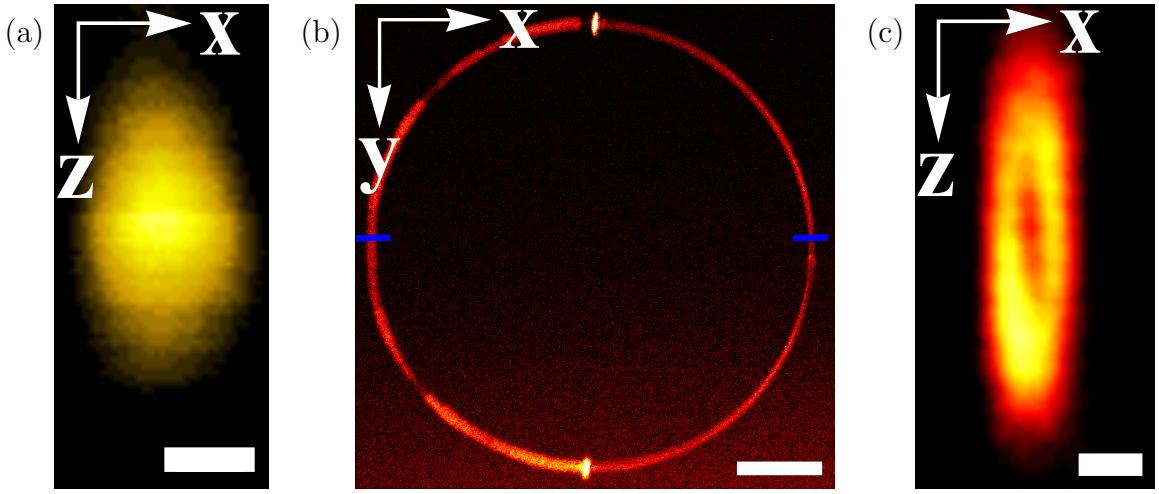


Figure 5.17: *xy THG image of a curved demonstration waveguide, fabricated at a depth of* 170μm *(b). xz slices were taken at the points indicated by the blue bars (a) and (c). Scale bars are* 1μm *(a) and (c), and* 20μm *(b). Guides courtesy of Patrick Salter, University of Oxford.*

Fg. 5.17(b) shows an image taken in the xy plane of the circular waveguide. The left half was fabricated whilst rotating the SLM phase mask to correct for aberrations and control the waveguide cross-section, whilst the right half was done without rotating the phase mask so removing the uniform cross-sectional control. The two blue lines show where xz image slices were taken of the waveguide: Fg. 5.17(a) shows the left-hand slice and Fg. 5.17(c) shows the right-hand slice. By correcting the aberrations in

the THG microscope, the differences in micron-scale features present in Fg. 5.17(a) and Fg. 5.17(c) can be imaged. Fg. 5.17(a) shows that by maintaining the holographic slit perpendicular to the waveguide direction approximately maintains the cross-sectional circular symmetry. However, without the hologram rotation, Fg. 5.17(c) shows the resulting cross-sectional waveguide structure. With no aberration correction applied to the THG imaging, no signal was obtained from any region of the circular waveguide except for at the damaged regions, visible in Fg. 5.17(b) in the centre at the top and bottom of the ring.

Waveguides with changing cross-section

By use of similar techniques to those used to fabricate curved guides, straight waveguides with varying cross-sections were fabricated [Salter et al., 2012]. These guides were imaged using the THG microscope, utilising the adaptive optics. As with the curved guides, it was impossible to image the guides without the use of adaptive optics; the images achieved with the aid of the DM are shown in Fig. 5.18. Fg. 5.18(a) shows an xy image

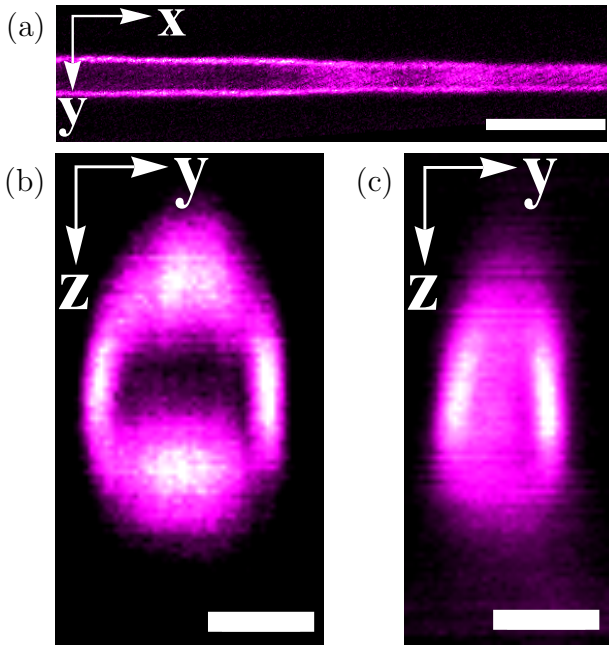


Figure 5.18: *xy THG image of a waveguide exhibiting a varying cross-section (a) with yz images of the two extremities of the cross section (b) and (c), fabricated at a depth of* $170\mu m$*. Scale bars are* $10\mu m$ *(a) and* $2\mu m$ *(b) and (c). Guides courtesy of Patrick Salter, University of Oxford.*

at the centre of the waveguide. This suggests that the waveguide is getting smaller

from left to right, however, from Fg. 5.18(b) and Fg. 5.18(c) it is clear that it is a more complex transformation. Fg. 5.18(b) is an image slice through the waveguide at the left-hand end of the image shown in Fg. 5.18(a). This region of the waveguide maintains an approximately circular cross-section, which gradually adjusts to an oval cross-section, shown in Fg. 5.18(c). As was exhibited in Fg. 5.17, by using the DM to perform aberration correction when imaging, micron-scale features are within the resolution limit of the microscope even at depths of 170μm, at which depth, without aberration correction, images of these structures would be impossible to obtain with the harmonic generation microscope.

5.3.4 Fabrication in diamond

Structures were fabricated within the bulk of diamond substrate, using adaptive correction, as demonstrated in Chapter 6. These structures were imaged using both the SHG and THG microscopes (see Fg. 6.12 and Fg. 6.13), with THG images shown in Fg. 5.19. Due to the very high refractive index of diamond ($n = 2.4$), the imaging of structures within the bulk will always be affected by extreme depth-dependent aberration. This is due to the refractive index mismatch introducing diffraction at the interface between the substrate and any immersion medium (the immersion medium with the highest refractive index is oil ($n = 1.5$)). Because the diamond is transparent and any fabricated graphitised regions are absorbent, it is possible to view any structures using a conventional microscope as long as the structures are not fabricated too far from the surface (as the severe aberrations will affect the imaging). However, it is very difficult to extract any 3D information about the structures with such microscopes. For imaging with 3D sectioning, to retain the 3D sectioning properties a microscope with adaptive optics is required.

Fg. 5.19(c) shows an xy image, taken using the THG microscope with aberration correction applied, of the date fabricated at a depth of 80μm below the surface of the diamond substrate. Fg. 5.19(a) and Fg. 5.19(b) show xz slices through the structures. Because the objective used in the THG microscope was a water-based objective, the

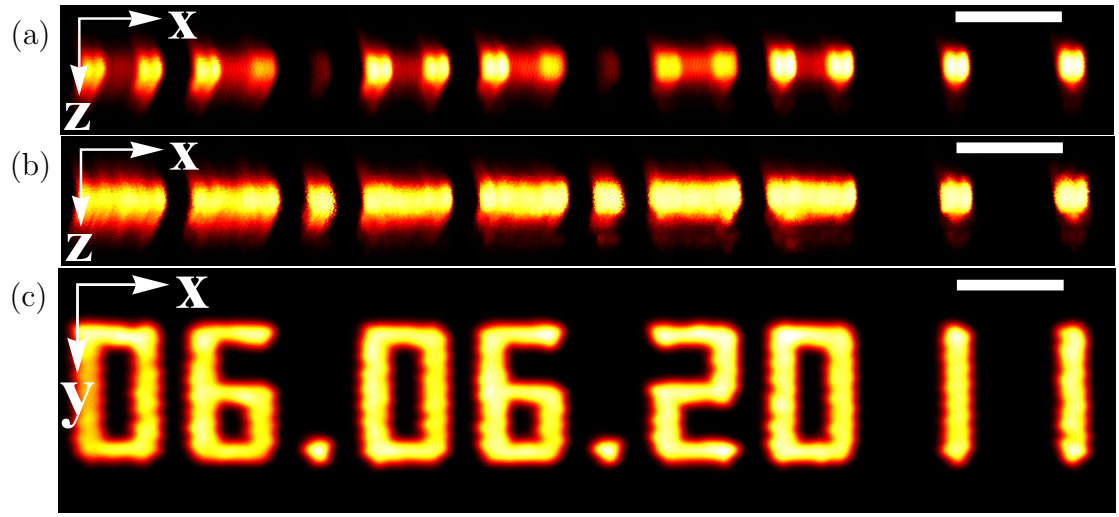


Figure 5.19: *xz (a) and (b), and xy (c) THG microscope images of structures fabricated* $80\mu m$ *below the surface in bulk diamond. Scale bars are* $10\mu m$.

aberrations affecting the illumination were more extreme than previous examples in this chapter due to a greater refractive index mismatch. However, it was still possible to correct for these aberrations (again, using the same aberration correction routine described in Appendix C) using a DM. The THG images in Fg. 5.19 show that the structures fabricated were of the order of 1μm in all directions, showing both that the depth dependent aberration correction in the fabrication and also the imaging were successful.

5.4 Conclusions

This chapter has shown that, for imaging a wide range of specimens in two-photon and harmonic generation microscopy, the use of adaptive optics can have a significant role to play. It has enabled new imaging of a range of structures and the harmonic generation microscope shows contrast of structures that no other microscope can provide.

Detail far below the surface of biological specimens is aberrated and indistinguishable from the background in a traditional two-photon microscope. However, by using adaptive optics for aberration correction, this detail can be recovered and imaged with a resolution potentially equal to that achievable when imaging at the surface.

A variety of waveguides have been imaged using the THG microscope with aberra-

tion correction, enabling 3D imaging of these structures in situ. The images of these waveguides were impossible to achieve without aberration correction, since the depth aberration is such that no signal can be obtained without the use of adaptive optics. But, by performing the aberration correction routine described in Appendix C, not only can the waveguides be imaged, but detail such as micron scale structures in the curved waveguides and the 0.5μm Bragg gratings can be resolved.

3D imaging of structures within the bulk of a diamond substrate has also been performed, which is impossible without the addition of adaptive optics. All of these demonstrations show just how essential adaptive optics and aberration correction are in current scanning optical microscopes.

Chapter 6

Laser processing of diamond

It has been shown in Chapter 3 that aberrations affect the quality of the focus. One significant cause of aberrations is the refractive index mismatch between the immersion medium and the specimen, as the illumination rays are refracted at the interface so distorting the focal spot. The larger the difference in refractive index is, the greater the aberration. For this reason, one application that is particularly challenging is fabrication in materials with a high refractive index such as diamond. In this chapter, femtosecond laser fabrication of three dimensional structures deep in the bulk of diamond is facilitated by a dual adaptive optics system. A deformable mirror is used in series with a liquid crystal spatial light modulator to compensate the extreme aberrations caused by the refractive index mismatch between the diamond substrate and the objective immersion medium. It is shown that aberration compensation is essential for the generation of controlled micron-scale features at depths greater than 200μm, and the dual adaptive optics approach demonstrates increased fabrication efficiency relative to experiments using a single adaptive element.

6.1 Introduction

Diamond is finding application in a multitude of new research avenues in photonics [Aharonovich et al., 2011]. For example, a range of colour centres within diamond are useful in quantum information processing [Wrachtrup and Jelezko, 2006] while the

large Raman gain coefficient provides an attractive medium for Raman lasing [Mildren and Sabella, 2009]. For microfabrication of diamond, either a focussed-ion-beam (FIB) [Fairchild et al., 2008] or a tightly focused femtosecond laser [Kononenko et al., 2008] may be used for the generation of localised graphitic structures. In this chapter, a system based upon the latter method enhanced with adaptive optics capability is described.

Diamond is transparent at near-infrared wavelengths. However, a tightly focused, ultrashort pulsed laser beam provides the high electric field required for multiphoton absorption. At powers above a threshold, the local diamond structure is converted into amorphous carbon as this is the lower energy state. The combination of tight spatial focussing and the ultrashort nature of the pulse confines the graphitisation to the focal volume. Such a process has previously been demonstrated in the creation of surface relief structures [Zalloum et al., 2010] and graphitic wires within the bulk [Kononenko et al., 2008]. However, the fabrication of controlled sub-surface features with diffraction-limited resolution is restricted by spherical aberration caused by the mismatch in the refractive index of the diamond and the immersion medium of the focusing objective lens [Booth et al., 1998, Jesacher and Booth, 2010]. This spherical aberration leads to a loss of resolution and power efficiency of fabrication, and increases with focussing depth (see Chapter 3). This problem is particularly pronounced for fabrication in diamond due to the material's high refractive index (2.4) and the need to use high numerical aperture (NA) optics to obtain the highest resolution. A dual adaptive optics approach that compensates for the depth dependent aberration is shown, enabling the fabrication of compact features deep within the diamond.

Adaptive optical elements have been utilised in various experimental situations employing ultrafast lasers, such as for manipulation of temporal pulse distribution [Weiner, 2000], resolution enhancement in multiphoton microscopes [Neil et al., 2000, Oron and Silberberg, 2005] and more recently in imaging through turbid media [Hsieh et al., 2010]. An adaptive optical element may be used to correct for depth dependent spherical aberration, by imposing on an incident wavefront a phase profile that is equal and opposite

to the aberration introduced by the refractive index mismatch at the sample surface, as demonstrated for imaging purposes in Chapter 5. Previously, both a membrane deformable mirror (DM) [Booth et al., 2006, Thomson et al., 2008] and a liquid crystal spatial light modulator (SLM) [Sanner et al., 2005, Mauclair et al., 2008, Jesacher and Booth, 2010] have been used for aberration correction in laser fabrication systems. A DM provides a continuous phase distortion with large amplitude, but typically has a low number of actuators with which to finely control the mirror shape. In contrast, a SLM benefits from a large number of pixels, but usually has a maximum modulation depth of 2π radians. To compensate larger aberrations, the phase profile must be wrapped into the range $[0, 2\pi)$ radians. Both a DM and SLM, operating in conjugate planes, are used to correct for the extreme spherical aberrations generated when using high NA lenses to focus into diamond. Drawing inspiration from "woofer-tweeter" configurations used to correct for atmospheric turbulence in telescopes [Hu et al., 2006], the DM is used to provide the bulk of the phase compensation, while the SLM is employed adaptively for finer phase adjustment. This enables the advantages of both adaptive optic devices to be utilised, whilst negating each element's disadvantages.

6.2 Experimental set-up

The experimental schematic is shown in Fg. 6.1. The laser (Newport Spectra Physics Solstice, central wavelength 790nm, 100fs pulse duration, repetition rate 1kHz) pulse energy was controlled using a half-wave plate and a Glan-laser polariser. The beam was expanded onto a phase only liquid crystal SLM (Hamamatsu X10468-02), which was subsequently imaged onto a DM (Imagine Optic MIRAO 52-e) with a pair of achromatic doublets in a $4f$ configuration. Both the SLM and DM were in practice operated at near-normal incidence. The plane of the deformable mirror was mapped onto the pupil of the objective (Olympus oil immersion, 60×, 1.4NA) with a further $4f$ image system and the beam was focused into the diamond substrate. The diamond was held on a 3D piezo translation stage which enabled 80μm travel in all axes. An LED illuminated widefield microscope was incorporated in order to monitor the fabrication. Initially, the DM was

calibrated by nulling a phase applied on the SLM (see Section 4.4).

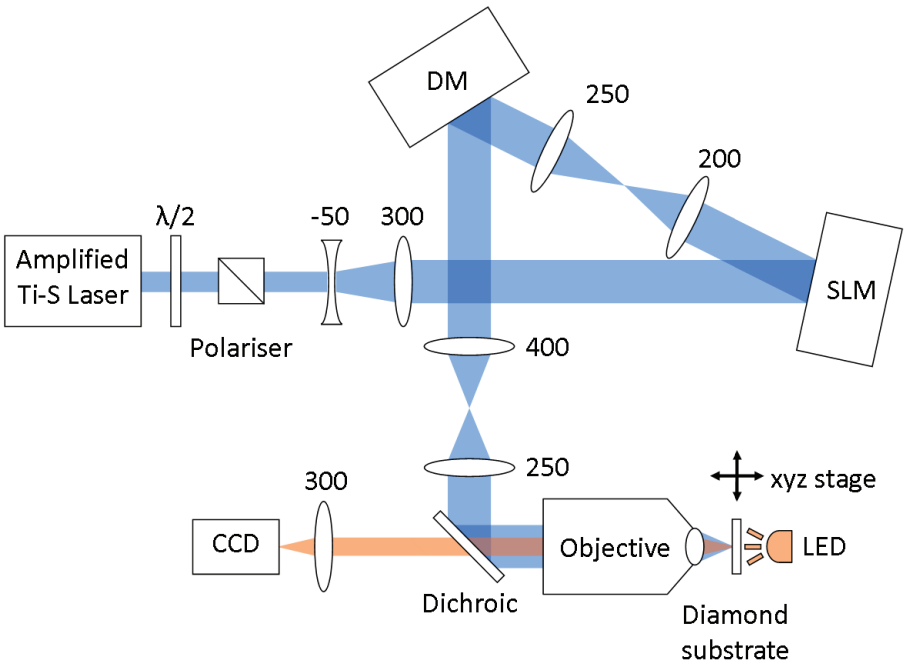


Figure 6.1: *Experimental schematic. Some intervening optics have been omitted for clarity. The lens focal lengths are in mm.*

6.3 Aberration correction routine

In order to perform adaptive aberration correction, the DM was used to apply a correction phase as required to correct for the depth dependent aberrations, as induced by the refractive index mismatch between the diamond substrate and the immersion medium (the training of the DM was discussed in Section 4.4). In order to ensure that the correction was optimised, the SLM was used with a feedback metric to correct for any residual aberration. The optical graphitisation of diamond has a very distinct pulse energy threshold for fabrication. By focussing the amplified laser illumination into the bulk diamond, but setting the pulse energy close to (but below) the fabrication threshold, a plasma can be maintained through non-linear absorption, the brightness of which can be used as the aberration correction metric. This use of the plasma was shown to be an effective method for aberration correction in glass and lithium niobate [Jesacher et al., 2010]. However, diamond ($n = 2.4$) has a larger refractive index than lithium niobate

($2.21 \leq n \leq 2.3$), so the refractive index mismatch between substrate and immersion medium is greater and, consequently, depth-dependent aberrations are worse. The effect of this is two-fold: firstly, the intensity of the laser at the focus will be decreased to a greater extent in diamond and so the plasma intensity will be less; and secondly, the depth-dependent aberration will also aberrate the light from the plasma returning to the detector, making it harder to distinguish. The first of these effects should be negated through the use of the DM to correct for the significant depth-dependent aberration. Observation of the plasma is performed through the transmission microscope. As there was no aberration correction present in this optical path, the imaging of the plasma onto the CCD camera was aberrated, which made measurement of plasma intensity difficult.

A further problem was discovered when using this method of aberration correction. The difficulty of using the plasma as a feedback metric was that, when the aberration correction was improved, often the pulse energy at the focus was raised to a level above the fabrication threshold. In performing the graphitisation, the plasma was lost and the signal seen was only the incandescence produced by heating the graphitised region (see Fg. 6.2), which was significantly less bright than the plasma. Therefore, the diamond

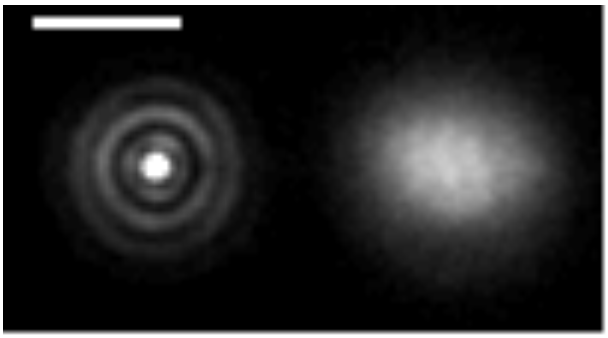


Figure 6.2: *The plasma as imaged when aberrated in diamond (left) and the incandescence viewed when graphitisation has occurred (right). Scale bar is* $5\mu m$.

must be moved to a new, un-graphitised region, the pulse energy reduced and the aberration correction continued. Due to the large aberrations affecting the imaging of the plasma, there was a very small window for pulse energy variation between inducing a visible plasma and fabricating a graphitised point. This made the aberration correction routine both difficult and time consuming (but not impossible), since often the aberra-

tion correction routine would result in graphitisation of the focus. As such, a further improvement to this method would be to introduce aberration correction to the live imaging path, such that the plasma can be more easily imaged and, hopefully, the pulse energy window between inducing a visible plasma and fabrication threshold increased.

By removing all sources of external illumination, it was possible to observe the induced plasma in real time. By adjusting the different Zernike mode polynomials on the SLM, the brightness of the plasma was also altered, from a peak intensity when the aberration mode was corrected for (following the theory expressed in Chapter 2), as shown in Fg. 6.3(a). By correcting the lower order Zernike polynomials, so the aberrations in the system and substrate were corrected for, returning the focal spot to a diffraction-limited spot. In this fashion, for each depth the aberrations could be completely corrected, to minimise the threshold pulse energy required for fabrication and ensure that any graphitisation was confined in three dimensions to the unaberrated focal spot.

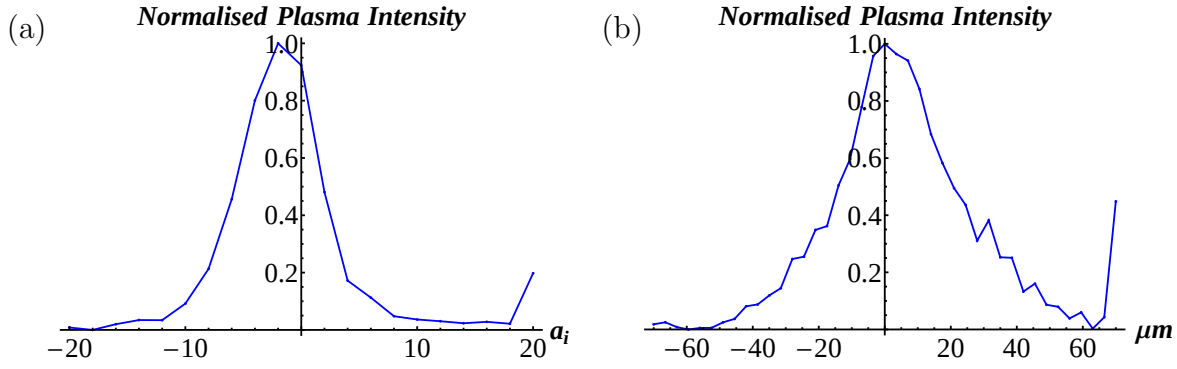


Figure 6.3: *The plasma intensity is plotted as a function of Zernike aberration amplitude, a_i, for Zernike mode 6 (a). With the DM set at 48μm, (b) shows the variation in plasma intensity with the SLM providing a range of additional depth corrections.*

In practice, from Fg. 4.15 we can see that the trained DM shape does not apply the phase required for correction of depth-dependent aberrations at depths greater than 100μm. Therefore, for dual correction it was decided to use the DM to correct for aberrations up to 48μm, using the SLM to only provide additional aberration correction as described above. However, for depths greater than 48μm, the DM was held at a constant phase shape (correcting for the 48μm of depth dependent aberration) with

the SLM used to correct for both the remaining depth dependent aberration and any additional aberration correction for Zernike modes. 48μm was chosen as the cut-off since it was at this correction depth that the threshold energy required when using the DM for aberration correction began to increase significantly relative to that when using the SLM for aberration correction (see Fg. 4.15(b)).

6.4 Aberration corrected point fabrication

Graphitic point defects were fabricated in the diamond crystal at a series of depths below the surface, as shown in Fg. 6.4. Fabrication was performed: (i) without any aberration correction applied, i.e. a flat phase profile was displayed on both the SLM and DM; (ii) using a single adaptive optic element (the SLM) for feedback correction to compensate the depth dependent spherical aberration while the DM remained flat; and (iii) with dual adaptive optics by assigning a predicted shape for each depth to the DM and again using the SLM for feedback correction, which was performed as follows. The spherical aberration function was calculated [Jesacher and Booth, 2010] and applied with different amplitudes at a given depth. The amplitude that allowed fabrication with the minimum threshold energy was taken as the optimum correction. The images were obtained with a transmission microscope by observing the features through a polished side facet. Bursts of 50 pulses were used for the fabrication of each feature; this was found to provide highly repeatable results at each depth. In Fg. 6.4, the threshold pulse energies shown next to each image were measured immediately before the objective.

Fg. 6.4(i) shows axial elongation of the graphitic structures for the uncorrected fabrication beam. This is symptomatic of the focal distortion caused by the refractive index mismatch between the sample and the objective immersion oil, as demonstrated by the simulations of the focal intensity in Fg. 6.4(a), at depth 40μm in the diamond (i) and with full aberration compensation (ii). The simulated images are normalised to the same peak intensity at the focus, not the input power, since that was the approximate requirement for experimental fabrication. The focal elongation increases with focussing depth, as seen in row (i). Correspondingly, the focal intensity is reduced and the pulse

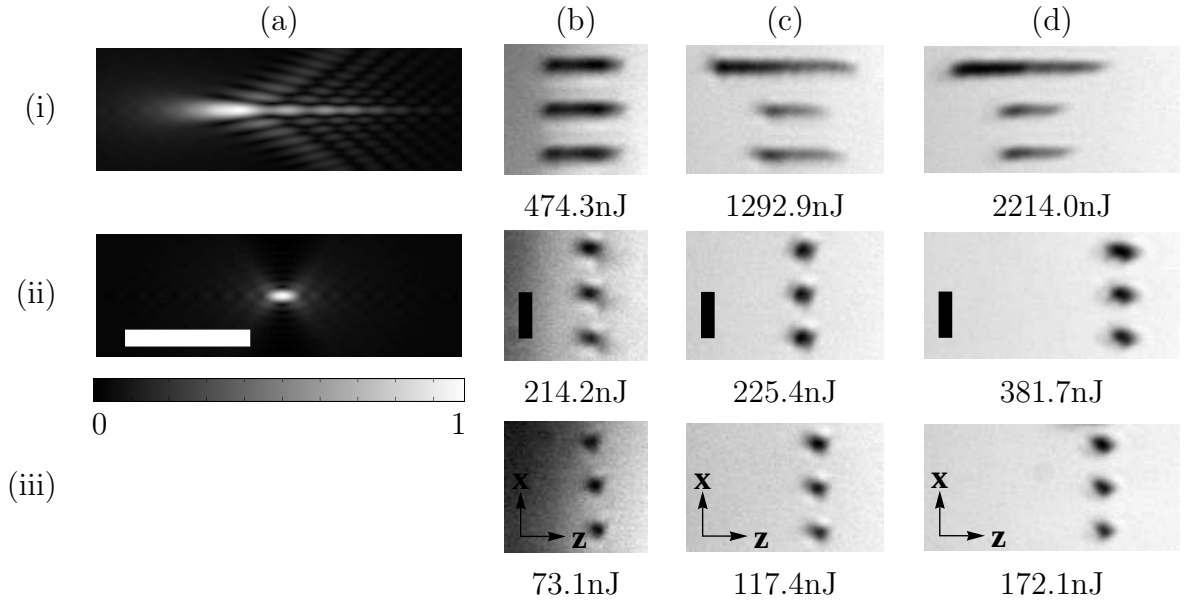


Figure 6.4: *Simulations of the focal spot intensity distribution at a depth of* $40\mu m$ *(a) when aberrated (i) and with aberration correction (ii). Images of graphitic defects fabricated at a depth of* $40\mu m$ *(b),* $80\mu m$ *(c) and* $130\mu m$ *(d), using no aberration correction (i), correction using the SLM alone (ii) and correction using a combination of the DM and SLM (iii). The laser propagation direction for both simulation and fabrication was parallel to the positive z axis. The scale bars are* $5\mu m$*. The pulse energy is shown below each image.*

energy for fabrication must be increased. The groups of three features shown in parts (c) and (d) were each fabricated sequentially from the top feature to the bottom. The shorter length of the second and third features in Fg. 6.4(i)(c) and (d) is attributed to the presence of the previously created (top) adjacent features affecting the fabrication process through partial obstruction of the illumination cone. By introducing aberration correction to the incident beam, initially using just the SLM, the elongation was reduced resulting in compact structures. The threshold pulse energy was also lower, due to tighter focal confinement. Using both the DM and SLM, the feature size was comparable to the SLM-only correction, but the threshold pulse energy was reduced even further. Although the features fabricated using the dual system appear slightly more compact, it was difficult to determine the exact dimensions as the feature sizes were near to the resolution limit of the microscope. This resolution was also affected by aberrations, as unlike the fabrication system, the microscope did not incorporate adaptive aberration correction.

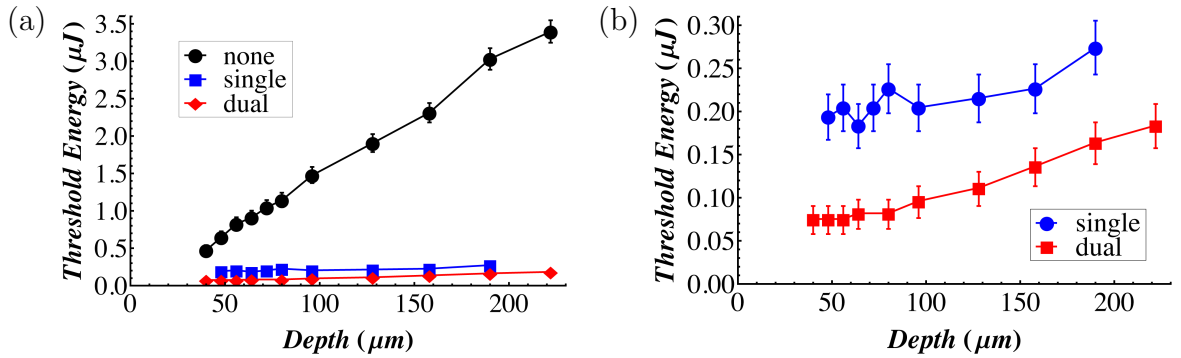


Figure 6.5: *Graphs comparing the threshold fabrication pulse energy over a range of fabrication depths when using no aberration correction, single (SLM only) aberration correction and dual aberration correction (a) and showing the detail of the two correction options (b). The error bars show the expected range in fabrication threshold energy due to system fluctuations.*

Fg. 6.5(a) plots the threshold pulse energy for fabrication as a function of depth in the diamond. Without aberration correction there is an approximately linear increase in the threshold pulse energy as the depth is increased. Both the single and dual adaptive optics approaches also exhibit a roughly linear increase, but the gradient is reduced by a factor of more than 25. Fg. 6.5(b) allows a closer inspection of the threshold pulse energy dependence on depth for the two adaptive optics approaches. It is clear to see that the power efficiency is improved when using the DM coupled to the SLM: the threshold pulse energy is approximately half that for the SLM-only correction across the entire range.

There are two factors to take into account when considering the greater power efficiency of the dual adaptive optics system. The SLM is a liquid-crystal device so it is typically limited to a 0 to 2π *rad.* phase range and relies on phase wrapping to generate higher phase amplitudes; the deformable mirror is (in this case) a continuous membrane device, so cannot perform the sharp phase changes that are possible on the SLM but it does not require phase wrapping to produce phase values greater than 2π *rad.* This is illustrated in Fg. 6.6, which shows a cross-section of a defocus phase distortion when produced by the DM (which produces a continuous phase change) and the SLM (which produces a wrapped phase change). As the SLM cannot produce an instant spatial transition from 2π radians to 0 radians, the phase wrapping is somewhat smoothed. Effectively, this leads to a loss of light at each phase wrapped contour. A second conse-

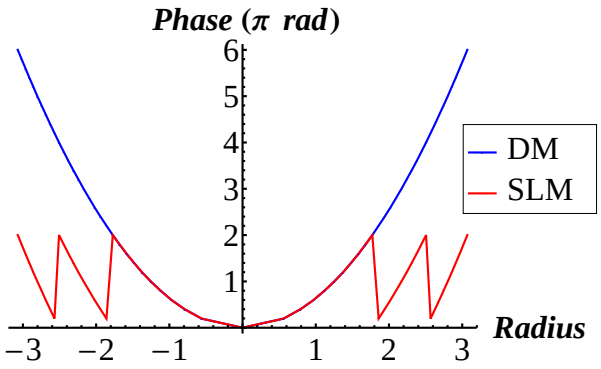


Figure 6.6: *A cross-sectional view of a defocus phase distortion when applied to each the DM and SLM. The DM produces a continuous phase change, but the SLM must wrap the phase as it limited phase range of* 0 *to* 2π *rad.*

quence of the SLM phase-wrapping is particular to pulsed lasers. Since the SLM corrects only the wavefront phase and not the full optical path length, in contrast to the continuous distortion of the membrane in the DM, the pulse fronts from spatially distinct regions of the pupil arrive at the focus at different times [Bor, 1989, Mecseki et al., 2010] (see Section 6.5). Both effects are exacerbated for large amplitude phase patterns, such as when correcting for greater depths, where more phase wraps are present.

6.5 Pulse front and phase front effects

The use of phase-wrapped correction by the SLM has an interesting and important effect on the focussing of laser pulses. To understand this effect, it is instructive to look at how phase fronts and pulse fronts are affected when using DMs and SLMs. Fg. 6.7(a) shows a pulse reflecting off a standard flat mirror. The blue lines in the pulse represent phase fronts and the red oval represents the pulse envelope, both of which maintain their original configuration after having been reflected. In Fg. 6.7(b) the flat mirror is replaced with a DM with a phase applied to the membrane. When the pulse is reflected, both the phase fronts and pulse envelope reflect the shape of the mirror as the full optical path length is changed. In Fg. 6.7(c) the DM is replaced with an SLM exhibiting the same phase, but using phase wrapping to represent values greater than 2π rad. Now in the reflected pulse the phase fronts are distorted in the same way as they were when using

the DM, but because the optical path length has not been fully corrected for the pulse envelope retains its original shape. So a wrapped phase function reproduced on the

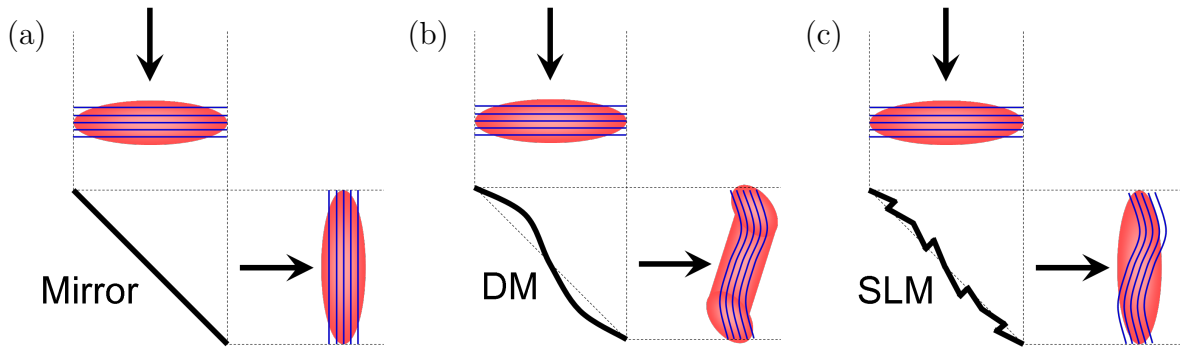


Figure 6.7: *A schematic of the reflection of a pulse front (red) and phase front (blue) by a flat mirror (a), a DM exhibiting a phase ϕ (b) and an SLM also exhibiting the same phase ϕ, but requiring phase wrapping to exhibit the larger phase values (c).*

SLM will always adjust the phase fronts within a pulse, but the pulse fronts will remain essentially unchanged. However, when the same phase is displayed on a DM, both the phase and pulse fronts will be adjusted. This effect has significant repercussions when a collimated beam is focussed by a lens.

The consequence of not correcting the optical path length by using an SLM for aberration correction rather than a DM is shown in Fg. 6.8. Fg. 6.8(a) shows an unaberrated scenario, with a lens focussing a pulse to an unaberrated focus and all parts of the pulse front arriving coincidentally. Fg. 6.8(b) shows the result of focussing into a substrate without any aberration correction. Due to the refractive index mismatch the focus becomes aberrated, and due to the different optical path lengths spatially distinct parts of the pulse arrive at the aberrated focus at different times. Fg. 6.8(c) demonstrates the result of using an SLM to correct the aberrated focus. Because the SLM corrects the phase fronts (not shown), the aberrations are compensated (resulting in a small, diffraction limited focus), but because the pulse envelope is not adjusted the different parts of the pulse front will still arrive temporally distinct. Fg. 6.8(d) shows the result of aberration correction using the DM. Now the optical path length is corrected for, so the pulse front entering the optical system has a shape applied. The consequence of this is that the different parts of the pulse front will arrive, at the aberration corrected focus, temporally coincident, just as in the unaberrated scenario shown in Fg. 6.8(a).

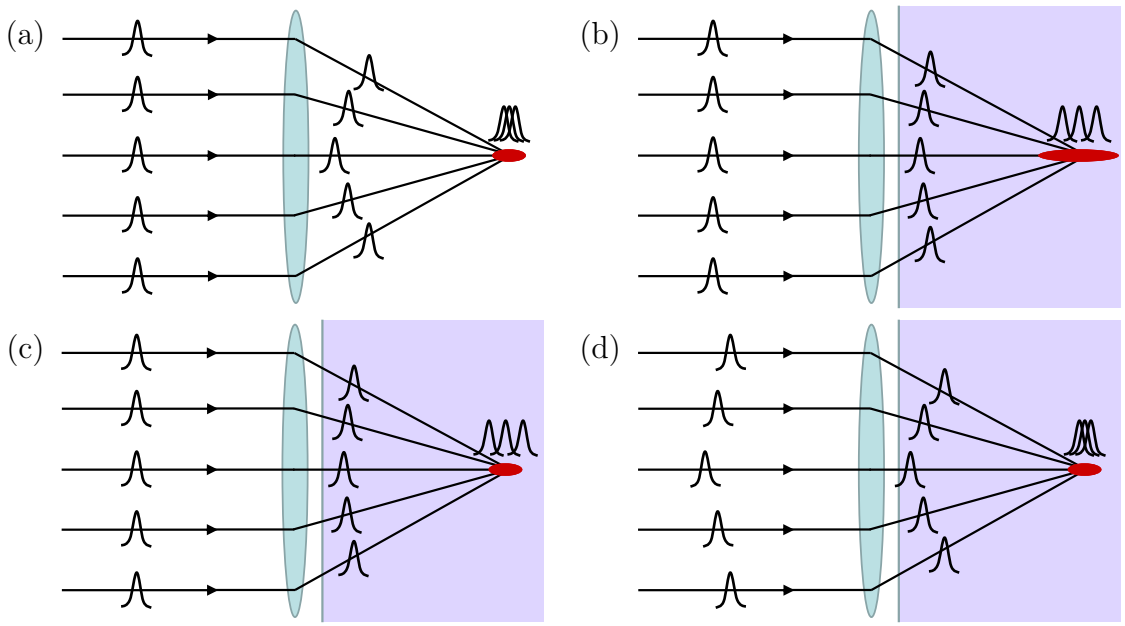


Figure 6.8: *A schematic of the pulse envelope entering a focussing lens and focussed to a diffraction limited spot, showing also the arrival time of different regions of the pulse envelope at the focus (a). Introducing a refractive index mismatched substrate, the focus becomes aberrated, and due to the optical path length difference spatially distinct regions of the pulse arrive at different times (b). Using an SLM to correct for the phase error corrects the focal spot but not the arrival times (c), but using a DM corrects both phase and path length, returning the scenario to the unaberrated result (d).*

When corrected by the SLM, the pulse front distortion (i.e. the arrival time difference between first and last pulse front) induced by the diamond is estimated to be 36.8fs at the greatest depth tested. For an incident pulse length of 100fs, this is significant and so will affect the multi-photon fabrication efficiency. In combination with light lost at each phase wrap, due to the inability of the SLM to replicate an infinite phase gradient, this causes the increase in threshold energy as the depth increases for the single adaptive element correction shown in Fg. 6.5(b). Using dual correction, the power efficiency is improved as less phase wrapping is required on the SLM (a not insignificant number of phase wraps are still required as the SLM does perform some of the depth-dependent correction in addition to the Zernike-based aberration correction). As the fabrication depth increases further, so does the degree of phase wrapping, resulting in the presented threshold power increase (see Fg. 6.5(b)). Whilst the DM does not have a limited phase range or suffer inefficiencies at phase wraps (as exhibited by the SLM), when correcting for aberrations at greater depths, a steeper gradient is required for the mirror shape.

The limited number of actuators restrict the accuracy with which the DM can generate a prescribed shape and so prevent the DM from performing the necessary correction [Shaw et al., 2010]. For this reason it is ideal to use both adaptive elements in tandem for fabrication at depth in diamond. Additionally, through use of both elements in this manner it is possible to independently control the pulse and phase fronts [Simmonds et al., 2012].

6.6 Fabrication of extended structures

In order to demonstrate 3D fabrication and highlight the necessity of using adaptive elements to compensate the depth dependent aberrations, a series of structures were written into the diamond. Fg. 6.9 shows fabrication at a constant depth of 80μm in the diamond (a) with no aberration correction and (b) using the dual AO system. With the laser incident along the z direction, graphitic tracks were drawn by translating the sample in the xy plane at a speed of 1μm/s under constant pulsed emission. The pulse energy used was the threshold for burst fabrication at that depth: (a) 1292.9 nJ and (b) 101.5 nJ. When viewing the results in the xy plane, both generated structures appear similar except that in the uncorrected fabrication (Fg. 6.9(a)), the graphitic tracks are slightly wider and the dots between the sections of the date are absent. However, when viewing the xz plane, the contrast is striking. The uncorrected structure (Fg. 6.9(a)) extends as much as 25μm above and below the intended fabrication depth whilst the corrected structure (b) has similar dimensions along the optic axis as it does in the plane of fabrication. The view in the xz plane also reveals why the dots are missing from the uncorrected structure. The previously written graphitic tracks partially obstruct the focussing cone of the fabrication beam, such that the focal intensity is reduced below threshold. We emphasise that the uncorrected structure was written with the lowest possible (i.e. threshold) pulse energy and when the pulse energy was reduced there were no observable features. It is therefore not possible to generate axially confined graphitic tracks in diamond simply by adjusting the power of the writing beam: adaptive compensation for depth dependent aberrations is essential.

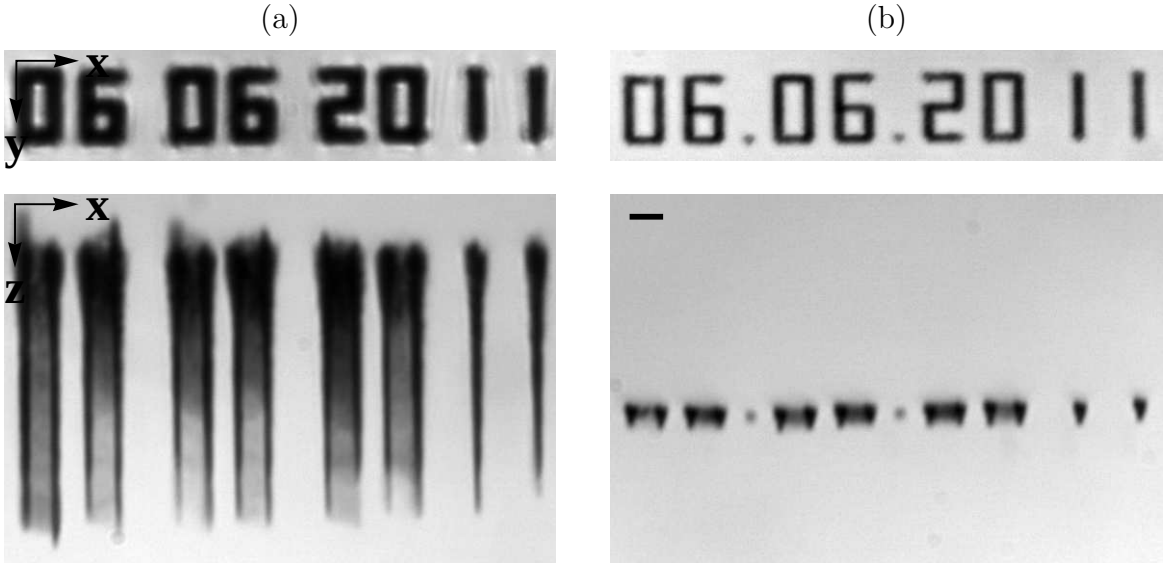


Figure 6.9: *Top (xy) and side (xz) view of the date fabricated in diamond at a depth of* $80\mu m$*. (a) without aberration correction (b) employing the dual adaptive optics system. The laser beam was incident along the z direction. The scale bar represents* $5\mu m$*.*

Fg. 6.10 shows fabrication in the xz plane, both without aberration correction and with the dual correction. The structure was built up by fabricating the deepest structures first so as not to obstruct the incoming beam. During fabrication the SLM phase profile was adjusted according to the focal depth. The writing speed was again 1μm/s and the pulse energy was kept constant at the fabrication threshold value at the structure's midpoint (80μm depth). The resultant fabrication confirms how sharp the threshold is, since there was no fabrication at any depth below the midpoint, even under constant pulsed emission (with exception of the structures extending from points focussed at or above the midpoint). Above the structure midpoint, it was possible to draw graphitic tracks but the axial elongation of the features due to spherical aberration completely obscured any internal structure. When the depth dependent aberration correction was applied (Fg. 6.10(b)), the xz structure was successfully fabricated at all depths, maintaining compact dimensions for the features throughout. It should be noted that this structure was fabricated starting with the deepest parts in order to prevent blocking the focussing cone for subsequent graphitisation.

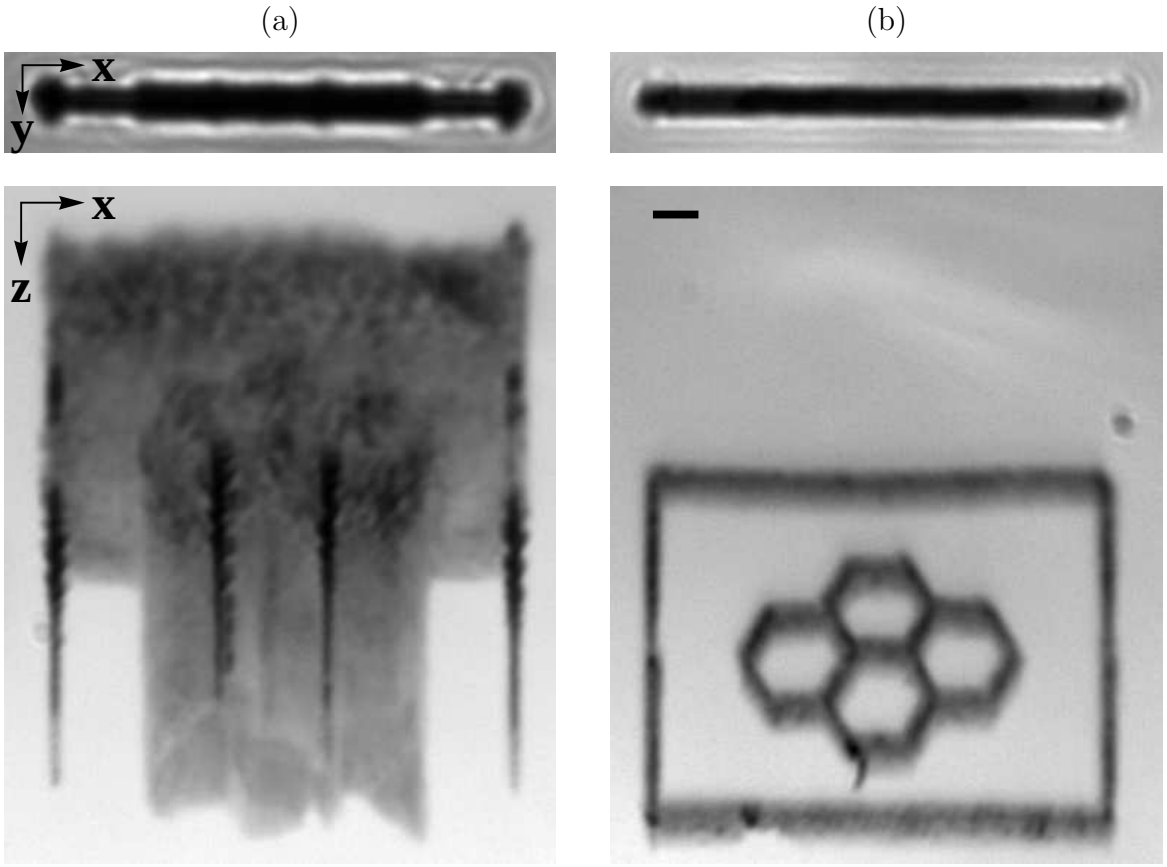


Figure 6.10: *Top (xy) and side (xz) view of graphitic structure fabricated in diamond. The midpoint of the structure is at a depth of 80 μm. (a) without aberration correction (b) employing the dual adaptive optics system. The laser beam was incident along the z direction. The scale bar represents 5 μm.*

6.7 Aberration corrected diamond imaging

At this point, it is important to appreciate that, whilst the graphitic structures have been fabricated using aberration-corrected illumination, the imaging in Fig, 6.4, Fg. 6.9 and Fg. 6.10 has been performed using a conventional widefield microscope. This has no three-dimensional sectioning capability and furthermore no way of performing any aberration correction, so it is impossible to achieve the three-dimensional resolution, and aberration-free images, that we require to precisely determine the dimensions of any graphitic structure created. A further problem for any replication of these results is that the xz images were taken by focussing through a polished side of the diamond. This means that both top and side surfaces must be polished, and that the structures are fabricated close to ($\approx 100\mu$m) the polished side for imaging. This would be ex-

tremely impractical, and very wasteful of bulk diamond, for future diamond fabrication work. The structures were therefore imaged using second- and third-harmonic generation microscopes (SHG and THG microscopes, see Sections 1.1 and 5.3) to confirm the suspected fabrication confinement along the optical axis, and to demonstrate that it is possible to obtain images showing the three-dimensional structure without requiring imaging through a polished side face.

6.7.1 Determining signal emission mechanism

When imaging the diamond specimens in the harmonic generation microscope, we have found that signals are detected in both the SHG and THG detectors. Prior to analysing any images, it is necessary to understand the process generating the signal in these two channels. Potential mechanisms for production of these signals include SHG and THG, 2- and 3-photon fluorescence and also incandescence as a result of heating of the graphitised regions. Determining which of these processes produced the signal is also necessary to determine the resolution capabilities of the microscope. If the images are a result of a first-order process (such as the incandescence) any part of the focussing cone may be a photon source. But, if it is indeed a second or third order process, then the probability that it originates from the focal spot is significantly increased since the likelihood of a signal is proportional to the square or cube of the excitation signal respectively. Because SHG and THG are dependent on the $\chi^{(2)}$ and $\chi^{(3)}$ of the specimen respectively, it may be possible to determine further properties of the specimen if this is the cause of the signal.

Two tests were performed to determine the mechanism producing the emission signal. First, if the process were to be a second- or third-harmonic signal then the polarisation of the emission would match the polarisation of the excitation signal [Débarre et al., 2005]. Incandescence and 2- and 3-photon fluorescence would have no polarisation, so by placing a linear polariser in the path of the emission signal before detection, it would be possible to determine whether the detected signal had a specific polarisation. Second, if the emission were due to harmonic generation, the relationship between excitation and

emission should be square or cubic [Thayil et al., 2010], i.e. the gradient of a log-log plot should be two, if it is a second order effect, or three, if it is a third order effect.

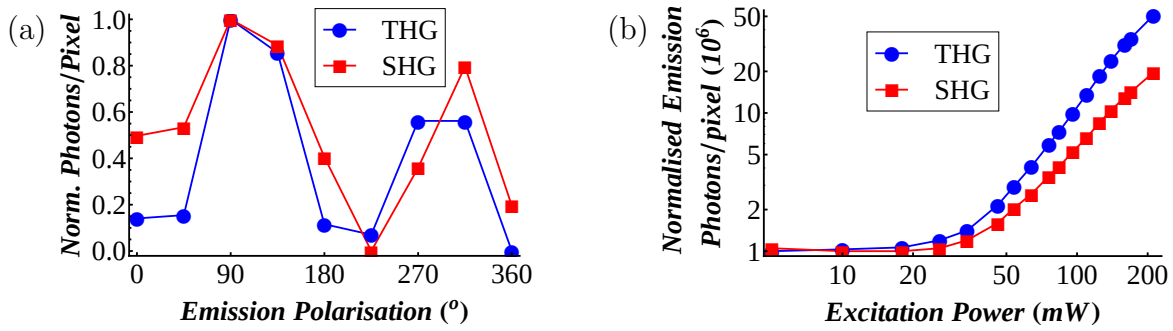


Figure 6.11: *Graphs to confirm the second and third harmonic relation of the emission to the excitation. (a) shows the angular polarisation of the emitted photons. (b) shows the linear log-log relationship between the excitation and emission power.*

Fg. 6.11(a) plots the polarisation of the emission at the second-harmonic wavelength (SHG) and at the third harmonic wavelength (THG). At both wavelengths the data has had the background level subtracted and the resulting signals normalised to give unity peak-to-peak amplitude. For both signals there is a clear linear polarisation dependence, with two maximums and two minimums occurring approximately 90 degrees apart across the full range of polarisation angles, suggesting that both signals may contain some of the respective harmonic signal. However, since there was background signal that had to be removed, it is also possible that there is some third source, potentially the incandescence postulated previously. This does not rule out fluorescence effects too, as it is possible to excite linearly polarised fluorescence. Fg. 6.11(b) adds weight to the argument that the signals consist primarily of the harmonic (or fluorescence) signals, and not incandescence. Again, the data has had the constant background signal removed. At low excitation power wavelengths, at the frequencies measured there was little or no signal produced by the graphitic structures. However, as the excitation power increases past 50mW (at the point of entry to the optical system), so the detected emission shows a linear relation to the excitation signal on the log-log plot. The gradients of the SHG and THG were calculated as 1.6 and 2.7 respectively. This is very close to the theoretical gradients of 2 for the SHG and 3 for the THG, hence it is reasonable to believe that the mechanism for producing the emission signal is indeed a second and third order one.

This still does not distinguish between a harmonic signal and a polarised fluorescence one, but both should give the desired resolution information.

Having determined that the signals are most likely from second and third harmonic processes, the resulting imaging process images are expected to have a strong three-dimensional sectioning capability, and so by using the aberration corrected SHG/THG microscope we can get a very precise impression of the dimensions of the graphitic structures created.

6.7.2 Harmonic generation diamond images

The number "6" from both the aberration corrected and uncorrected date structure shown in Fg. 6.9 were imaged again in both the SHG and THG microscopes, using a deformable mirror to perform aberration correction. This was achieved using an indirect method to determine the presence of aberrations, as discussed in Appendix C. In both cases, a three-dimensional image stack was taken, then the stack maximum recorded values taken to display the xy and xz projections shown in Fg. 6.12.

Fg. 6.12(a) and (b) show the uncorrected fabrication of the "6" number, as imaged by the second- and third-harmonic microscopes respectively. Comparing these to the aberration corrected fabrication, shown in Fg. 6.12(c) and (d), it is clear that the aberration corrected fabricated structure is more tightly confined in all directions, particularly along the z axis. Observing the xy projections, it is clear that the aberration correction significantly improves the lateral fabrication confinement, with the width of the structure reduced from approximately 2μm to 1μm in both x and y. Similarly, so in the xz projections does the fabrication confinement improve when applying the aberration correction. Significantly, the aberration correction has confined the fabrication to approximately 1μm along the optical axis, where the most significant effect of aberrations would be expected when fabricating deep in diamond. This corresponds to the observations made regarding Fg. 6.9. However, unlike in Fg. 6.9 where it was clear that the uncorrected structure was as much as 25μm in length in the z direction, both in Fg. 6.12(a) and, more clearly, in Fg. 6.12(b), whilst there is some evidence of fabrication

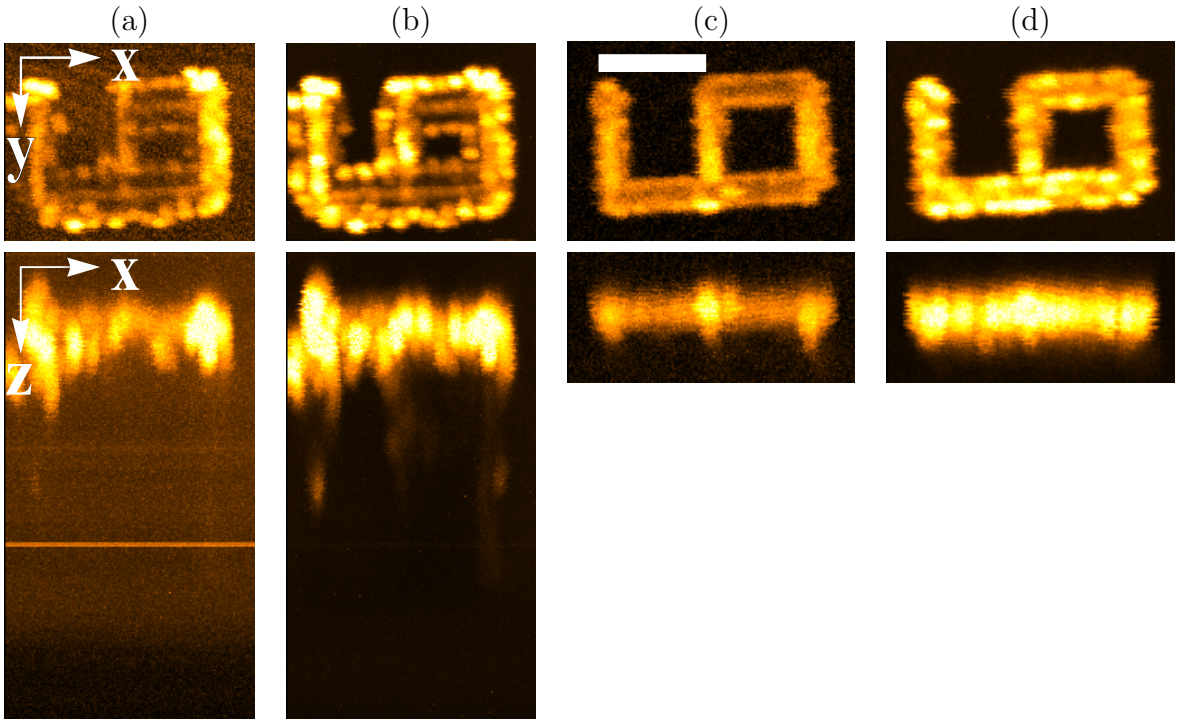


Figure 6.12: *Top (xy) and side (xz) projection, using the maximum detected values from a three-dimensional image stack, of the "6" from the date structure fabricated in diamond at a depth of* 80μm*. (a) SHG image and (b) THG projection of fabrication without aberration correction, (c) SHG and (d) THG projection of fabrication employing the dual adaptive optics system. The laser beam was incident along the z direction. The scale bar represents* 5μm*.*

deeper into the diamond bulk it is not as clearly demarcated as in the transmission images. This can be attributed to the method by which the structure is illuminated. Given that the illumination is incident in the positive z direction, so it must pass through the top part of the graphitisation to reach the lower regions. But since the graphitisation is highly optically absorbent, the illumination is unable to reach these lower structures, and so the focal intensity is lower. This reduction in intensity has a compound effect on the nonlinear signal generation effect.

However, the projections in Fg. 6.13 are less affected by this problem. The graphite structures were imaged in the same manner, taking a series of xy images to create a three-dimensional stack then producing the xz projection from the data gathered. Clearly there are fabricated regions present immediately below other fabricated regions, as are present in Fg. 6.12(a) and (b). However, the fundamental difference of the two structures is that the "6" in Fg. 6.12 has a significant cross-sectional area in the xy plane

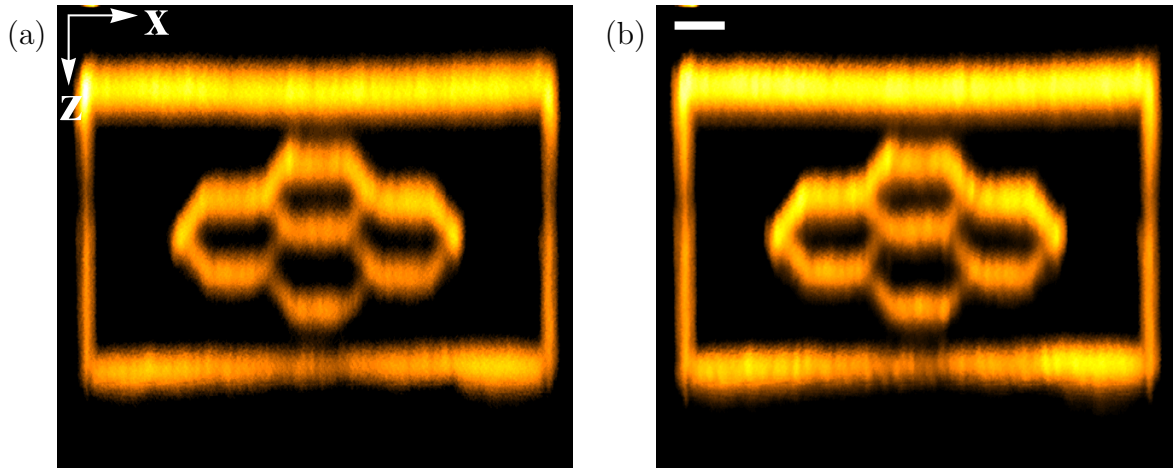


Figure 6.13: *SHG (a) and THG (b) xz projection, using the average detected values from a three-dimensional image stack, of the graphitic structure fabricated in diamond employing the dual adaptive optics system. The midpoint of the structure is at a depth of* $80\mu m$*. The laser beam was incident along the z direction. The scale bar represents* $5\mu m$*.*

that is able to block and absorb the illumination. Conversely, the graphite structure in Fg. 6.13 is present only in the xz plane, with a very narrow xy cross-sectional area (see Fg. 6.10). Therefore, whilst some of the illumination light is lost, it is a small enough fraction to not lose the three-dimensional imaging capability. There is a reduction in the emission intensity when comparing the regions of Fg. 6.13 below other fabricated regions, however, showing that whilst the structure is still visible, the effect is occurring.

6.8 Conclusions

Compact graphitic structures have been fabricated deep in the bulk of diamond using a femtosecond laser and a dual adaptive optics setup, consisting of an SLM and DM, to correct for depth dependent aberration. Adaptive aberration compensation was shown to be crucial for maintaining controlled fabrication, allowing micron-scale structures to be fabricated down to depths greater than 200μm . It was also shown that adjustment of the writing beam power was not sufficient to generate features that were confined along the optic axis. This was due to the axial extension of the focal spot when aberrated by the refractive index mismatch present at the surface of the diamond substrate. Sharing the load of the aberration between the two adaptive elements led to increased fabrication

efficiency compared to using the SLM alone.

The combination of femtosecond laser fabrication with high NA focussing and adaptive optics provides the capability to generate three-dimensional micron-scale structures deep within diamond. Subsequent reactive ion etching of the graphite, as has been demonstrated, for example, in combination with FIB machining [Fairchild et al., 2008], leads to the possibility of creation of complex high index contrast devices. These would have many applications in different areas of photonics. These dual adaptive methods also hold great potential benefit for optical microscopy, such as, for example, the observation of colour centres in diamond [Rittweger et al., 2009].

Fg. 6.12 and Fg. 6.13 have demonstrated that it is possible to optically image structures fabricated deep in the bulk of diamond, without requiring a polished side face through which to image. The projections have also demonstrated the optical confinement achieved in both the xy and xz planes by using aberration correction during the fabrication process, and an increase in fabrication precision is achieved. Whilst not presented, the necessity of using aberration correction in the imaging process was also noted, since without any correction, little or no emission signal was observed (see Chapter 5). However, also demonstrated was the limitation of this technique. Whilst it is possible to image the structures, for any extended three dimensional structure, particularly those with a significant xy cross-sectional area, there is a loss in the emission signal.

Chapter 7

Spatially variant aberration correction

Most previous implementations of adaptive optics in microscopy have used a single aberration correction across an image. It is, however, likely that in a typical image, aberrations vary across the field of view. In this chapter, techniques are introduced to measure the spatial variations of aberrations in biological specimens and for artificial structures. Multi conjugate adaptive optics (MCAO) is presented as a possible method for correcting these spatially-variant aberrations. MCAO is modelled to simulate the correction of aberrations, both in a simple model and for data measured in a *C. elegans* specimen.

7.1 Introduction

Imaging in optical microscopy has been seen to be significantly improved through the use of adaptive optics to correct for aberrations [Neil et al., 2000, Booth et al., 2002, Marsh et al., 2003, Booth, 2007, Fiolka et al., 2012, Jorand et al., 2012, Tang et al., 2012]. However, the sensorless adaptive optical methods presented in [Booth, 2006] and demonstrated in previous Chapters use a single metric relating to the aberrations across the entire image to optimise the aberration correction. Whilst this single aberration correction can dramatically improve the image quality, whether measured by total intensity,

brightness, sharpness or another metric, there are in practice instances where aberrations are not consistent across the entire field of view. Because of this, it is usual when using an optical microscope with adaptive optics to reduce the field of view as much as possible and concentrate on a small region. In this scenario, it is likely that any aberrations present are approximately constant across the field of view, and hence this is where the adaptive optics can be most effective. However, even in these situations the aberrations present may still vary across the image, for example, if an image has an aberration mode that is positive on one side and negative on the other, then the optimisation method may suggest a zero aberration. In this instance, reducing the field of view would reduce the aberration mode variation, but any correction would still be a compromise. Similarly, if an xz image is recorded it is highly likely that the depth-dependent aberrations will vary from top to bottom of the image. This effect is demonstrated in Fg. 7.1. Fg. 7.1(a)

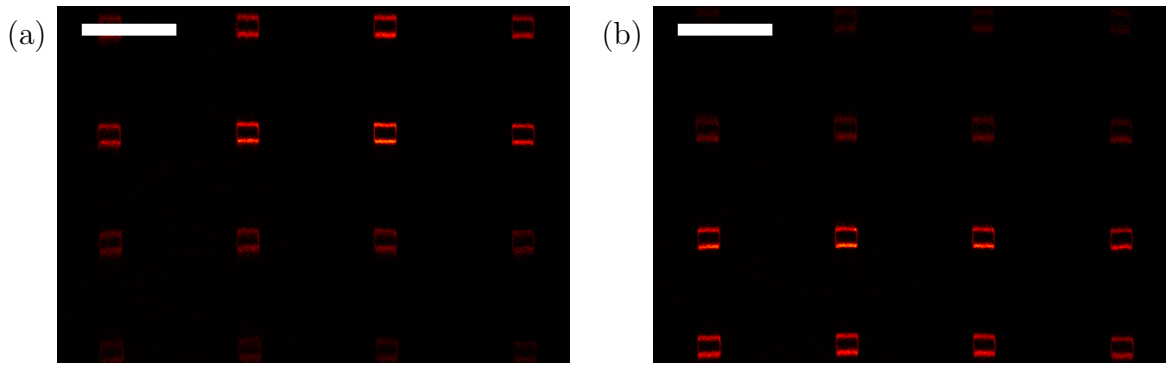


Figure 7.1: *xz images of a photonic lantern specimen taken using the THG microscope, with aberration correction applied correcting for the top two rows of waveguides (a) and the bottom two rows of waveguides (b). Scale bar is $40\mu m$.*

shows an xz slice of a photonic lantern (imaged previously in Section 5.3.3) taken using the THG microscope, using adaptive optics to correct for the aberrations affecting the upper two rows of waveguides. Fg. 7.1(b) shows an image of the same slice, but with the aberrations affecting the lower two rows of waveguides corrected for. Clearly the aberrations vary across the field of view, specifically from top to bottom, shown by the differing strength of signal exhibited by the upper and lower rows of waveguides in the two images.

For these reasons, it would be desirable to be able to correct for spatially variant aberrations. This would be possible for example in a scanning microscope if the adaptive

element could be changed at a sufficiently high speed as the beam was scanned. However, DMs are limited to approximately kHz change rates and are therefore too slow. In imaging systems (e.g. a conventional microscope) this would not work anyway, as the pixel data are acquired in parallel, so any adaptive optic correction is applied to all pixels simultaneously, so only a single correction phase is possible for the whole image. We investigate the measurement of spatially varying aberrations and suggest methods for their correction, particularly MCAO correction.

7.2 Measuring spatially variant aberrations

In order to correct for any spatially variant aberrations, we must first be able to measure the aberrations. Conceptually, one could measure the aberration at each point in an image when using a scanning optical microscope. From this, a detailed aberration map can be constructed. However, in all of the microscope setups used previously in this thesis, the preferred method of aberration measurement has been an indirect approach in which aberration biased images are acquired then processed (see Appendix C). For this case, a method of measuring spatially variant aberrations is described and demonstrated.

7.2.1 Calculating spatially variant aberrations

In image based sensorless adaptive optics, the method for determining the necessary aberration calculation for a particular image is described in Appendix C. A sequence of images with intentionally applied, predetermined aberrations is initially acquired, from which a series of quality metrics is obtained (e.g. total image intensity). These metrics in turn allow for the optimum aberration correction to be estimated. This process involves, in effect, taking an average across the image. Hence, corrective aberration amplitudes (or coefficients) determined in this way are also some form of average. Spatial variations are disregarded. Some spatial variation could be measured by subdividing the region of interest into smaller images before performing the above process on each sub-image, hence obtaining a different coefficient of each aberration mode for each sub region. This

provides a map of coefficients. The above method could also be performed with images of the whole region, but only confining the calculation (not the imaging) to a sub region. In the extreme (at least in concept) this could be on a pixel by pixel basis. Otherwise, some form of grouping of pixels, perhaps via smoothing, could be done first. From this we can now describe the aberration present, and how it varies, across the field of view.

Effects of smoothing

The pixel-by-pixel spatial measurement of aberration variation may require some smoothing to give a more accurate representation of the aberrations. Noise on individual pixels will result in the measurement, when taken pixel-by-pixel, also being noisy and so inaccurate. This can be improved by some form of averaging, for example taking the mean value of a small group of pixels. A second problem is that aberrations distort the point spread function (PSF). This can cause problems when performing the aberration measurement routine (as described in Appendix C), as local variations in the aberration coefficient can appear as artifacts. As an illustration of how this might arise, we can consider this simplified case of the image of a point object in a conventional microscope. The method explained in Appendix C requires the acquisition of images with bias aberrations applied. In the simplest variation of this approach, one can consider two measurements, one with a positive bias (M_+) and one with a negative bias (M_-). The correction aberration is then proportional to the difference $M_+ - M_-$ [Booth et al., 2002].

For the measurements of the images for M_+ and M_- the PSF will be aberrated, as shown for the measurement of coma when no initial aberration is present in Fg. 7.2(a) and Fg. 7.2(b) respectively. The difference between these two images is shown in Fg. 7.2(c). As the initial aberration was zero, so the resulting central aberration value from the calculation should be zero, which is clearly not the case in Fg. 7.2(c). This localised artefact could be alleviated if the a region somewhat wider than the focal spot could be averaged. For this reason, it is necessary to smooth the pixel values such that they are not distorted by spatial variations in the focal spot. Additionally, if the pixel dimension

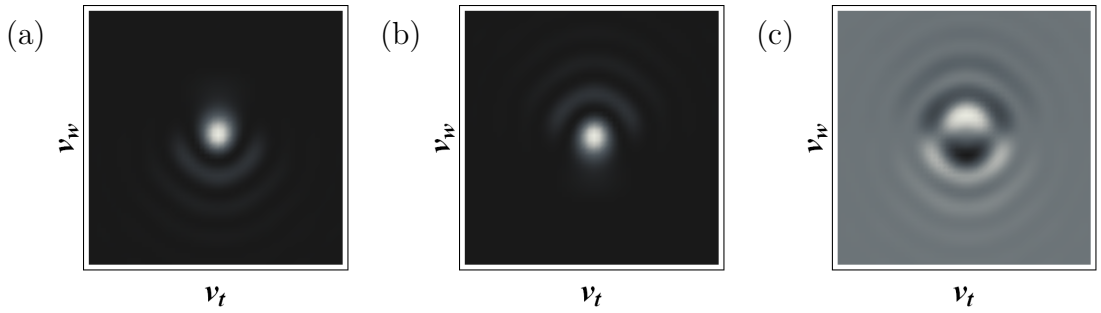


Figure 7.2: *Density plots showing the image of a point source in a conventional microscope, with* $0.7rad.$ *coma applied in the pupil (corresponding to the measurement for* M_+*) (a),* $-0.7rad.$ *coma applied in the pupil (corresponding to the measurement for* M_-*) (b) and the difference of the two (corresponding to the measurement for the aberration present,* d_{corr}*) (c).*

is small (it should be less than the FWHM to satisfy the Nyquist sampling criterion of the spatial frequencies), changes in the shape of the structure when aberrated and imaged could give misleading results (see e.g. Chapter 3). Smoothing, even over a small number of FWHMs, will help to reduce these effects. For these reasons it is necessary to determine the focal spot size in order to define a necessary smoothing region.

To find the focal spot radial dimension, we can utilise Eq. 2.13 to find:

$$\text{Focal spot diameter} \approx \frac{\lambda}{2NA} \tag{7.1}$$

This is true only in the radial dimension. For the axial focal spot dimensions, we must use Eq. 2.14, simplifying it to give:

$$\text{Focal spot length} \approx \frac{n\lambda}{(NA)^2} \tag{7.2}$$

In the case of the third-harmonic generation (THG) microscope used to take the images that follow, the focal spot size is given by:

$$\text{THG focal spot diameter} \approx \frac{1250nm}{2 \times 1.15} \approx 0.54\mu m \tag{7.3}$$

and

$$\text{THG focal spot length} \approx \frac{1.33 \times 1250nm}{1.15^2} \approx 1.26\mu m \tag{7.4}$$

We can use these values to indicate the level of smoothing that we should apply to our images. The smoothing should be a few times larger than each of these values.

There are two methods that spatially variant aberrations can be calculated from the images. As stated, the spatial aberration can be calculated by dividing the image into sub-regions and measuring the average aberration over each sub-region. It is the sizing of these sub-regions that determines if smoothing must be applied. If the sub-region is smaller than the focal spot (e.g. the size of a pixel, so the aberration is calculated on a pixel-by-pixel basis), the image must be smoothed before calculating the spatial aberrations. To smooth the image, it can be convolved with a radially symmetric Gaussian function with a FWHM equal to the focal spot size. This can be performed more quickly by multiplying the Fourier transform of the image with the Fourier transform of the Gaussian (the Fourier transform is itself also a Gaussian), then taking the inverse Fourier transform of the result. If the sub-region is approximately the same size as the focal spot itself, no smoothing of the image is required as the sub-region acts as an averaging. However, if the sub-region is larger than the focal spot, then the resulting spatial aberration map has a reduced effective resolution, but will be less susceptible to any noise present in the images (since it will be averaged out over a larger area). Images where the aberration is calculated over a smaller sub-region (i.e. focal spot size or less) will maintain the resolution of the microscope, but be more susceptible to noise and the spatial distribution of the PSF by the applied aberrations, so this compromise should be considered.

When considering the presence of spatially varying aberrations, by smoothing we are implicitly assuming that, for most structures, aberrations will vary gradually across the field of view. Depending on how gradual this variation is, it may be possible to apply a greater amount of smoothing without significant loss of spatially varying aberration detail. This would manifest itself as either smoothing with a larger Gaussian function, or else using sub-regions that are greater in size than the focal spot.

Calculation methods

For these calculations of the spatial aberrations, sets of five images were taken using a third-harmonic generation (THG) microscope with a MIRAO deformable mirror built into the pupil plane, as shown in Fg. 5.7. A single aberration mode was applied to each set with mode amplitudes of $-1.0, -0.5, 0.0, 0.5$ and 1.0 applied when imaging. These values are not easily expressed in any standard units (unlike the Zernike modes, which are normalised to have equal rms phase), since the modes used were the mirror modes calculated using the method described in Section 4.2. To measure the aberration indirectly, the method described in Apprendix C was utilised using image intensity (defined in this case as the sum of all pixel values) as the metric. To calculate the spatial aberrations, only part of each image was used calculate the aberration metric. Fg. 3.1 and Fg. 3.2 show the image intensity variation of different structures when imaged with specific aberrations in conventional and confocal or two-photon microscopes. For small aberration amplitudes, the plots of image intensity vs aberration mode amplitude can be approximated as Gaussian or quadratic fits. It is reasonable to assume that, in the THG microscope, the effect of aberrations can also be approximated in this way [Thayil et al., 2010].

Having acquired the five images for each aberration mode, the intensity data of each were fitted to a Gaussian model (using Matlab's inbuilt "trust region" algorithm). Due to the slow speed of this fit, this was not done on a pixel-by-pixel basis but rather the image was divided into sub-regions. Each sub-region consisted of pixel blocks of M×N pixels and a mean pixel intensity value was found for each such sub-region. The value of the equivalent block from each of the five images was fitted to the model. As sub-regions were used to calculate the aberration metric, it was not necessary to smooth the image prior to the fitting (as a mean value was used, so some smoothing had effectively been performed). Additionally, the image data were also fitted using the faster second-order polynomial fit. Since this method was faster, the metric could be calculated on a pixel-by-pixel basis, so it was necessary for the original images to be smoothed first, using the Gaussian smoothing function described above. To measure the spatial aberrations, first

the aberration amplitude with the peak image intensity for each sub-region or pixel of the image was calculated, by fitting the five metric values to a Gaussian or quadratic curve. These data were then used to produce an aberration mode map for the image region of the specimen.

7.2.2 Spatially variant aberration maps

Fg. 7.3(a) shows the raw THG microscope image of a *C. elegans* specimen section, with both system aberrations and global field-of-view aberrations corrected for. The pixel size of the image is approximately 0.1μm. Fg. 7.3(b) shows the resulting aberration map, calculated using the Gaussian fit method, from an image set taken from the mirror mode shown inset Fg. 7.3(b). Due to the speed of calculation it was impractical to do this calculation on a pixel-by-pixel basis. Indeed, even when choosing section sizes to match the focal spot size, the calculation time was still unacceptably long. This calculation was therefore done using eight-by-eight sub-regions, making each sub-region approximately 3μm $\times$3μm. This is much larger than the theoretical diffraction-limited focal spot (0.54μm), so no image smoothing was required prior to aberration calculation. Smoothing was however applied post-calculation, to show a more realistic gradual change in aberration, rather than eight-by-eight distinct values. This was performed by smoothing the aberration map with a Gaussian function, defined as:

$$g(x) = \exp\left[\frac{-x^2}{2\sigma^2}\right] \tag{7.5}$$

where the Gaussian FWHM (defined to be $2\sqrt{2\ln 2}\sigma$) was equal in size to the sub-regions.

Whilst Fg. 7.3(b) describes clearly (with use of the colour bar) the calculated spatially variant aberrations present, it may be somewhat misleading. Regions of the image that have structure present in them provide a good signal, and so provide a good estimate of the aberration present in the image. However, other regions in which there is little or no structure (i.e. dark regions in Fg. 7.3(a)) do not provide useful data for the metric to be calculated, so the metric is effectively calculated from the background

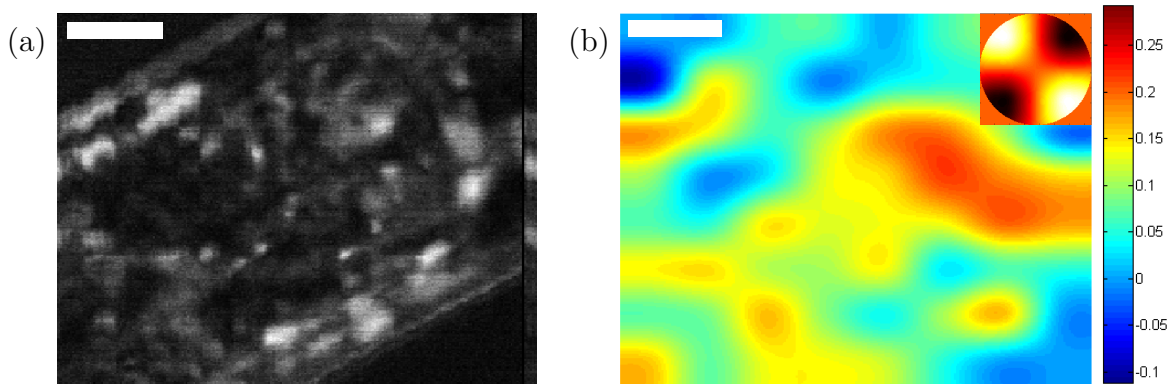


Figure 7.3: *Raw THG image of C. elegans specimen in the xy plane (a) and corresponding aberration map with colour scale (b). Inset: aberrating mirror mode (colour scale not shown). The aberration map was calculated using the Gaussian method, using* 8×8 *sections, each representing an area of* $3.13\mu m \times 3.08\mu m$*. Scale bar is* $5\mu m$*.*

signal and noise. It is therefore necessary that we distinguish between regions of more and less reliably calculated spatial aberration. The method used for this was to make the assumption that in regions where there is structure present in the original image, so there will be sufficient information with which to make an accurate prediction of the aberration. Equally, regions where there is little or no structure imaged there is not likely to be enough information to accurately predict the aberration present. Therefore, the aberration map was masked by the unaberrated original image (i.e. Fg. 7.3(a)) with reduced contrast applied. This has the effect of partially or completely obscuring the regions in the map where there was little or no signal respectively, whilst displaying clearly those regions where there was signal for the metric calculation. The resulting masked aberration map from Fg. 7.3(b) when masked by Fg. 7.3(a) is shown in Fg. 7.4(a).

Fg. 7.4 shows the masked aberration maps for the *C. elegans* specimen shown in Fg. 7.3(a) for four different mirror modes. These modes are very similar to Zernike aberration modes astigmatism (Fg. 7.4(a)), trefoil (Fg. 7.4(b)), coma (Fg. 7.4(c)) and spherical (Fg. 7.4(d)) and so will be discussed using these terms.

Across the image, the magnitude of the astigmatism-like mode remains low compared to the other modes tested, with most of the visible magnitudes in the centre of the amplitude range (Fg. 7.4(a)). Similarly, the magnitude of the trefoil-like mode is small across the image (Fg. 7.4(b)), but there does seem to be some positive aberration to one side and negative to the other. This is likely caused by the shape of the body and relative

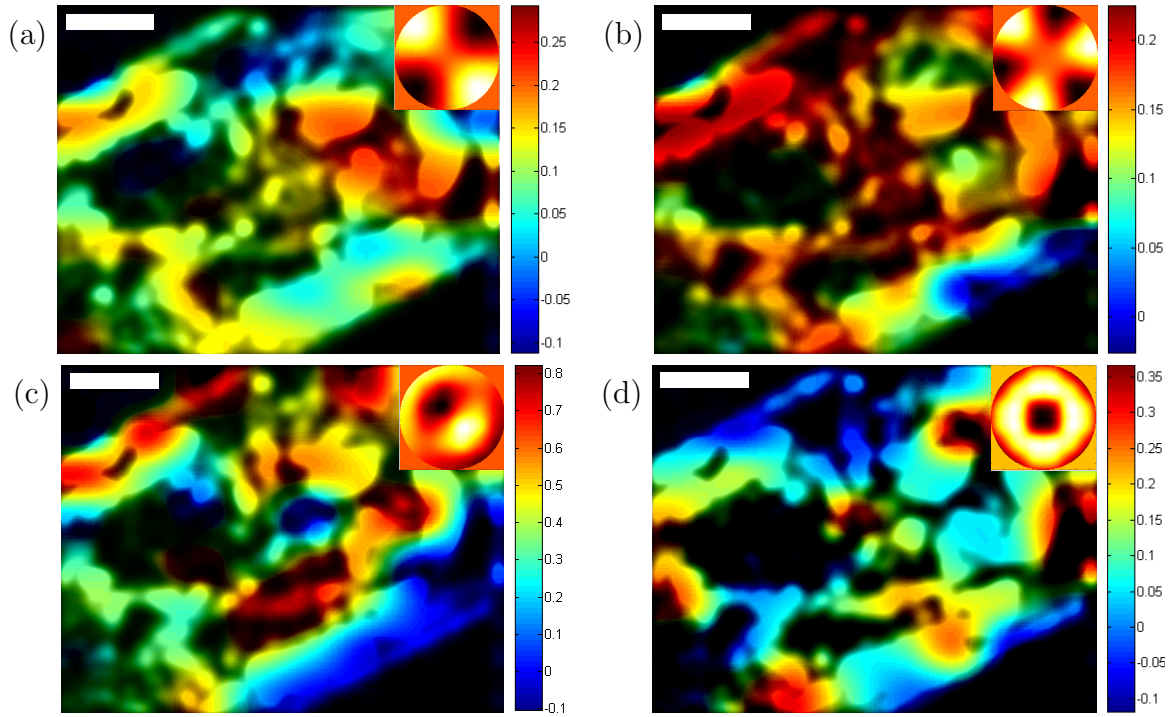


Figure 7.4: *Masked aberration maps for a C. elegans specimen with colour scales. Inset: aberrating mirror mode (colour scale not shown). The aberration map was calculated using the Gaussian method, using* 8×8 *sections, each representing an area of* $3.13\mu m \times 3.08\mu m$. *Scale bar is* $5\mu m$.

orientation of the trefoil-like mode. Given the *C. elegans*' cylindrically shaped body, it is reasonable to expect that for the coma-like mode with the orientation shown (Fg. 7.4(c)), the aberration is positive towards one side of the body and negative towards the other [Schwertner et al., 2004a]. This is reflected by the magnitude of aberration; there is more coma present than any other mode shown. From the body shape, we might also expect the amount of spherical aberration to be approximately constant along the axis of the body (bottom left to top right in the image), whilst having a similar magnitude along both edges. This is shown in Fg. 7.4(d), where there appears to be negative spherical-like aberration present along both edges, whilst through the middle of the body, the magnitudes of any aberration remain small.

So far, the results from the Gaussian fit method of calculation have been presented. Computationally, this is slow to calculate, so it would be useful if we were able to use the faster second order polynomial fit. In order for us to do this, we must first be confident that results produced by these methods are able to replicate those shown in Fg. 7.4.

Fg. 7.5 shows the masked aberration map from the second order polynomial fit. By comparing Fg. 7.5 to Fg. 7.4(c), the results seem to be very similar; the top left of the image has aberration values of around +0.8 in both, whilst bottom right regions are around -0.1 in Fg. 7.4(c) and -0.2 and lower in Fg. 7.5, showing a reasonable correlation in the two techniques.

Since the second order polynomial fit method is significantly quicker to computationally calculate, it is realistic to make aberration maps on a pixel-by-pixel level, rather than dividing the image into larger sub-regions first. This now means that, prior to calculation, the image must be smoothed to remove any sub-resolution sampling artifacts, or effects from the shape of the aberrated PSF. The image was smoothed with a Gaussian function where the FWHM was approximately the size of the radial focal spot, 0.5μm (or 5 pixels). For the second order polynomial fit, since there was significantly less smoothing than when using sub-regions (Fg. 7.3 and Fg. 7.4), the results were much more sensitive to noisy pixels. As such, a single noise-affected coefficient calculation could yield a very large or small value that would be much larger than the real aberration coefficient. When plotting the data, the range of coefficient values plotted was therefore restricted to values in the range that was measured (i.e. ± 1 in Fg. 7.5).

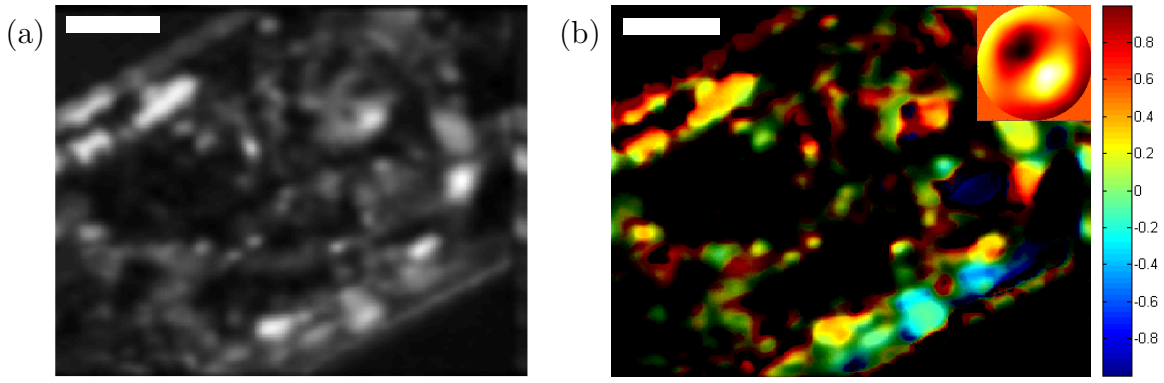


Figure 7.5: *C. elegans THG image, smoothed using* 0.5μ*m (5 pixel) Gaussian smoothing (a) and the masked spatial aberration map, calculated using the 2nd order polynomial fit, with colour scale (b). Inset: aberrating mirror mode (colour scale not shown). Scale bar is* 5μ*m.*

Fg. 7.5(a) shows the *C. elegans* specimen smoothed with a focal spot-sized Gaussian function. Fg. 7.5(b) shows the corresponding aberration map for the coma-like mirror mode, calculated using the second order polynomial method, limiting the resulting

aberration amplitudes to ±1. In the map, saturation of the aberration calculated is becoming evident due to the amplitude limitation imposed. By increasing the limits, the number of boundary lines is reduced but not eliminated, showing the effect of noise on the system (with no limits imposed, the peak aberration calculated was ±80, emphasising the issue of reducing the smoothing at the expense of noise susceptibility). Whilst not as pronounced, the results shown in Fg. 7.5(b) also exhibits the trend of positive aberration in the top left and negative in the bottom right seen previously in the Gaussian fit results (Fg. 7.4(c)). This does suggest that, despite the reduced smoothing in Fg. 7.5(b), equivalent results are obtained with both methods. But, since the calculation time is significantly reduced when using the second order polynomial fit, allowing the implementation of pixel-by-pixel mapping, this method gives us greater spatial precision than the Gaussian fit method.

Depth dependent aberrations

In the aberration maps discussed previously, because the images have been taken in a plane perpendicular to the illumination incidence direction, the aberrations have varied due to the overall specimen structure. Interpretation of these results was aided by the distinct cylindrical shape of the *C. elegans*. However, by imaging structures in planes that include the optical axis, we can observe the depth variations of certain aberrations, specifically spherical-like aberrations. Presented here are two more specimens, one biological and one artificial, where we are able to observe this depth variation when focussing through structures and more particularly show the spatially variations of aberrations across the field of view.

In the xy plane images seen previously, the smoothing Gaussian size determined by the focal spot lateral FWHM. However, in the xz plane the focal spot cross section is not radially symmetric. Therefore it was decided to take the average focal spot dimension to use as the smoothing Gaussian FWHM, which, from Eq. 7.3 and Eq. 7.4, is approximately 1μm.

Fg. 7.6(a) shows a THG mouse embryo xz image, smoothed using a Gaussian function

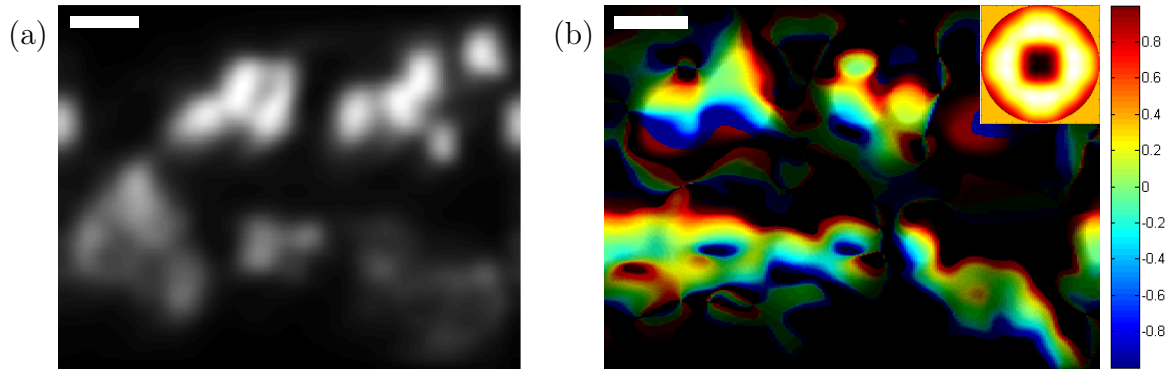


Figure 7.6: *THG xz image of mouse embryo specimen, smoothed using* $1\mu m$ *(10 pixel) Gaussian smoothing (a) and the masked spatial aberration map, calculated using the 2nd order polynomial fit, with colour scale (b). Inset: aberrating mirror mode (colour scale not shown). Scale bar is* $10\mu m$.

with a FWHM of 1μm. Fg. 7.6(b) shows the masked aberration map for the spherical-like mode calculated using a quadratic fit. The plot limits were set to mode amplitude of ± 2. Fg. 7.6(b) shows clearly the spherically aberrating effect of focussing through other structures. As the focal spot passes through the objects, the aberration changes from a positive aberration at the top to a negative aberration at the bottom. [Watanabe et al., 2010] showed that such bright objects in a mouse embryo were lipid objects. These have a higher refractive index than the surrounding medium and as such it is expected that they would produce aberrations, including spherical, such as that shown in Fg. 7.6(b).

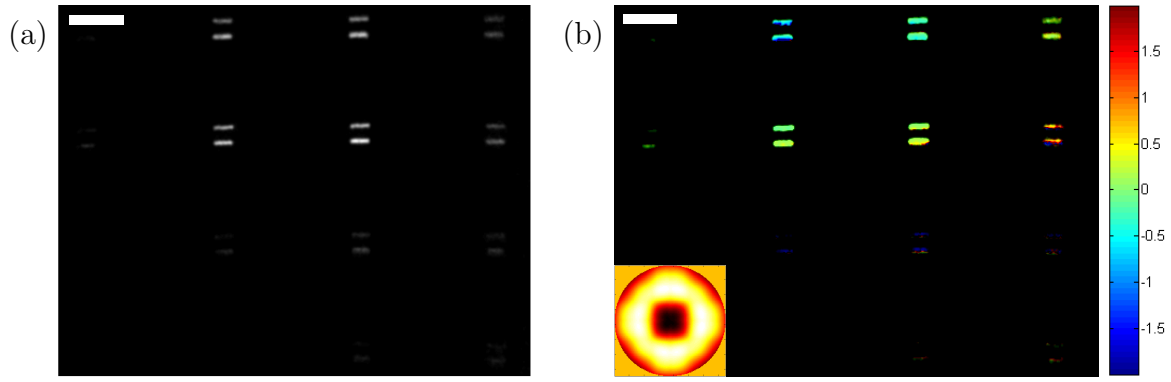


Figure 7.7: *Photonic lantern specimen, smoothed using* $1\mu m$ *(2.5 pixel) Gaussian smoothing (a) and the masked spatial aberration map, calculated using the 2nd order polynomial fit, with colour scale (b). Inset: aberrating mirror mode (colour scale not shown). Scale bar is* $20\mu m$.

Fg. 7.7(a) shows a THG image of the end section of a photonic lantern, consisting of a 4×4 array of single mode square waveguides (see Section 5.3.3 for a description

of the photonic lantern), smoothed using a Gaussian function with a FWHM of 1μm. As with Fg. 7.6, the aberration amplitudes were limited to ± 2, shown in Fg. 7.7(b). Since the scale of Fg. 7.7 is so large (approx. 130μm from top to bottom), and the spherical aberration was only corrected for one specific depth, it is to be expected that the aberration will vary in a linear fashion from the top to the bottom of the specimen. Indeed, this is shown (to some extent) in Fg. 7.7. The row of guides second from the top each have approximately zero aberration of this mode, since that was the level at which aberration correction was performed. The very fact that the second row has a very strong signal and as such is mostly very clear, whilst the other rows have much weaker signal and so not very distinct, is evidence in itself that the imaging of the rows becomes severely aberrated. Since regions with large aberration present have much weaker signals (as demonstrated by Fg. 3.1 and Fg. 3.2), the fact that particularly the lower rows of guides in Fg. 7.7 are difficult to distinguish suggests that they are extremely aberrated. Therefore, Fg. 7.7(a) looks as would be expected, but the method used to produce the aberration map Fg. 7.7(b) has given inconclusive results regarding aberration amplitude values, possibly due to the low signal to noise ratios in these regions.

The figures presented here have shown that it is possible to measure spatially variant aberrations within a range of specimens. The advantages of the method demonstrated include the simplicity of data acquisition (images are taken in the usual manner with simple, single-mode aberrations applied). By adjusting the degree of smoothing applies to the images it is also possible to control the balance of noise present with the achieved spatial resolution of the aberration measurement. However, this technique does require images with a strong signal level with aberrations that are within range and, ideally, not too complex (since only those modes measured can be calculated). However, this is true of most aberration measurement techniques, e.g. the Shack-Hartmann wavefront sensor.

7.3 Modelling multi-conjugate correction

In order to correct for spatially-variant aberrations, one possible method would be to change the adaptive element to correct for the phase aberration at each pixel. A significant problem of this is that the element would need to be driven at a speed equal to the pixel rate, which is in principle possible for slow scan rates (deformable mirrors currently have typical frame rates of $\approx 3kHz$, although they are quoted as capable of higher rates, $\approx 34kHz$ BM2 [2012]). However, for this the mirror shape needs to be calculated for each scan position. A more elegant solution is perhaps to have two adaptive elements, placing one in the pupil plane (as is standard practice in single-element systems) and a second outside the pupil plane, such that as the beam is scanned across the specimen, it is also scanned across the adaptive element, providing a unique phase addition for each scan position. Once the required DM shapes are found, the DMs would remain static during the image scan. This multi-conjugate adaptive optics (MCAO) setup greatly reduces the complexity of using one element in the pupil plane to correct for spatially variant aberrations, since regardless of image scan speed or region of interest, the adaptive element shapes would not need to be altered. This is similar to multiple adaptive element methods employed in astronomical adaptive optics [Salinari et al., 1994, Ellerbroek and Vogel, 2009, Hart, 2010]. However, the method used for astronomy positions each element conjugate to a specific layer of the atmosphere that is being corrected for [Davies and Kasper, 2012]. Therefore it is better to consider the astronomical method as multiple elements used independently, as each element corrects for a specific, independent source (i.e atmospheric layer) of aberrations, rather than multiple elements used in series, as is being proposed here [Kam et al., 2007]. The disadvantage of using the MCAO system where elements are positioned in series is that the exact location of each element is not only critical, but non-trivial to determine.

The correction aberrations achievable at each scan point would be limited by the shapes that could be created by each mirror. However, the inclusion of further DMs at other conjugate planes would increase the versatility of the system and the spatial complexity of aberrations that could be corrected. To simulate such a MCAO system

in a simple form, a one dimensional imaging system was modelled with a simulated circular object having a refractive index different to the surrounding medium. This was further expanded into a two-dimensional system with a simulated spherical aberrating object. Such a system is shown in Fg. 7.8. As the focussing cone is scanned across a specimen, some rays from the cone pass through the aberrating sphere and have a phase aberration contributed proportional to the ray's path through the sphere. By calculating the phase aberration contribution for each geometric ray, the pupil phase aberration can be calculated. This method does assume that there is no deviation of the ray when passing through the aberrating sphere.

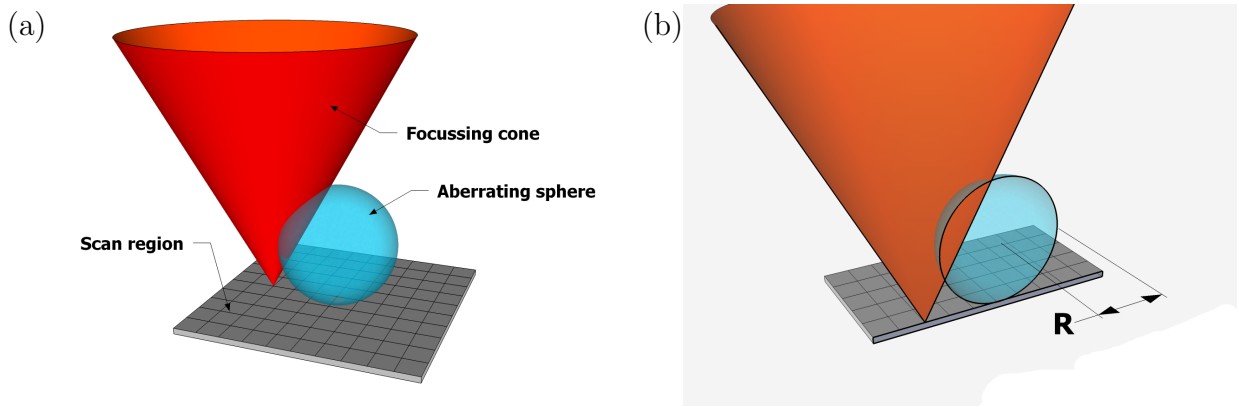


Figure 7.8: *Three-dimensional representation of the modelled aberrating system, showing the illumination focussing cone partially intersecting the aberrating sphere, and the region over which the illumination is scanned (a). The points scanned are at the intersections of the grid lines on the scan region. A slice through the model, used to model the one-dimensional aberrations (b). The radius of the circle (and sphere), R, is indicated.*

To correct for these phase aberrations, adaptive elements were added to the model (not shown in Fg. 7.8). One element was placed in the pupil plane, so adding a static phase function regardless of scan position, whilst others were added in other optical planes which added a different phase dependent on the scan position, so creating a multi-conjugate correction system.

To model correction for the spatially variant aberrations, the following method for both one- and two-dimensional (1D and 2D) aberrations was implemented. Firstly, the phase aberration for each scan position was calculated. This phase was then converted into orthogonal Legendre (for the 1D case) or Zernike (for the 2D case) modes and any piston and displacement modes (i.e. piston, tip, tilt and defocus modes) were removed

from the aberration. It is possible to try to correct also for these displacement modes, however, this would place significant extra demands on the adaptive elements. Hence the requirements were relaxed as image distortion can be tolerated, but not degradation of the focal quality. Removal of piston and displacement modes achieves this. The adaptive elements were modelled as being able to produce a finite number (seven/ten) of Legendre/Zernike modes (finite since the physical elements are realistically incapable of reproducing high order modes) and were adjusted to maximise the image Strehl ratio, a function relating to the image phase aberration, ϕ (as shown by Eq. 7.6), and a common measure of image quality [Born and Wolf, 1983].

$$Strehl\ ratio = \left| \frac{\sum \exp j(\phi - \hat{\phi})}{n_p} \right|^2 \tag{7.6}$$

where $\hat{\phi}$ is the displacement modes, removed from the total aberration, ϕ, normalised by the number of pixels, n_p. From the maximised Strehl ratio it was possible to compare the image Strehl ratio with no aberration correction applied, with traditional single-element correction and with multi-conjugate correction.

7.3.1 One-dimensional aberration correction

The system was initially modelled with no correction; one element correction with that element in the pupil plane; then with two elements, one of which was positioned in the pupil plane and the position of the second varied. The circle was defined as having a refractive index $n_1 = 1.36$ (i.e. typical of a biological structure [Pawley, 1995]) with the surrounding medium $n_0 = 1.33$ (i.e. water). The illumination wavelength modelled was $\lambda = 790$nm (typical of a two-photon microscope) and the aberrating sphere had a radius $R = 10\mu$m. The NA of the objective was $NA = 1.2$ (i.e. a typical water-based objective). Fg. 7.9 shows the one-dimensional system modelled. The circle provides a phase aberration with a refractive index mismatch, but any ray displacement was ignored. The extents of the focal cone are shown, as are the optical positions of three of the correction elements modelled.

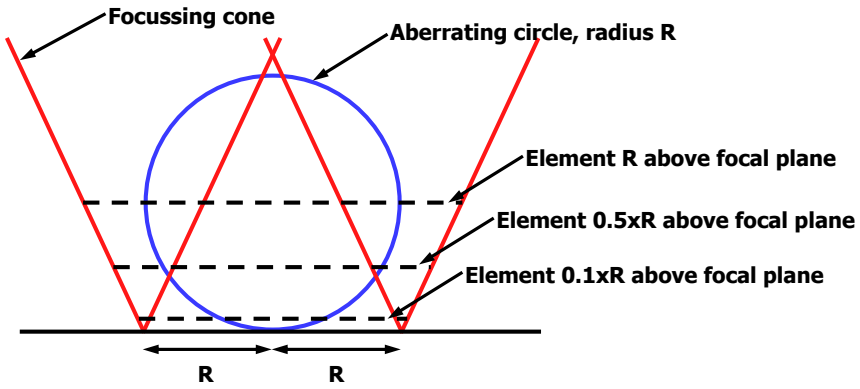


Figure 7.9: *The layout of the modelled scenario, including the aberrating circle, the focussing cones at the limits of the scan region, $\pm R$ (where R is the radius of the aberrating circle), and the optical positioning of corrective elements placed at distances $0.1 \times R$, $0.5 \times R$ and R above the focal plane. Not shown are the positions of the elements placed in the pupil plane and a distance of $10 \times R$ above the focal plane.*

Fg. 7.10 shows the results of the modelling. The effect of the aberrating circular object can be clearly seen in Fg. 7.10(a). The aberration from the centre-point of the circular object is well imaged, with the Strehl ratio dropping off as the focussing cone is only partially obscured, hitting a low at a scan position of $\approx \pm 0.5R$ before improving again as less of the focussing cone is obscured towards the extreme scan positions $\pm 1R$. Fg. 7.10(b) shows the effect of adding a single adaptive element in the pupil, as would be used in a typical adaptive microscope. The maximum Strehl has increased, but the optimisation was to increase the average Strehl ratio (shown above each plot), similar to what would be optimised in a real adaptive microscope. This has only increased by less than 1%, a negligible improvement. Whilst the capabilities of such adaptive microscopes has been demonstrated in Chapter 5, it is clear that in this particular configuration, the single element AO system would not provide good correction. Fg. 7.10(c), (d), (e) and (f) show the Strehl ratio improvement when adding a second adaptive element to a range of arbitrarily chosen multi-conjugate planes in the optical system. At each position, the size of the adaptive element was adjusted such that it matched the scan range in this optical plane. By adding a second element at a distance $10 \times R$ above the focal plane and finding the two element shapes that maximises the average Strehl ratio over the range of scan positions, the average Strehl ratio is improved by 44% compared to the uncorrected image (Fg. 7.10(c)). By moving the element closer to the focus,

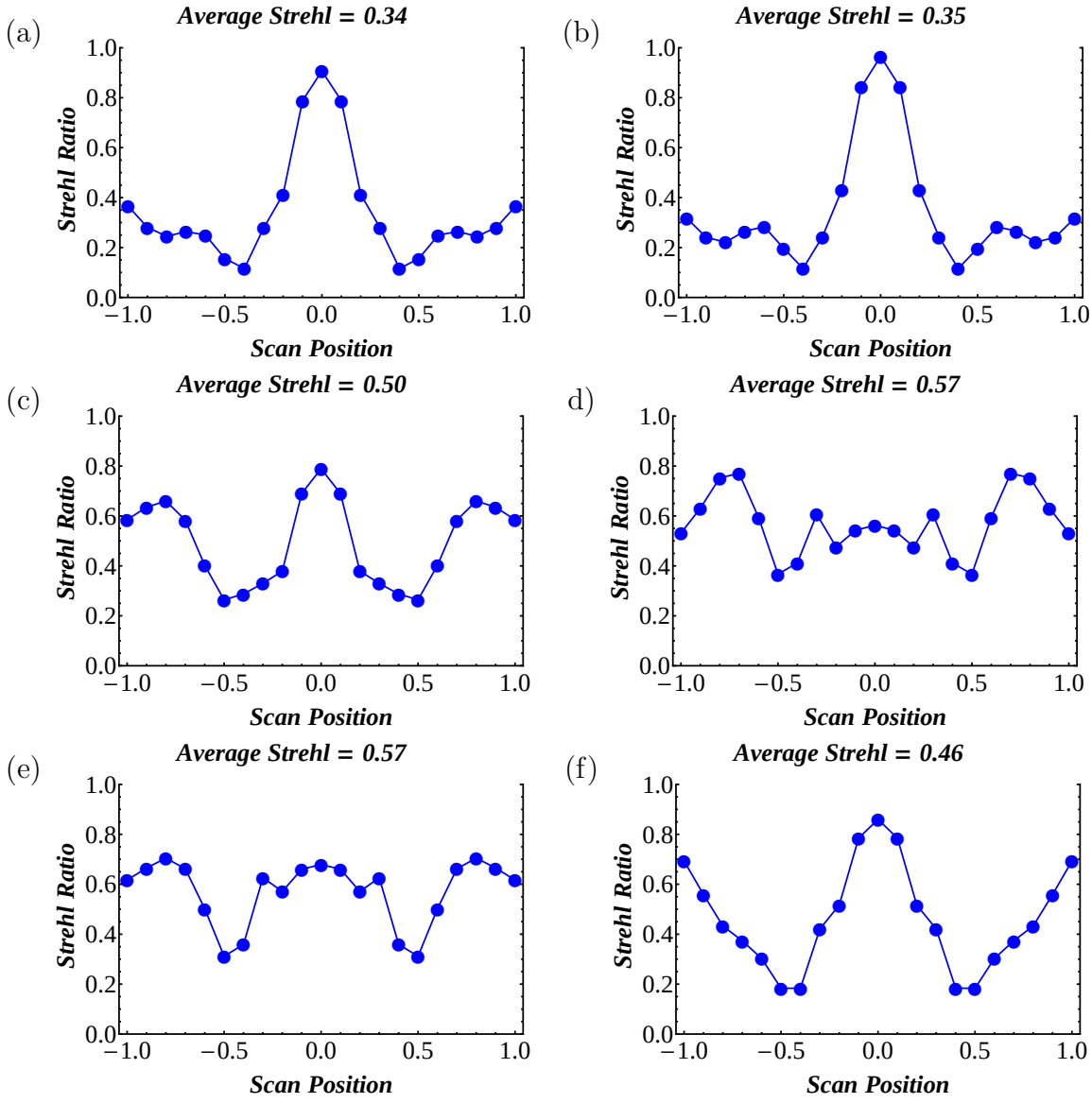


Figure 7.10: *The Strehl ratio across the field of view (i.e. for each scan position) with: no correction (a); one element correcting in the pupil (b); and two elements with one in the pupil and the second positioned a distance:* $10 \times R$ *above the focal plane (c);* R *above the focal plane (d);* $0.5 \times R$ *above the focal plane (e); and* $0.1 \times R$ *above the focal plane (f), where* R *is the radius of the aberrating circle.*

this can be improved further, improving the average Strehl by 65% (Fg. 7.10(d)) and 67% (Fg. 7.10(e)) compared to the uncorrected case when positioning the elements a distance R and $0.5 \times R$ above the focal plane respectively. However, since the adaptive elements have been modelled as only having the capability to replicate the first seven Legendre polynomials, this convergence does not continue indefinitely; by placing the second element a distance $0.1 \times R$ above the focal plane, the improvement drops back to 35% when compared to the uncorrected case (Fg. 7.10(f)). This is because, when

positioning the adaptive element too close to the focal plane, the aberration changes are too extreme for the element to replicate when it is limited to only the lower order Legendre polynomials. If the element were allowed to replicate an infinite series of the Legendre polynomials then it would be able to compensate for the aberration completely (when positioned in the focal plane). However, this is not realistic for a real adaptive element, which is only able to produce a limited displacement between any two points on its surface. Fg. 7.10(e) shows the best correction of the conjugate positions tested with two elements in different conjugate planes. This positioning has given an image average Strehl of 0.57 and much of the image, apart from the two regions directly below the edge of the circle, has a Strehl ratio of > 0.6, which represents reasonable image quality across most of the image. This is a huge improvement on no correction (Fg. 7.10(a)) or single element correction (Fg. 7.10(b)), although the peak Strehl ratio has been sacrificed to improve the average image Strehl ratio.

Fg. 7.11 shows the modelling of systems with one to four corrective elements present to see how much the average Strehl ratio can be increased by the addition of further multi-conjugate adaptive elements. The effect of having one or two elements, when compared to an uncorrected setup (shown in Fg. 7.10(a)), has been discussed and the Strehl ratios and the corresponding shapes of the corrective elements are shown in Fg. 7.11(a), (b), (c) and (d). The first element was placed in the pupil plane and the second at a position $0.5 \times R$ above the focal plane, since this was the position that saw the greatest improvement in Strehl ratio in Fg. 7.10. Adding a third adaptive element, positioned in this demonstration at a distance R above the focal plane, the average Strehl ratio is further improved to 73% above the uncorrected example (see Fg. 7.11(e)). Fg. 7.11(f) shows the shape of the three corrective elements, when each is restricted to the first seven Legendre polynomials, to produce this improvement. Fg. 7.11(g) shows the increase in the average Strehl ratio made when using four adaptive elements, an improvement of 92% over the uncorrected case. Much of the Strehl ratio at individual points on the plot is up around 0.8, which is generally considered to be well corrected [Torok and Kao, 2007]. Fg. 7.11(h) shows the adaptive element shapes required for this correction.

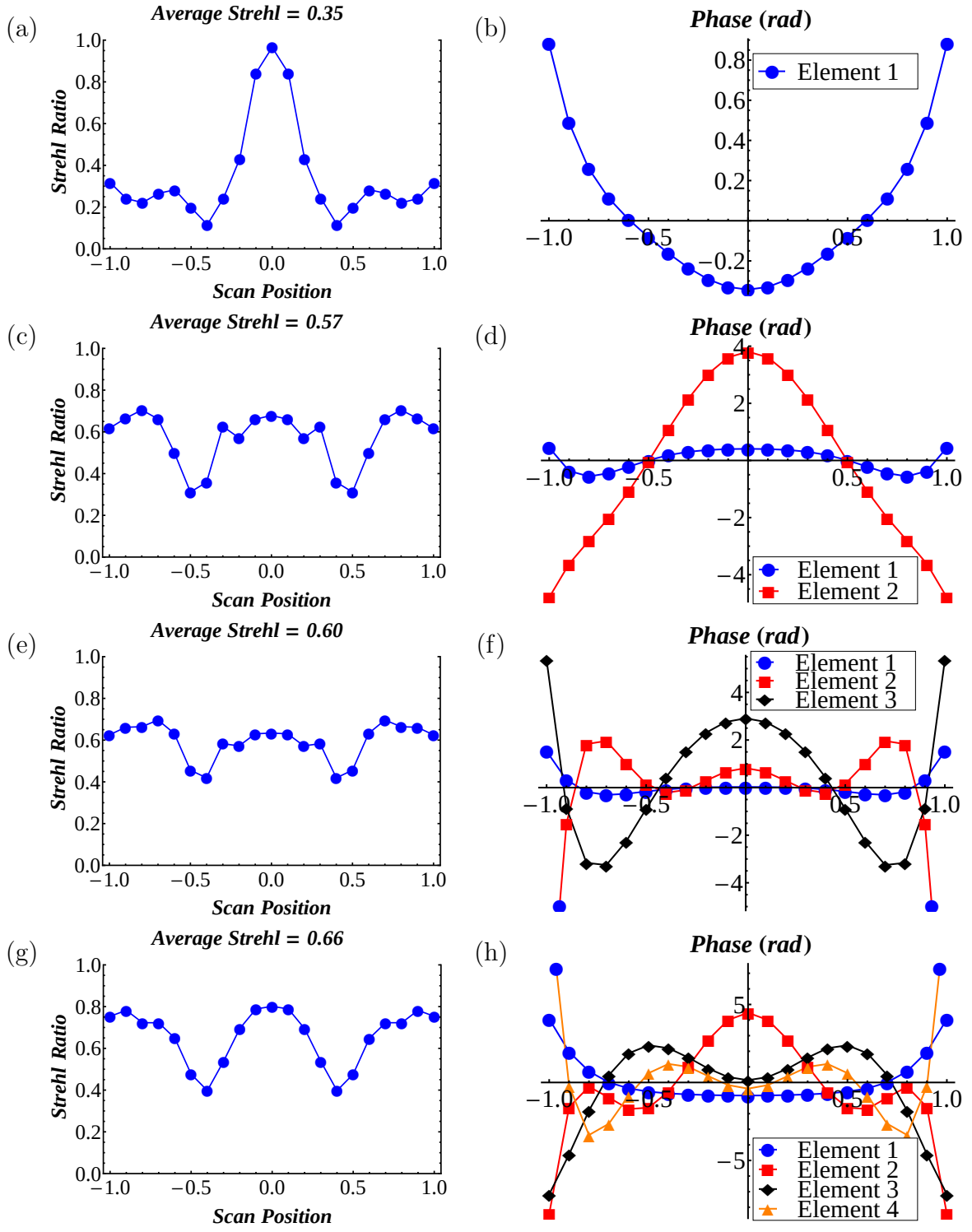


Figure 7.11: *The Strehl ratio across the field of view (i.e. for each scan position) and the corresponding adaptive element shapes with: one element correcting (a) and (b); two elements correcting (c) and (d); three elements correcting (e) and (f); and four elements correcting (g) and (h). The elements were positioned: Element 1 in the pupil plane; Element 2 at a distance of* $0.5 \times R$ *above the focal plane; Element 3 at a distance of* R *above the focal plane; and Element 4 at a distance of* $10 \times R$ *above the focal plane, where* R *is the radius of the aberrating circle.*

Although the shapes are more complex than when there are fewer elements present, they consist only of low order polynomials, and could be realistically reproduced for example by existing deformable mirrors.

The modelling of one-dimensional aberration correction has shown in principle how MCAO correction could function in a microscope. To model the more realistic systems, it is necessary to expand this model to correct for two-dimensional aberrations.

7.3.2 Two-dimensional aberration correction

To model two-dimensional aberrations in a three-dimensional system, the setup shown in Fg. 7.8 was used once more with the same parameters as were used in the one-dimensional case ($n_1 = 1.36$, $n_0 = 1.33$, $\lambda = 790$nm, $R = 10\mu$m, $NA = 1.2$). As before, the system was initially modelled with no aberration correction; then using single element correction with that element in the pupil plane; then adding further elements, one of which was positioned in the pupil plane and the position of the additional elements varied. The modes used for the correction must now be two-dimensional, so the Zernike polynomials were used. The adaptive element shapes were restricted to correction of modes 2 (tip) to 11 (spherical) to try and make the corrective shapes modelled realistic for replication on a commercial adaptive element.

Fg. 7.12 shows Strehl ratio results for 2D aberrations in a modelled 2D imaging system. Fg. 7.12(a) shows the modelled scan range of the system and the optical positioning of two ofthe corrective elements. Fg. 7.12(b) shows the Strehl ratio across the field of view with no aberration correction applied. The peak Strehl ratio is 0.57, which corresponds to a reasonably focussed image, however, as the average Strehl is 0.24, most of the field of view is not well imaged. By adding one adaptive element to the system (placed in the pupil plane), this makes a huge improvement: similar to the improvement demonstrated in the 1D system above, the peak Strehl ratio increases to 0.98, but more significantly the average Strehl ratio increases to 0.48, an increase of 99% on the uncorrected case. However, it is still predominantly the middle section of the image that is well imaged, with the edges showing a significantly lower Strehl ratio (see Fg. 7.12(c)).

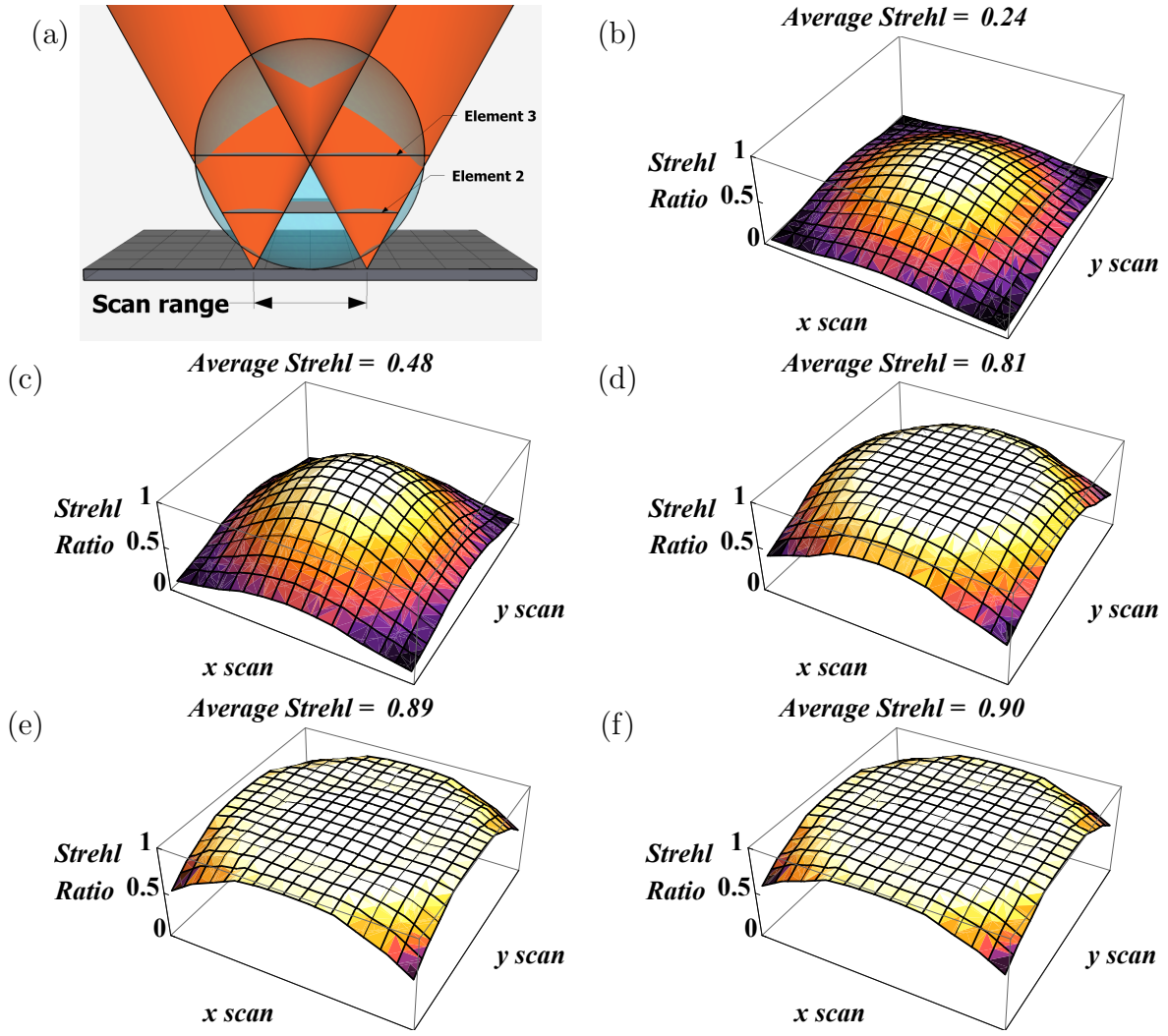


Figure 7.12: *The layout of the modelled scenario, including the aberrating sphere, the focussing cones at the limits of the scan region,* $\pm 0.5 \times R$ *(where* R *is the radius of the aberrating circle), and the optical positioning of corrective elements 2 and 3 (a). The Strehl ratio across the field of view (i.e. for each scan position) with: no aberration correction (b); one correction element (c); two correcting elements (d); three correcting elements (e); and four correcting elements (f). The elements were positioned: Element 1 in the pupil plane; Element 2 at a distance of* $0.5 \times R$ *above the focal plane; Element 3 at a distance of* R *above the focal plane; and Element 4 at a distance of* $10 \times R$ *above the focal plane.*

By adding a second adaptive element, positioned in this example in a plane $0.5 \times R$ above the focal plane, the peak Strehl remains up at 0.99 and the average Strehl increases to 0.81, an increase of 238% over the uncorrected case (see Fg. 7.12(d)). The significance now is that the central region remains up at an almost perfect Strehl ratio, but aberration correction is also improved in the peripheral regions. This trend continues by adding extra elements. Fg. 7.12(e) shows the Strehl ratio with three elements used for

aberration correction, the average Strehl now showing an improvement of 274% over the uncorrected case. These improvements are further, though incrementally, increased by adding a fourth element (see Fg. 7.12(f)), with the average Strehl increasing to 277% over the uncorrected model.

Fg. 7.12 has demonstrated the benefit of adding adaptive elements to a microscope with no aberration correction, or indeed adding further elements to create a microscope with multi-conjugate correction. From Fg. 7.12 it is clear that by adding more adaptive elements, whilst the average Strehl ratio does increase with each additional element, the additional benefit of new elements is reduced for each element already in place. As the specimen modelled in Fg. 7.12 is simple, both in terms of symmetry and complexity of aberration, other biological specimens may be more challenging to image and achieve such improvements in the Strehl ratio.

Fg. 7.13 shows the results from the same model, but with the scan range and corrective elements offset from the axis of the sphere, as shown in Fg. 7.13(a). This is, potentially, the hardest region over which to perform aberration correction since the aberrations are particularly complex when only part of the focussing cone passes through the spherical object. Fg. 7.13(b) shows the Strehl ratio without any aberration correction applied. By adding a single element in the pupil plane (Fg. 7.13(c)), the Strehl ratio can be improved by 68%, increasing to 90% with two or more multi-conjugate elements (see Fg. 7.13(d), Fg. 7.13(e) and Fg. 7.13(f)). This is not as significant an improvement as that demonstrated in Fg. 7.12, but up to 90% improvement is still significant, especially given that this is the most difficult region over which to perform aberration correction. These results therefore add weight to the claim that multi-conjugate adaptive optics can significantly improve the optical imaging system.

7.3.3 Simulation of correction for a real specimen

So far, all the results have been achieved through modelling an idealised specimen in the imaging system. By simulating correction for data from a real specimen that exhibits non-regularly varying spatial aberrations to the imaging process, the improvements of-

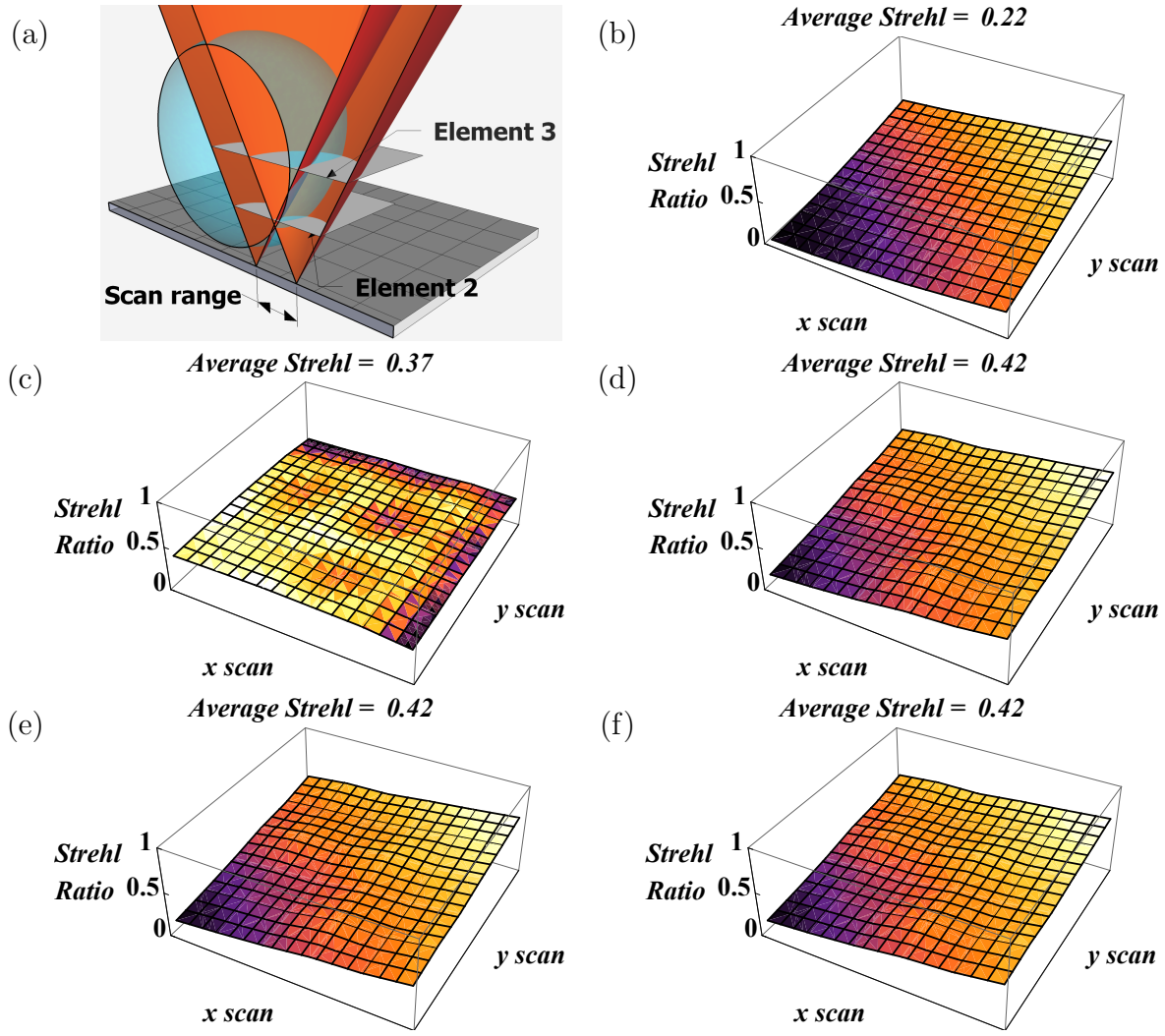


Figure 7.13: *The layout of the modelled scenario, including the aberrating sphere, the focussing cones at the limits of the scan region,* $0.5 \times R$ *to* $1.0 \times R$ *(where* R *is the radius of the aberrating circle), and the optical positioning of corrective elements 2 and 3 (a). The Strehl ratio across the field of view (i.e. for each scan position) with: no aberration correction (b); one correction element (c); two correcting elements (d); three correcting elements (e); and four correcting elements (f). The elements were positioned: Element 1 in the pupil plane; Element 2 at a distance of* $0.5 \times R$ *above the focal plane; Element 3 at a distance of* R *above the focal plane; and Element 4 at a distance of* $10 \times R$ *above the focal plane.*

fered by the multi-conjugate adaptive optics, particularly over single-element systems, can be compared. To test the effectiveness of a multi-conjugate adaptive optics system when imaging a real specimen, imaging of a *C. elegans* specimen was modelled using phase aberration data obtained using an interferometer. The phase aberration for each Zernike polynomial, from mode 2 to mode 22, was collected (data recorded by M. Schwertner, 2003 [Schwertner et al., 2004b]). Fg. 7.14 shows the phase aberration maps for

these modes.

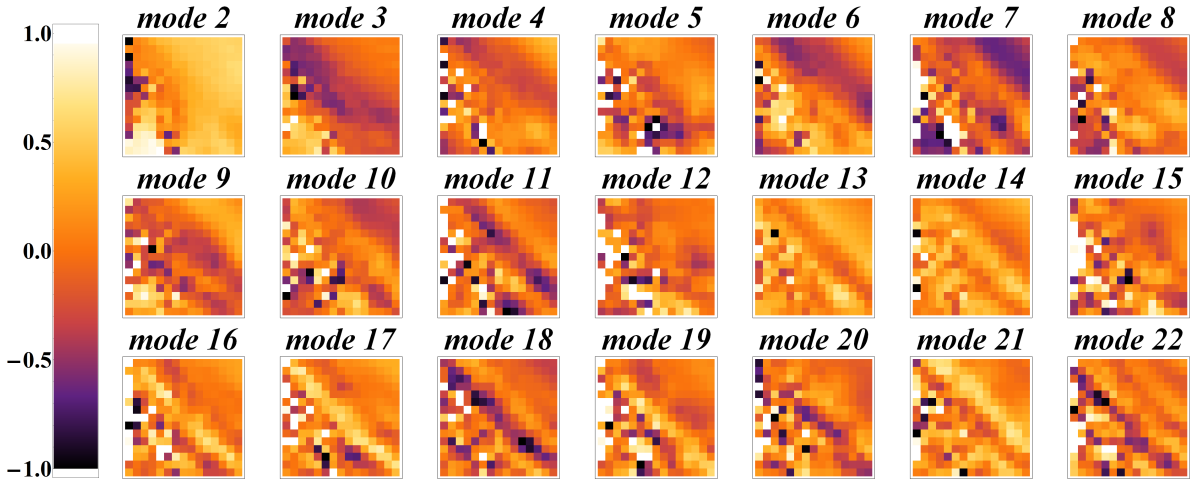


Figure 7.14: *Magnitude of Zernike aberrations, modes 2-22, of C. elegans specimen. Image is* $16\mu m$ *by* $16\mu m$ *and was imaged using a* $63 \times 1.2NA$ *water immersion objective. Aberration amplitude data is limited to* ± 1 *rad. These data were recorded by M. Schwertner, 2003 [Schwertner et al., 2004b].*

The phase aberration at each point in the image was constructed as the Zernike series using the coefficients obtained from the interferometer measurements. The optimal shapes for each correction element were found using the method explained in the previous section (Section 7.3.2). By summing the phase aberration contribution from each mode, the total phase aberration could be calculated. The resulting Strehl ratio for the aberrated image is shown in Fg. 7.15.

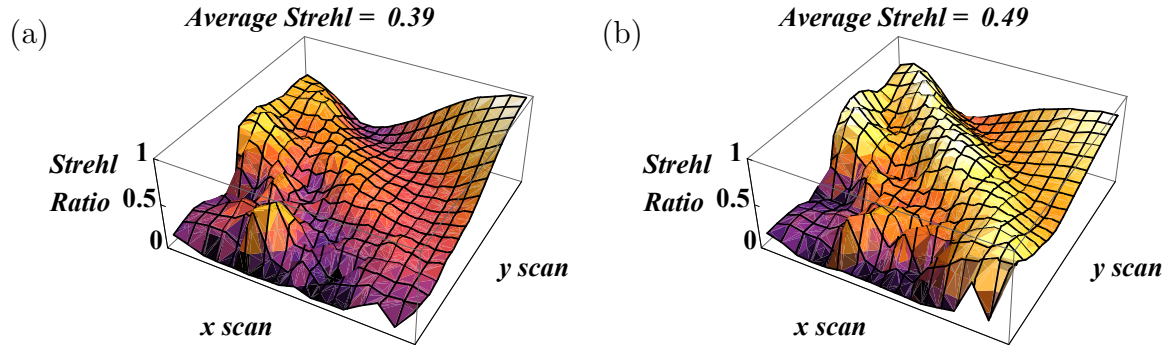


Figure 7.15: *The Strehl ratio across the field of view (i.e. for each scan position) for data gathered from a C. elegans specimen with no aberration correction (a) and four elements correcting (b). The elements were positioned: Element 1 in the pupil plane; Element 2 at a distance of* $0.5 \times R$ *above the focal plane; Element 3 at a distance of* R *above the focal plane; and Element 4 at a distance of* $10 \times R$ *above the focal plane, where* $R = 10\mu m$*. The image size (or effective scan range) is* $16\mu m \times 16\mu m$*.*

Fg. 7.15(a) shows the Strehl ratio across the field of view of the *C. elegans* spec-

imen, with no aberration correction. From Fg. 7.14 and Fg. 7.15(a), it is clear that the aberration amplitude towards the top right of the images is small and the variation smooth, whilst towards the bottom left the amplitude is much larger and the variation less smooth. It is probable, therefore, that the MCAO system would be able to correct for the top right region of aberrations much more easily than the bottom left region.

Fg. 7.15(b) shows the Strehl ratio over the image with correction modelled by four elements, one in the pupil plane and three in other optical planes. Comparing Fg. 7.15(b) to Fg. 7.15(a), it can be seen that the correction has improved the average Strehl ratio of the top right region (although the peak Strehl ratio has been reduced) and the back left to front right diagonal region. However, the front left region seems to have little or no improvement. This matches with the previous postulation, that better aberration correction would be achieved in the regions of constant or smoothly varying aberration than in those regions with high aberration variation. This aberration correction method optimised the average Strehl ratio of the complete field of view. This has clearly succeeded, since the average Strehl ratio has improved by 26% when compared to the uncorrected image. However, if there was some structure of interest, for example, in the lower left region of the image, where the Strehl ratio has had negligible change, then this correction would not be suitable. Therefore, the optimisation process was also repeated for specific regions of the image.

Fg. 7.16 shows the Strehl ratio for the complete field of view, but for the scenario where only a quarter of the field of view is used for the optimisation routine. Each quadrant optimisation, when compared to Fg. 7.15, shows some improvement over the optimisation for the complete field of view. For Fg. 7.16(a), Fg. 7.16(b) and Fg. 7.16(d) the improvement is large (the Strehl ratio is almost doubled) in comparison to Fg. 7.15(a). However, the improvement is less significant in Fg. 7.16(c). Fg. 7.15 and Fg. 7.16(c) both show this front left section to be the area worst affected by aberrations with a Strehl ratio of 0.21 with no correction, even with the modelled multi-conjugate correction applied the Strehl ratio remains down at approximately 0.3. To test the ability of the multi-conjugate correction, a region of 3.2μm $\times$3.2μm in the corner of the image

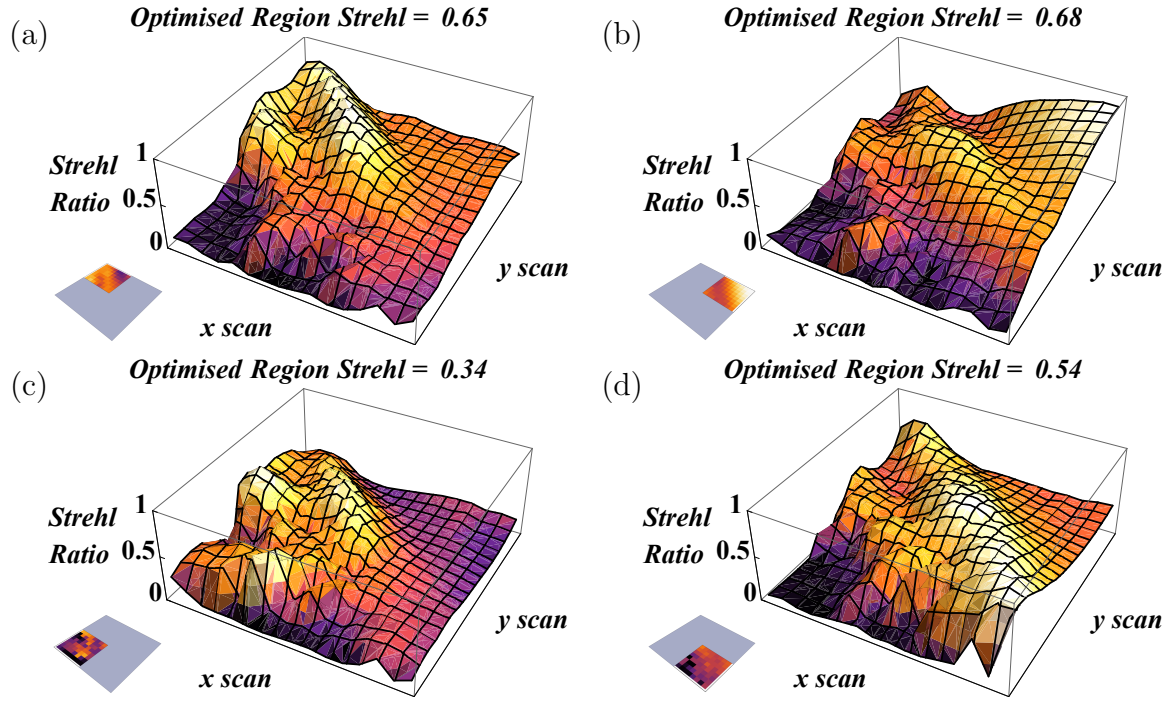


Figure 7.16: *The Strehl ratio across the field of view (i.e. for each scan position) for data gathered from a C. elegans specimen with aberration correction optimisation region shown in the inset. The average Strehl ratio for just the optimised region is shown. The corrective elements were positioned: Element 1 in the pupil plane; Element 2 at a distance of* $0.5 \times R$ *above the focal plane; Element 3 at a distance of* R *above the focal plane; and Element 4 at a distance of* $10 \times R$ *above the focal plane, where* $R = 10\mu m$*. The image size (or effective scan range) is* $16\mu m \times 16\mu m$*.*

was used for optimisation.

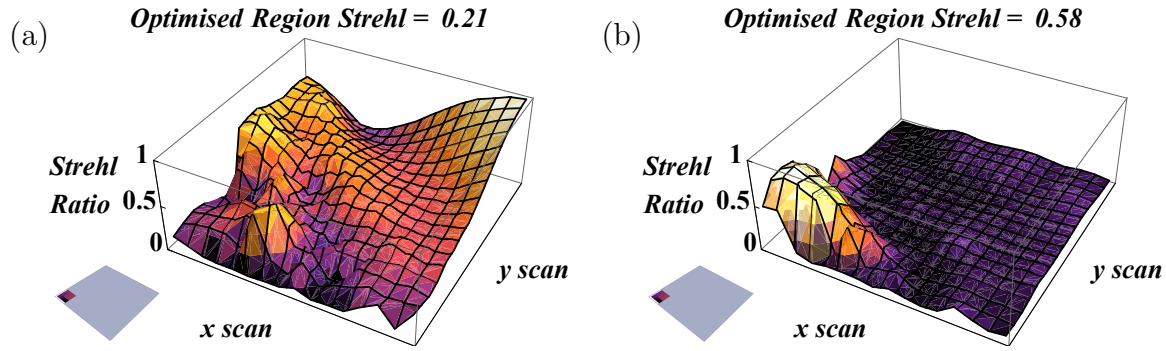


Figure 7.17: *The Strehl ratio across the field of view (i.e. for each scan position) for data gathered from a C. elegans specimen with no correction (a) and with aberration correction optimisation only over the front left* $3.2\mu m \times 3.2\mu m$*, region shown inset (b). The average Strehl ratio for the optimised* $3.2\mu m \times 3.2\mu m$ *region is shown for both. The corrective elements were positioned: Element 1 in the pupil plane; Element 2 at a distance of* $0.5 \times R$ *above the focal plane; Element 3 at a distance of* R *above the focal plane; and Element 4 at a distance of* $10 \times R$ *above the focal plane, where* $R = 10\mu m$*. The image size (or effective scan range) is* $16\mu m \times 16\mu m$*.*

Fig. 7.17(b) shows the Strehl ratio over the same *C. elegans* specimen but now only the front left 3.2μm $\times$3.2μm of the image has been used for the optimisation. With correction performed over quarter of the image, the average Strehl ratio for this region was approximately 0.3. However, now with the optimisation applied only over this worst affected region, the average Strehl ratio was increased to 0.58 (with a peak value > 0.8), a significant improvement in this region. This indicates that with multi-conjugate adaptive optics, even regions with extreme aberrations can be improved to achieve a reasonably clear image. A further outcome of this correction is that the Strehl ratio across the remainder of the image is significantly degraded, but if it were only the one small region that was of particular interest then this would not matter.

7.4 Conclusions

In this chapter, the phenomenon of spatially variant aberrations in microscopy have been introduced, methods have been presented for their measurement and options for correction have been discussed. Spatially variant aberrations have been shown to be present in a variety of both biological and artificial specimens. When aberrations vary across the field of view, then the simple image-based adaptive optic schemes utilised in Chapter 5 can break down.

The modelling of the spatially variant aberration correction has shown that for such aberrations, the introduction of multiple adaptive elements positioned in multi-conjugate planes in an imaging system can significantly improve the Strehl ratio for an image. Spatially variant aberrations can be largely compensated for, either by correcting for the full field of view or, if there is a specific region of interest, by correcting only over that particular region.

Whilst the potential benefits of an MCAO system are clear from the results, it is worth considering whether the extra effort of introducing more adaptive elements, and so greater complexity, to an optical system is worthwhile. To try to introduce spatially variant aberration correction, if the speed of a single adaptive element was increased, then it would be possible without introducing additional adaptive elements. However,

this may in itself introduce additional issues. For example, if the aberration present in each individual pixel is corrected for independently, any residual displacement introduced by the adaptive element will distort the data and produce an imprecise image. Therefore, it would seem preferable to introduce additional adaptive elements to avoid such image distortions. But, given that the MCAO system works best when correcting for a small region (and in doing so limit the extent of the spatially varying aberrations), this is also the scenario where single element correction is most effective when dealing with spatially variant aberrations. However, even when imaging over a small field of view, for many specimens, particularly biological specimens, the spatially variant aberrations can be significant. Therefore, for these scenarios it may be worthwhile to introduce additional adaptive elements into the system. It is also discussed how the adaptive elements could be positioned in a practical MCAO system (see Appendix D).

Chapter 8

Conclusions and summary

Operation at the diffraction limit has been a goal of many optical system designs. This has particularly been the case for high resolution microscopes and related optical systems for quite some time. But it is only since the creation of the laser, and from it the emergence of scanning optical microscopy techniques, that imaging and fabrication with three dimensional resolution below the surface of a material has been widely used. However, the aberrations encountered when focussing into a specimen or substrate reduce the ability to work at or close to the diffraction limit. The use of adaptive optics has subsequently been applied to these high-resolution microscopes and laser fabrication systems in order to compensate for the effects of aberrations. It is the use of adaptive optics that the work presented in this thesis has endeavoured to investigate and apply.

The effect of aberrations on the intensity of different idealised specimen structures was modelled for the conventional and sectioning microscopes. It was shown that, whilst the intensity of all structures was reduced in the presence of aberrations, the degree to which each was reduced varied. The consequence of this was that the contrast between different structures varied to different extents, so that in an aberrated image it may be possible for some structures to be visible whilst others are not. Specifically, finer specimen structures are likely to be harder to distinguish than larger structures. Furthermore, upon observation of such an aberrated image it may be possible to misinterpret results when small fluorescent objects are not visible but a fluorescent background is. For such a scenario, confocal and two-photon microscopy was shown to be preferable to

conventional microscopy due to the increased contrast between small and large objects. However, since all were negatively affected by aberrations it is therefore essential to correct for aberrations in order to produce reliable images, for which the use of adaptive optics was investigated.

Having built adaptive elements, such as deformable mirrors (DMs), into the optical setups, it is challenging but necessary to implement a system of control to produce the ideal shape of the element with which to correct for an aberration. By modelling the DM using the membrane equation, a set of aberration modes were produced that were idealised for that mirror. These modes were subsequently used to create empirical modes which optimised the indirect aberration correction routine for a two-photon microscope. It was shown that, for imaging below the surface of biological specimens, aberration correction is necessary in order to resolve the finer fluorescent structures. As these fluorescent structures bleach when exposed to the illumination, the optimised correction routine developed was ideal for this imaging. When imaging in non-biological specimens, for viewing structures such as waveguides the use of adaptive optics was essential. No signal was evident without the aberration correction, but detailed images of the precise structure were obtainable with the DM compensating for the aberrations.

In a fabrication system, the most significant aberration that affects the quality of fabrication is that due to a refractive index mismatch between immersion medium and substrate. A DM was installed into the setup and trained to correct for these depth-dependent aberrations by cancellation of a phase pattern displayed on a spatial light modulator (SLM). This training was shown to be successful for the range of depths over which the DM was trained, but when tested beyond this range using extrapolation of the control signals, it was shown to be much less accurate. By using the DM and SLM in series, micron scale structures were fabricated well beyond the DM training range, deep in the bulk of a diamond substrate. The use of both elements together also improved the fabrication efficiency over one element alone. This efficiency improvement is essential for direct laser writing in materials with a high refractive index, as otherwise the electric field used becomes so high that surface linear absorption becomes a possibility, restricting

the ability to fabricate deeper into the substrate bulk. This may in turn enable the manufacture of complex 3D structures in diamond and could, with further processing (e.g. removal of graphitised regions through etching) allow for the creation of devices such as high index contrast diamond waveguides.

Adaptive optics was shown to be extremely effective for use in both optical microscopy and fabrication systems. However, the use has been confined to positioning of the adaptive elements in the pupil plane. More sophisticated systems were also investigated by considering the possibility of alternative placement of the adaptive element, which would have the advantage of performing aberration correction that varied across the field of view. These multi-conjugate systems were modelled and shown to dramatically improve the Strehl ratio across the field of view for structures where the aberrations varied across the imaged region. This method holds potential for the future of adaptive optics in micron scale optical systems. Through the introduction of an adaptive element positioned outside the pupil plane, spatially variant image aberrations can be corrected for in a single image scan. However, this introduces issues of additional construction cost and complexity of the system. Compared to conventional adaptive systems, there is the further problem of aberration measurement to consider. Therefore, it is likely to be a non-trivial task to build such a system, but the benefits once built may be significant.

Appendix A

Mathematical functions

Bessel function

$$J_0(z) = \frac{1}{2\pi} \int_0^{2\pi} \exp[jz\cos(\theta - \phi)]\mathrm{d}\theta \tag{A.1}$$

$$aJ_1(a) = \int_0^a xJ_0(x)\mathrm{d}x \tag{A.2}$$

Convolution and correlation

Convolution and correlation are easily confused. The difference is subtle and is as follows.

$$\text{Convolution:} \qquad f(x) * g(x) = \int f(x - x')g(x')\mathrm{d}x' \tag{A.3}$$

$$\text{Correlation:} \qquad f(x) \otimes g(x) = \int f(x + x')g(x')\mathrm{d}x' \tag{A.4}$$

Convolution theorem

If a convolution is given by $f(x) * g(x)$, as defined in Eq. A.3, it can be redefined in frequency space using the convolution theorem:

$$f(x) * g(x) \longleftrightarrow F(m)G(m) \tag{A.5}$$

$$F(m) * G(m) \longleftrightarrow f(x)g(x) \tag{A.6}$$

where $F(m)$ and $G(m)$ are the Fourier transforms of $f(x)$ and $g(x)$ respectively, as defined by Eq. A.7.

Fourier transforms

The 2D Fourier transform can be defined as:

$$\mathfrak{F}\{f(x,y)\} = F(m,n) = \iint_{-\infty}^{\infty} f(x,y) \exp\left[-2\pi j(mx+ny)\right] \mathrm{d}x\mathrm{d}y \tag{A.7}$$

The inverse 2D Fourier transform can be defined as:

$$\mathfrak{F}^{-1}\{F(m,n)\} = f(x,y) = \iint_{-\infty}^{\infty} F(m,n) \exp\left[2\pi j(mx+ny)\right] \mathrm{d}m\mathrm{d}n \tag{A.8}$$

Appendix B

Zernike polynomials

The phase aberration $\phi(r,\theta)$ can be expressed as a Zernike series [Zernike, 1934, Tango, 1977]:

$$\phi(r,\theta) = \sum a_n^m Z_n^m(r,\theta) \tag{B.1}$$

where a_n^m is the amplitude of mode (m,n), Z_n^m is the Zernike polynomial and (r,θ) are normalised polar coordinates where the pupil radius is set at $r = 1$. Zernike polynomials are orthonormal functions over the unit circle and are most readily expressed in polar coordinates as [Noll, 1976]:

$$Z_n^m(r,\theta) = \begin{cases} m < 0 & \sqrt{2}\mathrm{R}_n^{-m}(r)sin(-m\theta) \\ m = 0 & \mathrm{R}_n^0(r) \\ m > 0 & \sqrt{2}\mathrm{R}_n^m(r)cos(m\theta) \end{cases} \tag{B.2}$$

where $\mathrm{R}_n^m(r)$ is defined as:

$$\mathrm{R}_n^m(r) = \sqrt{n+1} \sum_{s=0}^{(n-m)/2} \frac{(-1)^s (n-s)!}{s!\left(\frac{n+m}{2}-s\right)!\left(\frac{n-m}{2}-s\right)!} r^{n-2s} \tag{B.3}$$

The order n of the polynomial may be any positive integer or 0 but the index m is restricted to n, $\pm(n-2)$, ..., 0 (see table B.1). It is useful to be able to refer to the various modes by using a single index. The index i is commonly used, starting at 1 and increasing in integer steps for rising n then with rising magnitude of m, as shown in

table B.1 [Mahajan, 1994]. Some of the polynomials are shown in Fg. B.1.

i	n	m	$Z_i(r,\theta)$	Aberration term
1	0	0	1	piston
2	1	1	$2r\cos(\theta)$	tip
3	1	-1	$2r\sin(\theta)$	tilt
4	2	0	$\sqrt{3}(2r^2-1)$	defocus
5	2	2	$2\sqrt{3}r^2\cos(2\theta)$	astigmatism
6	2	-2	$2\sqrt{3}r^2\sin(2\theta)$	astigmatism
7	3	1	$2\sqrt{2}(3r^3-2r)\cos(\theta)$	coma
8	3	-1	$2\sqrt{2}(3r^3-2r)\sin(\theta)$	coma
9	3	3	$2\sqrt{2}r^3\cos(3\theta)$	trefoil
10	3	-3	$2\sqrt{2}r^3\sin(3\theta)$	trefoil
11	4	0	$\sqrt{5}(6r^4-6r^2+1)$	spherical
12	4	2	$\sqrt{10}(4r^4-3r^2)\cos(2\theta)$	astigmatism (2nd order)
13	4	-2	$\sqrt{10}(4r^4-3r^2)\sin(2\theta)$	astigmatism (2nd order)
14	4	4	$\sqrt{10}r^4\cos(4\theta)$	tetrafoil
15	4	-4	$\sqrt{10}r^4\sin(4\theta)$	tetrafoil
16	5	1	$2\sqrt{3}(10r^5-12r^3+3r)\cos(\theta)$	coma (2nd order)
17	5	-1	$2\sqrt{3}(10r^5-12r^3+3r)\sin(\theta)$	coma (2nd order)
18	5	3	$2\sqrt{3}(5r^5-4r^3)\cos(3\theta)$	trefoil (2nd order)
19	5	-3	$2\sqrt{3}(5r^5-4r^3)\sin(3\theta)$	trefoil (2nd order)
20	5	5	$2\sqrt{3}r^5\cos(5\theta)$	pentafoil
21	5	-5	$2\sqrt{3}r^5\cos(5\theta)$	pentafoil
22	6	0	$\sqrt{7}(20r^6-30r^4+12r^2-1)$	spherical (2nd order)
23	6	2	$\sqrt{14}(15r^6-20r^4+6r^2)\cos(2\theta)$	astigmatism (3rd order)
24	6	-2	$\sqrt{14}(15r^6-20r^4+6r^2)\sin(2\theta)$	astigmatism (3rd order)
25	6	4	$\sqrt{14}(6r^6-5r^4)\cos(4\theta)$	tetrafoil (2nd order)
26	6	-4	$\sqrt{14}(6r^6-5r^4)\sin(4\theta)$	tetrafoil (2nd order)
27	6	6	$\sqrt{14}(r^6)\cos(6\theta)$	hexafoil
28	6	-6	$\sqrt{14}(r^6)\sin(6\theta)$	hexafoil
29	7	1	$4(35r^7-60r^5+30r^3-4r)\cos(\theta)$	coma (3rd order)
30	7	-1	$4(35r^7-60r^5+30r^3-4r)\sin(\theta)$	coma (3rd order)

Table B.1: *The first 30 Zernike polynomials*

The mean of $Z_n^m(r,\theta)$ over the unit circle is zero, provided $n \neq 0$ (when $n = 0$ the mean value is 1 rad. rms). The polynomials form a complete function basis so can be combined to produced any phase aberration desired.

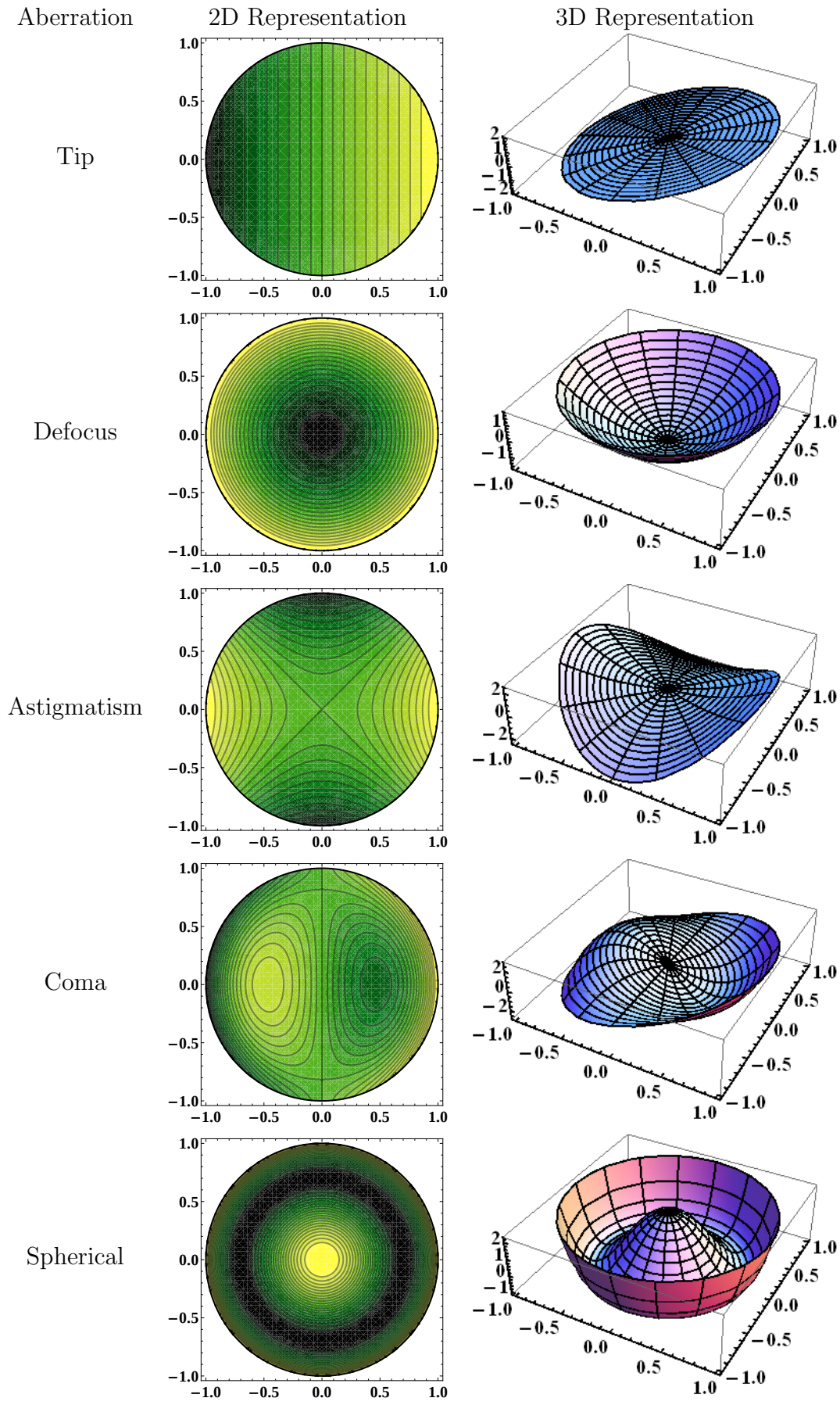


Figure B.1: *Images of some of the first Zernike polynomials*

Appendix C

Aberration correction routine

An indirect method of aberration correction is used throughout this thesis. Indirect aberration correction does not use a wavefront sensor to determine the aberration before correcting for it. Instead, an optimisation procedure is used to find the required aberration correction, by applying a quality metric value to intentionally aberrated images. This procedure is illustrated in Fg. C.1. First, an aberration mode is selected to be

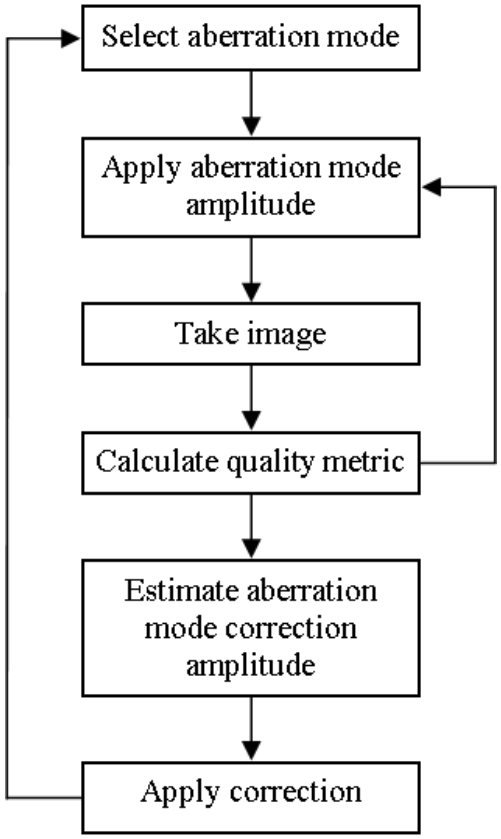


Figure C.1: *Flowchart of the process used to perform indirect aberration correction.*

corrected for. A small amplitude a of this mode is applied to the adaptive element and an image taken. A quality metric M is then found from the image (for example total image intensity, or image sharpness). Another small amplitude of the same aberration mode is then applied to the adaptive element and a second quality metric calculated. By using a sequence of these test aberrations and corresponding quality metrics, the optimal aberration mode amplitude can be determined which maximises (or minimises) the quality metric used. This process can be repeated for further aberration modes to mode completely correct for any aberration present [Booth, 2011].

Due to specimen fluorescence bleaching resulting from exposure, ideally the maximisation should be calculated from the smallest number of image measurements. This optimisation is also beneficial as it reduces the total time taken to perform the correction. The phase aberration was defined in terms of Zernike polynomials in Eq. 3.2 and Eq. B.1. By generalising this for any mode set X_i, we can write the aberration $\phi(r,\theta)$ as:

$$\phi(r,\theta) = \sum_{i=1}^{N} a_i X_i(r,\theta) \tag{C.1}$$

Using these definitions (or that of any mode set, and considering the aberration as consisting of two modes only), the optimisation metric M can be defined, close to the maximum, in a parabolic form [Booth, 2011]:

$$M \approx M_0 \left(1 - \sum_{k=1}^{N}\sum_{l=1}^{N} \alpha_{k,l} a_k a_l\right) \tag{C.2}$$

where M_0 and $\alpha_{k,l}$ are constants. This maximisation of M, using the coefficients of the two aberration modes, a_k and a_l, is illustrated in Fg. C.2(a). As the primary axes of the parabola do not coincide with those of the coefficients a_k and a_l, the two modes must be alternately maximised, resulting in repeat measurements (i.e. images) for correction of each mode. To optimise the maximisation, we can rewrite M in terms of one coefficient, by redefining the aberration mode set X_i to have the desired orthogonal properties:

$$M \approx M_0 \left(1 - \sum_{i=1}^{N} \beta_i d_i^2\right) \tag{C.3}$$

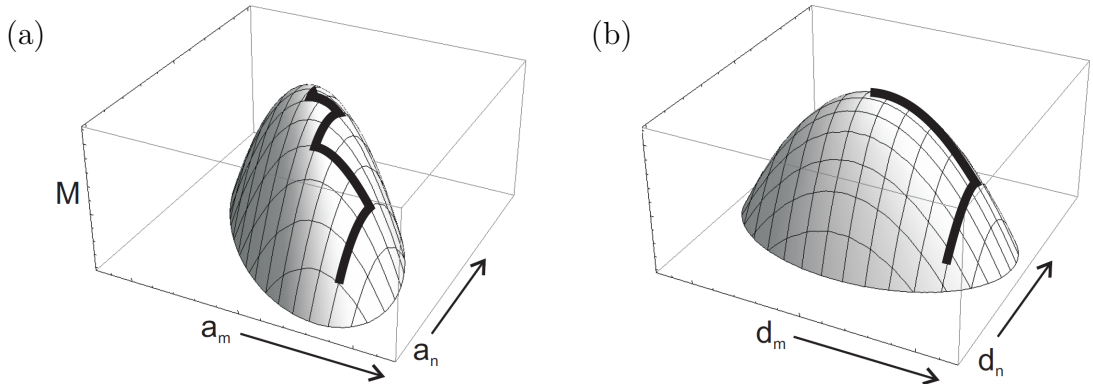


Figure C.2: *Illustration of maximisation of image metric M, using mode set X_i (a) and Y_i (b). Images taken from [Booth, 2011].*

where β_i is a set of constants and d_i is the set of coefficients for the new set of modes, Y_i. Now, when expanding M, each aberration mode appears independently of the others, so can be optimised independently. This is illustrated in Fg. C.2(b), where the primary axes of both the parabola and the new set of modes are coincident. Therefore each mode can be optimised separately, negating any repeat measurements required when defining the aberration using the Zernike (or other) mode set. This is done using the quadratic optimisation formula shown in Eq. C.4 [Booth, 2011]. Using the new mode set Y_i, an image is taken with no aberration applied ($d = 0$). From this, the image metric M_0 is calculated. Two further images are taken with aberration amplitudes $d = \pm b$ applied, from which the metrics M_+ and M_- are calculated. Using these data, the optimum correction value d_{corr} can be found.

$$d_{corr} = -\frac{b(M_+ - M_-)}{2M_+ - 4M_0 + 2M_-} \tag{C.4}$$

Appendix D

Design of multi-conjugate system

The main problem with the construction of a multi-conjugate imaging system would be the positioning of the non-pupil-plane adaptive elements. Through the use of some basic geometry, the plane that optimises the active area of an adaptive element can be determined. Fg. D.1 defines the geometrical terms used. The following equations can

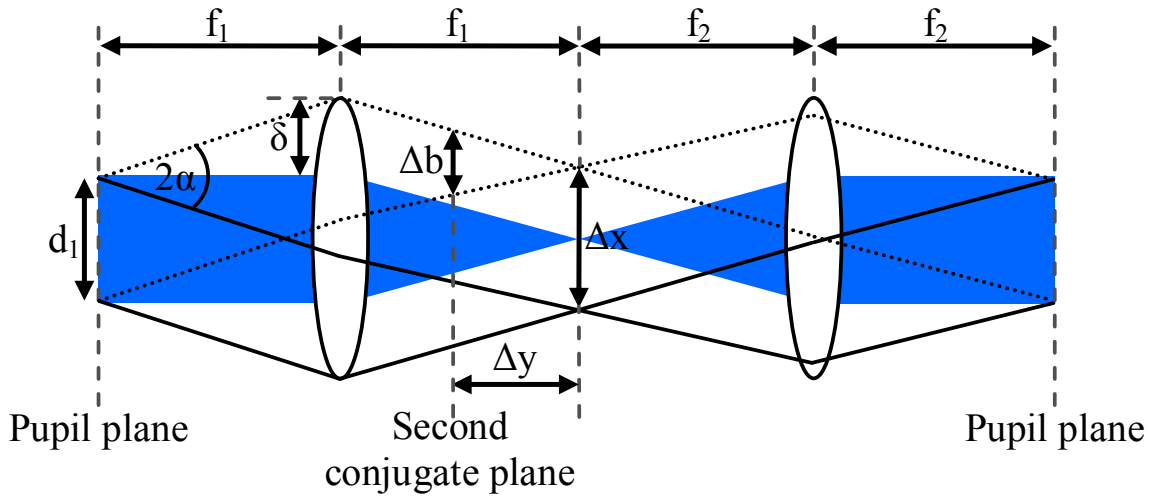


Figure D.1: *The geometrical terms used to determine the ideal multi-conjugate plane for one additional element are defined.*

be used to define the variables shown in Fg. D.1.

$$\triangle x = 2\delta = 2f_1 \tan\alpha \tag{D.1}$$

where $\triangle x$ is the total movement of the focal spot caused by scanning, δ is the positive displacement of the collimated beam entering the first lens, f_1 is the focal length of the first lens and α is the positive angle that the collimated beam is displaced. Observing now the second conjugate plane, we find:

$$d_2 = \triangle x + \triangle b \tag{D.2}$$

where d_2 is the diameter of the element that will be used in the second conjugate plane and $\triangle b$ is the width of the beam in the second conjugate plane. Finally, we introduce the position of the second conjugate plane, $\triangle y$:

$$\frac{\triangle b}{d_1} = \frac{\triangle y}{f_1} \tag{D.3}$$

where d_1 is the diameter of the incoming collimated beam. If desired, a first adaptive element could be positioned in the first pupil plane, in which case d_1 would be the diameter of the first adaptive element. Using Eq. D.1, Eq. D.2 and Eq. D.3, we can define the position of our multi-conjugate adaptive optic, $\triangle y$:

$$\triangle y = \frac{f_1}{d_1}(d_2 - 2f_1 \tan \alpha) \tag{D.4}$$

This allows us to position our multi-conjugate adaptive element using the focal length of the lens, the diameter of the incoming beam (or, potentially, the diameter of our adaptive element in the pupil plane), the diameter of the multi-conjugate adaptive element and the angle of scanning used. Using this calculation, it is possible to obtain values such that $\triangle y < 0$. This is not possible, and is generally resolved by adjusting the values used such that $\triangle x > d_2$, as it clearly must be from Eq. D.2.

Bibliography

Boston Micromachines, 2012. URL `http://www.bostonmicromachines.com/`.

Igor Aharonovich, Andrew D Greentree, and Steven Prawer. Diamond photonics. *Nature Photonics*, 5:397–405, July 2011.

Y Barad, H Eisenberg, M Horowitz, and Yaron Silberberg. Nonlinear scanning laser microscopy by third harmonic generation. *Applied Physics Letters*, 70(February): 1996–1998, 1997.

Martin J Booth. Direct measurement of Zernike aberration modes with a modal wavefront sensor. *Proc. SPIE*, 5162:79–90, December 2003.

Martin J Booth. Wavefront sensorless adaptive optics for large aberrations. *Optics Letters*, 32(1):5–7, January 2006.

Martin J Booth. Adaptive optics in microscopy. *Philosophical Transactions of the Royal Society*, 365(1861):2829–2843, 2007.

Martin J Booth. *Adaptive Optics in Microscopy*. Wiley, 1st edition, 2011.

Martin J Booth, Mark A A Neil, and Tony Wilson. Aberration correction for confocal imaging in refractive-index-mismatched media. *Journal of Microscopy*, 192(2):90–98, 1998.

Martin J Booth, Mark A A Neil, Rimas Juskaitis, and Tony Wilson. Adaptive aberration correction in a confocal microscope. *Applied Physical Sciences*, 99(9):5788–5792, April 2002.

Martin J Booth, Tony Wilson, Hong-Bo Sun, Taisuke Ota, and Satoshi Kawata. Methods for the characterization of deformable membrane mirrors. *Applied Optics*, 44(24): 5131–5139, August 2005.

Martin J Booth, Michael Schwertner, Tony Wilson, Masaharu Nakano, Yoshimasa Kawata, Masahito Nakabayashi, and Sou Miyata. Predictive aberration correction for multilayer optical data storage. *Applied Physics Letters*, 88:31109, January 2006.

Zsolt Bor. Femtosecond-resolution pulse-front distortion measurement by time-of-flight interferometry. *Optics Letters*, 14(16):862–864, August 1989.

M Born and E Wolf. *Principles of Optics*. Pergamon Press, 6th edition, 1983.

Ji-xin Cheng and X Sunney Xie. Green's function formulation for third-harmonic generation microscopy. *J. Opt. Soc. Am. B*, 19(7):1604–1610, 2002.

Richard Davies and Markus Kasper. Adaptive Optics for Astronomy. pages 1–47, 2012.

K M Davis, Kiyotaka Miura, N Sugimoto, and Kazuyuki Hirao. Writing waveguides in glass with a femtosecond laser. *Optics letters*, 21(21):1729–31, November 1996. ISSN 0146-9592.

Delphine Débarre, Willy Supatto, and Emmanuel Beaurepaire. Structure Sensitivity in Third-Harmonic Generation Microscopy. *Optics Letters*, 30(16):2134–2136, August 2005.

Delphine Débarre, Martin J Booth, and Tony Wilson. Image based adaptive optics through optimisation of low spatial frequencies. *Optics Express*, 15(13):8176–8190, June 2007.

Delphine Débarre, Edward J Botcherby, Martin J Booth, and Tony Wilson. Adaptive optics for structured illumination microscopy. *Optics Express*, 16(13):9290–9305, June 2008.

Delphine Débarre, Edward J Botcherby, Tomoko Watanabe, Shankar Srinivas, Martin J Booth, and Tony Wilson. Image-based adaptive optics for two-photon microscopy. *Optics Letters*, 34(16):2495–2497, August 2009.

Delphine Débarre, T Vieille, and Emmanuel Beaurepaire. Simple characterisation of a deformable mirror inside a high numerical aperture microscope using phase diversity. *Journal of microscopy*, 244(2):136–43, November 2011. ISSN 1365-2818.

Winfried Denk, James H Strickler, and Watt W Webb. Two-Photon Laser Scanning Fluorescence Microscopy. *Science*, 248(4951):73–76, April 1990.

Alberto Diaspro, Federico Federici, and Mauro Robello. Influence of refractive-index mismatch in high-resolution three-dimensional confocal microscopy. *Applied Optics*, 41(4):685–690, February 2002.

B L Ellerbroek and C R Vogel. Inverse problems in astronomical adaptive optics. *IOP Publishing*, 25:1–37, 2009.

Aurélie Facomprez, Emmanuel Beaurepaire, and Delphine Débarre. Accuracy of correction in modal sensorless adaptive optics. *Optics express*, 20(3):2598–612, January 2012. ISSN 1094-4087.

Barbara A Fairchild, Paolo Olivero, Sergey Rubanov, Andrew D Greentree, Felix Waldermann, Robert A Taylor, Ian Walmsley, Jason M Smith, Shane T Huntington, Brant C Gibson, David N Jamieson, and Steven Prawer. Fabrication of Ultrathin Single-Crystal Diamond Membranes. *Advanced Materials*, 20:4793–4798, October 2008.

Reto Fiolka, Ke Si, and Meng Cui. Complex wavefront corrections for deep tissue focusing using low coherence backscattered light. *Optics Express*, 20(15):16532–16543, 2012.

Rafael R Gattass and Eric Mazur. Femtosecond laser micromachining in transparent materials. *Nature Photonics*, 2(4):219–225, April 2008. ISSN 1749-4885.

S F Gibson and F Lanni. Experimental test of an analytical model of aberration in an oil-immersion objective lens used in three-dimensional light microscopy. *Journal of the Optical Society of America A*, 9(1):154–166, January 1992.

John M Girkin, Simon P Poland, and Amanda J Wright. Adaptive optics for deeper imaging of biological samples. *Current Opinion in Biotechnology*, 20:106–110, March 2009.

Joseph W Goodman. *Introduction to Fourier Optics*. Roberts & Company, 3rd edition, 2005.

Ronald P Grosso and Martin Yellin. The membrane mirror as an adaptive optical element. *J. Opt. Soc. Am. A*, 67(3):399–406, 1977.

Min Gu. *Advanced optical imaging theory*. Springer, 1st edition, 1999.

John W. Hardy. *Adaptive Optics for Astronomical Telescopes*. Oxford University Press, 1998.

M Hart. Recent advances in astronomical adaptive optics. *Applied Optics*, 49(16):17–29, June 2010.

Stefan W Hell, G Reiner, C Cremer, and E H K Stelzer. Aberrations in confocal fluorescence microscopy induced by mismatches in refractive index. *Journal of Microscopy*, 169(3):391–405, 1993.

Chia-Lung Hsieh, Ye Pu, Rachel Grange, and Demetri Psaltis. Digital phase conjugation of second harmonic radiation emitted by nanoparticles in turbid media. *Optics Express*, 18(12):12283–12290, June 2010.

Shijie Hu, Bing Xu, Xuejun Zhang, Jing Hou, Jian Wu, and Wenhan Jian. Double-deformable-mirror adaptive optics system for phase compensation. *Applied Optics*, 45 (12):2638–2642, April 2006.

N Huot, R Stoian, A Mermillod-Blondin, C Mauclair, and E Audouard. Analysis of the effects of spherical aberration on ultrafast laser-induced refractive index variation in glass. *Optics Express*, 15(19):12395–12408, September 2007.

Alexander Jesacher and Martin J Booth. Parallel direct laser writing in three dimensions with spatially dependent aberration correction. *Optics Express*, 18(20):21090–21099, September 2010.

Alexander Jesacher, Anisha Thayil, Kate Grieve, Delphine Débarre, Tomoko Watanabe, Tony Wilson, Shankar Srinivas, and Martin J Booth. Adaptive harmonic generation microscopy of mammalian embryos. *Optics Letters*, 34(20):3154–3156, October 2009.

Alexander Jesacher, Graham D Marshall, Tony Wilson, and Martin J Booth. Adaptive optics for direct laser writing with plasma emission aberration sensing. *Optics Express*, 18(2):656–661, January 2010.

Na Ji, Daniel E Milkie, and Eric Betzig. Adaptive optics via pupil segmentation for high-resolution imaging in biological tissues. *Nature Methods*, 7(2):141–147, February 2010.

Raphael Jorand, Gwénaële Le Corre, Jordi Andilla, Amina Maandhui, Céline Frongia, Valérie Lobjois, Bernard Ducommun, and Corinne Lorenzo. Deep and clear optical imaging of thick inhomogeneous samples. *PloS one*, 7(4):e35795, January 2012. ISSN 1932-6203.

Zvi Kam, Peter Kner, David Agard, and John W Sedat. Modelling the application of adaptive optics to wide-field microscope live imaging. *Journal of Microscopy*, 226(1): 33–42, April 2007.

Tyson N. Kim, Kyle Campbell, Alex Groisman, David Kleinfeld, and Chris B. Schaffer. Femtosecond laser-drilled capillary integrated into a microfluidic device. *Applied Physics Letters*, 86(20):201106, 2005. ISSN 00036951.

D A Kleinman. Theory of Second Harmonic Generation of Light. *Physical Review*, 128 (1961):1761–1775, 1962.

T V Kononenko, M Meier, M S Komlenok, S M Pimenov, V Romano, V P Pashinin, and V I Konov. Microstructuring of diamond bulk by IR femtosecond laser pulses. *Applied Physics A*, 90:645–651, 2008.

Virendra N Mahajan. Zernike Circle Polynomials and Optical Aberrations of Systems with Circular Pupils. *Supplement to Applied Optics, Applied Optics*, 33(34):8121–8124, December 1994.

Virendra N Mahajan. *Optical Imaging and Aberrations*. SPIE, 2001.

P N Marsh, D Burns, and John M Girkin. Practical implementation of adaptive optics in multiphoton microscopy. *Optics Express*, 11(10):1123–1130, May 2003.

C Mauclair, A Mermillod-Blondin, N Huot, E Audouard, and R Stoian. Ultrafast laser writing of homogeneous longitudinal waveguides in glasses using dynamic wavefront correction. *Optics Express*, 16(8):5481–5492, April 2008.

K Mecseki, A. P. Kovacs, and Z L Horvath. Measurement of Pulse Front Distortion Caused by Aberrations Using Spectral Interferometry. In *Light at extreme intensities: LEI 2009, AIP Conference Proceedings*, volume 1228, pages 190–196. American Institute of Physics, 2010.

Richard P Mildren and Alex Sabella. Highly efficient diamond Raman Laser. *Optics Letters*, 34(18):2811–2813, September 2009.

L P Murray, J Chris Dainty, and L Daly. Wavefront correction through image sharpness maximisation. *Proc. S.P.I.E., 'Opto-Ireland 2005: Imaging and Vision'*, 5823:40–47, 2005.

Mark A A Neil, Rimas Juskaitis, Martin J Booth, Tony Wilson, Tomokazu Tanaka, and Satoshi Kawata. Adaptive aberration correction in a two-photon microscope. *Journal of Microscopy*, 200(2):105–108, November 2000.

Robert J Noll. Zernike polynomials and atmospheric turbulence. 06856(October 1975): 207–211, 1976.

Dan Oron and Yaron Silberberg. Spatiotemporal coherent control using shaped, temporally focused pulses. *Optics Express*, 13(24):9903–9908, November 2005.

Carl Paterson, I Munro, and J Chris Dainty. A low cost adaptive optics system using a membrane mirror. *Optics express*, 6(9):175–85, April 2000. ISSN 1094-4087.

James Pawley. *Handbook of Biological Confocal Microscopy*. Springer, 1995.

Eva Rittweger, Kyu Young Han, Scott E Irvine, Christian Eggeling, and Stefan W Hell. STED microscopy reveals crystal colour centres with nanometric resolution. *Nature Photonics*, 3:144–147, March 2009.

P Salinari, C Del Vecchio, and V Biliotti. A Study of an Adaptive Secondary Mirror. *Proceedings of Active and Adaptive Optics*, pages 247–253, 1994.

P S Salter, Alexander Jesacher, J B Spring, B J Metcalf, N Thomas-Peter, Richard D Simmonds, N K Langford, Ian Walmsley, and Martin J Booth. Adaptive slit beam shaping for direct laser written waveguides. *Optics Letters*, 37(4):470–2, February 2012. ISSN 1539-4794.

N Sanner, N Huot, E Audouard, C Larat, P Laporte, and J P Huignard. 100-kHz diffraction-limited femtosecond laser micromachining. *Applied Physics B*, 80:27–30, 2005.

Michael Schwertner, Martin J Booth, Mark A A Neil, and Tony Wilson. Measurement of specimen-induced aberrations of biological samples using phase stepping interferometry. *Journal of Microscopy*, 213(1):11–19, January 2004a.

Michael Schwertner, Martin J Booth, and Tony Wilson. Characterizing specimen induced aberrations for high NA adaptive optical microscopy. *Optics Express*, 12(26): 6540–6552, 2004b.

Michael Schwertner, Martin J Booth, and Tony Wilson. Specimen-induced distortions in light microscopy. *Journal of Microscopy*, 228(1):97–102, October 2007.

Michael Shaw, Simon Hall, Steven Knox, Richard Stevens, and Carl Paterson. Characterization of deformable mirrors for spherical aberration correction in optical sectioning microscopy. *Optics Express*, 18(7):6900–6913, March 2010.

Richard D Simmonds, Patrick S Salter, and Martin J Booth. Adaptive optics for combined pulse front and phase front control, 2012.

Peter T C So, Chen-Yuan Dong, Barry R Masters, and Keith M Berland. Two Photon Excitation Fluorescence Microscopy. *Annu. Rev. Biomed. Eng*, 2:399–429, 2000.

Jason B Stewart, Alioune Diouf, Yaopeng Zhou, and Thomas G Bifano. Open-loop control of a MEMS deformable mirror for large-amplitude wavefront control. *Journal of the Optical Society of America*, 24(12):3827–3833, December 2007.

Jianyong Tang, Ronald N Germain, and Meng Cui. Superpenetration optical microscopy by iterative multiphoton adaptive compensation technique. *Proc Natl Acad Sci U S A*, 109(22):8434–8439, 2012.

William J Tango. The Circle Polynomials of Zernike and Their Application in Optics. *Applied Physics*, 13:327–332, 1977.

Anisha Thayil and Martin J Booth. Self calibration of sensorless adaptive optical microscopes. *Journal of the European Optical Society - Rapid Publications*, 6:1–8, 2011.

Anisha Thayil, Alexander Jesacher, Tony Wilson, and Martin J Booth. Influence of aberrations in third harmonic generation microscopy. *Journal of Optics*, 12(8), 2010.

Robert R Thomson, A S Bockelt, E Ramsay, S Beecher, A H Greenaway, Ajoy K Kar, and D T Reid. Shaping ultrafast laser inscribed optical waveguides using a deformable mirror. *Optics Express*, 16(17):12786–12793, August 2008.

Robert R Thomson, T a Birks, S G Leon-Saval, Ajoy K Kar, and J Bland-Hawthorn. Ultrafast laser inscription of an integrated photonic lantern. *Optics express*, 19(6): 5698–705, March 2011. ISSN 1094-4087.

P Torok and Fu-Jen Kao. *Optical Imaging and Microscopy*. Springer, 2007.

R K Tyson. *Principles of Adaptive Optics*. Academic Press, London, 1991.

G Della Valle, R Osellame, and P Laporta. Micromachining of photonic devices by femtosecond laser pulses. *Journal of Optics*, 11:1–18, 2009.

Biru Wang and Martin J Booth. Optimum deformable mirror modes for sensorless adaptive optics. *Optics Communications*, 282:4467–4474, 2009.

Tomoko Watanabe, Anisha Thayil, Alexander Jesacher, Kate Grieve, Delphine Débarre, Tony Wilson, Martin J Booth, and Shankar Srinivas. Characterisation of the dynamic behaviour of lipid droplets in the early mouse embryo using adaptive harmonic generation microscopy. *BMC cell biology*, 11:38, January 2010. ISSN 1471-2121.

A M Weiner. Femtosecond pulse shaping using spatial light modulators. *Review of Scientific Instruments*, 71(5):1929–1960, May 2000.

W. T. Welford. *Aberrations of Optical Systems*. A. Hilger, 1986.

Tony Wilson. *Confocal Microscopy*. Academic Press, 1990.

Tony Wilson and Colin J R Sheppard. *Theory and Practice of Scanning Optical Microscopy*. Academic Press, London, 1984.

Sean Wong, Markus Deubel, Fabian Perez-Willard, Sajeev John, Geoffrey A Ozin, Martin Wegener, and Georg von Freymann. Direct Laser Writing of Three-Dimensional Photonic Crystals with a Complete Photonic Bandgap in Chalcogenide Glasses. *Advanced Mater*, 18:265–269, 2006.

Jorg Wrachtrup and Fedor Jelezko. Processing quantum information in diamond. *Journal of Physics: Condensed Matter*, 18:S807–S824, May 2006.

D Yelin and Yaron Silberberg. Laser scanning third-harmonic-generation microscopy in biology. *Optics express*, 5(8):169–75, October 1999. ISSN 1094-4087.

Othman H Y Zalloum, Matthew Parrish, Alexander Terekhov, and William Hofmeister. On femtosecond micromachining of HPHT single-crystal diamond with direct laser writing using tight focusing. *Optics Express*, 18(12):13122–13135, June 2010.

F Zernike. Diffraction theory of the knife-edge test and its improved form, the phase contrast method. *Mon. Not. R. Astron. Soc.*, 94:377–384, 1934.

Lijun Zhu, Pang-Chen Sun, Dirk-Uwe Bartsch, William R Freeman, and Yeshaiahu Fainman. Adaptive control of a micromachined continuous-membrane deformable mirror for aberration compensation. *Applied Optics*, 38(1):168–176, January 1999a.

Lijun Zhu, Pang-Chen Sun, Dirk-Uwe Bartsch, William R Freeman, and Yeshaiahu Fainman. Wave-front generation of Zernike polynomial modes with a micromachined membrane deformable mirror. *Applied Optics*, 38(28):6019–6026, October 1999b.

Publications arising from this research

1. Richard D Simmonds, Patrick S Salter, Alexander Jesacher and Martin J Booth, "Three dimensional laser microfabrication in diamond using a dual adaptive optics system" *Optics Express*, vol. 19, issue 24, p. 24122-8, 2011.

2. Giovanni Carbone, Daniel Corbett, Steve J Elston, Peter Raynes, Alexander Jesacher, Richard D Simmonds, Martin J Booth, "Uniform Lying Helix Alignment on Periodic Surface Relief Structure Generated via Laser Scanning Lithography" *Molecular Crystals and Liquid Crystals*, vol. 544, issue 1, p. 37-49, 2011.

3. Patrick S Salter, Alexander Jesacher, Richard D Simmonds and Martin J Booth, "Aberration correction in laser micro-fabrication" *The Laser User*, 2011.

4. Patrick Salter, Richard Simmonds, Martin J Booth, "Active and adaptive optical methods for rapid fabrication of 3D photonic structures" *Proc. S.P.I.E.*, vol. 8249, p. 82490M-82490M-6, 2012.

5. R D Simmonds, T Wilson, M J Booth, "Effects of aberrations and specimen structure in conventional, confocal and two-photon fluorescence microscopy" *Journal of Microscopy*, vol. 245, issue 1, p. 63-71, 2012.

6. P S Salter, Alexander Jesacher, J B Spring, B J Metcalf, N Thomas-Peter, Richard D Simmonds, N K Langford, Ian Walmsley, Martin J Booth, "Adaptive slit beam shaping for direct laser written waveguides" *Optics Letters*, vol. 37, issue 4, p. 470-472, 2012.

7. Richard D Simmonds, Patrick S Salter and Martin J Booth, "Adaptive optics for combined pulse front and phase front control" *Patent Application No. GB1204846.8*, 2012.